

Advances in Meteorology

Variability of Atmospheric, Oceanic, and Hydrological Phenomena

Guest Editors: Leonard J. Pietrafesa, Alan Blumberg, and Xiaofeng Li





Variability of Atmospheric, Oceanic, and Hydrological Phenomena

Advances in Meteorology

**Variability of Atmospheric, Oceanic,
and Hydrological Phenomena**

Guest Editors: Leonard J. Pietrafesa, Alan Blumberg,
and Xiaofeng Li



Copyright © 2016 Hindawi Publishing Corporation. All rights reserved.

This is a special issue published in "Advances in Meteorology." All articles are open access articles distributed under the Creative Commons Attribution License, which permits unrestricted use, distribution, and reproduction in any medium, provided the original work is properly cited.

Editorial Board

José Antonio Adame, Spain
Cesar Azorin-Molina, Spain
Guillermo Baigorria, USA
Marina Baldi, Italy
Abderrahim Bentamy, France
Massimo A. Bollasina, UK
Stefania Bonafoni, Italy
Isabella Bordi, Italy
Alex Cannon, Canada
Claudio Carbone, Italy
Dominique Carrer, France
Charles Chemel, UK
Annalisa Cherchi, Italy
James Cleverly, Australia
Jill S. M. Coleman, USA
Gabriele Curci, Italy
Mladjen Ćurić, Serbia
Maher A. Dayeh, USA
Klaus Dethloff, Germany
Panuganti C. S. Devara, India
Julio Diaz, Spain
Arona Diedhiou, France
Stefano Dietrich, Italy
Eugenio Domínguez Vilches, Spain
Antonio Donateo, Italy
Igor Esau, Norway
Stefano Federico, Italy
Enrico Ferrero, Italy
Rossella Ferretti, Italy
Roberto Fraile, Spain
Charmaine Franklin, Australia
Jan Friesen, Germany

Maria Ángeles García, Spain
Herminia García Mozo, Spain
Eduardo García-Ortega, Spain
Luis Gimeno, Spain
Jorge E. Gonzalez, USA
Ismail Gultepe, Canada
Rafiq Hamdi, Belgium
Adel Hanna, USA
Hiroyuki Hashiguchi, Japan
Tareq Hussein, Jordan
Bradley G. Illston, USA
Ivar S A Isaksen, Norway
Yasunobu Iwasaka, Japan
Pedro Jiménez-Guerrero, Spain
Kuruvilla John, USA
Charles Jones, USA
Hann-Ming H. Juang, USA
George Kallos, Greece
Harry D. Kambezidis, Greece
Nir Y. Krakauer, USA
Simon O. Krichak, Israel
Hisayuki Kubota, Japan
Haim Kutiel, Israel
Richard Leaitch, Canada
Monique Leclerc, USA
Ilan Levy, Israel
Gwo-Fong Lin, Taiwan
Anthony R. Lupo, USA
Paolo Madonia, Italy
Andreas Matzarakis, Germany
Samantha Melani, Italy
Nicholas Meskhidze, USA

Christophe Messenger, France
Mario M. Miglietta, Italy
Takashi Mochizuki, Japan
Goro Mouri, Japan
Brian R. Nelson, USA
Efthymios I. Nikolopoulos, USA
Sandip Pal, USA
Giulia Panegrossi, Italy
Giulia Pavese, Italy
Kyaw T. Paw, USA
Olivier P. Prat, USA
Sara C. Pryor, USA
Philippe Ricaud, France
Tomeu Rigo, Spain
Filomena Romano, Italy
Jose Antonio Ruiz-Arias, Spain
Haydee Salmun, USA
Pedro Salvador, Spain
Arturo Sanchez-Lorenzo, Spain
Andres Schmidt, USA
Shraddhanand Shukla, USA
Fiona Smith, UK
Francisco J. Tapiador, Spain
Yoshihiro Tomikawa, Japan
Tomoo Ushio, Japan
Rogier Van Der Velde, Netherlands
Sergio M. Vicente-Serrano, Spain
Francesco Viola, Italy
Alastair Williams, Australia
Olga Zolina, France

Contents

Variability of Atmospheric, Oceanic, and Hydrological Phenomena

Leonard J. Pietrafesa, Alan Blumberg, and Xiaofeng Li

Volume 2016, Article ID 4525036, 1 page

Boundary-Layer Characteristics of Persistent Regional Haze Events and Heavy Haze Days in Eastern China

Peng Huaqing, Liu Duanyang, Zhou Bin, Su Yan, Wu Jiamei, Shen Hao, Wei Jiansu, and Cao Lu

Volume 2016, Article ID 6950154, 23 pages

Impacts of Wind Stress Changes on the Global Heat Transport, Baroclinic Instability, and the Thermohaline Circulation

Jeferson Prietsch Machado, Flavio Justino, and Luciano Ponzi Pezzi

Volume 2016, Article ID 2089418, 15 pages

Adjusting of Wind Input Source Term in WAVEWATCH III Model for the Middle-Sized Water Body on the Basis of the Field Experiment

Alexandra Kuznetsova, Georgy Baydakov, Vladislav Papko, Alexander Kandaurov, Maxim Vdovin, Daniil Sergeev, and Yuliya Troitskaya

Volume 2016, Article ID 8539127, 13 pages

Remote Sensing Observations of the Winter Yellow Sea Warm Current Invasion into the Bohai Sea, China

Jie Guo, Hua Zhang, Tingwei Cui, Yijun He, Jie Zhang, Kai Guo, Chawei Hou, and Rongjie Liu

Volume 2016, Article ID 8170296, 10 pages

Analysis of the Global Swell and Wind Sea Energy Distribution Using WAVEWATCH III

Kaiwen Zheng, Jian Sun, Changlong Guan, and Weizeng Shao

Volume 2016, Article ID 8419580, 9 pages

Impacts of Model Bias on the Climate Change Signal and Effects of Weighted Ensembles of Regional Climate Model Simulations: A Case Study over Southern Québec, Canada

Hyung-Il Eum, Philippe Gachon, and René Laprise

Volume 2016, Article ID 1478514, 17 pages

The Parameters Estimation for a $PM_{2.5}$ Transport Model with the Adjoint Method

Daosheng Wang, Ning Li, Youli Shen, and Xianqing Lv

Volume 2016, Article ID 9873815, 13 pages

Climatological Features of Korea-Landfalling Tropical Cyclones

Jae-Won Choi, Yumi Cha, Hae-Dong Kim, and Sung-Dae Kang

Volume 2016, Article ID 5051476, 15 pages

Latitudinal Change of Tropical Cyclone Maximum Intensity in the Western North Pacific

Jae-Won Choi, Yumi Cha, Hae-Dong Kim, and Sung-Dae Kang

Volume 2016, Article ID 5829162, 8 pages

A Semianalytical Model Using MODIS Data to Estimate Cell Density of Red Tide Algae (*Aureococcus anophagefferens*)

Lingling Jiang, Lin Wang, Xinyu Zhang, Yanlong Chen, and Deqi Xiong

Volume 2016, Article ID 1780986, 12 pages

Editorial

Variability of Atmospheric, Oceanic, and Hydrological Phenomena

Leonard J. Pietrafesa,¹ Alan Blumberg,² and Xiaofeng Li³

¹*The Coastal Carolina University, Conway, AR, USA*

²*The Stevens Institute of Technology, Hoboken, NJ, USA*

³*The National Oceanic & Atmospheric Administration, College Park, MD, USA*

Correspondence should be addressed to Leonard J. Pietrafesa; ljpietra@ncsu.edu

Received 27 December 2015; Accepted 27 December 2015

Copyright © 2016 Leonard J. Pietrafesa et al. This is an open access article distributed under the Creative Commons Attribution License, which permits unrestricted use, distribution, and reproduction in any medium, provided the original work is properly cited.

The temporal and spatial scales of atmospheric, oceanic, and hydrologic environmental phenomena span the time frame from isolated events to that of subseasonal variability in the Earth's interactively coupled atmospheric, oceanic, and hydrological systems globally. There are significant associated implications for global human and ecological systems and these have become an emerging topic around which issues of societal and economic value and sustainability can be examined and used for societal response and planning. In this special issue, massive observational data sets and mathematical modeling tools have been applied to couple the observed and/or modeled environmental processes to societal impacts. Examples include coastal and inshore flooding events, normally associated with tropical cyclones which, because of sea level rise, could extend into the winter season when extratropical cyclones are present and also include a higher frequency of flood events in the Americas, Europe, Asia, Africa, and Australia. The societal implications of these events are huge and other evolving and emerging phenomena in kind have been revealed.

The topics covered in this special issue generally include the following: feasibility and “proof-of-concept” studies utilizing diagnostic and prognostic tools; pilot to mature studies relevant to the use of atmospheric, oceanic, and hydrological data sets including in situ and remotely sensed data sets, to drive societally relevant research; modern analytics and informatics including utilizing environmental and socioeconomics data; numerical modeling results focusing

on leveraging interoperability and knowledge management; value assessments of environmental data, including investments in satellite and other technologies; studies using new methodological paradigms in environmental research; and environmental information that provides enabling capacity for environmental managers and society. The specific topics include the following: rainfall and cloud dynamics; flood hazard mapping by using geographic information systems and hydraulic models; the detection of abrupt changes in runoff and river discharge; the historical and future spatial and temporal variability of precipitation; the suitability and sustainability of water harvesting; the dynamics of a typhoon and a related high ozone episode; the forecasting of oceanic surface currents via the assimilation of radar data in a numerical model; the impact of wind stress on the global heat transport, thermohaline circulation, and oceanic instability; the onset and evolution of hydrological drought in human disturbed areas; projections of future drought hazard areas based on climate change scenarios; and the effects of climate and anthropogenic activity on hydrologic riverine features.

This special issue was intended to present scientific breakthrough results which are expected to reveal the couplings of environmental event scale with subseasonal variability scale to the implications for society at local to regional and global scale environments. It has succeeded in doing so.

*Leonard J. Pietrafesa
Alan Blumberg
Xiaofeng Li*

Research Article

Boundary-Layer Characteristics of Persistent Regional Haze Events and Heavy Haze Days in Eastern China

Peng Huaqing,¹ Liu Duanyang,² Zhou Bin,¹ Su Yan,¹
Wu Jiamei,¹ Shen Hao,¹ Wei Jiansu,² and Cao Lu²

¹Wuxi Meteorological Observatory of Jiangsu Province, Wuxi 214101, China

²Observatory of Jiangsu Province, Nanjing 210008, China

Correspondence should be addressed to Liu Duanyang; liuduanyang2001@126.com

Received 22 March 2015; Revised 1 June 2015; Accepted 4 June 2015

Academic Editor: Xiaofeng Li

Copyright © 2016 Peng Huaqing et al. This is an open access article distributed under the Creative Commons Attribution License, which permits unrestricted use, distribution, and reproduction in any medium, provided the original work is properly cited.

This paper analyzed the surface conditions and boundary-layer climate of regional haze events and heavy haze in southern Jiangsu Province in China. There are 5 types with the surface conditions which are equalized pressure (EQP), the advancing edge of a cold front (ACF), the base of high pressure (BOH), the backside of high pressure (BAH), the inverted trough of low pressure (INT), and saddle pressure (SAP) with the haze days. At that time, 4 types are divided with the regional haze events and each of which has a different boundary-layer structure. During heavy haze, the surface mainly experiences EQP, ACF, BOH, BAH, and INT which also have different boundary-layer structures.

1. Introduction

The people of East China, the Yangtze River Delta, and the Pearl River Delta have been subjected to health risks due to haze since the 21st century, particularly during autumn and winter. The nature of haze is suspended dust particles. In meteorological terms, these particles are called aerosols. Over the last century, many international experts have researched haze [1–15]. In recent years, domestic experts gradually began studying zonal haze and urban haze [16–19].

Regional haze research has also progressed. In China, experts have suggested that the spatial distribution of haze days is expansive in the east and localized in the west; three high-incidence regions in the east were the middle and lower reaches of the Yangtze River, North China, and South China [20–23]. Research has noted distinct transboundary pollution between the cities of the Yangtze River Delta [24]. Experts have analyzed haze and fog in East China and have indicated that haze days gradually increased in most East China cities over the last 30 years [25, 26]. Song et al. [27] analyzed haze days in Jiangsu Province and indicated that frequent haze days occurred in southern Jiangsu Province due to economic development and urbanization. By analyzing the haze of the

Pearl River Delta, experts found that the regional haze process was related to the airflow stagnation zone, where pollutants accumulate in the boundary layer; thus, pollution becomes highly concentrated near the surface to form haze [28–30]. Regional haze in Beijing, Tianjin, and Hebei has also been researched by Zhao et al. [31] and Wang et al. [32].

Because haze is greatly influenced by weather, many experts have analyzed the synoptic backgrounds in these cases. Ren et al. [33] suggested that the high-pressure equalizing zone has a cumulative effect on pollutants when researching weather systems and atmospheric pollution of the boundary layer. Rao et al. [34] indicate that forward trough structure and inversion layer provide favorable conditions for regional haze in East-Central China. Zhang et al. [35] noted that the background climate plays an active role in haze formation in autumn, when the haze significantly increases. Many experts have discussed the main causes of haze in terms of low visibility and weather/climate [36–43].

As research on haze has progressed in recent years, the meteorological features of the boundary layer during haze have gradually become an important research direction. Xu et al. [44] suggested that a thick temperature inversion layer occurred near the surface on haze days. Within this layer,

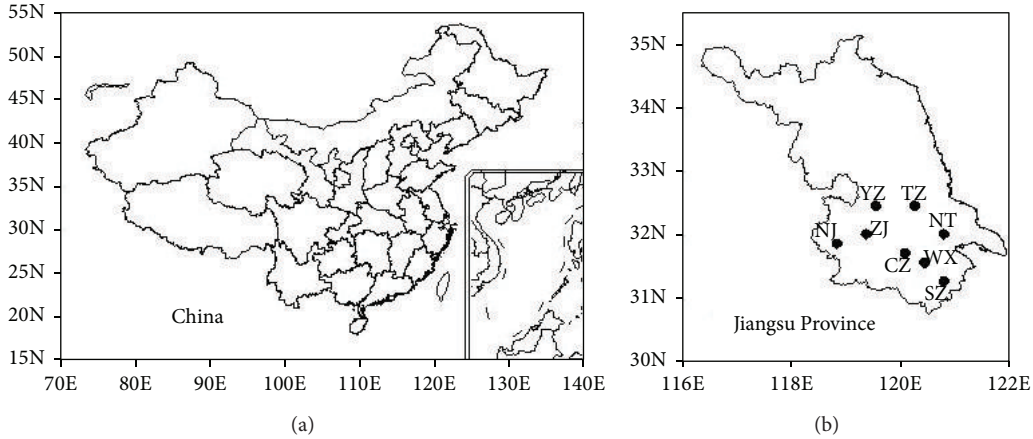


FIGURE 1: China (a) and Jiangsu (b). NanJing (NJ), YangZhou (YZ), TaiZhou (TZ), ZhenJiang (ZJ), ChangZhou (CZ), WuXi (WX), SuZhou (SZ), and NanTong (NT).

materials cannot easily disperse; thus, pollutants accumulate. Wu et al. [45] found that vertically dynamic and thermal variations in the boundary layer affect pollutant concentrations. Xiu et al. [46] indicated that stable air over Beijing prevents air movement; as a result, photochemical pollution occurs. Moreover, many experts suggest that a stable temperature inversion, weak atmospheric turbulence, and low winds are the main causes of haze [47–54]. Research has also noted that the diffusion and sedimentation processes of atmospheric chemical materials largely depend on the physical conditions of the vertical boundary layer [55–59].

Existing research focuses on spatiotemporal haze distributions or the synoptic situation and boundary-layer characteristics of specific case studies. However, the weather and boundary-layer climate over many years are not well-known, particularly in terms of persistent haze and heavy haze. In this study, we classify haze and associated weather systems in southern Jiangsu from 1980 to 2012, especially the surface weather conditions of the persistent regional haze and regional heavy haze. Then, we focus on the boundary-layer characteristics of regional haze events especially the air temperature various in vertical and regional heavy haze in southern Jiangsu. This research provides a basis for haze forecasting.

2. Data and Methods

In this study, we obtain data on artificial observation visibility, relative humidity, daily precipitation, and weather in the following cities (Figure 1): NanJing (NJ), YangZhou (YZ), TaiZhou (TZ), ChangZhou (CZ), WuXi (WX), SuZhou (SZ), and NanTong (NT); the data are valid from 1980 to 2012 three times per day (08 h, 14 h, and 20 h). We also use sounding data, such as temperature profiles, for XuZhou (XZ), SheYang (SY), NanJing (NJ), and ShangHai (SH). The sea level pressure at 709 stations across the country from 1980 to 2012 is also used.

We adopt the haze definition of Guo et al. [60]. When the visibility was less than 10 km and the relative humidity was

less than 90% at any of the three times, the day was considered a haze day unless there was rain, sand storms, blowing sand, suspended dust, smoke, blowing snow, or a snow storm at the same time.

A regional haze event occurred when 3 or more of the 8 cities in southern Jiangsu Province experienced simultaneous haze days. Persistent regional haze was described as regional haze occurrence for 5 or more consecutive days.

Four haze classifications are provided according to visibility (China Meteorological Administration, 2010) [61]. When the visibility is between 5 km and 10 km, slight haze occurs; when the visibility is between 3 km and 5 km, mild haze occurs; when the visibility is between 2 km and 3 km, moderate haze occurs; and when the visibility is less than 2 km, heavy haze occurs. A more severe haze classification is more harmful to humans and is unfavorable for outdoor activities. Therefore, regional heavy haze is defined as when 3 or more of the 8 cities have simultaneous heavy haze.

The lower height of a temperature inversion (LHTI) is the pressure nearest the surface when the first temperature inversion layer develops. The upper height of a temperature inversion (UHTI) is the pressure at the top of the first temperature inversion layer. The temperature difference in the temperature inversion is the upper temperature of the first temperature inversion layer (UTTI) minus the low-level temperature of the first temperature inversion layer (LTTI). The height difference in the temperature inversion is the pressure of the LHTI minus the pressure of the UHTI. The intensity of the temperature inversion (ITI) is the temperature difference divided by the height difference multiplied by 100($^{\circ}\text{C}/100\text{ hPa}$):

$$\text{ITI} = \left(\frac{(\text{UTTI} - \text{LTTI})}{(\text{LHTI} - \text{UHTI})} \right) * 100. \quad (1)$$

3. Results

3.1. Synoptic Conditions of Regional Haze. According to the definition of regional haze, 4851 regional haze days occurred

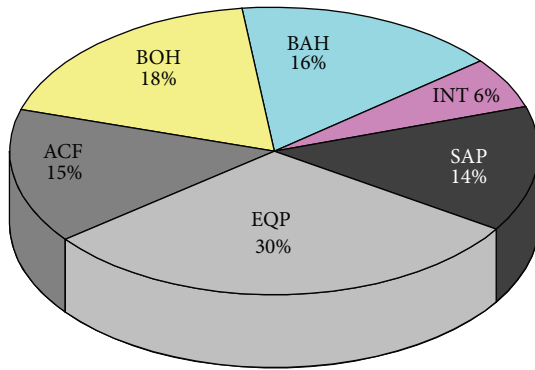


FIGURE 2: Surface conditions of regional haze days (equalized pressure: EQP, advancing edge of a cold front: ACF, base of high pressure: BOH, backside of high pressure: BAH, inverted trough: INT, and saddle pressure: SAP).

from 1980 to 2012. Regional haze lasted for 5 or more days 246 times.

3.1.1. Surface Conditions of Regional Haze. According to the definition of regional haze, we analyze the sea level pressure. Six types of weather patterns are considered: equalized pressure (EQP), advancing edge of a cold front (ACF), base of high pressure (BOH), backside of high pressure (BAH), inverted trough (INT), and saddle pressure (SAP). Figure 2 shows the frequency of the pressure types. When regional haze occurs, the main surface conditions (79% of cases) are EQP, ACF, BOH, or BAH.

Figure 3(a) shows the 246 instances of 5 or more consecutive regional haze days. In this figure, there are 97 cases of 5 days, 51 cases of 6 days, 32 cases of 7 days, 21 cases of 8 days, 16 cases of 9 days, 11 cases of 10 days, and 18 cases of 10 or more days. The longest haze case was 18 days; however, 80% of the haze cases were 8 days or less.

Figure 3(b) shows the surface conditions of 5 or more consecutive regional haze days from 1980 to 2012. Compared with Figure 2, the main structures are similar. The primary weather pattern was EQP (36% of the cases). BOH and ACF accounted for 19% and 17%, respectively, of the cases; BAH occurred during 12% of the haze events. The 4 pressure types accounted for 84% of the cases overall.

By filtering the regional haze days, we obtained 50 days with regional heavy haze.

The surface conditions of the regional heavy haze were mainly equalized pressure (EQP), advancing edge of a cold front (ACF), base of high pressure (BOH), backside of high pressure (BAH), and inverted trough (INT). (1) EQP (Figure 4(a)): when the cold air was blocked in the north, the domain was controlled by equalized pressure. (2) ACF (Figure 4(b)): when the cold air strongly advanced, the domain was controlled by the advancing edge of the cold front. (3) BOH (Figure 4(c)): when the mainland high pressure moved southward, the domain was overtaken by the base of the high pressure. (4) BAH (Figure 4(d)): when the mainland high pressure disbanded, the domain was located on the backside of the high pressure. (5) INT (Figure 4(e)):

when the domain was controlled by the back of the weak high pressure, the high pressure receded, the inverted trough developed, and the domain was overtaken by the top of the inverted trough.

3.1.2. Surface Weather Conditions of Persistent Regional Haze. We analyze the surface conditions during the 246 regional persistent haze cases. Four types of persistent regional haze can be obtained according to the surface weather conditions on the first day of the regional haze event (Figure 4): EQP, ACF, BOH, and BAH. These 4 patterns occurred 214 times. In 5 instances, the 4 patterns were hybrids during regional haze events; the remaining weather patterns occurred 27 times. The detailed variations of the 4-type surface weather conditions are presented as below.

Type I (EQP) occurred 91 times (Figure 5). Often, the domain experienced EQP, then BOH, BAH, or ACF. If the EQP transitioned to BOH, along with high-pressure movement toward the sea, then the region was controlled by BAH, cold air pushed southward, and the domain was controlled by the ACF (9 instances). If the EQP transitioned to BAH, then there was a low trough developing in the southwest. Then, the domain was controlled by the top of an inverted trough. If the EQP transitioned to an ACF, then the domain would be controlled by the BAH when the high pressure weakened. Following the high-pressure progression toward the sea, the area was controlled by SAP. At this time, there was a cold vortex blocking the cold air to the north, and the domain was controlled by the EQP again. If the domain was controlled by the EQP on the first day of a persistent haze case, then an inverted trough developed to the southwest and moved toward the northeast; the domain was controlled by the top of the inverted trough. Because the inverted trough moved out of the domain, the high pressure over the mainland shifted to the southeast; if the speed was slow, then the domain was controlled by the EQP. Or when the speed was rapid, the domain was controlled by the BAH. The domain was controlled by the EQP 70 times at the beginning of a haze period and by BOH, BAH, or ACF at the end of the period.

Type II (ACF) occurred 57 times (Figure 5). At the beginning of persistent haze cases, the domain was controlled by an ACF. When the cold front passed, the domain was controlled by the EQP. Notably, two cold air processes occurred during haze cases. There were three options during the two cold-front processes. First, when the high pressure was separated into two small high-pressure systems, the domain was occupied by the BAH and then by the SAP. When another cold air system moved southward, the domain was controlled by the ACF (14 instances). Second, if there was a vortex over North China, when the vortex moved toward the sea and another cold air system moved southward, the domain was dominated by the ACF (21 instances). Third, if the vortex over North China was strong and weakened the cold air, when the vortex moved seaward, the domain was occupied by BAH and then by the ACF (8 instances). Fourth, when the high pressure was undisturbed or the cold vortex was not blocked, the domain was controlled by the BOH,

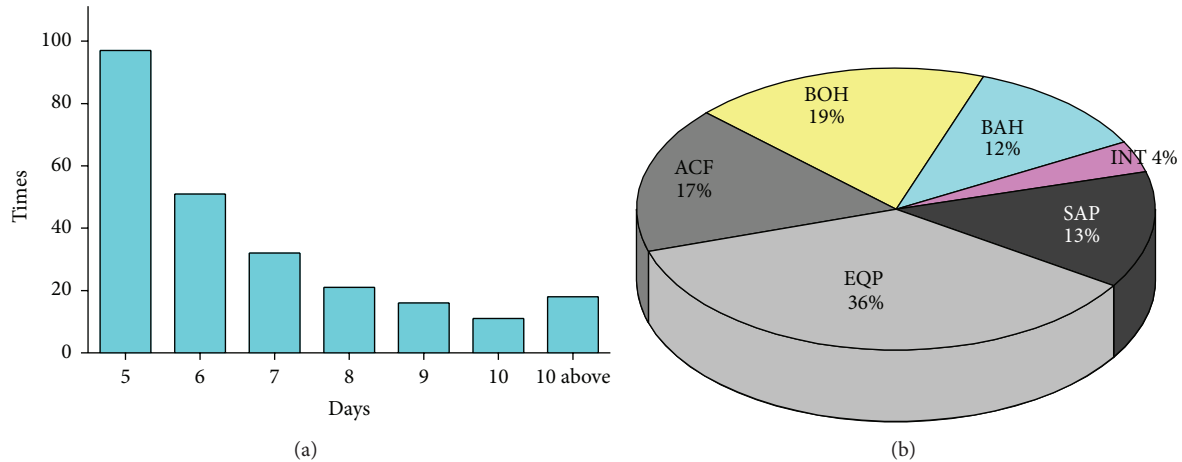


FIGURE 3: Count of consecutive regional haze days between 1980 and 2012 (a); surface conditions during 5 or more consecutive haze days (b) (equalized pressure: EQP, advancing edge of a cold front: ACF, base of high pressure: BOH, backside of high pressure: BAH, inverted trough: INT, and saddle pressure: SAP).

the EQP of high pressure, and then cold air. Overall, type II is characterized by two passages of cold air. The greatest differences were the high-pressure dissipation, cold vortex blocking, low-pressure vortex movement toward sea, and the time interval between the two cold air systems.

Type III (BOH), which is complex, occurred 54 times (Figure 5). When the haze days began, the domain was characterized by the BOH.

When the system was moving slowly, it was controlled by the EQP, which is similar to type I. If there was an inverted trough developing, then the top of the trough became dominant. If cold air moved southward, then the domain was controlled by the ACF and then by the EQP. Following the southward trajectory of the high pressure, the area was occupied by BOH. However, when the oceanic high pressure and vortex in the north occurred at the same time, SAP was present over the domain; then, the ACF was dominant when cold air pushed south.

In that case, if the system moved quickly, then the domain was controlled by the BAH as the high pressure moved out. At that time, if an inverted trough was developing, then it dispersed the cold air and the top of the inverted trough was dominant. Then, the ACF accompanying the cold air strengthened. On condition that the cold vortex in the north was replaced, the SAP and EQP were dominant, followed by the top of the inverted trough. Type III was characterized by an inverted low-pressure trough and saddle pressure due to the weak high pressure or cold vortex in the northeast or the vortex in the southwest.

Type IV (BAH) occurred 12 times (Figure 5). When a haze case began, the domain was controlled by the BAH. If the cold vortex was weak when the cold air strongly pushed toward the south, then the domain was occupied by the ACF (4 instances). In case the cold vortex was strong and steady and accompanied by mainland high pressure to the east, then the domain was controlled by the high EQP. Then, the cold vortex strengthened in the north, and the high pressure moved out; the domain was controlled by the BOH. Then,

the EQP dominated, with high pressure moving toward the sea and the cold vortex moving eastward. At that time, a cold-core high-pressure system developed; the domain was controlled by the BOH. Type IV was characterized by a cold vortex. The differences stemmed from the strength of the cold vortex in the northeast and the speed or strength of the cold air movement.

Hybrid patterns occurred 5 times.

Between 1994-10-30 and 1994-11-12, when the haze began, the domain was controlled by the ACF and then the EQP; however, because of the effect of the cold vortex in the north, the high pressure was broken up and the domain was overtaken by the BAH. As the cold vortex moved south, the domain was located on the backside of the cold vortex. Following cold air intrusion and the cold vortex retreat to the north and east, the domain experienced the BOH. Then, the cold air in the north developed again, and the domain was overtaken by the BAH and then the SAP as the high pressure dissipated. At that time, there was weak cold air to the south; the domain was occupied by the EQP of high pressure and then by BOH. When the high pressure moved out, the BAH dominated. Then, the high pressure moved toward the sea, and the domain was again controlled by the EQP. When the newly formed cold air mass moved south, an inverted trough developed in the southwest and moved northeast; then, the domain was located along the top of the inverted trough. This entire process characterized the ACF transition into the BOH. The haze ended at the base of the high pressure with strong cold air.

Between 2004-11-02 and 2004-11-08, when the haze started, the domain experienced the EQP. Following the high-pressure movement, the domain was controlled by the BAH. Along with the advancing cold air, the BOH and BAH replaced the high pressure. At that time, there was inverted trough in the southwest, which tracked toward the northeast; finally, the domain was centered on the inverted trough. This process characterized the EQP transition into the BOH.

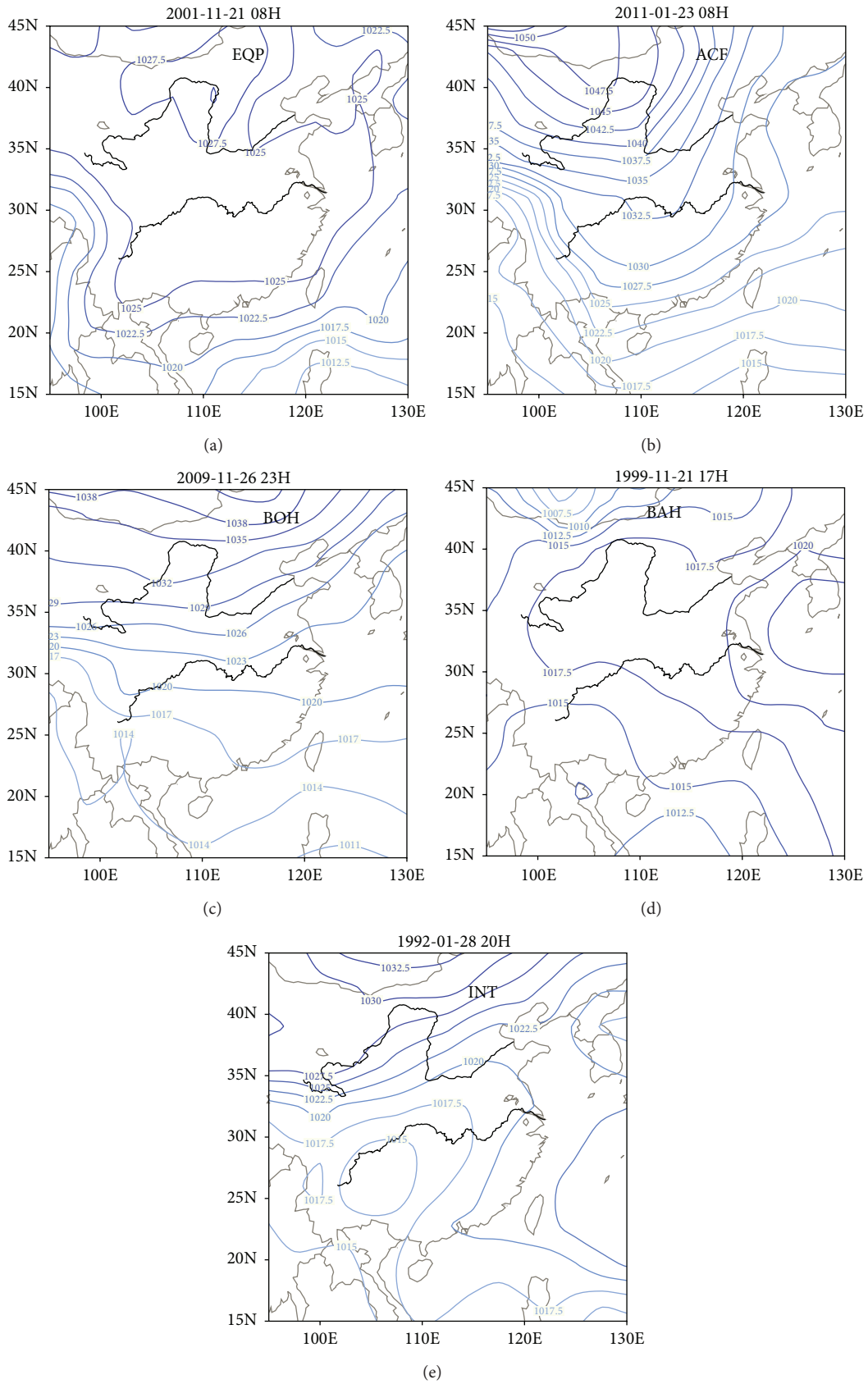


FIGURE 4: Surface conditions during heavy haze days ((a) equalized pressure: EQP, (b) advancing edge of a cold front: ACF, (c) base of high pressure: BOH, (d) backside of high pressure: BAH, and (e) inverted trough: INT).

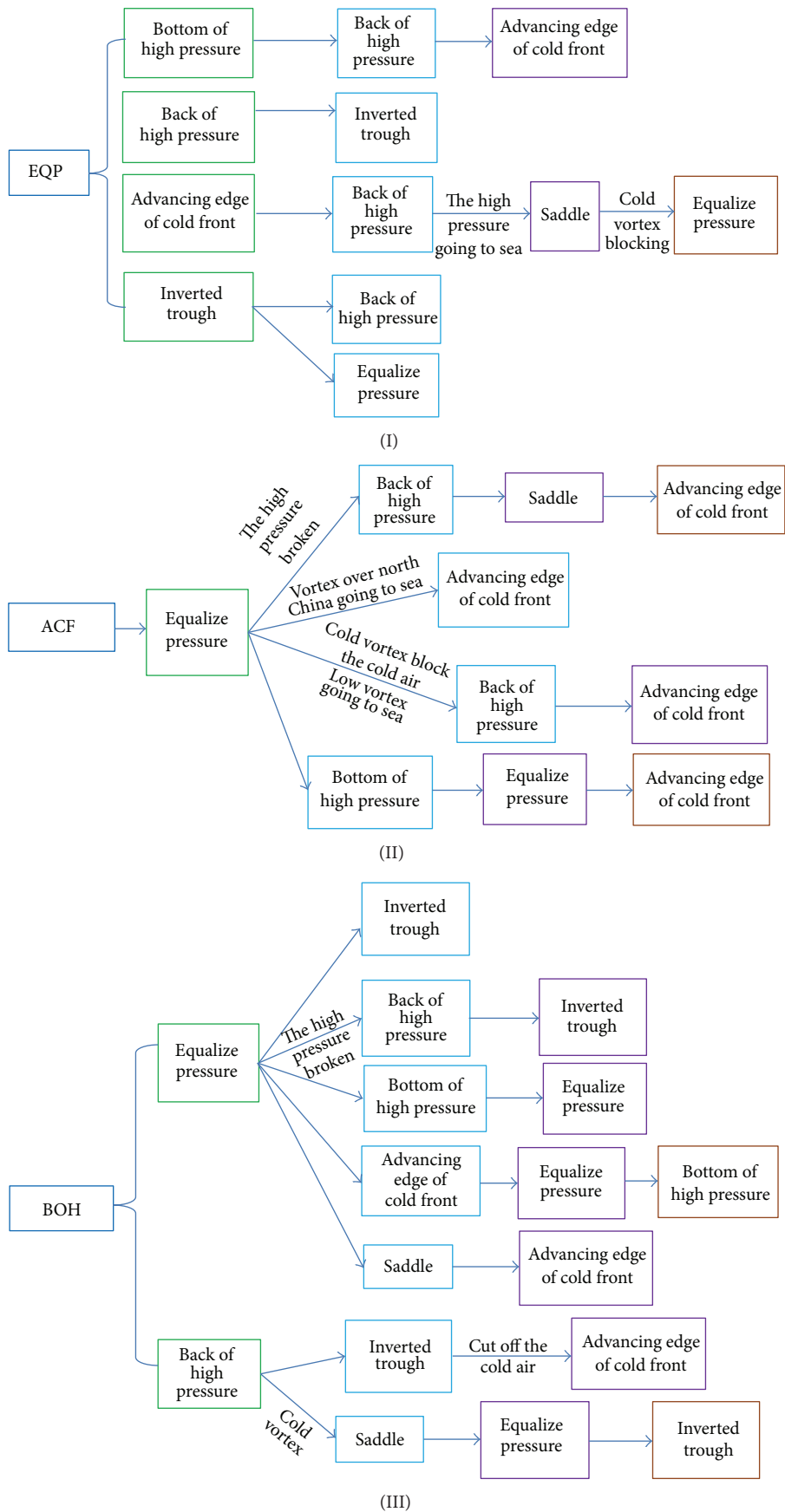
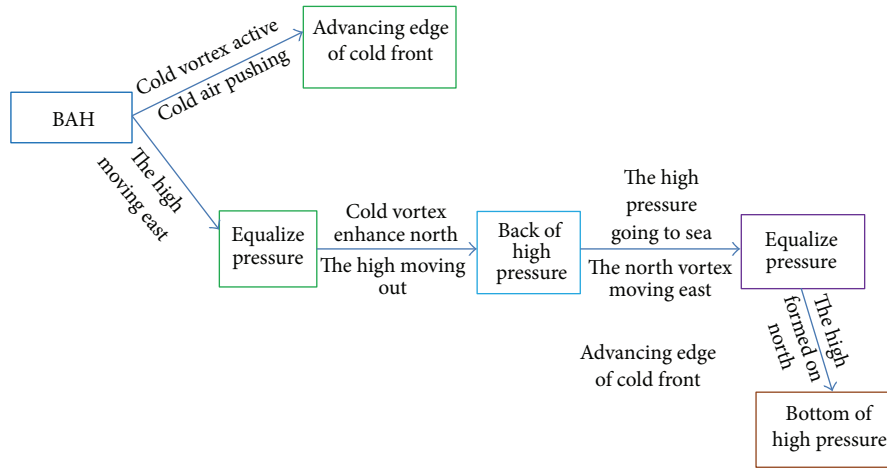


FIGURE 5: Continued.



(IV)

FIGURE 5: The 4 types of weather patterns during regional persistent haze events (equalized pressure: EQP, advancing edge of a cold front: ACF, base of high pressure: BOH, backside of high pressure: BAH, inverted trough: INT, and saddle pressure: SAP).

From 2006-03-01 to 2006-03-08 and 2009-11-20 to 2009-11-26, these two synoptic patterns were the same. Initially, the domain was located along the ACF as the cold air passed. Then, the domain was controlled by the EQP of the high pressure and successively by the BAH as the high pressure moved toward the sea. Then, the domain was dominated by the EQP. As the cold air gradually moved east, the BAH dominated. These two processes describe the ACF transition to the BAH.

Between 2011-03-08 and 2011-03-13, when the haze began, the domain was located along the ACF. As the cold air advanced, the EQP of the high pressure dominated. When the high pressure moved east, the domain was located on the BAH. At that time, strong cold air pushed south, but the low inverted trough weakened the cold air mass, so the domain was located at the top of the inverted trough. The haze ended with another cold air intrusion. This process describes the ACF transition to the BOH.

The other weather patterns occurred 27 times; 23 instances between May to September were characterized by a northern cold vortex shaping the structure of the northerly low and southerly high, the base of the low vortex, or typhoons. Four instances occurred in autumn and winter. For example, from 1990-12-04 to 1990-12-10, 1998-04-14 to 1998-04-21, and 1998-11-11 to 1998-11-15, the domain was affected by the base of the cold vortex from the north. As the cold vortex moved toward the sea, the domain experienced the EQP. Then, the domain experienced the ACF because the cold air moved south.

Between 2002-10-08 and 2002-10-16, after the BOH, the domain was affected by BAH as high pressure moved toward the sea. Then, the domain was controlled by the EQP. At that time, another mainland high-pressure system was located to the south: that is, the BOH transitioned to the EQP. Then, the low vortex of the north was affected by the base of the low vortex. As the low vortex moved toward the east and the sea, the domain was controlled by the backside of the high pressure over the sea.

3.1.3. *Surface Conditions of Regional Heavy Haze.* Table 1 shows the categories of the surface and high-pressure patterns during regional heavy haze. When regional heavy haze occurred, the 850 hPa pressure was uniform near the backside of the high-pressure system or the saddle pressure. At 500 hPa, the airflow was northwesterly, westerly, or southwesterly.

Table 2 reveals the seasonal distribution of regional heavy haze during different pressure types. From the table, the EQP and the ACF occurred 12 times, the BOH occurred 5 times, the BAH occurred 10 times, the INT occurred 6 times, and other weather types occurred 5 times. The main 4 types accounted for 78% of the haze cases. We also find that the regional heavy haze mainly occurred in autumn and winter. Only 3 events occurred in summer.

3.2. Boundary-Layer Structures of Regional Haze

3.2.1. *Boundary-Layer Structures of Persistent Regional Haze.* According to the previous analysis, we selected representative regional haze events during EQP, ACF, BOH, and BAH.

(1) *EQP.* On the basis of the EQP departure, we selected 5 typical events (Table 3). Then, we analyzed the 5 associated processes.

Figure 6 shows the temperature profiles of the events. In Figure 6, the x -axes are the data and the y -axes are the pressures. The shaded area is the vertical temperature distribution. The broken lines are the LHTI and UHTI of the temperature inversion. The dotted line is the ITI of the temperature inversion (the same below).

From 1984-10-31 to 1984-11-08, when the haze days began, the domain had uniform pressure ahead of the cold front; then, cold air advanced and the domain was controlled by the ACF. When the high pressure weakened, the domain was under the BAH. Then, the high pressure moved seaward, and the domain was controlled by the SAP. However, at that time, the cold vortex to the north blocked the cold air, and

TABLE I: Surface and high-pressure conditions on heavy haze days.

Series	Types	Date (yyyy-mm-dd)	500 hPa	850 hPa	Stations recording heavy haze days	Stations recording haze days
1		1987-12-26	Southwest	Equalizing zone	4	7
2		1992-10-28	West	Equalizing zone	3	6
3		1994-04-28	Northwest	Equalizing zone	3	7
4		1998-12-27	Northwest to west	Equalizing zone	3	7
5		2001-11-21	West	Equalizing zone	3	8
6	EQP	2001-11-22	West	Equalizing zone	3	7
7		2002-02-05	Northwest to west	Equalizing zone	3	7
8		2005-10-26	Northwest to southwest	Saddle	3	8
9		2007-04-06	West	Equalizing zone	3	8
10		2008-07-17	Equalizing zone	Saddle	3	5
11		2008-11-01	West	Equalizing zone	3	6
12		2012-03-06	Southwest to west		3	8
13		1981-12-28	West	Saddle	3	8
14		1985-11-16	West	Equalizing zone	3	8
15		1990-10-15	Northwest	Equalizing zone	3	8
16		1999-10-28	West		3	8
17		2002-12-31	Northwest	Inverted trough	3	8
18	ACF	2003-12-12	Northwest	Equalizing zone	3	6
19		2003-12-16	Northwest	Base of cold vortex	3	7
20		2003-12-17	Northwest	Base of cold vortex	3	8
21		2009-01-09	Northwest to west		3	8
22		2010-11-21	Front of trough	Base of trough	3	7
23		2011-01-23	Northwest to west	Equalizing zone	3	5
24		2012-01-20	West	Equalizing zone	3	8
25		1992-01-25	West	Equalizing zone	3	8
26		2005-10-18	West	Equalizing zone	3	8
27	BOH	2008-03-11	West	Backside of the high pressure	3	8
28		2009-11-26	West	Backside of the high pressure	3	6
29		2011-10-08	West	Backside of the high pressure	3	6
30		1987-12-24	West	Equalizing zone	3	6
31		1992-01-27	Northwest	Equalizing zone	4	8
32		1992-05-31	Equalizing zone	Equalizing zone	3	6
33		1992-11-14			3	6
34	BAH	1996-04-26	Northwest		3	8
35		1999-11-21	West		3	8
36		2005-10-31	West	Equalizing zone	3	6
37		2008-04-18	Southwest	Backside of the high pressure	3	6
38		2008-10-15	Southwest to west	Equalizing zone	3	8
39		2011-06-13	West	Equalizing zone	4	6
40		1984-04-26	Northwest to southwest	Equalizing zone	3	7
41		1992-01-28	Northwest	Equalizing zone	3	8
42	INT	1994-11-11	Northwest to southwest	Equalizing zone	3	6
43		2004-02-19	Front of ridge	Backside of the high pressure	3	8
44		2004-05-10	Front of ridge	Backside of the high pressure	3	8
45		2009-11-08	Southwest to west	Saddle	3	7
46		2002-01-03	Northwest		3	5
47		2003-06-25	Equalizing zone	Saddle	3	8
48	Others	2004-11-07	West	Equalizing zone	4	8
49		2008-05-26	Northwest	Equalizing zone	4	8
50		2011-06-03	Equalizing zone	Equalizing zone	3	7

Equalized pressure: EQP, advancing edge of a cold front: ACF, base of high pressure: BOH, backside of high pressure: BAH, and inverted trough: INT.

TABLE 2: Types of consecutive heavy haze days.

Type	Month				
	3-5	6-8	9-11	12-2	1-12
EQP	3	1	5	3	12
ACF			4	8	12
BOH	1		3	1	5
BAH	3	1	4	2	10
INT	2		2	2	6
Others	2	1	1	1	5

Equalized pressure: EQP, advancing edge of a cold front: ACF, base of high pressure: BOH, backside of high pressure: BAH, and inverted trough: INT.

TABLE 3: Typical processes of equalized pressure (EQP) during consecutive regional haze days.

Series	Start day	End day	Duration
1	1984-10-31	1984-11-08	9
2	1991-06-20	1991-06-27	8
3	1999-09-25	1999-09-29	5
4	2000-12-03	2000-12-09	7
5	2007-09-08	2007-09-17	10

the domain was again controlled by the EQP. When the haze began, the temperature inversion layer extended from the surface to 950 hPa. During the haze days, the base of the temperature inversion remained, and the temperature inversion at 950 hPa developed until the end of the haze period. The intensity of the temperature inversion had an obvious diurnal variation: strong in the daytime and weak in the nighttime. Meanwhile, the temperature inversion was weak in the mid-haze period. During this process, the temperature inversion layer was near the surface and shallow; double temperature inversion layers occurred at low altitudes.

From 1991-06-20 to 1991-06-27, the temperature inversion occurred in the middle of the persistent haze case. The inversion was low, thin, and weak. During this process, the summer harvest and a large seeded area occupied the domain. The weather was hot and humid, in accordance with the Meiyu period. Therefore, we assumed that the haze was mainly affected by solid particles and gas produced by straw burning [62, 63]; the particles and gas accumulated with the high humidity, causing persistent haze.

From 1999-09-25 to 1999-09-29, when the haze days began, the domain had uniform high pressure. Then, the high pressure moved eastward, and the domain was on the backside of the high pressure. At that time, the inverted trough was developing, and the domain was located along the top of the trough. When the newly formed cold air mass moved southward, the domain was affected by the ACF. When the haze began, the temperature inversion was just above the surface. The event lasted 2 days; 3 stations (XZ, SH, and SY) had high-altitude temperature inversions, but the inversion at the NJ station was still near the surface. In Figure 6(c), the surface-layer temperature inversion was thin at the NJ station, and high-altitude inversions at the other stations were also thin. The variable temperature inversion intensity was severe.

TABLE 4: Typical processes of the advancing edge of a cold front (ACF) pattern during persistent regional haze days.

Series	Start day	End day	Duration
1	1982-12-11	1982-12-24	14
2	2003-10-24	2003-11-03	11
3	2005-01-11	2005-01-20	10
4	2011-12-28	2012-01-07	11

Initially, the inversion intensity was strong to the north and weak to the south. Then, the temperature inversion weakened at XZ and SY and strengthened at NJ and SH. At the end of the haze period, the temperature inversion was strong at XZ and weak at the other stations. This difference may be due to the movement of the system during the late haze period.

From 2000-12-03 to 2000-12-09, at the early stage of the haze, the temperature inversion or isothermal layer was recorded at all 4 stations. The height of the layer increased from north to south. When the haze days were consecutive, the surface layer of the temperature inversion was still recorded at XZ, SY, and NJ. However, the significant daily variation at SH was characterized as low in the daytime and high at nighttime. The temperature inversion was thin, with a variable intensity. When the intensity was strong, the top of the temperature inversion layer was low and vice versa.

From 2007-09-08 to 2007-09-17, the temperature inversion was initially near the surface. With persistent haze days, the base of the temperature inversion minimally changed at XZ and SY, but the thickness increased. At that time, the base of the temperature inversion clearly lifted, and the thickness increased at NJ and SH. At the end of the haze period, the base of the temperature inversion gradually lifted, and the thickness weakened from north to south. The intensity was initially stronger to the north. With persistent haze development, the intensity was weaker at XZ and SY and stronger at NJ and SH during the middle of the haze period.

Table 3 shows that a haze event between 5 and 10 days has an EQP. The duration depended on the system development at the middle and end of the persistent haze case. The duration was shorter when the domain was controlled by the EQP, the BAH, and then the INT. If the domain was initially controlled by the EQP and then overtaken by the INT, EQP, and SAP, the duration was longer. The base of the shallow temperature inversion layer was low, and the intensity was variable for different cases.

(2) *ACF*. Based on the developing features of an ACF, we selected 4 significant processes (Table 4). Based on the table, we find that this weather pattern lasts several days. We analyzed the 4 processes (Figure 7).

From 1982-12-11 to 1982-12-24 (Figure 7(a)), when the haze days began, the temperature inversions were elevated or no temperature inversion occurred. Following the haze-day development, the temperature inversion occurred near the ground. The top of the temperature inversion layer was approximately 1000 hPa. At the middle and end of the haze-day period, the surface layer of the temperature inversion persisted, and the multiple layers of the temperature inversion

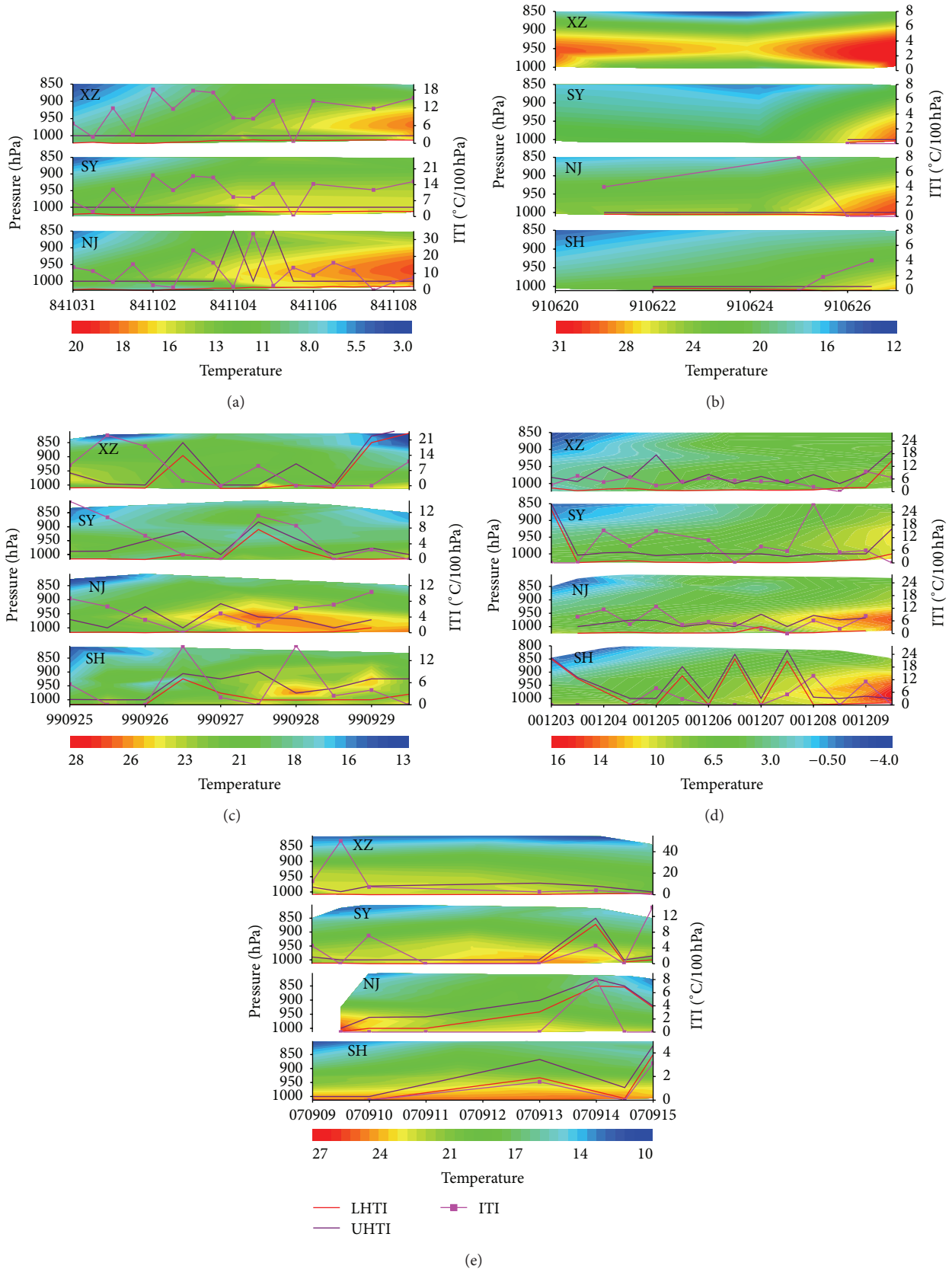


FIGURE 6: Temperature profiles of the equalized pressure (EQP) type during persistent regional haze days at XuZhou (XZ), SheYang (SY), NanJing (NJ), and ShangHai (SH) ((a) 1984-10-31–1984-11-08, (b) 1991-06-20–1991-06-27, (c) 1999-09-25–1999-09-29, (d) 2000-12-03–2000-12-09, and (e) 2007-09-08–2007-09-17). Lower height of temperature inversions (LHTI), upper height of temperature inversions (UHTI), and intensities of the temperature inversions (ITI).

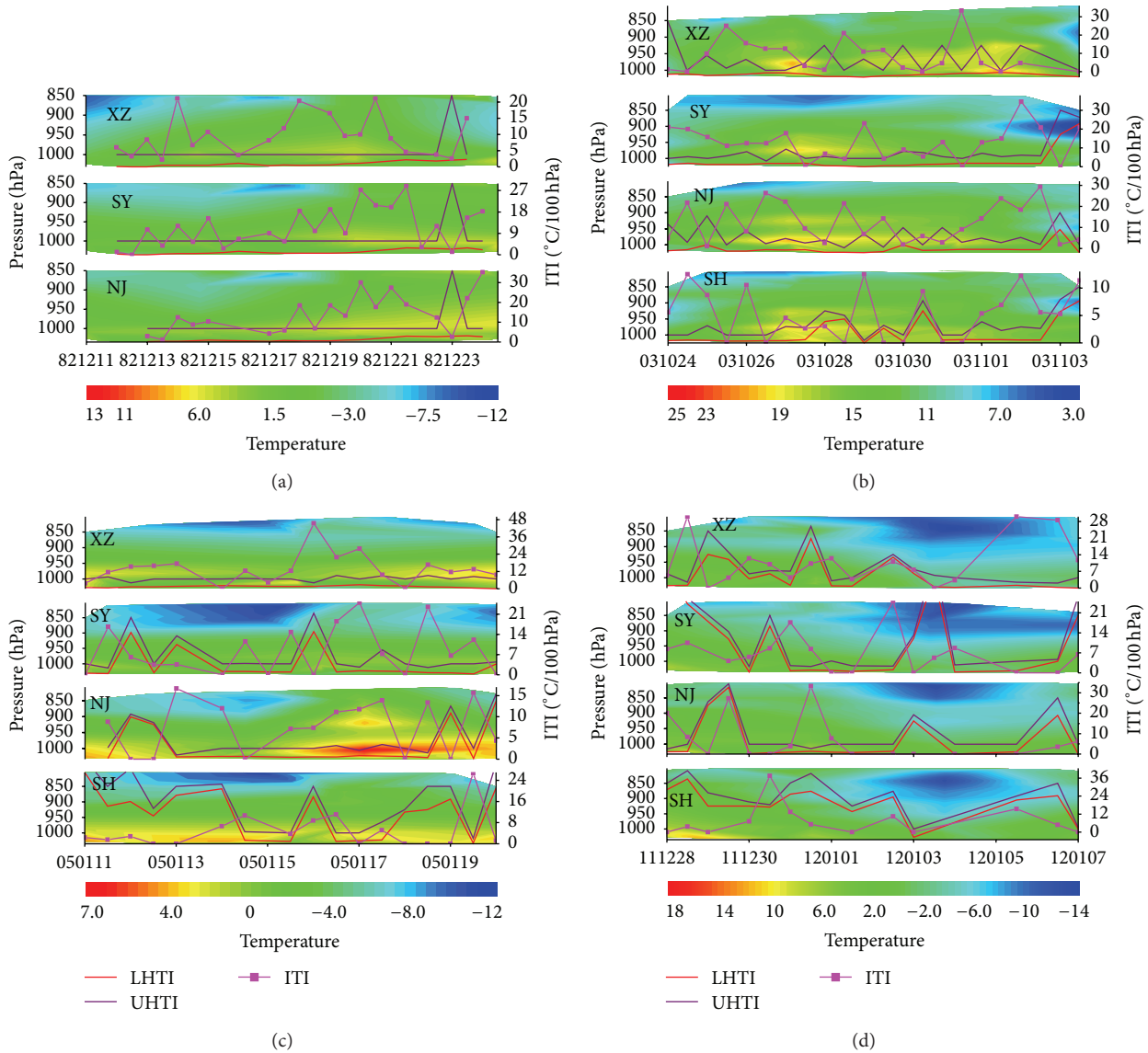


FIGURE 7: Temperature profiles of the advancing edge of a cold front (ACF) pattern during consecutive regional haze days at XuZhou (XZ), SheYang (SY), NanJing (NJ), and ShangHai (SH) ((a) 1982-12-11–1982-12-24, (b) 2003-10-24–2003-11-03, (c) 2005-01-11–2005-01-20, and (d) 2011-12-28–2012-01-07). Lower height of temperature inversions (LHTI), upper height of temperature inversions (UHTI), and intensities of the temperature inversions (ITI).

were at low altitudes. The intensity of the temperature inversion gradually increased in the early stage. In the middle to late period, the intensity gradually decreased. The intensity of the temperature inversion was strong and variable. The thickness of the temperature inversion did not noticeably change.

From 2003-10-24 to 2003-11-03 (Figure 7(b)), when consecutive haze days began, no temperature inversion appeared at the XZ and SY stations, but the surface layer of the temperature inversion was recorded at NJ and SH, which experienced another layer at 1000 hPa. Following the developing of haze days, the surface layer of the temperature inversion was recorded at all 4 stations. At that time, there were multiple layers of temperature inversions. The top height of the temperature inversion had distinct diurnal variation:

the top height was higher in the daytime and lower at night. Therefore, the thickness of the temperature inversion was also diurnally variable. During the entire process, the intense variation in the temperature inversion was strong.

From 2005-01-11 to 2005-01-20 (Figure 7(c)), when a persistent haze period began, the surface layer of the temperature inversion was recorded at the XZ and SY stations. There was no temperature inversion or higher layers at the NJ and SH stations. During the middle of the period, there were multiple temperature inversions from the surface to the middle level. The intensity of the temperature inversion was strong and diurnal.

From 2011-12-28 to 2012-01-07 (Figure 7(d)), the 4 stations all recorded temperature inversions when the haze period

TABLE 5: Typical processes of the base of high-pressure (BOH) pattern during consecutive regional haze days.

Series	Start day	End day	Duration
1	2003-03-21	2003-03-26	6
2	2003-11-11	2003-11-15	5
3	2004-01-27	2004-01-31	5
4	2005-09-14	2005-09-20	7
5	2009-09-02	2009-09-08	7
6	2010-10-06	2010-10-10	5

began. The height of the layer diurnally varied. In long-duration haze cases, there were multiple thin temperature inversion layers. The intensity of the temperature inversion was strong and variable.

During haze cases with the ACF pattern, the temperature inversion was not notable; however, as the cold front advanced, the surface layer remained until the end of the haze case. In the middle of the haze case, there were multiple temperature inversions at low and high levels. These features allowed for the 10-day haze cases. The height of the temperature inversion layer had obvious changes: it was lower in the daytime and higher at night. The intensity of the temperature inversion was strong and variable.

(3) *BOH*. The distinguishing feature of the BOH pattern was the short-duration haze cases (Table 5).

From 2003-03-21 to 2003-03-26 (Figure 8(a)), when the haze case began, a temperature inversion up to 900 hPa was recorded at all stations except XZ during the daytime. At night, the top of the temperature inversion reached 850 hPa at XZ and SY, and the top height decreased to 1000 hPa at NJ and SH when the layer thinned. On the second haze day, the temperature inversion reached the surface at the XZ and SY stations, but the top of the temperature inversion elevated to 800 hPa at NJ and SH. Hereafter, the temperature inversion was at the surface at XZ; it gradually reached the ground at the other stations three days later. The intensity of the temperature inversion varied during long haze cases.

From 2003-11-11 to 2003-11-15 (Figure 8(b)), on the first day of haze, multiple temperature inversions were elevated from north to south. At night, the temperature inversion occurred near the surface at the XZ station, and the height increased to 100 hPa at other stations. Afterward, the surface-based temperature inversion lasted for 5 days, except for the nighttime layer on November 13, which was elevated to 925 hPa. The intensity of the temperature inversion greatly changed. The peak of the intensity occurred on the third day of the persistent haze case, when SAP and cold air were present. Then, multiple temperature inversion layers occurred at the 4 stations.

From 2004-01-27 to 2004-01-31 (Figure 8(c)), a temperature inversion formed near the surface and lasted until the end of the haze case; however, the base of the temperature inversion at the NJ station increased to 900 hPa at night on January 27. The intensity of the temperature inversion appeared to increase from north to south during the daytime of January 27 to the night of January 28. During the daytime

of January 30, a second peak appeared at XZ and NJ. Then, the SY station experienced obvious diurnal variation while the SH station experienced weak diurnal variation.

From 2005-09-14 to 2005-09-20 (Figure 8(d)), when the haze case began, a temperature inversion appeared at all stations except NJ; double inversions occurred at the XZ and SY stations. Afterward, the base of the temperature inversion was below 950 hPa, but it increased to 850 hPa between the daytime on September 17 and the nighttime on September 18 at the SH station. The intensity peak of the temperature inversion appeared at the SH station on September 15 during the day ($0.33^{\circ}\text{C}/\text{hPa}$). At the other stations, the peak intensity appeared from September 16 at night to September 17 during the day, with intensity between 0.15 and $0.22^{\circ}\text{C}/\text{hPa}$. Specifically, the temperature inversion was thin and was mainly a single layer.

From 2009-09-02 to 2009-09-08 (Figure 8(e)), when the haze case began, a temperature inversion occurred at all stations except SY. The height increased from north to south and over time at the 4 stations. Afterward, the temperature inversion became increasingly shallow between September 3 and September 5. Between September 7 and September 8, the temperature inversion did not continue to elevate. The base of the temperature inversion was positively related to the inversion intensity: that is, when the base was higher, the intensity was strong and vice versa. The variation in the thickness was inhomogeneous and greatly different among the stations. Additionally, the layer was thin at the stations.

From 2010-10-06 to 2010-10-10 (Figure 8(f)), when the haze period began, the temperature inversion was low. The base height dropped from north to south. Afterward, the temperature inversion was at the surface at XZ. The layer ascended twice at the SY station on October 7 and October 9; at other times, the temperature inversion was at the surface. At the NJ station, the base of the temperature inversion increased to 950 hPa during the daytime of October 8. At the SH station, a temperature inversion occurred during the daytime of October 9 and October 10; the inversion ascended at other times. During this process, the inversion was shallow at the 4 stations. The intensity of the temperature inversion was weak at XZ; the intensity peaked on the night of October 8. The intensity was strong in the daytime and weak at nighttime at SY; the opposite occurred at the NJ station. The intensity gradually receded during the haze days. The inversion was uniformly shallow with this type of weather pattern.

Because of the changing velocity of the system during consecutive haze days, there were larger height differences from south to north. Following haze development, the shallow temperature inversion slightly ascended while the intensity was strong.

(4) *BAH*. The representative processes of the BAH pattern during persistent regional haze are shown in Table 6. From the table, we found that the duration was short with this type of pattern.

From 1989-05-27 to 1989-06-02 (Figure 9(a)), when the haze case began, only 1 station had a temperature inversion. Although the temperature inversion developed soon

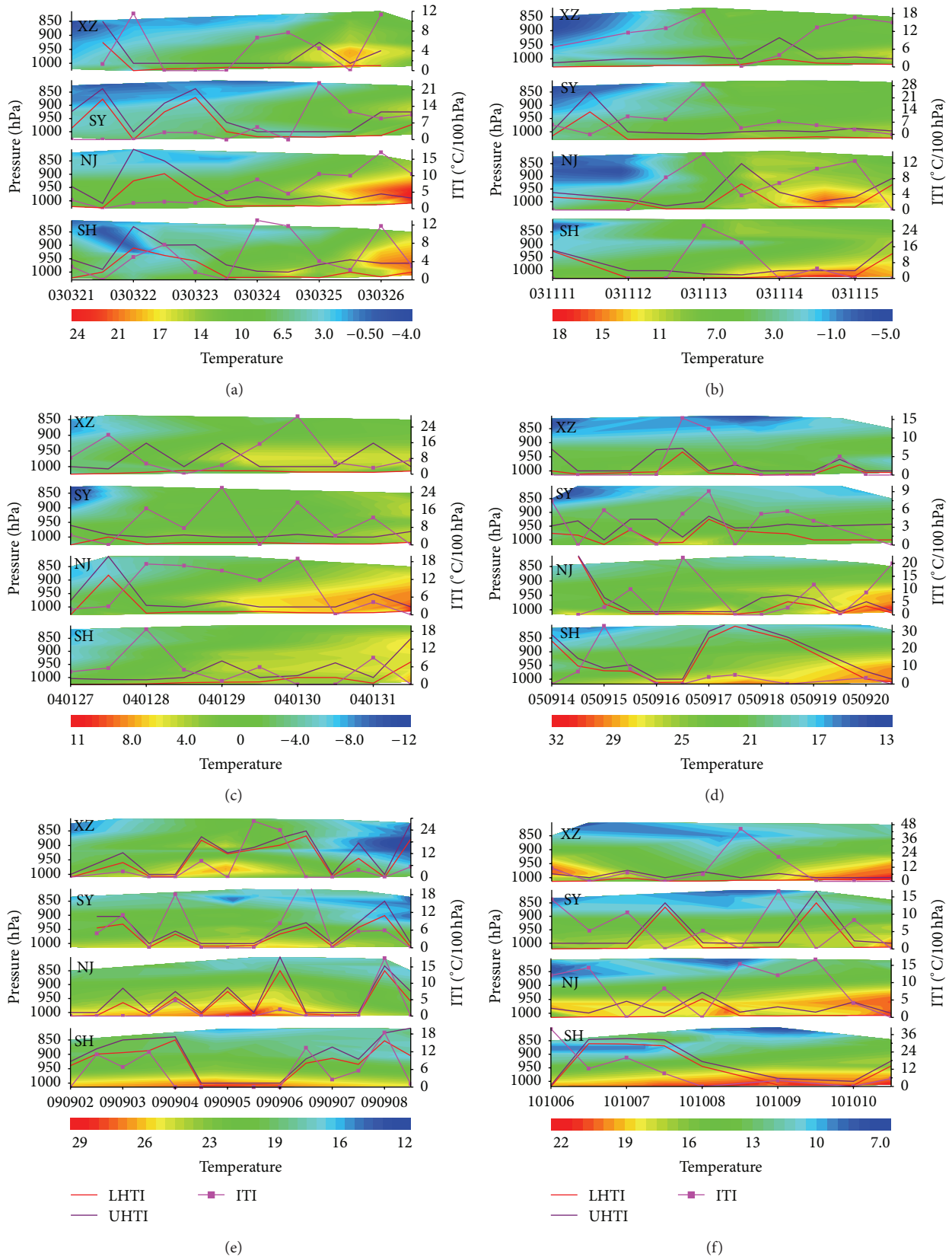


FIGURE 8: Temperature profiles of the base of high-pressure (BOH) pattern during consecutive regional haze days at XuZhou (XZ), SheYang (SY), NanJing (NJ), and ShangHai (SH) ((a) 2003-03-21–2003-03-26, (b) 2003-11-11–2003-11-15, (c) 2004-01-27–2004-01-31, (d) 2005-09-14–2005-09-20, (e) 2009-09-02–2009-09-08, and (f) 2010-10-06–2010-10-10). Lower height of temperature inversions (LHTI), upper height of temperature inversion (UHTI), and intensities of the temperature inversions (ITI).

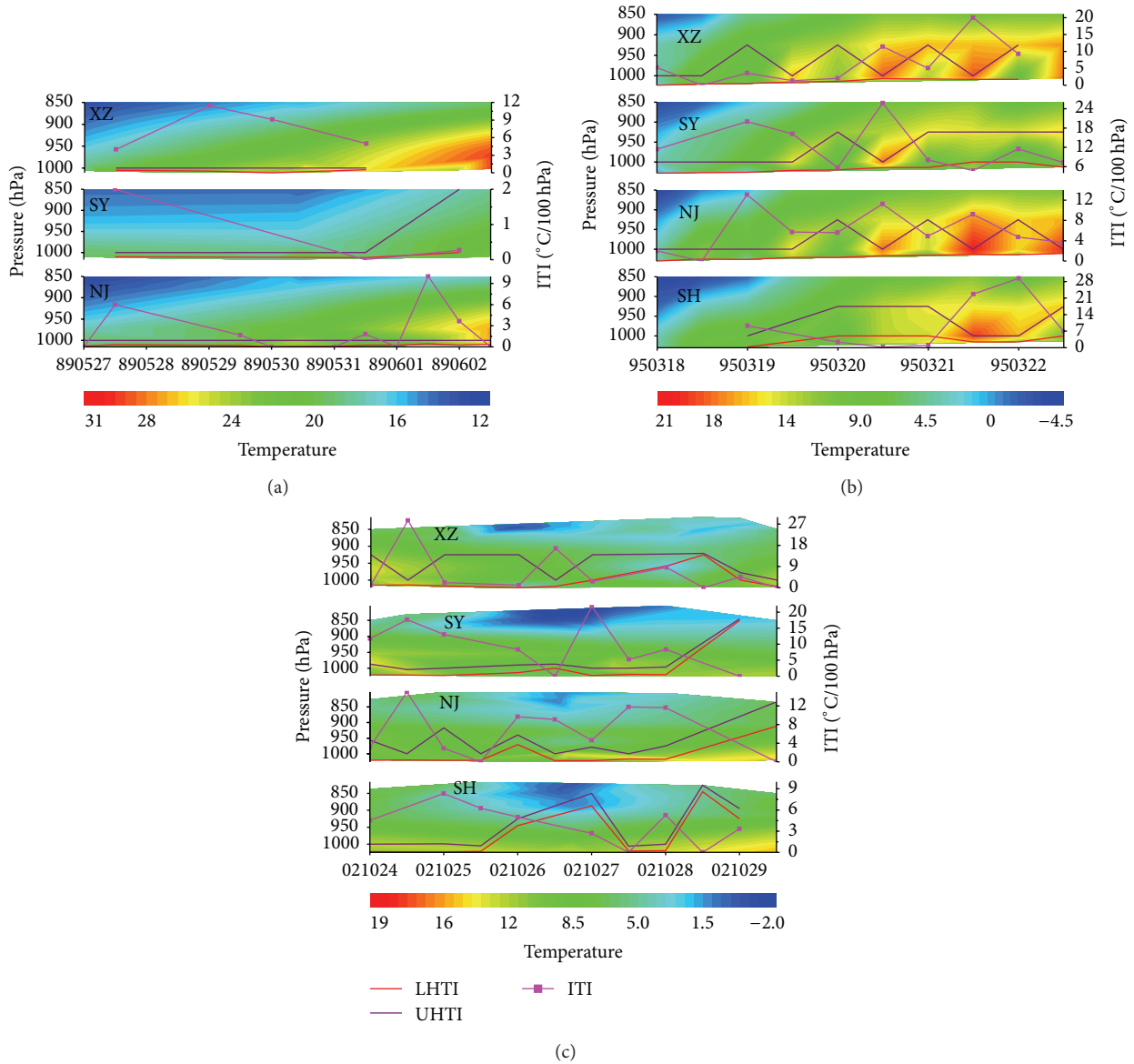


FIGURE 9: Temperature profiles of the backside of high-pressure (BAH) pattern during consecutive regional haze days at XuZhou (XZ), SheYang (SY), NanJing (NJ), and ShangHai (SH) ((a) 1989-05-27-1989-06-02, (b) 1995-03-18-1995-03-22, and (c) 2002-10-24-2002-10-29). Lower height of a temperature inversion (LHTI), upper height of a temperature inversion (UHTI), and intensity of the temperature inversion (ITI).

TABLE 6: Typical processes of the backside of high-pressure (BAH) pattern during consecutive regional haze days.

Series	Start day	End day	Duration
1	1989-05-27	1989-06-02	7
2	1995-03-18	1995-03-22	5
3	2002-10-24	2002-10-29	6

afterward, the duration was short. The temperature inversion was above the surface, weak, and thin.

From 1995-03-18 to 1995-03-22 (Figure 9(b)), the temperature inversion was just above the surface. The thickness had a notable diurnal variation: thick in the daytime and thin at

night. The intensity of the temperature varied among the 4 stations: it was stronger at night than during the day (opposite effect with the thickness). The intensity gradually increased at XZ following the haze development, but it gradually decreased at NJ. The peak of the intensity occurred overnight on March 20 at SY and during the daytime on March 22 at SH.

From 2002-10-24 to 2002-10-29 (Figure 9(c)), when the haze days began, a temperature inversion occurred near the surface, and the base of the temperature inversion increased to 950 hPa on the night of October 28 at XZ. The base of the temperature inversion increased on October 25 and the night of October 28 at SY; the inversion reached 850 hPa during the day on October 29. The base of the temperature

inversion reached 1000 hPa during the daytime on October 26 and nighttime of October 29 at NJ. The temperature inversion was generally higher after October 26. The thickness of the temperature inversion was variable: it was thick initially and thinned later. The base of the temperature varied in opposition to the intensity.

The surface layer of the temperature inversion was a major feature of the BAH pattern. Initially, the temperature inversion was thick; with the development of haze, the layer thinned and weakened.

3.2.2. Boundary-Layer Structures during Regional Heavy Haze

(1) *EQP*. In total, 12 days had regional heavy haze during the EQP pattern, 8 of which occurred in autumn or winter.

The boundary layer had 4 distinct structures. First, there was an inversion layer on the surface or an isothermal layer at all 4 stations (Figures 10(c), 10(d), 10(e), 10(f), 10(g), 10(h), and 10(j)); Figure 10(c) displays the single structure. The inversion layer or the isothermal layer structure occurred at 800 hPa in Figures 10(d), 10(e), 10(f), 10(g), and 10(h); at this height, the temperature inversion layer was thin and weak. A stronger inversion layer occurred between 850 hPa and 925 hPa in Figure 10(j). Second, 3 stations had inversion layers that occurred near the surface (Figures 10(b) and 10(k)), and only 1 station had a temperature inversion or isothermal structure between 925 hPa and 975 hPa. Third, 2 stations had inversion layers near the ground. Although no ground inversion layer occurred at the SY station, a thick temperature inversion layer occurred at 1000 hPa. Fourth, no apparent inversion layer existed, but a weak structure occurred at 975 hPa at the SH station in Figure 10(i).

This weather pattern was mainly characterized by a single or double inversion layer or isothermal layer near the ground. No inversion layer was present, only Figure 10(i) process. Generally, the atmospheric stability was slightly weak in summer, so stable stratification had difficulty forming. Therefore, we believe that heavy pollution was mainly caused by the sudden emissions release locally or overseas; because the air purification was insufficient, heavy haze formed.

(2) *ACF*. All instances of this weather pattern were associated with temperature inversions, but differences in height occurred. The inversion layer or the isothermal layer may have been at the surface (Figures 11(a), 11(h), and 11(i)), while other cases had multiple inversion layers (Figures 11(h) and 11(i)) between 800 hPa and 1000 hPa. Some cases had a surface temperature inversion at 3 stations (Figures 11(b) and 11(c)). Although one of the 4 stations had no temperature inversion at the surface (it occurred between 975 hPa and 1000 hPa). Some cases had a surface-layer temperature inversion at 2 stations (Figures 11(d), 11(e), and 11(f)); however, at the other 2 stations, an inversion layer occurred between 900 hPa and 1000 hPa. Figure 11(j) shows that only 1 station had a surface-based temperature inversion, while the other 3 stations had inversions between 850 hPa and 1000 hPa. Figure 11(g) shows that a surface-based inversion did not occur at any of the stations, but the temperature inversion

occurred between 925 hPa and 1000 hPa, except at the SY station.

The ACF pattern shows temperature inversions at different heights; the main feature was a single-layer temperature inversion and a high-altitude isothermal layer.

(3) *BOH*. A temperature inversion occurred near the surface at all 4 stations (Figures 12(c) and 12(d)), and there were multiple layers of temperature inversions between 800 hPa and 975 hPa (Figure 12(d)). Figure 12(a) shows a temperature inversion at the surface at 3 stations; the remaining station had an inversion at 1000 hPa. In some cases, 2 stations had temperature inversions at the surface, while the inversions occurred between 950 hPa and 1000 hPa at the other 2 stations. Figure 12(b) shows that only 1 station had a surface temperature inversion, while the other 3 stations had temperature inversions between 950 hPa and 1000 hPa.

In this weather pattern, the height of the temperature inversion layer greatly varied. However, all of the inversion layers formed below 950 hPa.

(4) *BAH*. Most of the cases were similar (Figures 13(a), 13(b), 13(d), 13(e), 13(f), 13(g), and 13(i)), with inversion layers or isothermal layers at the surface. Some cases had multiple temperature inversion layer structures (Figures 13(a), 13(b), 13(d), 13(e), 13(f), and 13(i)). Figure 13(h) shows temperature inversions and isothermal layers at the surface at all stations except XZ. Figure 13(c) shows that the temperature inversion layer was at 1000 hPa at the XZ and SY stations only. Figure 13(j) shows that the temperature inversion occurred at the surface at the NJ and SH stations and at 980 hPa at the XZ and SY stations.

This type of heavy haze case is associated with an inversion layer or isothermal layer on the ground; most cases had multiple inversion structures.

(5) *INT*. All of the cases of INT were similar at the 4 stations (Figures 14(a), 14(d), and 14(e)). The layer of the temperature inversion was above 1000 hPa, and the base of the inversion layer was also coincident. Figures 14(b) and 14(f) show that multiple temperature inversions occurred at the surface. Figure 14(c) reveals that the base of the temperature inversion was at 1000 hPa at the NJ station and was near the surface at the other stations.

The temperature inversion was thick and elevated in these cases.

(6) *Other Weather Patterns*. Figures 15(a) and 15(c) show an inversion and isothermal layer at the surface and multilayer temperature inversions. Figure 15(b) reveals the isothermal layer at the surface. Figure 15(d) shows the isothermal layer at the surface at the SY and XZ stations; the structure of the temperature inversion was not obvious. Figure 15(e) shows the isothermal layer at the surface and the thin inversion layer at 980 hPa. The cases in Figures 15(b), 15(d), and 15(e) occurred in late spring or early summer (May to June). The structure of the temperature inversion was not significant, and the temperature inversion was thin. Therefore, the cause

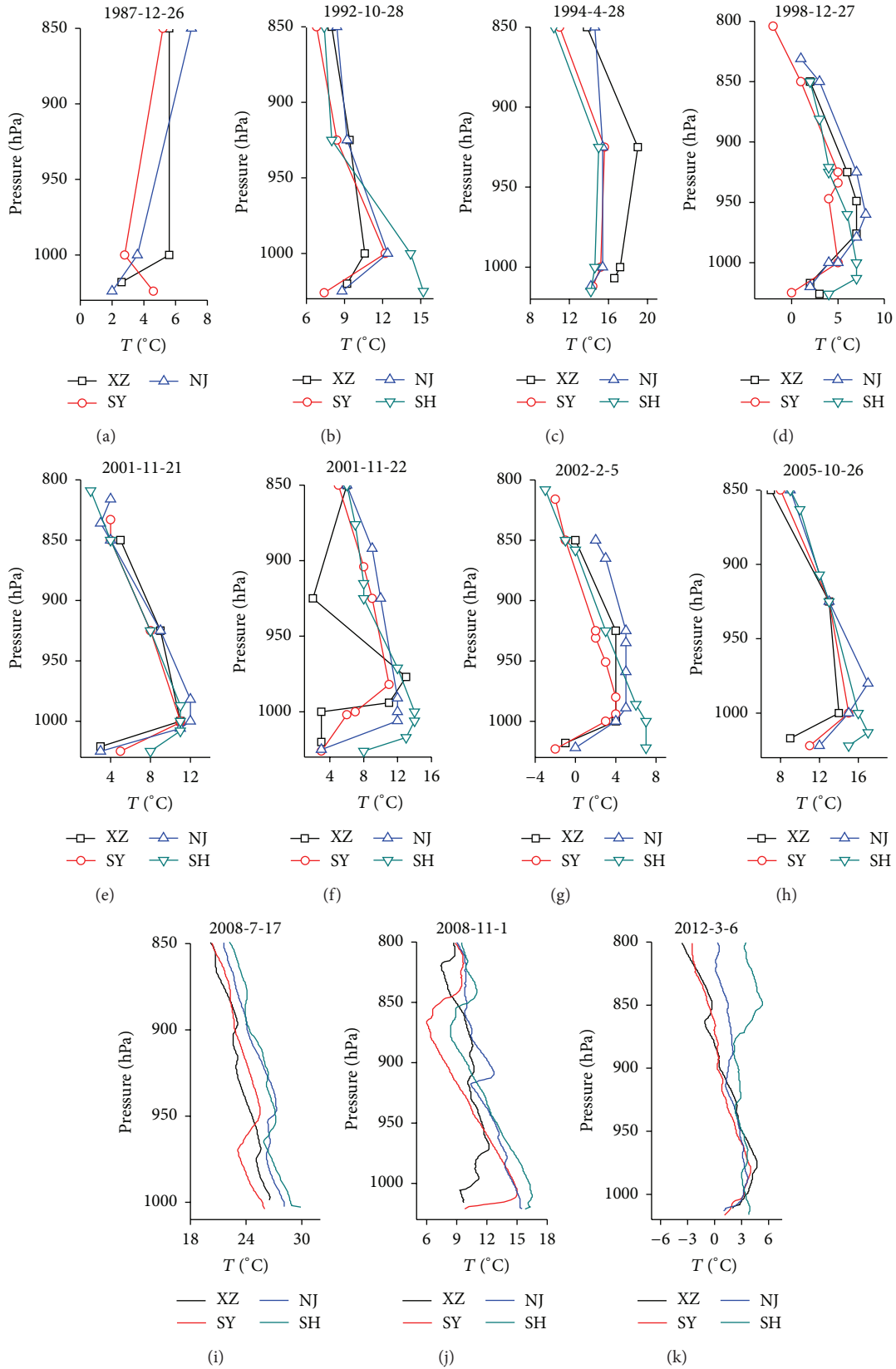


FIGURE 10: Temperature profiles of the EQP pattern during regional heavy haze days at XuZhou (XZ), SheYang (SY), NanJing (NJ), and ShangHai (SH). The x-axis is the temperature, the y-axis is the pressure, and the curved lines are the temperature profiles at the sounding stations ((a) 1987-12-26, (b) 1992-10-28, (c) 1994-04-28, (d) 1998-12-27, (e) 2001-11-21, (f) 2001-11-22, (g) 2002-02-05, (h) 2005-12-26, (i) 2008-07-17, (j) 2008-11-01, and (k) 2012-03-06).

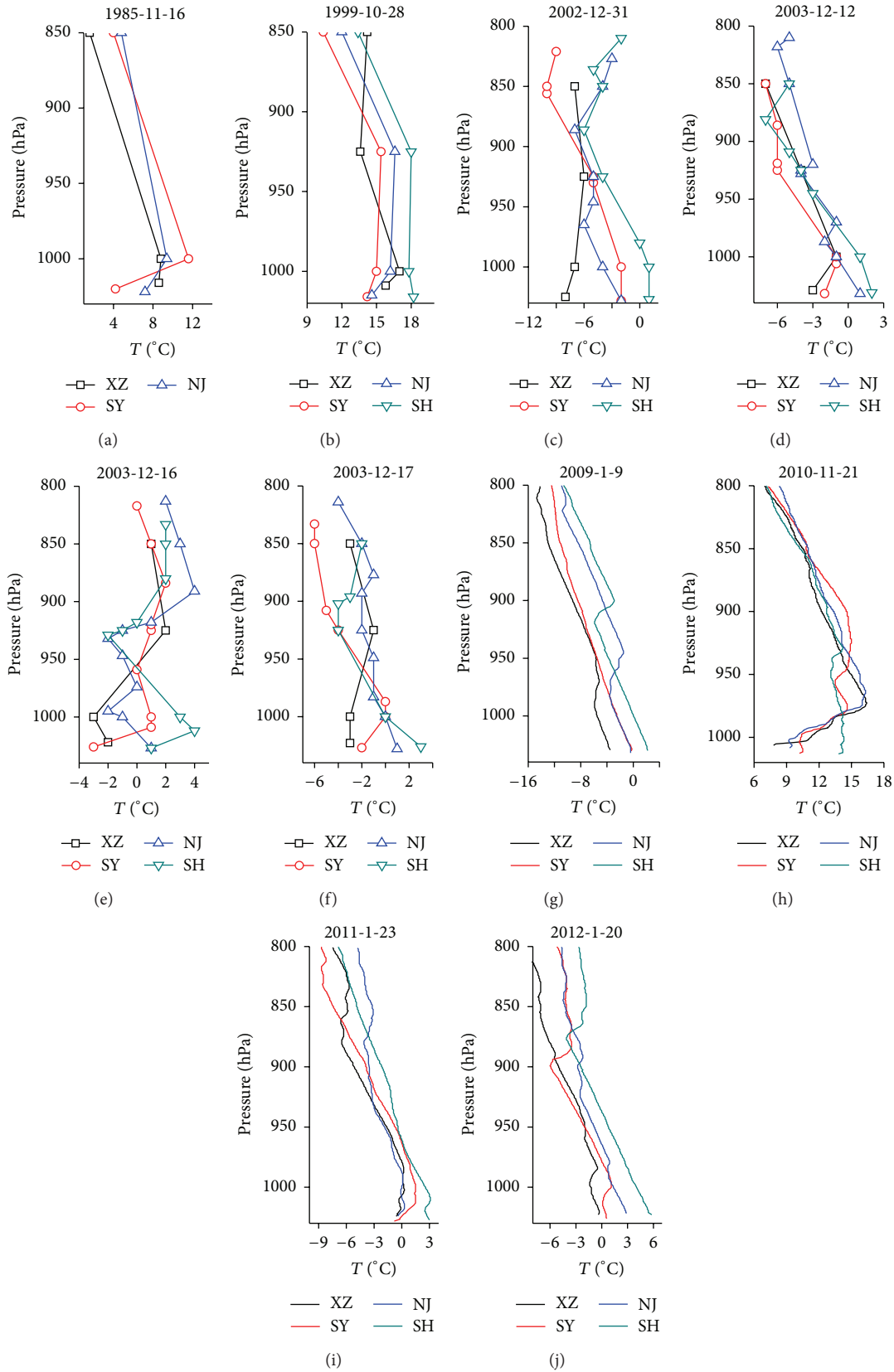


FIGURE 11: Temperature profiles of the ACF pattern during regional heavy haze days at XuZhou (XZ), SheYang (SY), NanJing (NJ), and ShangHai (SH). The x -axis is temperature, the y -axis is pressure, and the curved lines are the temperature profiles at the sounding stations ((a) 1985-11-16, (b) 1999-10-28, (c) 2002-12-31, (d) 2003-12-12, (e) 2003-12-16, (f) 2003-12-27, (g) 2009-01-09, (h) 2010-11-21, (i) 2011-01-23, and (j) 2012-01-20).

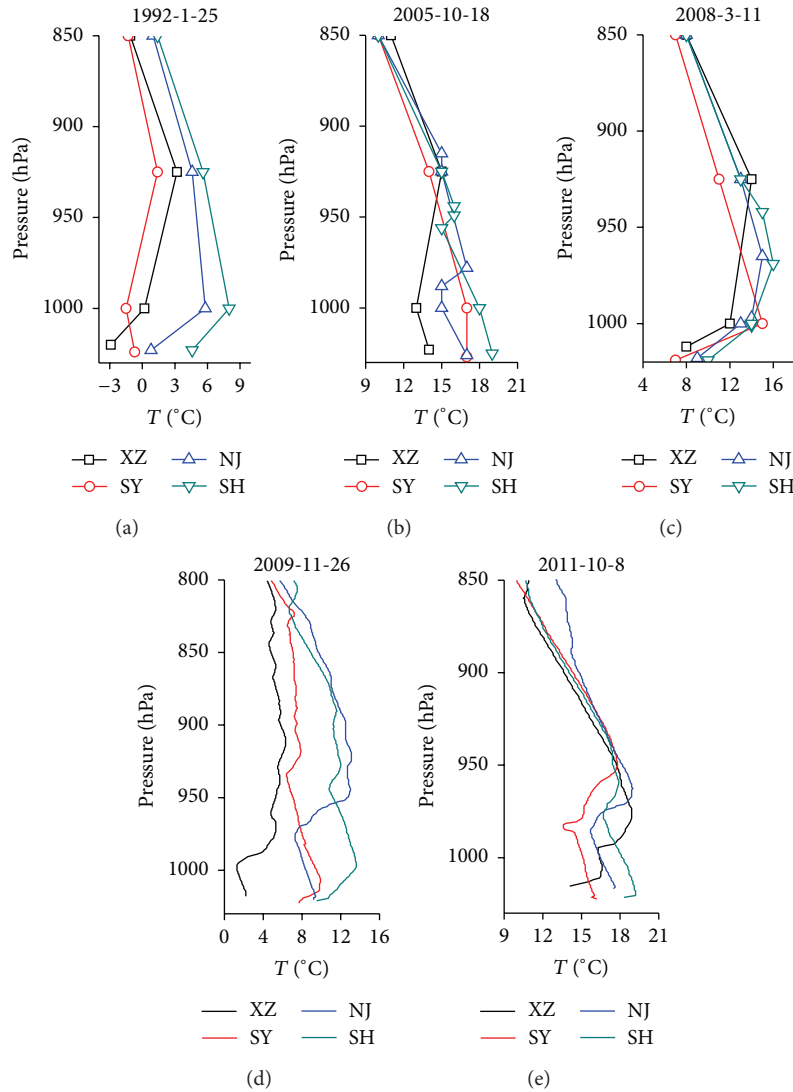


FIGURE 12: Temperature profiles of the BOH pattern during regional heavy haze days at XuZhou (XZ), SheYang (SY), NanJing (NJ), and ShangHai (SH). The x -axis is temperature, the y -axis is pressure, and the curved lines are the temperature profiles at the sounding stations ((a) 1992-01-25, (b) 2005-10-18, (c) 2008-03-11, (d) 2009-11-26, and (e) 2011-10-08).

of the heavy haze may be regional summer harvesting and seeding [64].

4. Conclusions

Existing research focuses on spatiotemporal haze distributions or the synoptic situation and boundary-layer characteristics of specific case studies. However, the weather and boundary-layer climate over many years are not well-known, particularly in terms of persistent haze and heavy haze. In this study, we classify haze and associated weather systems in southern Jiangsu from 1980 to 2012; the boundary-layer characteristics of regional haze events and regional heavy haze were also studied. The main conclusions are as follows:

- (1) The surface conditions were dominated by equalized pressure (EQP), the advancing edge of a cold front

(ACF), the base of high pressure (BOH), the backside of high pressure (BAH), the inverted trough of low pressure (INT), and saddle pressure (SAP).

- (2) Based on the surface conditions, regional haze events could be divided into 4 types, each of which has a different boundary-layer structure. Type I is EQP, in which the boundary layer is that the bottom height of the temperature inversion layer is lower, the thickness is thinner, and the intensity is diverse with the different cases. Type II is the ACF, in which a cold front gradually advances and creates a near-surface temperature inversion in most processes. The intensity of the temperature inversion was strong and varied. Type III is the BOH, in which a shallow but intense temperature inversion is elevated as haze event progresses. Type IV is the BAH, at the start of

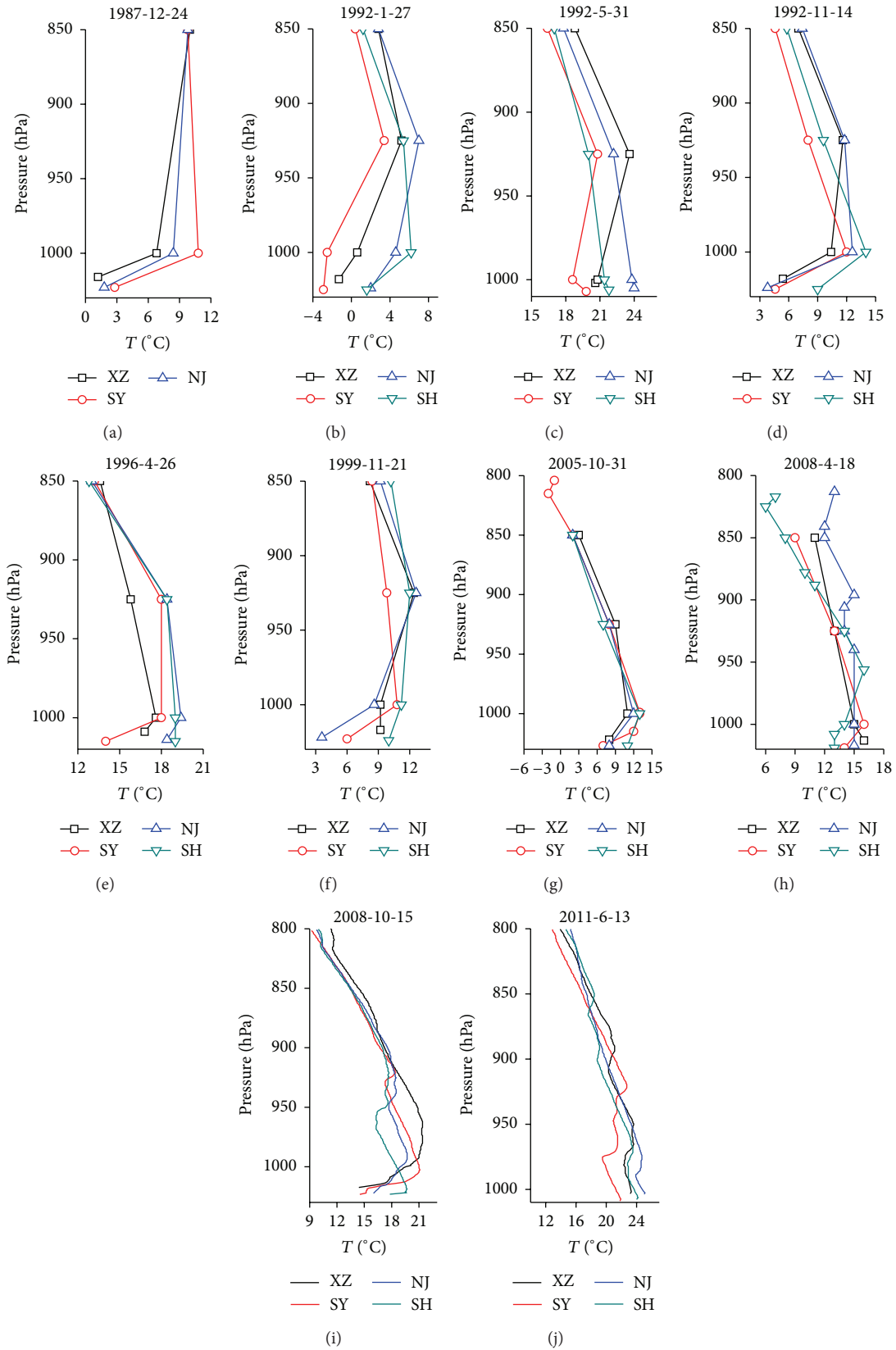


FIGURE 13: Temperature profiles of the BAH pattern during regional heavy haze days at XuZhou (XZ), SheYang (SY), NanJing (NJ), and ShangHai (SH). The x -axis is temperature, the y -axis is pressure, and the curved lines are the temperature profiles at the sounding stations ((a) 1987-12-24, (b) 1992-01-27, (c) 1992-05-31, (d) 1992-11-11, (e) 1996-04-26, (f) 1999-11-21, (g) 2005-10-31, (h) 2008-04-18, (i) 2008-10-15, and (j) 2011-06-13).

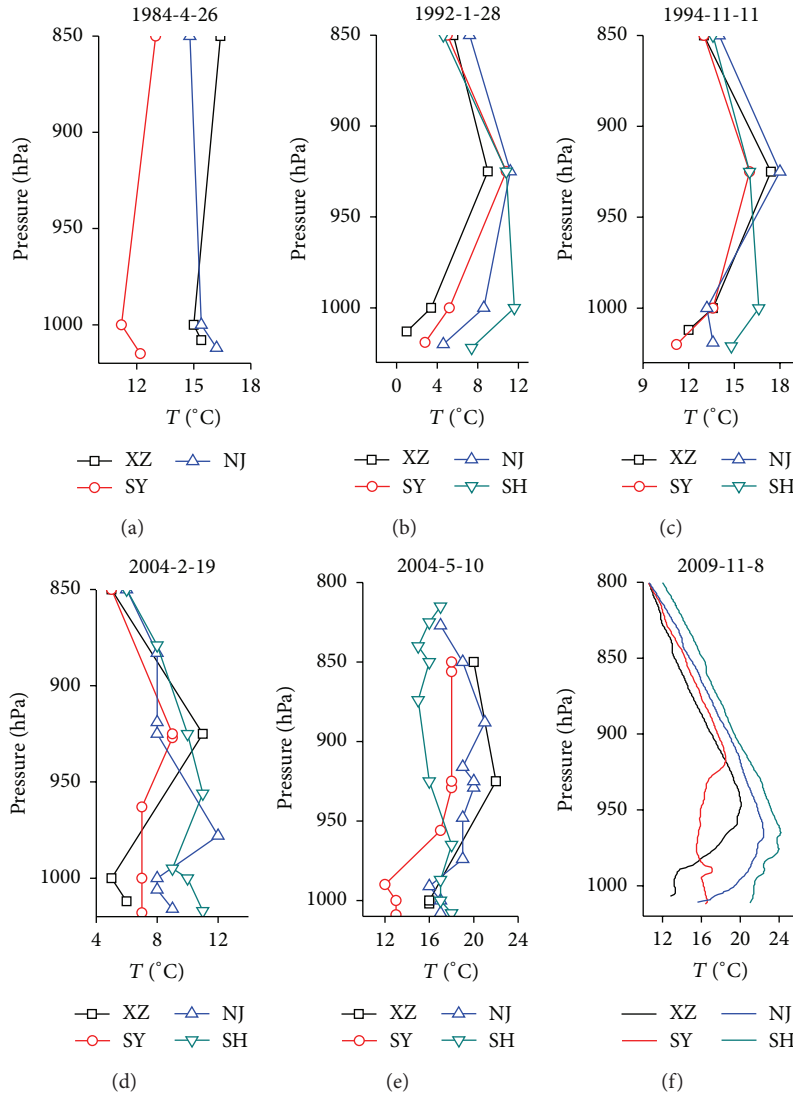


FIGURE 14: Temperature profiles of the INT pattern during regional heavy haze days at XuZhou (XZ), SheYang (SY), NanJing (NJ), and ShangHai (SH). The x-axis is temperature, the y-axis is pressure, and the curved lines are the temperature profiles at the sounding stations ((a) 1984-04-26, (b) 1992-01-28, (c) 1994-11-11, (d) 2004-02-19, (e) 2004-05-10, and (f) 2009-11-08).

the haze-day case, in which the temperature inversion is vertically extensive. However, as the haze event progresses, the layer becomes shallow and weak.

- (3) During heavy haze, the surface mainly experiences EQP, ACF, BOH, BAH, and INT. The boundary-layer structure of EQP is characterized by a single or double inversion or isothermal layer near the surface. The ACF is associated with a unique inversion layer height, which is often a single layer. An isothermal layer is common at high altitudes. The BOH reveals a low-level temperature inversion. The BAH pattern displays a multilayer temperature inversion or isothermal layer at the surface. The INT has an extensive boundary layer with an elevated temperature inversion.

Conflict of Interests

The authors declare that there is no conflict of interests regarding the publication of this paper.

Acknowledgments

Funding for this work was jointly provided by the Natural Science Foundation of Jiangsu Province (Grant no. BK20130111), the Key Projects of Jiangsu Meteorological Bureau (Grant no. KZ201405), the Social Development Projects of Wuxi (Science and Technology Development) (Grant no. CSE11N1301), and the National Key Technology Support Program (Grant no. 2014BAC22B04).

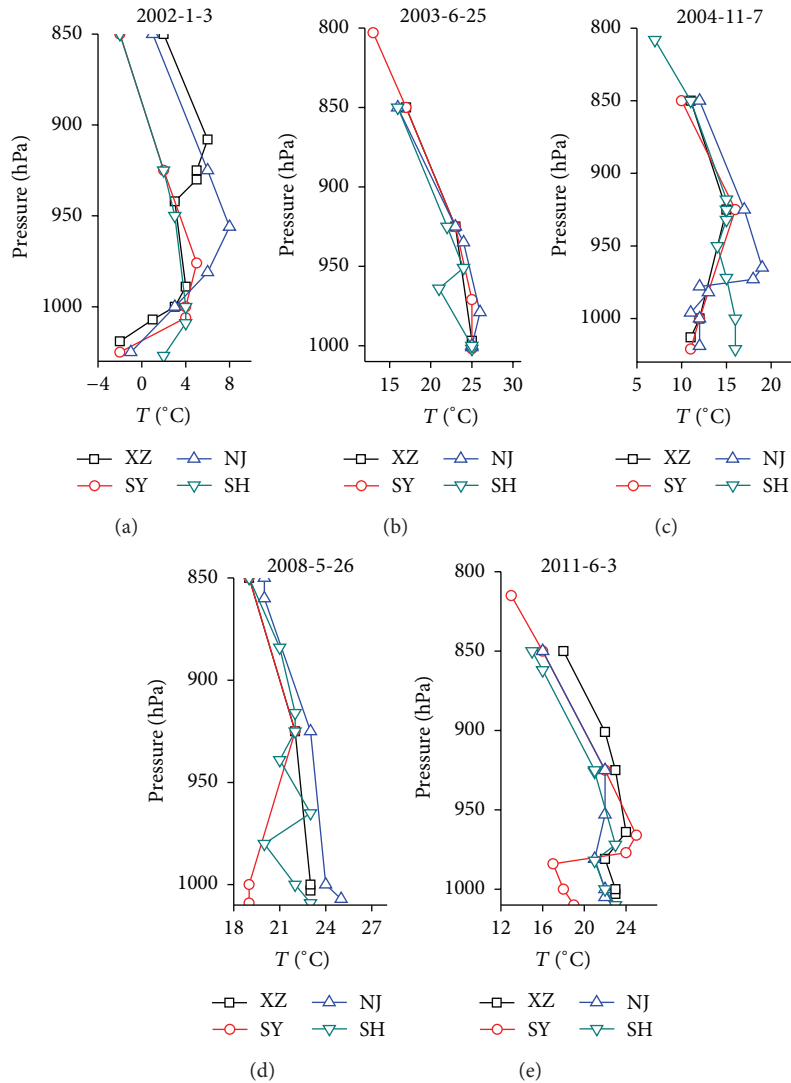


FIGURE 15: Temperature profiles of other weather types during regional heavy haze days at XuZhou (XZ), SheYang (SY), NanJing (NJ), and ShangHai (SH). The x-axis is temperature, the y-axis is pressure, and the curved lines are the temperature profiles at the sounding stations (a) 2002-01-03, (b) 2003-06-25, (c) 2004-11-07, (d) 2008-05-26, and (e) 2011-06-03).

References

[1] R. G. Elridge, "Climatic visibilities of the United States," *Journal of Applied Meteorology*, vol. 5, pp. 227–282, 1966.

[2] M. E. Miller, N. L. Canfield, T. A. Ritter, and C. R. Weaver, "Visibility changes in Ohio, Kentucky, and Tennessee from 1962 to 1969," *Monthly Weather Review*, vol. 100, no. 1, pp. 67–71, 1972.

[3] R. E. Munn, "Secular increases in summer haziness in the Atlantic provinces," *Atmosphere*, vol. 11, pp. 156–161, 1973.

[4] R. E. Weiss, A. P. Waggoner, R. J. Charlson et al., "Sulfate aerosol: its geographical extent in the midwestern and southern United States," *Science*, vol. 197, pp. 997–998, 1977.

[5] R. B. Husar, D. E. Poll, J. M. Holloway et al., "Trends of eastern U.S. haziness since 1948," in *Proceedings of the 4th Symposium on Turbulence, Diffusion and Air Pollution*, pp. 249–256, American Meteorological Society, Boston, Mass, USA, 1979.

[6] R. B. Husar, J. M. Holloway, D. E. Patterson, and W. E. Wilson, "Spatial and temporal pattern of eastern U.S. haziness: a summary," *Atmospheric Environment*, vol. 15, no. 10-11, pp. 1919–1928, 1981.

[7] M. A. Ferman, G. T. Wolff, and N. A. Kelly, "The nature and sources of haze in the Shenandoah Valley/Blue Ridge Mountains area," *Journal of the Air Pollution Control Association*, vol. 31, no. 10, pp. 1074–1082, 1981.

[8] G. T. Wolff, N. A. Kelly, and M. A. Freman, "Source regions of summertime ozone and haze episodes in the eastern United States," *Water, Air, and Soil Pollution*, vol. 18, no. 1-3, pp. 65–81, 1982.

[9] J. Trijonis, "Existing and natural background levels of visibility and fine particles in the rural East," *Atmospheric Environment*, vol. 16, no. 10, pp. 2431–2445, 1982.

[10] C. S. Sloane, "Visibility trends. I. Methods of analysis," *Atmospheric Environment*, vol. 16, no. 1, pp. 41–51, 1982.

[11] C. S. Sloane, "Visibility trends—II. Mideastern United States 1948–1978," *Atmospheric Environment*, vol. 16, no. 10, pp. 2309–2321, 1982.

- [12] C. S. Sloane, "Summertime visibility declines: Meteorological influences," *Atmospheric Environment*, vol. 17, no. 4, pp. 763–774, 1983.
- [13] C. S. Sloane, "Meteorologically adjusted air quality trends: visibility," *Atmospheric Environment Part A: General Topics*, vol. 18, no. 6, pp. 1217–1229, 1984.
- [14] R. B. Husar and W. E. Wilson, "Haze and sulfur emission trends in the eastern United States," *Environmental Science & Technology*, vol. 27, no. 1, pp. 12–16, 1993.
- [15] M. Radojevic and H. Hassan, "Air quality in Brunei Darussalam during the 1998 haze episode," *Atmospheric Environment*, vol. 33, no. 22, pp. 3651–3658, 1999.
- [16] L. D. Zhang, W. J. Ye, D. H. Chen et al., "Discuss the haze weather impaction on the visibility of Xiamen city," *Journal of Meteorological Research and Application (Chinese Edition)*, vol. 28, no. 11, pp. 149–150, 2007.
- [17] X. L. Chen, Y. R. Feng, S. J. Fan et al., "Effect of the off-shore background flow and sea-land breezes on haze weather over the pearl river delta region," *Chinese Journal of Atmospheric Sciences (Chinese Edition)*, vol. 32, no. 3, pp. 530–542, 2008.
- [18] Y. F. Liao, X. Y. Wu, Z. X. Pan et al., "Climatic characteristics of haze in hunan province during 1961–2006," *Advances in Climate Change Research (Chinese Edition)*, vol. 3, no. 5, pp. 260–265, 2007.
- [19] Z. J. Jiang, F. X. Long, Y. Y. Li et al., "Haze variation characteristics of Guilin city in recent 10 years," *Journal of Meteorological Research and Application (Chinese Edition)*, vol. 30, no. 1, pp. 68–79, 2009.
- [20] G. Gao, "The climatic characteristics and change of haze days over China during 1961–2005," *Acta Geographica Sinica*, vol. 63, no. 7, pp. 761–768, 2008.
- [21] Y. D. Hu and Z. J. Zhou, "Climatic characteristics of haze in China," *Meteorological Monthly (Chinese Edition)*, vol. 35, no. 7, pp. 73–78, 2009.
- [22] D. Wu, X. J. Wu, F. Li et al., "Temporal and spatial variation of haze during 1951–2005 in Chinese mainland," *Acta Meteorologica Sinica (Chinese Edition)*, vol. 68, no. 5, pp. 680–688, 2010.
- [23] L. C. Song, R. Gao, Y. Li, and G. F. Wang, "Analysis of China's haze days in winter half year and climatic background during 1961–2012," *Advances in Climate Change Research*, vol. 9, no. 5, pp. 313–318, 2013.
- [24] Z. Cheng, C. Chen, C. Huang, H. Huang, L. Li, and H. Wang, "Trans-boundary primary air pollution between cities in the Yangtze River Delta," *Acta Scientiae Circumstantiae (Chinese Edition)*, vol. 31, no. 4, pp. 686–694, 2011.
- [25] J. Shi, L. L. Cui, Q. S. He, and L. Sun, "The changes and causes of fog and haze days in eastern China," *Acta Geographica Sinica*, vol. 65, no. 5, pp. 533–542, 2010.
- [26] J. Shi and L.-L. Cui, "Characteristics and influencing factors of haze in the Yangtze River Delta region," *China Environmental Science*, vol. 33, no. 12, pp. 2113–2122, 2013.
- [27] J. Song, T. Chen, Z. Q. Xie, and Q. Miao, "Impact on spatio-temporal variation of fog and haze days due to rapid urbanization in Jiangsu," *Journal of the Meteorological Sciences*, vol. 32, no. 3, pp. 275–281, 2012.
- [28] X.-L. Chen, Y.-R. Feng, A.-Y. Wang et al., "Numerical experiment research on air pollutants during atmospheric haze over the multi-cities of pearl river delta region," *Acta Scientiarum Natralium Universitatis Sunyatseni (Chinese Edition)*, vol. 46, no. 4, pp. 103–107, 2007.
- [29] D. Wu, G. L. Liao, X. J. Deng et al., "Transport condition of surface layer under haze weather over the Pearl River Delta," *Journal of Applied Meteorological Science*, vol. 19, no. 1, pp. 1–9, 2008 (Chinese).
- [30] H. H. Chen, D. Wu, H. B. Tan et al., "Study on the character of haze weather process from the year 2001 to 2008 over the Pearl River Delta," *Journal of Tropical Meteorology (Chinese Edition)*, vol. 26, no. 2, pp. 147–155, 2010.
- [31] P. S. Zhao, X. F. Xu, W. Meng et al., "Characteristics of hazy days in the region of Beijing, Tianjin, and Hebei," *China Environmental Science*, vol. 32, no. 1, pp. 31–36, 2012.
- [32] X. Q. Wang, M. S. Sun, T. Yang et al., "Interdecadal change in frequency of dust-haze episodes in north China plain," *Climatic and Environmental Research (Chinese Edition)*, vol. 18, no. 2, pp. 165–170, 2013.
- [33] Z. H. Ren, F. Q. Su, Z. H. Chen et al., "Influence of synoptic systems on the distribution and evolution process of PM10 concentration in the boundary layer in summer and autumn," *Chinese Journal of Atmospheric Sciences*, vol. 32, no. 4, pp. 741–751, 2008 (Chinese).
- [34] X. Q. Rao, F. Li, N. F. Zhou et al., "Analysis of a large-scale haze over middle and eastern China," *Meteorological Monthly (Chinese Edition)*, vol. 34, no. 6, pp. 89–96, 2008.
- [35] P. B. Zhang, A. J. Jiang, J. L. Sun, Y. Jiang, P. He, and D. Liu, "Decadal change characteristics of autumn haze days in Jiangsu Province and its influential factors," *Advances in Climate Change Research*, vol. 8, no. 3, pp. 205–212, 2012 (Chinese).
- [36] J.-C. Duan, X.-H. Bi, J.-H. Tan, G.-Y. Sheng, and J.-M. Fu, "Particle diameter distribution of polycyclic aromatic hydrocarbons (PAHs) in atmospheric particle during haze period in Guangzhou," *China Environmental Science (Chinese Edition)*, vol. 26, no. 1, pp. 6–10, 2006.
- [37] Y.-Q. Tong, Y. Yin, L. Qian, and J.-L. An, "Analysis of the characteristics of hazy phenomena in Nanjing area," *China Environmental Science*, vol. 27, no. 5, pp. 584–588, 2007 (Chinese).
- [38] W. B. Tang, "The climatic characteristics of haze and the influence of heat island effect in Guilin in the past 50 years," *Journal of Meteorological Research and Application (Chinese Edition)*, vol. 28, no. 4, pp. 20–25, 2007.
- [39] J. P. Zhao, J. H. Tan, X. H. Bi et al., "The mass concentrations of inorganic elements in atmospheric particles during haze period in Guangzhou," *Environmental Chemistry (Chinese Edition)*, vol. 27, no. 3, pp. 322–326, 2008.
- [40] Y. Y. Guo, A. M. Miao, and H. Y. Zhang, "Analysis on the climate characteristics of the haze-weather for nearly 47 years in Taiyuan City," *Sci-Tech Information Development & Economy (Chinese Edition)*, vol. 18, no. 33, pp. 120–121, 2008.
- [41] J. Guo, "Climatic characteristics of atmospheric haze in Tianjin area," *Urban Environment & Urban Ecology (Chinese Edition)*, vol. 2, no. 3, pp. 12–14, 2008.
- [42] N. F. Zhou, F. Li, X. Q. Rao, and K. Yang, "Study on haze weather in China during winter-time of 2006," *Meteorological Monthly*, vol. 34, no. 6, pp. 81–88, 2008 (Chinese).
- [43] H. Pan, F. Geng, Y. Chen et al., "Analysis of a haze event by micro-pulse light laser detection and ranging measurements in Shanghai," *Acta Scientiae Circumstantiae*, vol. 30, no. 11, pp. 2164–2173, 2010.
- [44] H. G. Xu, S. Deng B, X. G. Zhou et al., "Effect of fog on urban boundary layer and environment," *Journal of Applied Meteorological Science (Chinese Edition)*, vol. 13, no. 1, pp. 170–176, 2002.

- [45] Z. L. Wu, A. X. Liu, C. C. Zhang et al., "Vertical distribution feature of PM_{2.5} and effect of boundary layer in Tianjin," *Urban Environment & Urban Ecology (Chinese Edition)*, vol. 22, no. 4, pp. 24–29, 2009.
- [46] T. Y. Xiu, Y. Sun, T. Song, and Y. Wang, "The vertical distribution of ozone and boundary layer structure analysis during summer haze in Beijing," *Acta Scientiae Circumstantiae (Chinese Edition)*, vol. 33, no. 2, pp. 321–331, 2013.
- [47] M. Xu, Y.-Q. Zhu, and W.-T. Yu, "Preliminary study on haze in Tianjin," *The Chinese Journal of Process Engineering*, vol. 6, no. 2, pp. 127–132, 2006.
- [48] X. Zhang, X. H. Cai, and F. H. Chai, "Structures and characteristics of the atmospheric boundary layer over Beijing area in autumn," *Acta Scientiarum Naturalium Universitatis Pekinensis*, vol. 42, no. 2, pp. 220–225, 2006.
- [49] J. W. Yu, Y. Sun, B. Zhang et al., "Analysis of one heavy haze case happened in the region around Yangtze River in Jiangsu province," *Journal of the Meteorological Sciences (Chinese Edition)*, vol. 29, no. 5, pp. 664–669, 2009.
- [50] H. Zhang, C. E. Shi, M. Y. Qiu, and W. Xie, "Long-term variation of haze phenomena in Heifei and its impact factors," *Acta Scientiae Circumstantiae (Chinese Edition)*, vol. 30, no. 4, pp. 714–721, 2010.
- [51] Y. H. Zhang, Y. J. Ma, N. W. Liu, D. Zhou, Y. Wang, and Y. Hong, "Study on environmental characteristics of haze in Shenyang," *Ecology and Environmental Sciences*, vol. 19, no. 11, pp. 2636–2641, 2010 (Chinese).
- [52] X. L. Zhang and R. H. Chen, "Inversion characteristic analysis of Nanyang boundary layer," *Meteorological and Environmental Sciences (Chinese Edition)*, vol. 34, no. S1, pp. 116–119, 2011.
- [53] J.-L. Zhu, T.-J. Wang, L. Xing, Q. Mu, and D.-R. Zhou, "Analysis on the characteristics and mechanism of a heavy haze episode in Jiangsu Province," *China Environmental Science (Chinese Edition)*, vol. 31, no. 12, pp. 1943–1950, 2011.
- [54] Y. Zhang, Y. Yin, L. X. Shi et al., "An observational study of aerosol property under typical polluted weather condition," *Plateau Meteorology (Chinese Edition)*, vol. 31, no. 5, pp. 1432–1438, 2012.
- [55] J. Zhang and S. T. Rao, "The role of vertical mixing in the temporal evolution of ground-level ozone concentrations," *Journal of Applied Meteorology*, vol. 38, no. 12, pp. 1674–1691, 1999.
- [56] P. Solomon, E. Cowling, G. Hidy, and C. Furiness, "Comparison of scientific findings from major ozone field studies in North America and Europe," *Atmospheric Environment*, vol. 34, no. 12–14, pp. 1885–1920, 2000.
- [57] G. M. Hidy, "Ozone process insights from field experiments—part I: overview," *Atmospheric Environment*, vol. 34, no. 12–14, pp. 2001–2022, 2000.
- [58] C.-H. Lin, Y.-L. Wu, C.-H. Lai, P.-H. Lin, H.-C. Lai, and P.-L. Lin, "Experimental investigation of ozone accumulation overnight during a wintertime ozone episode in south Taiwan," *Atmospheric Environment*, vol. 38, no. 26, pp. 4267–4278, 2004.
- [59] J. E. Yorks, A. M. Thompson, E. Joseph, and S. K. Miller, "The variability of free tropospheric ozone over Beltsville, Maryland (39N, 77W) in the summers 2004–2007," *Atmospheric Environment*, vol. 43, no. 11, pp. 1827–1838, 2009.
- [60] Y. F. Guo, D. Y. Liu, B. Zhou et al., "Study on haze characteristics in Wuxi and its impact factors," *Meteorological Monthly*, vol. 39, no. 10, pp. 1314–1324, 2013.
- [61] China Meteorological Administration, "Observation and prediction of haze," the meteorological industry standard of the People's Republic of China, QX/T113-2010, 2010.
- [62] M. Tao, L. Chen, Z. Wang, J. Tao, and L. Su, "Satellite observation of abnormal yellow haze clouds over East China during summer agricultural burning season," *Atmospheric Environment*, vol. 79, pp. 632–640, 2013.
- [63] G. Wang, K. Kakawamura, M. Xie et al., "Organic molecular compositions and size distributions of Chinese summer and autumn aerosols from Nanjing: characteristic haze event caused by wheat straw burning," *Environmental Science & Technology*, vol. 43, no. 17, pp. 6493–6499, 2009.
- [64] G.-L. Cao, X.-Y. Zhang, D. Wang, and F.-C. Zheng, "Inventory of atmospheric pollutants discharged from biomass burning in China continent," *China Environmental Science*, vol. 25, no. 4, pp. 389–393, 2005.

Research Article

Impacts of Wind Stress Changes on the Global Heat Transport, Baroclinic Instability, and the Thermohaline Circulation

Jeferson Prietsch Machado,¹ Flavio Justino,² and Luciano Ponzi Pezzi³

¹Universidade Estadual Paulista Júlio de Mesquita Filho (UNESP), 17012-633 Bauru, SP, Brazil

²Universidade Federal de Viçosa (UFV), 36570-000 Viçosa, MG, Brazil

³Instituto Nacional de Pesquisas Espaciais (INPE), 12227-010 São José dos Campos, SP, Brazil

Correspondence should be addressed to Jeferson Prietsch Machado; jefpmac@gmail.com

Received 9 August 2015; Revised 5 November 2015; Accepted 29 November 2015

Academic Editor: Leonard J. Pietrafesa

Copyright © 2016 Jeferson Prietsch Machado et al. This is an open access article distributed under the Creative Commons Attribution License, which permits unrestricted use, distribution, and reproduction in any medium, provided the original work is properly cited.

The wind stress is a measure of momentum transfer due to the relative motion between the atmosphere and the ocean. This study aims to investigate the anomalous pattern of atmospheric and oceanic circulations due to 50% increase in the wind stress over the equatorial region and the Southern Ocean. In this paper we use a coupled climate model of intermediate complexity (SPEEDO). The results show that the intensification of equatorial wind stress causes a decrease in sea surface temperature in the tropical region due to increased upwelling and evaporative cooling. On the other hand, the intensification of wind stress over the Southern Ocean induces a regional increase in the air and sea surface temperatures which in turn leads to a reduction in Antarctic sea ice thickness. This occurs in association with changes in the global thermohaline circulation strengthening the rate of Antarctic Bottom Water formation and a weakening of the North Atlantic Deep Water. Moreover, changes in the Southern Hemisphere thermal gradient lead to modified atmospheric and oceanic heat transports reducing the storm tracks and baroclinic activity.

1. Introduction

The coupling between the atmosphere and ocean has been investigated by several studies. The pioneer works by Walker and Bilss [1], Bjerknes [2], and Wyrski [3] are the starting point to the understanding of the El Niño-Southern Oscillation (ENSO), the air-sea interaction, and the decadal climate variability. Recently, studies have analyzed the impacts caused by fluctuations of wind stress on oceanic and atmospheric circulations [4–10]. This recent motivation is directly related to climate projections for the coming decades. In this context, numerical models designed with the increase in the concentration of CO₂ in the atmosphere indicate a maximum displacement of wind stress to higher latitudes than normal, due to the intensification of the winds in extratropical latitudes [11–14]. On this hypothesis, it becomes important to numerical climate simulations forced by wind stress anomalies to analyze the impacts caused on the oceanic and atmospheric circulations. In the following several studies

based on numerical modeling will be shown, demonstrating the importance of wind stress for the coupling between the atmosphere and ocean.

McCreary and Lu [15] and Liu and Philander [16] argued that the strength of the oceanic subtropical cells as well as the magnitude of the equatorial upwelling is tightly dependent on the wind stress near 10°N–20°N. One should expect that changes in the magnitude of the winds can intensify the vertical oceanic circulation through changes in the Ekman transport. Indeed, an intensification of the equatorial wind stress by about 30–50% leads to an enhancement of the meridional water transport by about 2 Sv (1 Sverdrup = 10⁶ m³ s⁻¹) and an equatorial cooling of approximately 2°C. This has been a common feature in climate simulations focusing on the Last Glacial Maximum [17–19]. It is noteworthy that England et al. [20] showed that a pronounced strengthening in Pacific trade winds over the past two decades is sufficient to account for the cooling of the tropical Pacific and a substantial slowdown in surface warming through increased subsurface ocean heat

uptake. Furthermore, they showed that the accelerated trade winds have increased equatorial upwelling in the central and eastern Pacific, lowering sea surface temperature (SST) there, which drives further cooling in other regions.

On the other hand, Timmermann and Goosse [6] and MacMynowski and Tziperman [21] highlighted the importance of the wind stress to the global thermohaline circulation (THC). The wind stress changes on the Southern Ocean may also be responsible for modulating the intensity of the Atlantic Meridional Overturning Circulation (MOC) [22]. These wind-induced changes of the MOC can regulate the glacial-interglacial periods due to changes in air-sea CO₂ fluxes [23–25]. Timmermann and Goosse [6], by disregarding the influence of wind stress, have found an interruption in the MOC. This has been attributed to changes in the equator-pole density gradient which is not maintained without the wind stress forcing, because the wind stress contributes to the horizontal transport of salinity due to the wind-driven circulation. It plays also an important role in the vertical transport of salinity and in the oceanic convection due to Ekman pumping.

Also it is important to highlight how the wind stress influences the oceanic and atmospheric circulation patterns at mid and high latitudes of the Southern Hemisphere. In the study made by Yang et al. [7] they analyze changes in wind stress for decadal periods in the Southern Ocean and associated with ozone depletion in the Antarctic region. These authors used the 40 years of European Centre for Medium-Range Weather Forecasts (ECMWF) Reanalysis (ERA 40) data and found an increasing wind stress trend between latitudes of 45°S and 60°S in the past 20 years. According to the authors, this occurs due to the wind anomalies due to the Antarctic Oscillation, which interacts with the medium flow and meridional circulation.

Menviel et al. [8], based on LOVECLIM climate simulations, found that 15% intensification of the near surface winds between 40°S and 60°S increases the Antarctic Bottom Water (AABW) rate of formation from 16 to 32 Sv.

Saenko [9] examining the impact of the wind stress changes on SSTs has demonstrated surface temperature reduction at high latitudes accompanied by increased sea ice area. Changes in the wind stress are also responsible for increasing the atmospheric poleward heat transport in both hemispheres due to modulation of the storm tracks [26].

Ma et al. [10] concluded that an absence of wind stress over 40°S leads to a reduction of approximately 50% in the MOC. This reveals the strong coupling between the atmosphere and the ocean at high latitudes as well as its control on the THC. Indeed, the absence of wind stress in 40°S leads to a reduction of vertical mixing and upwelling, inducing the surface cooling and sea ice expansion. However, warming is observed in subsurface waters due to the weakening of the vertical mixing.

Recently, Machado et al. [27] showed that the wind stress intensification in the equatorial region causes changes in Atlantic Dipole and enhanced precipitation over Brazilian northeast. Moreover, the wind stress intensification in the extratropical Southern Hemisphere region induces weakening of positive Antarctic Oscillation phase.

Therefore, the aim of this study is to analyze the oceanic and atmospheric circulation response to increased wind stress at different latitudes in the SH. We also focus on the baroclinic instability and storm tracks changes as well as on the identification of the main changes in the atmospheric and oceanic heat transport. In particular, changes in the global thermohaline circulation are analyzed. It should be stressed that the response of the atmospheric and oceanic heat transport to modified wind stress has been partially overlooked in the literature.

This paper is organized as follows: Section 2 provides a description of the numerical coupled model used and details on the employed methodology. Section 3 shows the anomalies found in atmospheric and oceanic circulations. This study presents in Section 4 the conclusions and final remarks.

2. Numerical Model and Experiments Design

This study is based on simulations conducted with the coupled climate model Speedy-Ocean (SPEEDO) [28]. SPEEDO may be classified as an Earth system model of intermediate complexity. This model was chosen in order to fill a gap between the global models, which have physical representation quite complex and conceptual models, which are rather simplified [28].

The atmospheric component of the SPEEDO coupled model, called Simplified Parameterization primitive-Equation Dynamics (SPEEDY), is a hydrostatic spectral model with 8 vertical layers (925, 850, 700, 500, 300, 200, 100, and 30 hPa) and horizontal truncation T30, which corresponds to a horizontal resolution of 3.75°. This uses the divergence-vorticity equation as described by Bourke [29]. The parameterizations include the short- and long-wave radiation schemes, large-scale condensation and convection, momentum, heat and humidity fluxes, and vertical diffusion processes. The convection is represented by a mass flow scheme that is activated when conditional instability occurs. This version is coupled to physical parameterizations for the hydrological cycle [30]. Additional details about the model formulation can be found in Molteni [31].

Although the atmospheric model proposed in the study is of intermediate resolution, previous studies showed its ability to reproduce the main features of the climate system both in tropical latitudes and extratropical regions [28, 31–34]. A detailed comparison between the simulated climate by SPEEDY and CCM3 and ERA40 models can be seen at <http://esp.ictp.it>.

The oceanic component of the SPEEDO is the *Coupled Large-Scale Ice-Ocean model* (CLIO) [35]. This model is based on the primitive equations (Navier-Stokes equations) and uses free surface with thermodynamic/dynamic parameterization for the sea ice component. CLIO also employs parameterizations for vertical diffusivity, which is a simplification of the Mellor and Yamada turbulence scheme [36]. The oceanic model includes parameterizations of vertical and horizontal mixing and turbulent diffusion processes along the isopycnals to represent the effect of mesoscale turbulent eddies in the ocean transport [37].

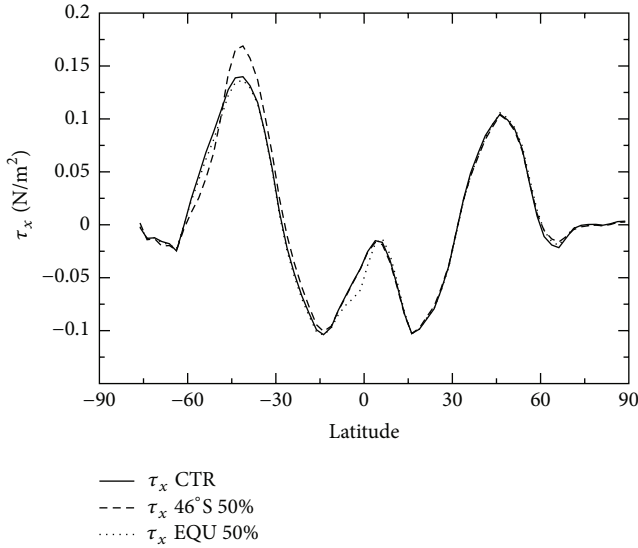


FIGURE 1: Annual wind stress zonally averaged τ_x (N/m^2) for the CTR, EQU 50%, and 46°S 50% simulations.

The CLIO horizontal resolution is approximately 3° of latitude and longitude, with 20 vertical levels unevenly spaced. The model has more levels concentrated close to the surface in order to better represent the oceanic processes that occur in the oceanic mixing layer.

The investigation made here is based on three climate sensitivity experiments: the control simulation (CTR), which was run for 200 years taking into account the current conditions of albedo, vegetation, and topography. The same boundary conditions were employed to another two simulations, however, intensifying the wind stress by 50%. The modified wind stress was applied over two regions, centered at the 1°S of latitude (EQU 50%) and 46°S of latitude (46°S 50%).

In order to investigate the influence of the wind stress to changes on the climate, the forcing function in the meridional direction is multiplied with the simulated zonal wind stress component. The function is defined as

$$\left[1 + a * e \left[\frac{2(\gamma r - \gamma)^2}{\alpha} \right] \right], \quad (1)$$

where “ a ” is the amplitude factor, “ γr ” is the latitude anomaly maximum, and “ α ” is the width of the anomalous wind stress forcing. The EQU 50% experiment is based on an increase by 50% of wind stress in the equatorial region; that is, the factor “ a ” was regarded as 0.5 and “ γr ” the value of 1°S latitude on CLIO model. The third simulation (46°S 50%) also considered the amplitude factor of 0.5, but with the wind stress changes applied to the latitude of 46°S. The reasoning behind the use of this function is to prevent border problems in simulations; that is, it acts as a damping factor, which has a maximum value at the latitude chosen, which will decrease as initial latitude.

Figure 1 shows a zonal average τ_x for the three simulations, which is taken from the average of τ_x values for all

longitude points, while the values vary for each latitude, taking the average of the past twenty years for each experiment (1980–1999). Note that by multiplying τ_x by β function, there is an increase in the wind stress, with major differences in 1°S (dotted line) and 46°S (dashed line), falling within a range of approximately 15° to the two simulations.

3. Results and Discussion

3.1. Oceanic Changes

3.1.1. Sea Surface Temperature and Antarctic Sea Ice. The annual mean climate simulated by SPEEDO has been discussed extensively by Severijns and Hazeleger [28] and Justino et al. [34]; thus no effort will be done to describe this in detail. The 50% increase in the wind stress in the equatorial region and 46°S generates distinct climate responses. Indeed, wind stress increasing in the equatorial region induces a cooling of the equatorial Pacific by up to 2°C (EQU 50%, Figure 2(a)). Decreasing of SST is also noted in the tropical Atlantic and Indian Oceans, with values of about 1°C. Similar results were obtained by Klinger et al. [38] and Liu and Philander [16], due to stronger upwelling in the region and associated strengthening of the oceanic vertical cells. Therefore, the intensification of wind stress in the equatorial region causes a pattern similar to the La Niña condition, being associated with the Ekman transport. The oceanic Ekman transport and pumping are among the most important parameters in studying the ocean general circulation and its variability. Upwelling due to the Ekman transport divergence has been identified as a leading mechanism for the seasonal to interannual variability of the upper-ocean heat content in many parts of the World Ocean, especially along coasts and the equator [39].

On the other hand, positive SST anomalies are found in the SH extratropical region by changing the wind stress at 46°S (46°S 50% experiment, Figure 2(b)) with values of up to 3°C; small values are found throughout the Global Ocean. Differently the Nordic Sea experiences a drop in SST values. The observed anomalies SST in 46°S 50% show a reverse pattern to that in EQU 50%; that is, they may be associated with a condition of Ekman pumping. The Ekman pumping is the primary mechanism that drives basin-scale circulations in subtropical and subpolar oceans [39]. Therefore, alterations in the transport Ekman in extratropical latitudes favor the changes in water masses and, consequently, they can cause changes on the THC associated with the weakening of the North Atlantic Deep Water (NADW). The changes in THC will be shown later.

However, changes in the wind stress in extratropical regions are not yet clear. According to Ma et al. [10], weaker wind stress over high latitudes of the SH leads to negative SST anomalies of 2°C in the Pacific between 40°S and 60°S, while a warming of up to 0.5°C is observed in the Atlantic. Delworth and Zeng [40] argued that SST anomalies due to an intensification of the wind stress in the Southern Ocean do not occur uniformly. They found positive anomalies of about 2°C between the Atlantic and the Indian Ocean, related to the displacement of warm water of subtropical origin. However,

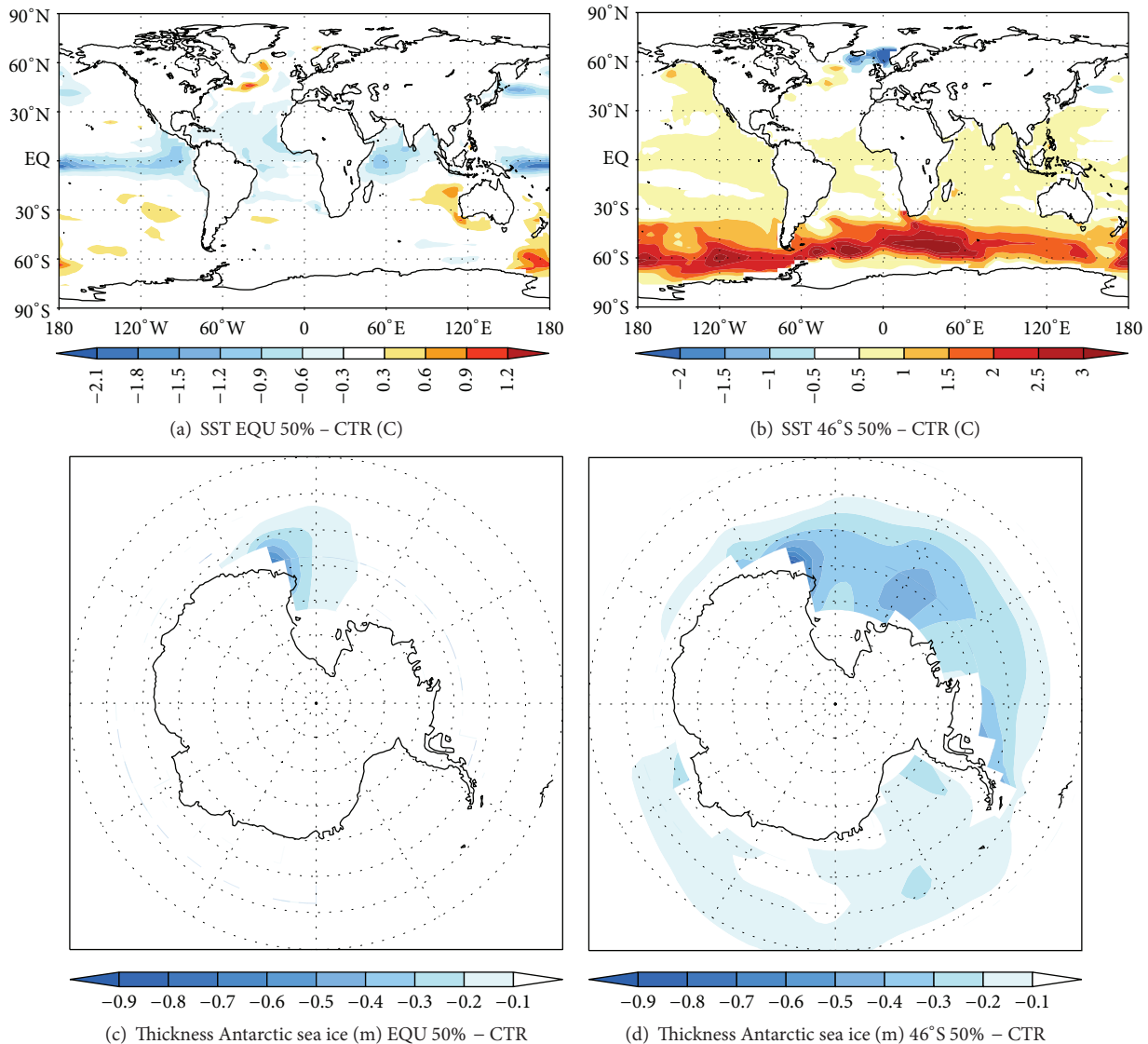


FIGURE 2: (a) SST anomalies ($^{\circ}\text{C}$) for EQU 50% - CTR, (b) SST anomalies ($^{\circ}\text{C}$) for 46°S 50% - CTR, (c) Thickness Antarctic sea ice anomaly (m) for EQU 50% - CTR, and (d) thickness Antarctic sea ice anomalies (m) for 46°S 50% - CTR.

influenced by increased upwelling negative anomalies are dominant in the western Pacific.

The simulations with the SPEEDO model show changes in SST patterns, favoring changes in the Antarctic sea ice thickness. Figures 2(c) and 2(d) show anomalies in the Antarctic sea ice thickness for both simulations (EQU 50% and 46°S 50%) as compared to CTR. The increased wind stress in the equatorial region causes little modifications on sea ice (Figure 2(c)). However, a reduction in thickness is observed from 50 to 60 cm for Ross Sea region. The link between the equatorial SST and the sea ice variability was previously noted by Yuan [41] and Kwok and Comiso [42].

The intensification of the wind stress in the region of 46°S (Figure 2(d)) shows an overall reduction in the sea ice thickness around Antarctica with substantial anomalies (values of up to 60–70 cm) occurring in the Ross, Bellingshausen, and

Amundsen Seas. In a twofold manner, the melting of sea ice allows higher SST values leading to further reduction of sea ice thickness. This dynamic feedback is associated with larger absorption of solar radiation and reinforces the initial heating [43].

3.1.2. Global Thermohaline Circulation. Changes on the oceanic characteristics in the extratropical and polar regions can affect the rate of deep water formation in both hemispheres [44, 45]. Figure 3 shows the average flow of the Atlantic Meridional Overturning Circulation (MOC) at 30°W longitude for the last 20 years of the CTR simulation by EQU 50% and 46°S 50% experiments. It is demonstrated that in the CTR experiment (Figure 3(a)) there is a southward transport of water with values between 8 and 12 Sv, associated with the NADW between 30°N and 50°N in a depth ranging

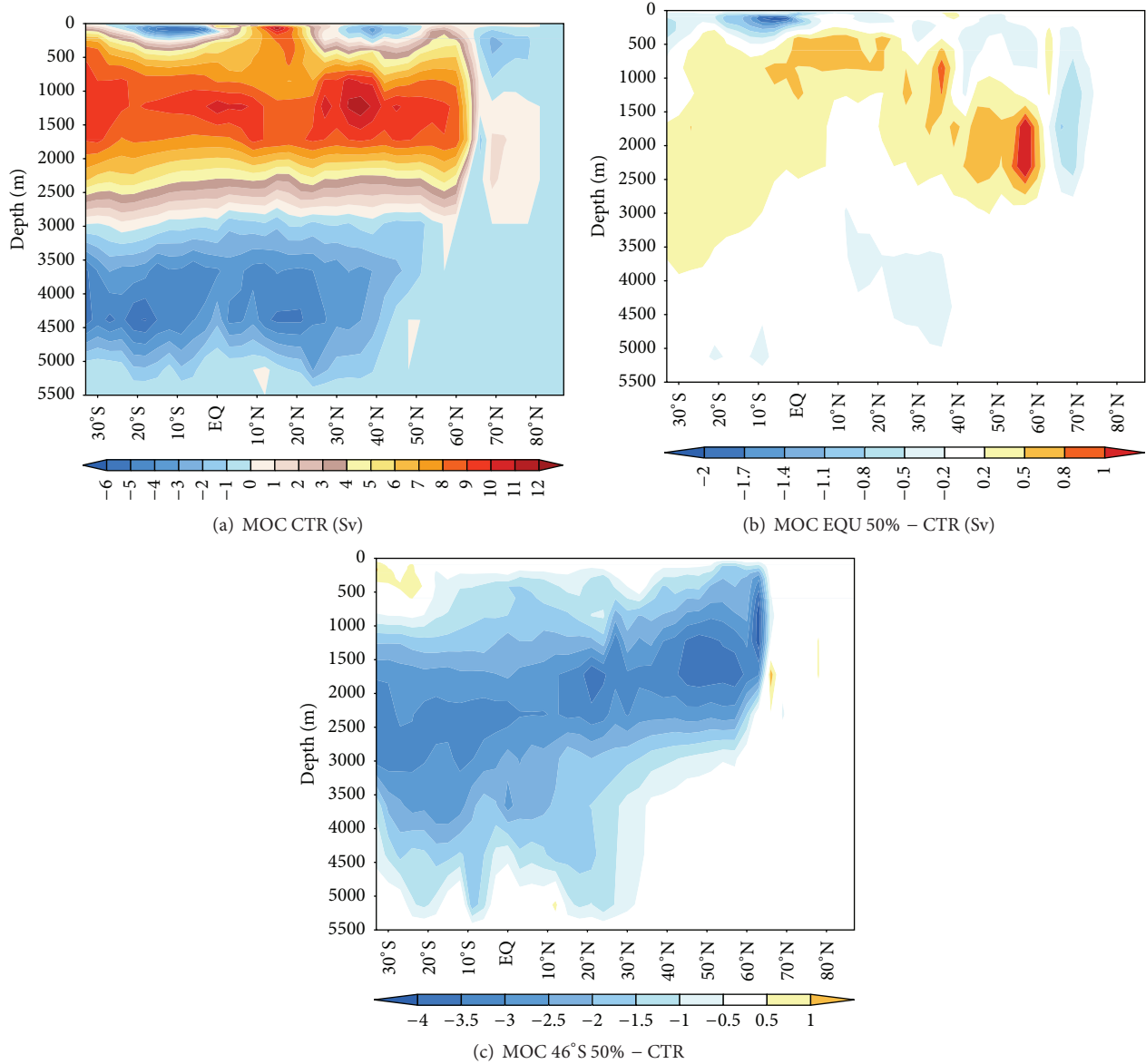


FIGURE 3: Annual thermohaline global circulation average for Atlantic Ocean (Sv). (a) CTR simulation, (b) difference of experiments for EQU 50% - CTR, and (c) difference of experiments for 46°S 50% - CTR.

from 500 to 2000 meters. The underneath northward flow is related to the formation of the Antarctic Bottom Water (AABW) with values reaching -6 Sv.

It is important to remark that SPEEDO underestimates the NADW, when compared to results found by Talley et al. [46] using observations and Gent [47] based on the NCAR model results. Both show NADW maxima by about 20 Sv. Cunningham et al. [48] found 18.7 Sv from observations. However, SPEEDO maximum stream function in the North Atlantic can reach values up to 16 Sv. The global (Atlantic + Pacific + Indian) AABW strength of 12 Sv is in close agreement with observation and other modeling results [49].

The THC anomalies between CTR and EQU 50% experiment (Figure 3(b)) demonstrate that the intensification of

winds stress in the equatorial region leads to slight intensification of the NADW (1 Sv) between 40°N and 60°N . However, no changes are observed with respect to AABW. Timmermann and Goose [6] highlight that this intensification on trade winds strengthens the subtropical gyres in the Atlantic and consequently increases the transport of saline waters to extratropical latitudes. However, in EQU 50% simulation, an increase of the 1 Sv in NADW does not cause significant changes in THC.

By intensifying the wind in the region of 46°S , changes in THC are observed. In this new climate scenario, there is a weakening of NADW by about 4 Sv distributed throughout the Atlantic from 500 meters to 2000 meters of depth (Figure 3(c)), which is accompanied by a strengthening in

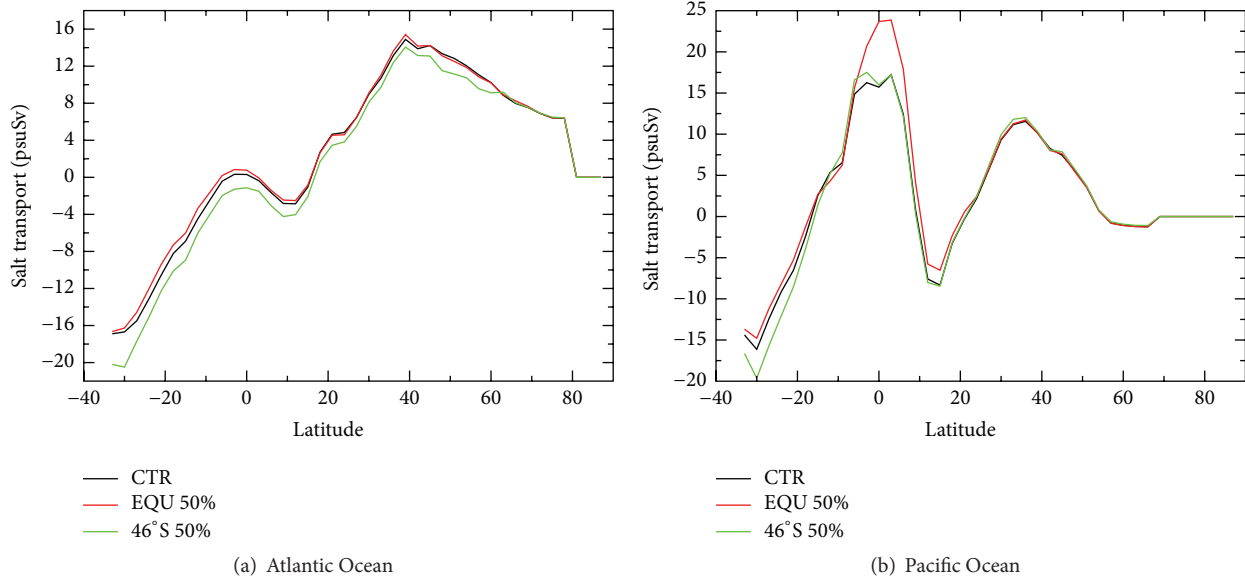


FIGURE 4: Annual salt transport zonally averaged (Sv). (a) Atlantic Ocean and (b) Pacific Ocean. Black line: CTR simulation; red line: EQU 50% simulation; and green line: 46°S 50% simulation.

the AABW in the 46°S 50% experiment. As will be discussed later, changes in the NADW further lead to changes in the oceanic heat transport which plays a substantial role in driving SST and sea ice. Through the magnitude anomalies of ocean current between 46°S 50% and CTR experiments (not shown), there is an occurrence of negative anomalies in the North Atlantic, which shows the weakening of the Gulf Stream in this situation. This condition contributes to lower transport salt and heat and as a result weakens the APAN. This explains the negative SST anomalies in the North Atlantic (Figure 2(b)). This is in agreement with results proposed by Menviel et al. [8], which found an increase in the transport of AABW associated with more vigorous winds near the surface and an increase of SST in the same region. Numerical simulations suggest that a change in Agulhas leakage, due to changes of the winds in extratropical regions of the Southern Hemisphere, can impact the thermohaline properties of the Atlantic Ocean and hence stratification and deep convection formation, which are directly linked to MOC [50]. Justino et al. [34] by analysing the climate response to reduced Antarctic ice sheet height argued that reducing the sea ice thickness and allowing for enhanced heat loss from the ocean surface to the atmosphere increase the water density underneath the mixing layer favoring convection. The second effect that can lead to a strengthening of the AABW formation rate is associated with the heat-salt distribution of subsurface water.

However, different results are found by Delworth and Zeng [40] that report an intensification of THC in deeper layers, by considering stronger and southward wind stress in the Southern Ocean. Hirabara et al. [51] also highlighted that an intensification of the wind stress in the Southern Ocean promotes an intensification of NADW as a response to the baroclinic wave propagation to the North Atlantic.

3.1.3. Salt Transport. Despite the importance of salinity to deep water formation, the influence of wind stress changes on the salt transport in both equatorial and extratropical belts has been partially overlooked. In the following the salt transport changes in the Atlantic and Pacific oceans due to modification in the wind stress are discussed. Figures 4(a) and 4(b) show the zonal average salt transport in the Atlantic and Pacific oceans for CTR, EQU 50%, and 46°S 50% experiments.

The salt transport analyses in Atlantic Ocean show that the simulations forced with increased wind stress do not differ substantially from the CTR outside the region of the applied forcing. The maximum values occur in the region of 40° latitude in both hemispheres, linked to the contribution of the Gulf Stream in transporting saline waters into the North Atlantic and in the SH associated with the Brazil current in the South Atlantic.

It should be noted that the transport of salt is intensified (reduced) in the South (North) Atlantic in the 46°S 50% experiment. Figure 4(a) shows an intensification of 4 Sv at 35°S. The opposite occurs in the North Atlantic, where the salt transport decreases between 40°N and 60°N. This anomalous pattern contributes to an increase in the salinity in the South Atlantic but favors a reduction in the North Atlantic, insofar the salt contribution is concerned. This salt transport feature is in agreement with the response of the THC to wind stress changes previously discussed.

Figure 4(b) shows the zonal averaged salt transport in the Pacific Ocean. In the EQU 50% simulation, it is clear that the increase of the wind stress in the equatorial region generates an additional northward salt transport by up to 10 Sv, as compared to the CTR simulation. This remarkable change occurs in the equatorial belt, whereas changes in

the northern hemisphere are smaller. The intensification of the wind stress in 46°S 50% experiment indicates that changes in the Pacific Ocean salt transport are more intense in the SH, where there is an increase in the transport of about 5 Sv between 30°S and 40°S. This anomalous pattern of the salt transport is in agreement with increase in salinity in the vicinity of the Antarctic ocean (not shown).

3.2. Atmospheric Changes

3.2.1. Baroclinic Instability. Large-scale temperature and atmospheric circulation changes have potential to modify the statistics of transient and steady waves. This is predominantly generated by baroclinic instabilities from the background flow, which has been attributed to enhanced meridional/zonal thermal contrast [52]. It is worth mentioning that the baroclinic and barotropic instability mechanisms are responsible for the formation and maintenance of waves and eddies that act regulating the heat and momentum balance in oceanic frontal regions. One good example is the tropical instability waves that occur in the equatorial regions of the Pacific [53] and the Atlantic [54].

The Eady growth rate (σ_{b1}) is computed in the mid-troposphere at 500 hPa level, in order to investigate changes to atmospheric baroclinicity induced by the wind stress anomalies. This is a simplified measure of atmospheric baroclinicity that can be employed to quantify the potential for instabilities and cyclone growth [52, 55]. The Eady growth rate estimates baroclinic instability from the vertical wind shear and the static stability of the atmosphere. It is defined as

$$\sigma_{b1} = 0.31 \frac{f}{N} \left(\frac{\partial V}{\partial Z} \right), \quad (2)$$

where f is the Coriolis parameter, N the Brunt-Väisälä frequency, Z the upward vertical coordinate, and V the horizontal wind speed.

Figures 5(a) and 5(b) show the averaged σ_{b1} for the CTR simulation, for December-January-February (DJF) and June-July-August (JJA), respectively. Negative values for the SH and positive values for the Northern Hemisphere are related with the Coriolis parameter. The σ_{b1} is more intense on each hemisphere during the winter period due to higher thermal contrasts over the mid-latitudes and consequently associated with stronger wind shear [56]. The maximum values are observed between Asia and North Pacific and over the SH mid-latitudes and Antarctica (Figures 5(a) and 5(b)).

Figures 5(c) and 5(d) show the baroclinic activity anomalies as a result of the wind stress intensification over the equatorial region during DJF and JJA. Note that during DJF (Figure 5(c)), there are no significant anomalies in the Southern Hemisphere. This result is reasonable since no remarkable changes are simulated in the atmospheric circulation. On the other hand, stronger baroclinic activity is predicted to occur in the NH mid-latitudes and extratropical regions. These anomalies of σ_{b1} in the Northern Hemisphere follow changes in the vertical wind profile (not shown). During JJA, small changes in σ_{b1} occur on both hemispheres (Figure 5(d)).

By changing wind stress in the Southern Ocean (Figures 5(e) and 5(f)), a reduction σ_{b1} (positive anomalies) is

demonstrated, mainly between 45°S and 60°S. Differences of σ_{b1} between the 46°S 50% and CTR experiment during JJA are shown in Figure 5(f); we obtain a reduction of the baroclinic activity in the SH around 60°S. One can argue that the reduction of the thermal gradient between the tropics and the extratropical region and the consequent weakening of the westerlies can promote the reduction of the baroclinic activity in this climate scenario.

3.2.2. Storminess. Changes in the atmosphere baroclinic structure are closely linked to transient eddy anomalies, more commonly known as storm. Storm track is often defined by the regions where there is a maximum variance of geopotential height in the upper and mid-troposphere, arising from disturbances with periods less than one week approximately [52, 57]. According to Wu et al. [58], the storms act as regulators of the precipitation. These transient eddies are also responsible for large part of the poleward heat transport reducing the meridional thermal gradient between the tropics and the polar regions [59]. Therefore, changes in the position and magnitude of the storms can influence heat, moisture, and momentum transports in the atmosphere [60].

In this study, storms are estimated in terms of the eddy heat flux ($\overline{v'T'}$) at 700 hPa and eddy momentum flux ($\overline{u'v'}$) at 200 hPa, both for DJF and JJA periods. It is important to highlight that $\overline{v'T'}$ represents the exchange between basic state potential energy and potential energy available for the disturbances. The $\overline{u'v'}$ characterizes the exchange between kinetic energy of the disturbances and kinetic energy of the basic state [61].

The activity of the eddy heat flux ($\overline{v'T'}$) at 700 hPa is shown in Figure 6 as well as its anomalies between the wind stress experiments and the CTR simulation for DJF and JJA. It should be noted that the ($\overline{v'T'}$) is intensified over mid-latitudes and high latitudes during the winter season in each hemisphere (Figures 6(a) and 6(b)), with maximum values ranging from -25 to 35 Km s^{-1} . According to Trenberth [56], the intensified jet in winter favors the eastward advection of the transient waves. The SPEEDO model underestimates the magnitude of the storms when compared to finer resolution models. The continuous pattern of the storms in the Southern Ocean when compared with the Northern Hemisphere is remarkable.

Figures 6(c) and 6(d) show $\overline{v'T'}$ anomalies during DJF and JJA between the EQU 50% and the CTR experiments. Stronger storm activity is noted over the northern part of Eurasia and Nordic Seas but reduced activity over the northern Pacific in DJF (Figure 6(c)). No changes are predicted to occur during JJA. Seager et al. [62] argued that changes in the tropical Pacific due to ENSO events generate anomalous pattern of storm tracks. Indeed, the EQU 50% experiment resembles a permanent La Niña-like event and therefore may alter the wave propagation paths.

Eddy heat flux ($\overline{v'T'}$) anomalies between the 46°S 50% experiment and the CTR simulation during the summer and winter in both hemispheres are shown in Figures 6(e) and 6(f). During DJF (Figure 6(e)) there are no significant

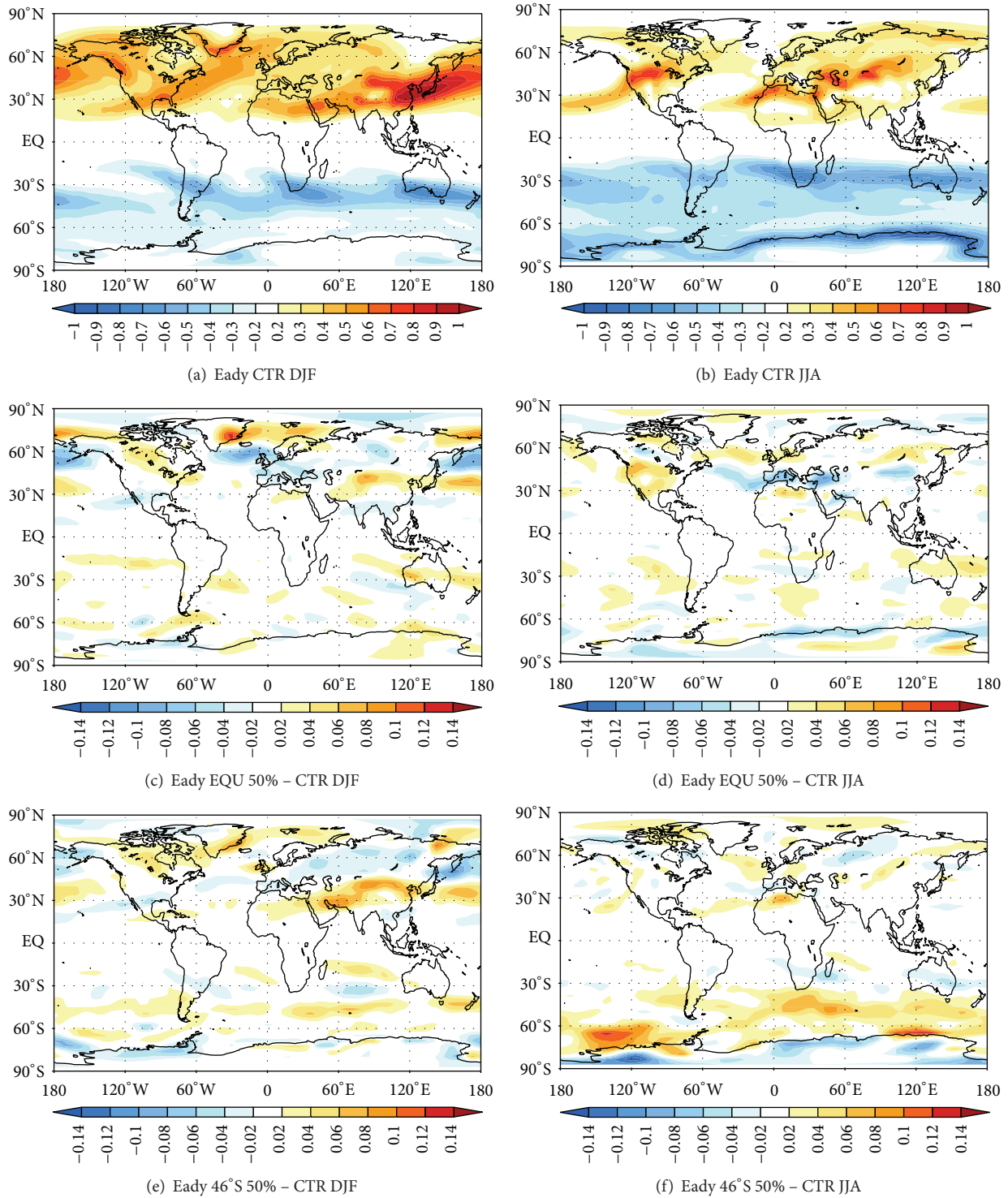


FIGURE 5: Baroclinic instability (σ_{b1}): (a) CTR simulation in DJF, (b) CTR simulation in JJA, (c) EQU 50% - CTR in DJF, (d) EQU 50% - CTR in JJA, (e) 46°S 50% - CTR in DJF, and (f) 46°S 50% - CTR in JJA. Units are in day^{-1} .

anomalies. However, a weakening of the eddy momentum flux is observed in the North Pacific and Atlantic Ocean. Changes on the pattern of storms during SH winter (Figure 6(f)) depict positive values (weaker $\overline{v'T'}$) throughout the Southern Ocean, primarily due to the overall warming

over extratropical latitudes as predicted to occur under stronger wind stress forcing.

The second storm quantity evaluated is the upper troposphere eddy momentum flux ($\overline{u'v'}$) at 200 hPa (Figure 7). $u'v'$ is directly associated with the westerly flow on both

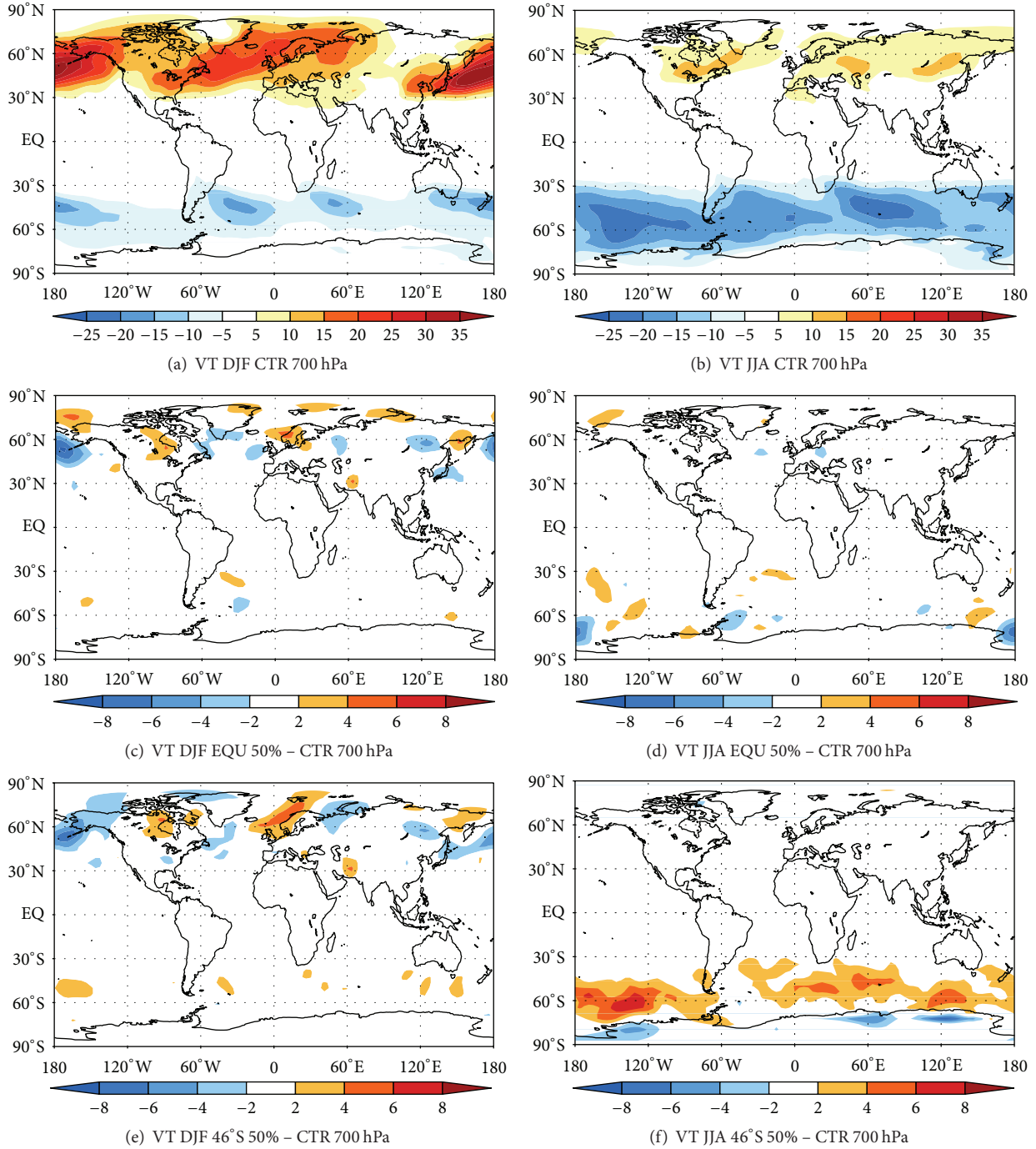


FIGURE 6: Eddy heat flux ($\overline{v'T'}$). (a) CTR simulation in DJF, (b) CTR simulation in JJA, (c) EQU 50% - CTR in DJF, (d) EQU 50% - CTR in JJA, (e) 46°S 50% - CTR in DJF, and (f) 46°S 50% - CTR in JJA. Units are in km s^{-1} .

hemispheres and is more intense during DJF (JJA) in the Northern (Southern) Hemisphere (Figures 7(a) and 7(b)). In the Southern Hemisphere $\overline{u'v'}$ is predominantly confined between 30° and 45°S in both seasons. In the NH $\overline{u'v'}$ spatial distribution and magnitude exhibit stronger seasonal cycle as compared to the SH.

Figures 7(c) and 7(d) show anomalies of $\overline{u'v'}$ between CTR and EQU 50% experiments for DJF and JJA. As shown for $\overline{v'T'}$, the intensification of wind stress in the equatorial region does not contribute significantly to changes in the storm tracks pattern but enhanced activity is noted over Hudson Bay and Japan Sea/Eastern Asia in DJF (Figure 7(c)).

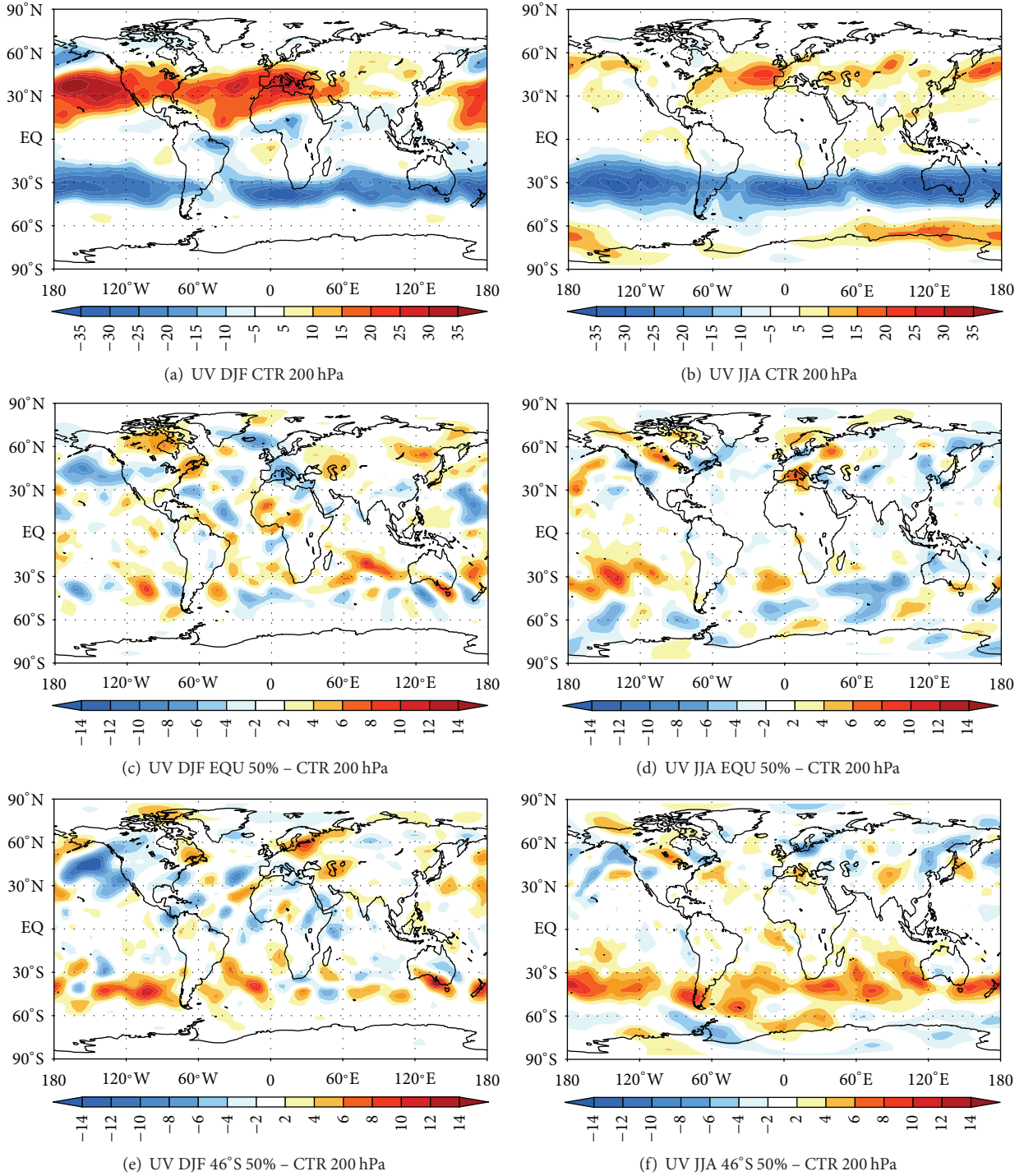


FIGURE 7: Eddy momentum flux ($\overline{u'v'}$). (a) CTR simulation in DJF, (b) CTR simulation in JJA, (c) EQU 50% - CTR in DJF, (d) EQU 50% - CTR in JJA, (e) 46°S 50% - CTR in DJF, and (f) 46°S 50% - CTR in JJA. Units are in $\text{m}^2 \text{s}^{-2}$.

During JJA in the Southern Hemisphere (Figure 7(d)), positive values are observed at Pacific Ocean in the region of 30°S. This indicates a storm weakening for EQU 50% simulation as compared to the unperturbed CTR conditions.

For 46°S 50% simulation (Figures 7(e) and 7(f)), the largest differences occur over Southern Hemisphere mid-latitudes during JJA (Figure 7(f)), $\overline{u'v'}$ is weakened by $12 \text{ m}^2/\text{s}^2$ between 30°S and 45°S. It is important to point out that the wind stress intensification in mid-latitudes also leads

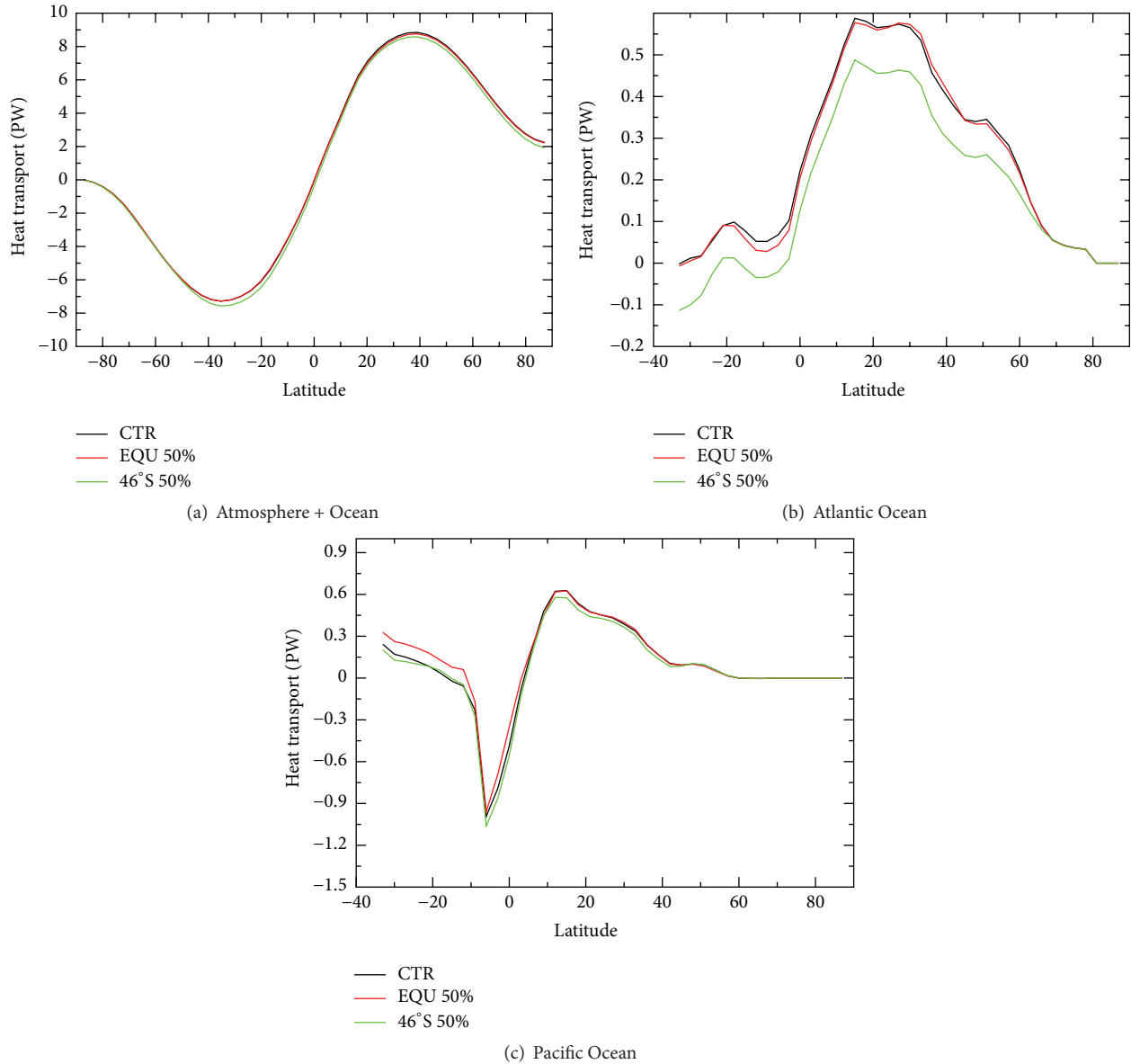


FIGURE 8: Heat transport zonally averaged (PW). (a) Total heat transport, (b) heat transport in Atlantic Ocean, and (c) heat transport in Pacific Ocean. Black line: CTR simulation, red line: EQU 50% simulation, and green line: 46°S 50% simulation.

to weaker baroclinic instability and $\overline{v'T'}$ at 700 hPa. This was not anticipated because enhanced zonal wind stress at mid-latitudes should be associated with stronger meridional thermal gradient and atmospheric baroclinicity.

Recently, Justino et al. [34] performed numerical simulations with SPEEDO coupled model using a modified Antarctic topography. Their results indicate that modifications of the Antarctic ice sheet height induce a weakening of the meridional thermal gradient and $\overline{v'T'}$ and $\overline{u'v'}$.

3.2.3. Total Poleward Heat Transport. As discussed earlier, the intensification of wind stress in the equatorial region and the Southern Ocean favors the occurrence of anomalies in atmospheric and oceanic circulations. These changes may be associated with anomalies in the atmospheric and oceanic

poleward heat transport. The total poleward heat transport of the ocean-atmosphere system in each latitudinal band is computed from the difference between net shortwave radiation and outgoing long-wave radiative flux at the top of the atmosphere [63–65]. It can be expressed as

$$\begin{aligned}
 H(\phi)_{\text{total}} &= H_{\text{ATM}} + H_{\text{OCE}} \\
 &= 2a^2\pi \int (S_{\text{TOA}}(\phi)' - L_{\text{TOA}}(\phi)') \cdot \cos\phi' \cdot d\phi', \quad (3)
 \end{aligned}$$

where H_{total} , H_{ATM} , and H_{OCE} are the total, atmospheric, and oceanic heat transports, a is the radius of the Earth, ϕ is the latitude, S_{TOA} is the zonal averaged net shortwave radiation, and L_{TOA} is the zonal averaged outgoing long-wave radiation. Both fluxes are computed at the top of the atmosphere.

TABLE 1: Heat transport at 30°S for the numerical experiments. Units are PW.

Experiments	Total heat transport	Global ocean	Atlantic	Indi./Pac.	Atmosphere
CTR	-7.21	-0.86	0.01	-1.04/0.17	-6.35
EQU 50%	-7.21	-0.92	0.01	-1.19/0.26	-6.29
46°S 50%	-7.52	-1.12	-0.10	-1.14/0.12	-6.40

TABLE 2: Heat transport in 30°N for the numerical experiments. Units are PW.

Experiments	Total heat transport	Global Ocean	Atlantic	Pac.	Atmosphere
CTR	8.63	0.96	0.57	0.39	7.67
EQU 50%	8.53	0.97	0.57	0.40	7.56
46°S 50%	8.38	0.82	0.46	0.36	7.56

Figure 8 shows zonal averaged total heat transport (Ocean + Atmosphere) and the oceanic contribution for the Atlantic and Pacific regions for the CTR, EQU 50%, and 46°S 50% simulations. The sum of the heat transport from the ocean and the atmosphere (Figure 8(a)) shows a similar pattern between the CTR and the simulations forced with the intensification of wind stress. The maximum values of total heat transport occur between the latitudes of 30° and 40° at both hemispheres. Negative (positive) values indicate heat transport towards the South (North) Pole. The SPEEDO model simulates the total heat transport with values close to those seen in Trenberth and Caron [65] and Wu et al. [58]; however, the model overestimates this transport up to 1PW at 30° latitude in both hemispheres. It should be noted that the values proposed in the literature are based on reanalysis and uncertainties are still present.

By analyzing the total heat transport between CTR and EQU 50% experiments small differences are observed (Table 1). In the Northern Hemisphere, the total heat transport is weakened in the EQU 50% simulation in 0.1PW in 30°N (Table 2). However, the total heat transport is substantially modified when the wind stress is intensified in the Southern Ocean. This situation is evident in Figure 8(a), where there is a heat transport intensification in the Southern Hemisphere and a weakening in the Northern Hemisphere. By analyzing Tables 1 and 2, it should be noted that the total heat transport increases by up to 0.31PW at 30°S, while in the Northern Hemisphere a weakening of 0.25PW occurs. This southward heat transport increase in the Southern Hemisphere can favor an increase of SST and air temperature over the extratropical region. Thus, the ocean transport of heat changes direction, favoring the formation process of the interhemispheric seesaw. According to Broecker [66], a reduction in deep water formation rates of the South Atlantic or the North Atlantic should occur, so that this phenomenon occurs. Machado et al. [45] also show this process due to a weakening in the MOC. Although the ocean heat transport contributes only 10% of the total, the results show that a small enhancement associated with a change of direction contributes significantly to changes in atmospheric and ocean circulations in this climate scenario.

When considering only the contribution of heat transport of the Atlantic and Pacific oceanic regions (Figures 8(b)

and 8(c)), it is clear that the maximum values occur in the equatorial region. From Tables 1 and 2 one may note that the oceanic heat transport contributes to about 15% of the total transport. The impact of the intensification of the wind stress in the oceanic heat transport is remarkable on 46°S 50% experiment. Specifically, changes on heat transport occur significantly in the Atlantic Ocean (Figure 8(b)). The oceanic heat transport is intensified in the South Atlantic and the opposite occurs in the North Atlantic. It should be noted that this is in close agreement with the changes in the THC. It is well known that the THC contributes significantly with the transport of heat from the Southern to the Northern Hemisphere as well as from the Atlantic to Indian-Pacific basins [67, 68].

4. Conclusions and Final Remarks

Based on simulations conducted by the climate model SPEEDO, the atmospheric and oceanic response to wind stress anomalies applied in the equatorial (EQU 50%) and extratropical region (46°S 50%) was evaluated. It has been demonstrated that the forcing applied on the equatorial and the Southern Ocean regions leads to different responses of the climate system. When the wind stress is enhanced over the equatorial region (EQU 50% experiment) an intensification of the Ekman transport and consequent acceleration of the oceanic subtropical cells was verified leading to an equatorial cooling due to the increased upwelling and evaporation.

By increasing the wind stress over the Southern Ocean (46°S 50%), there is a local warming of the sea surface up to 3°C and a reduction in the Antarctic sea ice thickness. On the other hand the North Atlantic is cooled down. This anomalous negative SST pattern is associated with the North Atlantic Deep Water formation rate decreasing and an increasing in the Antarctic Bottom Water. Thus, the total heat transport (Ocean + Atmosphere) is affected and it is most related by changes in the oceanic heat transport, in the Atlantic Ocean.

This increased wind stress in the Southern Ocean induces the positive temperature anomalies found around the Antarctic region. This fact is an evident consequence from the intensification of heat fluxes exchanges between the ocean and the atmosphere. The warming in the Southern Hemisphere

favors the slowdown of the jet stream due to the meridional weakening of the thermal gradient. As a result, the baroclinic instability and storm are reduced.

It is noteworthy that, with the simulations, it can be concluded that upwelling is the mechanism responsible for changes in oceanic and atmospheric circulations when the wind stress is intensified in the equatorial region. However, changes in ocean patterns for extratropical regions, due to the wind stress intensification, need further investigation, since the answer is not yet clear when you compare our results with other works. Thus, it is important to conduct similar modeling experiments based on climate models with higher degree of complexity, involving more vertical atmospheric layers and recent developments in cloud parameterization.

Conflict of Interests

The authors declare that there is no conflict of interests regarding the publication of this paper.

Acknowledgment

This research has been supported by the CNPq Project Proposals 407681/2013-2 and 305586/2012-2.

References

- [1] G. T. Walker and E. W. Bliss, "World Weather V," *Memoirs of the Royal Meteorological Society*, vol. 4, no. 36, pp. 53–84, 1932.
- [2] J. Bjerknes, "Atlantic air-sea interaction," *Advances in Geophysics*, vol. 10, pp. 1–82, 1964.
- [3] K. Wyrski, "Teleconnections in the equatorial Pacific Ocean," *Science*, vol. 180, no. 4081, pp. 66–68, 1973.
- [4] F. Justino, *The influence of glacial boundary conditions on the climate system during the last glacial maximum [Ph.D. thesis]*, Leibniz Institute of Marine Sciences, Kiel, Germany, 2004.
- [5] L. P. Pezzi, J. Vialard, K. J. Richards, C. Menkes, and D. Anderson, "Influence of ocean-atmosphere coupling on the properties of Tropical Instability Waves," *Geophysical Research Letters*, vol. 31, no. 16, Article ID L16306, 2004.
- [6] A. Timmermann and H. Goosse, "Is the wind stress forcing essential for the meridional overturning circulation?" *Geophysical Research Letters*, vol. 31, no. 4, Article ID L04303, 2004.
- [7] X.-Y. Yang, R. X. Huang, and D. X. Wang, "Decadal changes of wind stress over the Southern Ocean associated with Antarctic ozone depletion," *Journal of Climate*, vol. 20, no. 14, pp. 3395–3410, 2007.
- [8] L. Menviel, A. Timmermann, A. Mouchet, and O. Timm, "Climate and marine carbon cycle response to changes in the strength of the Southern Hemispheric westerlies," *Paleoceanography*, vol. 23, no. 4, Article ID PA4201, 2008.
- [9] O. A. Saenko, "On the climatic impact of wind stress," *Journal of Physical Oceanography*, vol. 39, no. 1, pp. 89–106, 2009.
- [10] H. Ma, L. X. Wu, and C. Li, "The role of southern high latitude wind stress in global climate," *Advances in Atmospheric Sciences*, vol. 27, no. 2, pp. 371–381, 2010.
- [11] N. P. Gillett and D. W. J. Thompson, "Simulation of recent Southern Hemisphere climate change," *Science*, vol. 302, no. 5643, pp. 273–275, 2003.
- [12] J. C. Fyfe and O. A. Saenko, "Simulated changes in the extratropical Southern Hemisphere winds and currents," *Geophysical Research Letters*, vol. 33, no. 6, Article ID L06701, 2006.
- [13] J. C. Fyfe, O. A. Saenko, K. Zickfeld, M. Eby, and A. J. Weaver, "The role of poleward-intensifying winds on Southern Ocean warming," *Journal of Climate*, vol. 20, no. 21, pp. 5391–5400, 2007.
- [14] N. C. Swart and J. C. Fyfe, "Observed and simulated changes in the Southern Hemisphere surface westerly wind-stress," *Geophysical Research Letters*, vol. 39, no. 16, Article ID L16711, 2012.
- [15] J. McCreary and P. Lu, "Interaction between the subtropical and the equatorial ocean circulations: the subtropical cell," *Journal of Physical Oceanography*, vol. 24, pp. 466–497, 1994.
- [16] Z. Liu and S. Philander, "How different wind stress pattern affect the tropical-subtropical circulations of the upper ocean," *Journal of Physical Oceanography*, vol. 25, pp. 449–462, 1995.
- [17] A. B. G. Bush and S. G. H. Philander, "The climate of the Last Glacial Maximum: results from a coupled atmosphere-ocean general circulation model," *Journal of Geophysical Research: Atmospheres*, vol. 104, no. 20, Article ID 1999JD900447, pp. 24509–24525, 1999.
- [18] S.-I. An, A. Timmermann, L. Bejarano et al., "ENSO dynamics during the Last Glacial Maximum," *Paleoceanography*, vol. 19, pp. 1–11, 2004.
- [19] A. Timmermann, F. Justino, F.-F. Jin, U. Krebs, and H. Goosse, "Surface temperature control in the North and tropical Pacific during the last glacial maximum," *Climate Dynamics*, vol. 23, no. 3–4, pp. 353–370, 2004.
- [20] M. H. England, S. McGregor, P. Spence et al., "Recent intensification of wind-driven circulation in the Pacific and the ongoing warming hiatus. The world ocean thermohaline circulation," *Nature Climate Change*, vol. 4, pp. 222–227, 2014.
- [21] D. G. MacMynowski and E. Tziperman, "Two-way feedback interaction between the thermohaline and wind-driven circulations," *Journal of Physical Oceanography*, vol. 36, no. 5, pp. 914–929, 2006.
- [22] J. R. Toggweiler, "Shifting westerlies," *Science*, vol. 323, no. 5920, pp. 1434–1435, 2009.
- [23] J. R. Toggweiler and J. Russell, "Ocean circulation in a warming climate," *Nature*, vol. 451, no. 7176, pp. 286–288, 2008.
- [24] R. F. Anderson, S. Ali, L. I. Bradtmiller et al., "Wind-driven upwelling in the southern ocean and the deglacial rise in atmospheric CO₂," *Science*, vol. 323, no. 5920, pp. 1443–1448, 2009.
- [25] J. Marshall and K. Speer, "Closure of the meridional overturning circulation through Southern Ocean upwelling," *Nature Geoscience*, vol. 5, no. 3, pp. 171–180, 2012.
- [26] T. A. Shaw and O. Pauluis, "Tropical and subtropical meridional latent heat transports by disturbances to the zonal mean and their role in the general circulation," *Journal of the Atmospheric Sciences*, vol. 69, no. 6, pp. 1872–1889, 2012.
- [27] J. P. Machado, F. Justino, and L. P. Pezzi, "Efeitos do aumento da tensão de cisalhamento do vento no clima do Hemisfério Sul obtido do modelo acoplado SPEEDO," *Revista Brasileira de Meteorologia*, vol. 29, no. 4, pp. 597–612, 2014.
- [28] C. A. Severijns and W. Hazeleger, "The efficient global primitive equation climate model SPEEDO V2.0," *Geoscientific Model Development*, vol. 3, no. 1, pp. 105–122, 2010.
- [29] W. Bourke, "A multilevel spectral model. I. Formulation and hemispheric integrations," *Monthly Weather Review*, vol. 102, no. 10, pp. 687–701, 1974.

- [30] I. Held and M. Suarez, "A two-level primitive equation atmosphere model designed for climate sensitivity experiments," *Journal of the Atmospheric Sciences*, vol. 35, pp. 206–229, 1978.
- [31] F. Molteni, "Atmospheric simulations using a GCM with simplified physical parametrizations. I: model climatology and variability in multi-decadal experiments," *Climate Dynamics*, vol. 20, no. 2–3, pp. 175–191, 2003.
- [32] F. Kucharski, F. Molteni, and A. Bracco, "Decadal interactions between the western tropical Pacific and the North Atlantic Oscillation," *Climate Dynamics*, vol. 26, no. 1, pp. 79–91, 2006.
- [33] A. Bracco, F. Kucharski, R. Kallummal, and F. Molteni, "Internal variability, external forcing and climate trends in multi-decadal AGCM ensembles," *Climate Dynamics*, vol. 23, no. 6, pp. 659–678, 2004.
- [34] F. Justino, J. Marengo, F. Kucharski, F. Stordal, J. Machado, and M. Rodrigues, "Influence of Antarctic ice sheet lowering on the Southern Hemisphere climate: modeling experiments mimicking the mid-Miocene," *Climate Dynamics*, vol. 42, no. 3–4, pp. 843–858, 2014.
- [35] H. Goosse and T. Fichefet, "Importance of ice-ocean interactions for the global ocean circulation: a model study," *Journal of Geophysical Research*, vol. 104, no. 10, Article ID 1999JC90215, pp. 23337–23355, 1999.
- [36] G. L. Mellor and T. Yamada, "Development of a turbulence closure model for geophysical fluid problems," *Reviews of Geophysics and Space Physics*, vol. 20, no. 4, pp. 851–875, 1982.
- [37] P. Gent and J. McWilliams, "Isopycnal mixing in ocean general circulation model," *Journal of Physical Oceanography*, vol. 20, pp. 150–155, 1990.
- [38] L. F. Klinger, Q. J. Li, A. B. Guenther, J. P. Greenberg, B. Baker, and J. H. Bai, "Assessment of volatile organic compound emissions from ecosystems of China," *Journal of Geophysical Research: Atmospheres D*, vol. 107, no. 21, pp. ACH 16–1–ACH 16–21, 2002.
- [39] J. Yang, "The seasonal variability of the Arctic Ocean Ekman transport and its role in the mixed layer heat and salt fluxes," *Journal of Climate*, vol. 19, no. 20, pp. 5366–5387, 2006.
- [40] T. L. Delworth and F. R. Zeng, "Simulated impact of altered Southern Hemisphere winds on the Atlantic Meridional Overturning Circulation," *Geophysical Research Letters*, vol. 35, no. 20, Article ID L20708, 2008.
- [41] X. Yuan, "ENSO-related impacts on Antarctic sea ice: a synthesis of phenomenon and mechanisms," *Antarctic Science*, vol. 16, no. 4, pp. 415–425, 2004.
- [42] R. Kwok and J. C. Comiso, "Southern Ocean climate and sea ice anomalies associated with the Southern Oscillation," *Journal of Climate*, vol. 15, no. 5, pp. 487–501, 2002.
- [43] F. Justino, F. Hastenreiter, and A. Grimm, "Impacto do dióxido de carbono atmosférico no gelo marinho Antártico," *Oecologia Brasiliensis*, vol. 11, no. 1, pp. 69–77, 2007.
- [44] R. J. Stouffer, J. Yin, J. M. Gregory et al., "Investigating the causes of the response of the thermohaline circulation to past and future climate changes," *Journal of Climate*, vol. 19, no. 8, pp. 1365–1387, 2006.
- [45] J. P. Machado, F. Justino, and L. P. Pezzi, "Changes in the global heat transport and eddy-mean flow interaction associated with weaker thermohaline circulation," *International Journal of Climatology*, vol. 32, no. 15, pp. 2255–2270, 2012.
- [46] L. D. Talley, J. L. Reid, and P. E. Robbins, "Data-based meridional overturning streamfunctions for the global ocean," *Journal of Climate*, vol. 16, no. 19, pp. 3213–3226, 2003.
- [47] P. R. Gent, "Will the North Atlantic Ocean thermohaline circulation weaken during the 21st century?" *Geophysical Research Letters*, vol. 28, no. 6, pp. 1023–1026, 2001.
- [48] S. A. Cunningham, T. Kanzow, D. Rayner et al., "Temporal variability of the Atlantic meridional overturning circulation at 26.5°N," *Science*, vol. 317, no. 5840, pp. 935–938, 2007.
- [49] A. H. Orsi, G. C. Johnson, and J. L. Bullister, "Circulation, mixing, and production of antarctic bottom water," *Progress in Oceanography*, vol. 43, no. 1, pp. 55–109, 1999.
- [50] R. J. Haarsma, E. J. D. Campos, S. Drijfhout, W. Hazeleger, and C. Severijns, "Impacts of interruption of the Agulhas leakage on the tropical Atlantic in coupled ocean-atmosphere simulations," *Climate Dynamics*, vol. 36, no. 5–6, pp. 989–1003, 2011.
- [51] M. Hirabara, H. Ishizaki, and I. Ishikawa, "Effects of the westerly wind stress over the Southern Ocean on the meridional overturning," *Journal of Physical Oceanography*, vol. 37, no. 8, pp. 2114–2132, 2007.
- [52] B. J. Hoskins and P. J. Valdes, "On the existence of storm tracks," *Journal of the Atmospheric Sciences*, vol. 47, no. 15, pp. 1854–1864, 1990.
- [53] L. P. Pezzi and K. J. Richards, "Effects of lateral mixing on the mean state and eddy activity of an equatorial ocean," *Journal of Geophysical Research C*, vol. 108, no. 12, article 3371, 2003.
- [54] A. C. V. Caltabiano, I. S. Robinson, and L. P. Pezzi, "Multi-year satellite observations of instability waves in the Tropical Atlantic Ocean," *Ocean Science*, vol. 1, no. 2, pp. 97–112, 2005.
- [55] C. J. Paciorek, J. S. Risbey, V. Ventura, and R. D. Rosen, "Multiple indices of Northern Hemisphere cyclone activity, winters 1949–99," *Journal of Climate*, vol. 15, no. 13, pp. 1573–1590, 2002.
- [56] K. E. Trenberth, "Storm tracks in the Southern Hemisphere," *Journal of the Atmospheric Sciences*, vol. 48, pp. 2151–2178, 1991.
- [57] F. Justino, A. Timmermann, U. Merkel, and E. P. Souza, "Synoptic reorganization of atmospheric flow during the last glacial maximum," *Journal of Climate*, vol. 18, no. 15, pp. 2826–2846, 2005.
- [58] Y. Wu, M. Ting, R. Seager, H.-P. Huang, and M. A. Cane, "Changes in storm tracks and energy transports in a warmer climate simulated by the GFDL CM2.1 model," *Climate Dynamics*, vol. 37, no. 1, pp. 53–72, 2011.
- [59] K. E. Trenberth, "The role of eddies in maintaining the westerlies in the Southern Hemisphere winter," *Journal of the Atmospheric Sciences*, vol. 44, no. 11, pp. 1498–1508, 1987.
- [60] J. H. Yin, "A consistent poleward shift of the storm tracks in simulations of 21st century climate," *Geophysical Research Letters*, vol. 32, no. 18, Article ID L18701, pp. 1–4, 2005.
- [61] A. M. C. Carmo, *Os Storm Tracks no Hemisfério Sul. Tese (Doutorado em Meteorologia)*, Instituto Nacional de Pesquisas Espaciais, São Paulo, Brazil, 2004.
- [62] R. Seager, N. H. Naik, M. F. Ting, M. A. Cane, N. Harnik, and Y. Kushnir, "Adjustment of the atmospheric circulation to tropical Pacific SST anomalies: variability of transient eddy propagation in the Pacific-North America sector," *Quarterly Journal of the Royal Meteorological Society*, vol. 136, no. 647, pp. 277–296, 2010.
- [63] J. R. Miller and G. L. Russell, "Ocean heat transport during the last glacial maximum," *Paleoceanography*, vol. 4, no. 2, pp. 141–155, 1989.
- [64] J. Peixoto and A. Oort, *Physics of Climate*, Springer, 1992.
- [65] K. E. Trenberth and J. M. Caron, "Estimates of meridional atmosphere and ocean heat transports," *Journal of Climate*, vol. 14, no. 16, pp. 3433–3443, 2001.

- [66] W. S. Broecker, "Paleocean circulation during the last deglaciation. A bipolar seesaw?" *Paleoceanography*, vol. 13, no. 2, pp. 119–121, 1998.
- [67] K. Döös, J. Nilsson, J. Nycander, L. Brodeau, and M. Ballarotta, "The world ocean thermohaline circulation," *Journal of Physical Oceanography*, vol. 42, no. 9, pp. 1445–1460, 2012.
- [68] M. Vellinga and R. A. Wood, "Global climatic impacts of a collapse of the atlantic thermohaline circulation," *Climatic Change*, vol. 54, no. 3, pp. 251–267, 2002.

Research Article

Adjusting of Wind Input Source Term in WAVEWATCH III Model for the Middle-Sized Water Body on the Basis of the Field Experiment

Alexandra Kuznetsova,^{1,2} Georgy Baydakov,^{1,2} Vladislav Papko,¹ Alexander Kandaurov,^{1,2} Maxim Vdovin,^{1,2} Daniil Sergeev,^{1,2} and Yuliya Troitskaya^{1,2}

¹Institute of Applied Physics of the Russian Academy of Sciences, 46 Ulyanov Street, Nizhny Novgorod 603950, Russia

²Nizhny Novgorod State University, 23 Gagarina Avenue, Nizhny Novgorod 603950, Russia

Correspondence should be addressed to Alexandra Kuznetsova; alexandra@hydro.appl.sci-nnov.ru

Received 20 August 2015; Accepted 18 November 2015

Academic Editor: Alan Blumberg

Copyright © 2016 Alexandra Kuznetsova et al. This is an open access article distributed under the Creative Commons Attribution License, which permits unrestricted use, distribution, and reproduction in any medium, provided the original work is properly cited.

Adjusting of wind input source term in numerical model WAVEWATCH III for the middle-sized water body is reported. For this purpose, the field experiment on Gorky Reservoir is carried out. Surface waves are measured along with the parameters of the airflow. The measurement of wind speed in close proximity to the water surface is performed. On the basis of the experimental results, the parameterization of the drag coefficient depending on the 10 m wind speed is proposed. This parameterization is used in WAVEWATCH III for the adjusting of the wind input source term within WAM 3 and Tolman and Chalikov parameterizations. The simulation of the surface wind waves within tuned to the conditions of the middle-sized water body WAVEWATCH III is performed using three built-in parameterizations (WAM 3, Tolman and Chalikov, and WAM 4) and adjusted wind input source term parameterizations. Verification of the applicability of the model to the middle-sized reservoir is performed by comparing the simulated data with the results of the field experiment. It is shown that the use of the proposed parameterization $C_D(U_{10})$ improves the agreement in the significant wave height H_s from the field experiment and from the numerical simulation.

1. Introduction

Prediction of surface wind waves on the inland water bodies is recognized as an important problem involving many environmental applications, such as safety of the inland navigation and protection from the banks erosion. Lake waves also strongly affect the processes of exchange of momentum, heat, and moisture in the low atmosphere and thus determine microclimate of the adjacent areas, which should be taken into account in planning structure of recreation zones [1].

The major physical problem of numerical wave modeling in inland water bodies is associated with short fetches, when parameters of wave excitation and development are strongly different from long-fetch condition typical for the open ocean [2]. Typically, in these conditions, the numerical description of waves in lakes and reservoirs is based on empirical models

(see, e.g., [3, 4]). But the empirical relationships are based on the averaged characteristics that cannot predict the extremes important for many tasks of operational meteorology (storm conditions such as Great Lakes storm, discussed in [5]), and numerical wave models are required. Now there are a number of examples of application of third generation models for waves forecast in large lakes. So, WAVEWATCH III [2] is used successfully for the wave forecasts on the Great Lakes in the USA [6, 7]. The data for a current wave situation is presented on the open website and is updated every three hours [8]. Furthermore, WAVEWATCH III and SWAN [9] are applied to Caspian Sea and Ladoga Lake to analyze the wind and waves climate hindcasting [10]. Nevertheless, lakes and reservoirs of smaller sizes (less than 100 km linear size, the so-called middle-sized reservoirs) also have examples of hurricane-force wind and severe surface

wave states conditions. The first attempt of application of a global wave model WAM [11] for the wave forecasting on a middle-sized reservoir was reported recently in [12].

Among the peculiarities of the low-fetch waves at the middle-sized reservoirs is the stronger wind input, which is proportional to the ratio of wind friction velocity (or 10 m wind speed) to the wave phase velocity [2]. Another feature is the enhanced nonlinearity caused by higher steepness of the waves. Then the tuning of the ocean wave model to the inland water conditions should be twofold: adjusting of the wind source and ‘‘collision integral.’’ Dissipation due to wave breaking can be expected to be similar to wave conditions due to their universal nature.

One more problem of tuning of numerical models to the conditions of middle-sized reservoirs and lakes is the small amount of experimental data that can be used for its verification. Rare examples of such experiments are studied [13, 14], which show the specificity of wind-wave interaction in the indicated circumstances. In this paper, we present a tuning of the wind input term in WAVEWATCH III model to the conditions of the middle-sized reservoir on an example of Gorky Reservoir belonging to the Volga Cascade. The tuning is based on the data of the field experiment held by our group. The methods of the experiment are different from those used in [13, 14], and they focus on the study of airflow in close proximity to water surface. The comparison of results of the numerical experiments with the results of the field experiments on Gorky Reservoir is presented.

The paper has the following structure. In Section 2, the basic parameterizations of wind and wave interactions in WAVEWATCH III v.3.14 are presented. In Section 3, the studied reservoir and the field experiment setup with its instrumentation and methods are described. In Section 4, the field data processing and the results of the field experiment are presented. In Section 5, numerical experiment within tuned to the conditions of the middle-sized reservoir WAVEWATCH III is set out. In Section 6, the adjustment of wind input source term in tuned WAVEWATCH III and the results of numerical experiments within tuned WAVEWATCH III and within a tuned WAVEWATCH III with the adjusted wind input are presented.

2. Wind Input Parameterizations in WAVEWATCH III

WAVEWATCH III [2, 15, 16] is based on the numerical solution of the equation for the spectral density of wave action N in the approximation of phase averaging:

$$\frac{\partial N}{\partial t} + \nabla_x \dot{x}N + \frac{\partial}{\partial \sigma} \dot{\sigma}N + \frac{\partial}{\partial \theta} \dot{\theta}N = \frac{1}{\sigma} (S_{\text{in}} + S_{\text{dis}} + S_{\text{nl}}). \quad (1)$$

The left hand side of (1) describes the kinematics of waves, σ is the radian frequency, and θ is the wave direction. In the right hand side, there are terms that describe the wind-wave growth S_{in} , dissipation mainly due to wave breaking S_{dis} , and 4-wave nonlinear interaction of waves S_{nl} .

This paper focuses on the wind input parameterizations, whose parameters can be adjusted on the basis of the field

measurements data. Generally, the term describing the wind input is determined as

$$S_{\text{in}} = \beta(k, \theta) N(k, \theta) \sigma, \quad (2)$$

where $\beta(k, \theta)$ is the dimensionless wind-wave growth rate parameter approximated in WAVEWATCH III v.3.14 by different parameterizations (WAM 3, Tolman and Chalikov, and WAM 4). Among them, the WAM 3 parameterization [17–19] is defined by two empirical formulas. The first one is for the wind-wave growth rate

$$\beta(k, \theta) = C_{\text{in}} \frac{\rho_a}{\rho_w} \max \left[0, \left(\frac{28u_*}{c_{\text{ph}}} \cos(\theta - \theta_w) - 1 \right) \right], \quad (3)$$

where $C_{\text{in}} = 0.25$ is a constant, ρ_a/ρ_w is the ratio of the densities of air and water, u_* is the friction velocity, c_{ph} is the phase velocity, and θ_w is the main wind direction. The second one is a relation between the 10 m wind speed U_{10} and a friction velocity $u_* = U_{10} \sqrt{C_D}$ provided by the empirical formula of the parameterization of the surface drag coefficient C_D , proposed in [19]:

$$C_D = 0.001 \times (0.8 + 0.65U_{10}). \quad (4)$$

In the Tolman and Chalikov parameterization [20], the dimensionless coefficient depends on the drag coefficient and on the dimensionless frequency of the spectral components. In the WAM 4 parameterization [21], the wind-waves interaction parameter β is presented by the adjusted Miles formula. To calculate the roughness parameter, the feedback of the wind-waves spectra is taken into account as well. So, in the considered parameterizations, the wind input is determined by the wind-wave interaction parameter β and by the dependence $u_*(U_{10})$ which is defined by C_D .

3. Field Experiment

The tuning of WAVEWATCH III to the conditions of the middle-sized reservoir was performed for conditions of Gorky Reservoir on the basis of field experiment.

Measurements were carried out in 2012–2014 from May to October in the waters of Gorky Reservoir. It has an elongated shape (Figure 1), which allows studying wind waves of different fetch, depending on the wind direction. Gorky Reservoir is an artificial lake in the central part of the Volga River formed by the dam of Nizhny Novgorod Hydroelectric Station. Its lake part is 85 km long and up to 15 km wide. The mean depth of the reservoir varies in the range of 4–20 meters, and the depth in the area of measurements is 9–12 meters depending on the season and the point of measurement.

3.1. Instrumentation. Instrumentation was placed on a buoy station with the original design based on the oceanographic Froude buoy. Froude buoy is a mast submerged in water and held in a vertical position by the float close to the surface and by the load on the depth (Figures 2(a) and 2(b)). Buoy's total length is 12 m, and the length of the part above the water

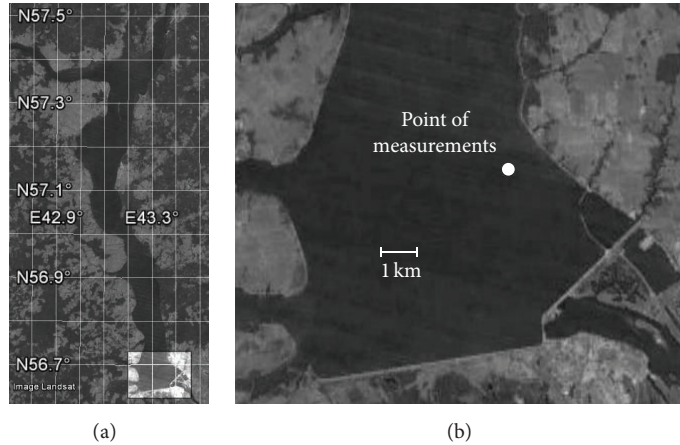


FIGURE 1: (a) Gorky Reservoir (Google Earth data). (b) Zoom view of the measurements area.

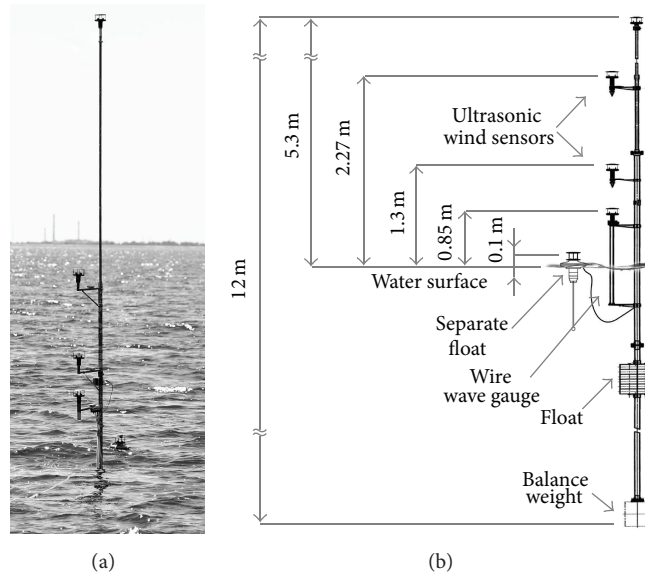


FIGURE 2: Froude buoy: (a) real view of the operating state and (b) scheme.

is 5.3 m. The resonant frequency of the vertical oscillations is 0.25 Hz, which corresponds to a wavelength of 25 m. On the buoy mast, 4 ultrasonic speed sensors (WindSonic Gill Instruments Production) are located at heights of 0.85 m, 1.3 m, 2.27 m, and 5.26 m over the mean water surface. A fifth sensor is located on the float tracking waveform that allows measuring the wind speed in close proximity to the water surface. The distance from the float to the buoy mast is 1 m; the height of the wind speed measuring zone is 10 cm from the water surface. The buoy is also equipped with air temperature sensors (at heights of 0.1 m (float), 0.85 m, and 1.3 m), water temperature sensors, and three-channel wire wave gauge that allows us to retrieve the wave space-time spectra.

WindSonic is two-component ultrasonic sensor with 4% measurement accuracy and velocity resolution of 0.01 m/s. Operating range of wind speed measurements 0–60 m/s includes measurements in calm conditions. Resistive temperature sensors measure the environmental temperature with

resolution of 0.01°C and 3% measurement accuracy. Wave gauge consists of three pairs of resistive wire sensors, located at the vertices of an equilateral triangle with a side of 62 mm, and the data sampling rate is 100 Hz.

3.2. *Surface Wave Spectra.* Three-dimensional frequency-wavenumber spectra were retrieved from wave gauge data by the algorithm similar to the wavelet directional method (WDM) suggested in [22]. The details of the applied method are described in [23]. Time series of water elevation from each pair of wire sensors were processed by the window FFT with the window width 2^N (N is an integer) with 50% overlapping. The complex amplitudes of harmonics at each frequency ω $A_\omega(x_n, y_n) \exp(i\phi_\omega(x_n, y_n))$ were calculated; here A_ω is the wave magnitude, ϕ_ω is the wave phase, $n = 1, 2, 3$ is the number of the wave sensors, and (x_n, y_n) are the n -sensor's Cartesian coordinates. Suppose that the wave field is a superposition of harmonic waves with the wavenumbers

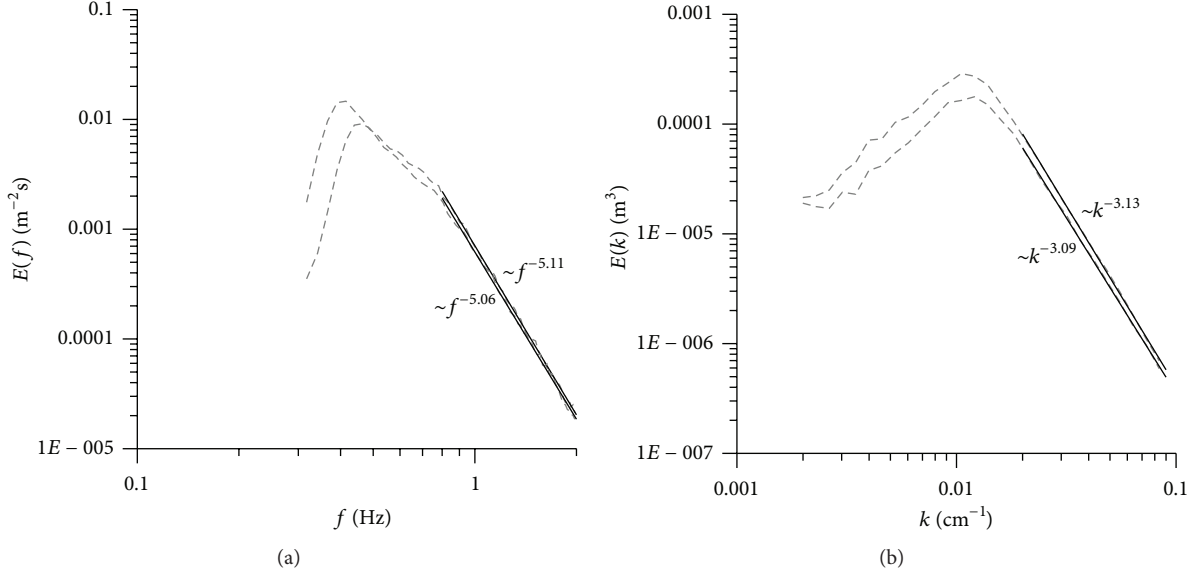


FIGURE 3: Wave spectra for $U_{10} = 6-7$ m/s averaged over 60 minutes: (a) 1D frequency spectrum and (b) 1D wavenumber spectrum.

$\vec{k} = (k_x, k_y)$ and one harmonic wave dominates in each interrogation window, and then their phases are

$$\phi_\omega(x_n, y_n) = k_x x_n + k_y y_n. \quad (5)$$

Thus, the wavenumber components can be calculated by the phase difference at different wave sensors. To obtain the directional spectra, the Cartesian coordinates (k_x, k_y) were transformed to the polar coordinates (k, θ) and then 3D spectrum $E(\sigma, k, \theta)$ was obtained similar to [22] by binning the amplitudes squared into calculated bins in k and θ . Integration of $E(\sigma, k, \theta)$ over wavenumber or frequency yields frequency $E(\sigma, \theta)$ or wavenumber $E(k, \theta)$ directional spectra, respectively. Integrating over θ gives the 1D frequency and wavenumber spectra correspondingly (examples are in Figure 3). The system allows estimating the parameters of the wave, whose length exceeds the double distance d between the sensors:

$$k_{\max} = \frac{\pi}{d} = 0.5 \text{ cm}^{-1}. \quad (6)$$

The developed algorithm is based on the supposition that the dominating wave field within the interrogation window at a given frequency σ is a harmonic wave, which is correct for a rather short time interval due to grouping of the surface wave field. Several periods of the energy-wave should fit into the interrogation window. For typical values of the observed peak frequency $f_p = 0.35-0.8$ Hz (or the observed peak period $T_p = 1.25-2.80$ s), the size of interrogation window is selected to be 20.48 s (2048 points).

Frequency and wavenumber spectra shown in Figure 3 are obtained by processing of two consecutive recordings 60 minutes long. It should be noted that the asymptotic behavior of frequency spectrum and wavenumber spectrum (σ^{-5}, k^{-3}) correspond to Philips saturation spectrum (see, e.g., [24]), but they do not correspond to Toba spectrum (see, e.g., [25]) which is typical for the ocean conditions.

For the comparison with the numerical modeling results, the values of significant wave height H_S are estimated as four-standard deviation of the water surface elevation, which are calculated as the integral of the frequency spectrum:

$$H_S = 4 \left(\int E(\sigma) d\sigma \right)^{1/2}. \quad (7)$$

3.3. Parameters of Low Atmosphere over the Inland Water Body. The location of wind velocity sensors corresponds to the structure of the airflow. It is well known (see, e.g., [26]) that the velocity profile in the constant flux layer (where the turbulent momentum flux $\tau_{\text{turb}} = \rho_{\text{air}} \langle u'_x u'_z \rangle$ does not depend on the vertical coordinate z ; here ρ_{air} is the air density and u'_x and u'_z are the fluctuations of horizontal and vertical components of the wind velocity, resp.) has a logarithmic form:

$$U(z) = \frac{u_*}{\kappa} \ln \left(\frac{z}{z_0} \right), \quad (8)$$

where $u_* = \sqrt{\tau_{\text{turb}} / \rho_{\text{air}}} = \sqrt{\langle u'_x u'_z \rangle}$ is the friction velocity determined by the turbulent momentum flux, z_0 is the surface roughness parameter, and κ is the von Karman constant. In [27], a distortion of the velocity field in the presence of a rough surface is considered, and it is shown that, in case of a monochromatic wave propagating along the wind, for the stream function φ averaged over the turbulent fluctuations, an equation can be written as

$$(U - c) \left(\frac{d^2 \varphi}{d\eta^2} - k^2 \varphi \right) - \frac{d^2 U}{d\eta^2} \varphi = 0, \quad (9)$$

where $U(\eta)$ is the dependence of wind speed on height above the surface (in curvilinear coordinates), c is phase velocity of the wave, and k is wavenumber. When the magnitude

$U''/k^2(U - c)$ is much greater or much less than 1, an approximate solution is the function $\varphi = A(U - c)e^{-k\eta}$, where A is wave amplitude. In the case of the logarithmic velocity profile, this condition takes the form (see [27])

$$\frac{u_*/\kappa}{(k\eta)^2 |U - c|} \ll 1 \quad (10)$$

or

$$\frac{u_*/\kappa}{(k\eta)^2 |U - c|} \gg 1,$$

and it is performed well enough at the height of the order of the wave amplitude and higher. Thus, the perturbation is the bending of the flow lines along the rough surface, and it decreases exponentially with altitude. Therefore, to fix speed sensor relatively to the mean streamlines, the speed at a distance from surface must be measured at a fixed horizon, and the measurements close to the surface should be carried out using a tracking waveform sensor located on the float.

It is important that the lower sensor should not be located in the wave boundary layer. The magnitude of the wave boundary layer ε can be estimated in accordance with [28]

$$\tilde{k} \left(\frac{\tilde{u}_*}{\kappa} \ln \left(\frac{z}{z_0} \right) - \tilde{c} \right) \Big|_{z=\varepsilon} = \frac{\kappa \tilde{u}_* z}{\varepsilon^2} \Big|_{z=\varepsilon}, \quad (11)$$

where \tilde{k} , \tilde{c} , and \tilde{u}_* denote typical values of the mentioned above variables. In the conditions of the Gorky Reservoir ($\tilde{k} = 2-3 \text{ m}^{-1}$, $\tilde{u}_* = 0.1-0.4 \text{ m/s}$), the evaluation of the height of the wave boundary layer gives a value $\varepsilon \sim 1 \text{ mm}$ that is significantly less than the height of the lower sensor measuring wind speed location.

It should be noted that the buoy is connected to the vessel by the cable and is located at a fixed distance of 30 meters; the cross section of the vessel is approximately equal to $3 \times 3 \text{ m}$. Thus, the buoy is located at a distance of about 10 characteristic dimensions from the obstacle. According to the recommendations of Gill Instruments [29], it is enough to consider the airflow to be unperturbed, but the measurements show the presence of small (3–6%) deviations of the measured profile from the logarithmic form even in a steady wind and neutral stratification (Figure 4). This deviation consists of the speed increasing at a height of 5.26 m on 3–6% compared with the logarithmic approximation. Apparently, this is due to the effect of the vessel shielding on the 4 lower sensors.

To estimate the perturbations introduced by vessel, the formulas of the defect rate attenuation in the turbulent wake are used. It is known [30] that the perturbation introduced by the body in the unlimited turbulent flow decreases in proportion $(x/D)^{-2/3}$ along the flow and in proportion $\exp(-r^2/2\bar{\sigma}^2)$ along the cross section. Here, D is the characteristic size of the body, x and r are the cylindrical coordinates, $\bar{\sigma}$ is a width of the Gaussian function, and

$$\frac{\bar{\sigma}}{D} \sim \left(\frac{x}{D} \right)^{1/3}; \quad (12)$$

the coefficients of the proportionality are determined empirically. In the case of airflow vessel shielding in a semibounded

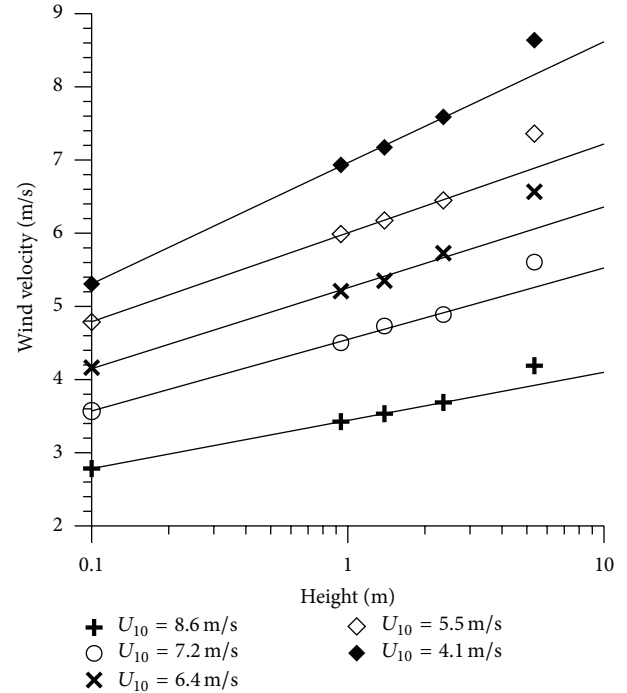


FIGURE 4: Examples of the deviation of the wind velocity profile (5 minutes averaging) from the logarithmic form under different conditions.

space, it is fair to expect that the nature of the turbulent wake is the same, but the appropriate factors must be chosen. Since the top speed sensor is located outside the vessel shielding zone, and the lower four are well approximated by a logarithmic dependence, the value $\bar{\sigma}$ should be between the heights of the fourth and fifth sensors. The linear coefficient is selected so that the velocity profiles are well approximated by a logarithmic dependence in average. Finally, to determine the magnitude of the perturbation introduced by the vessel in the airflow, the dependence

$$\gamma = \frac{U'}{U_0} = 0.3 \left(\frac{x}{D} \right)^{-2/3} \exp \left(-\frac{r^2}{2\bar{\sigma}^2} \right) \quad (13)$$

is used, where $\bar{\sigma}/D = 0.4(x/D)^{1/3}$, U_0 is the estimated wind speed in the unperturbed flow, and U' is the magnitude of the perturbation. Note that the selected coefficients are similar to those obtained in [31] for the wake behind the sphere. To determine the wind velocity in the unperturbed flow, the wind speed measured by sensors is multiplied by the coefficient $\alpha = (1 - \gamma)^{-1}$. The coefficients α for the various sensors are equal to 1.069, 1.065, 1.061, 1.047, and 1.009, respectively, from the bottom up to the top.

4. Field Data Processing and Results

Investigation of the wind flow parameters is carried out by profiling. General recording of wind speed is up to 5-hour duration and is divided into 5-minute sections (300 measuring points) with a 50% of overlap. As a result of

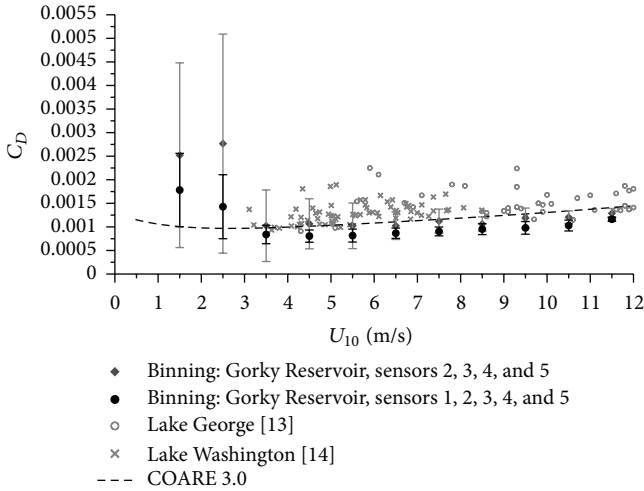


FIGURE 5: Comparison of the retrieved dependence $C_D(U_{10})$ with and without the lower sensor: gray diamonds denote the binning of data with the lower sensor (the standard deviation as the error gates); black solid circles are the binning of the data without the lower sensor (the standard deviation as the error gates); gray circles are the results of field experiment [13]; gray crosses are the results of field experiment [14]; dashed line is the empiric oceanic parameterization COARE 3.0.

the averaging, 5 values of wind speed corresponding to five horizons of measurements are received for each section. The resulting averaged profile is approximated by function (8) with the parameters of the approximation u_* (friction velocity) and z_0 (surface roughness). The values of the 10 m wind speed U_{10} and of the drag coefficient C_D are retrieved from the resulting approximation.

The impact of data obtained from different horizons on the resulting approximation of the wind velocity profile is analyzed. Figure 5 shows a comparison of the retrieved dependence $C_D(U_{10})$ for two combinations of speed sensors: with and without the lower sensor. The points on the plot are the result of the binning of the wind speed data within a cell with size of $\Delta U_{10} = 0.5$ m/s. The error gates correspond to the standard deviation. Also the results of field experiments [13, 14] and empiric oceanic parameterization COARE 3.0 [32] are shown in Figure 5. It is evident that, without the lower sensor data, the values $C_D(U_{10})$ are characterized by a slightly greater spread and are located higher and more close to the results of [13, 14, 32], while taking the lower sensor into account shows lower values of the drag coefficient. In [13], the sensors are located at the heights of 0.89 m up to 10 m from the mean water level; in [14], the sensors are located at heights from 0.5 m up to 4 m. In both cases, all the sensors are firmly fixed on the masts, and the approximation is performed throughout the wind speed profile.

Figure 6 shows a comparison of the retrieved dependence $C_D(U_{10})$ using two lower sensors only and using all five sensors. The use of two sensors only reveals significant differences in the wind parameters recovery in the weak winds area: the scatter and absolute value of $C_D(U_{10})$ decreases. In the field of moderate and strong winds, the retrieved values

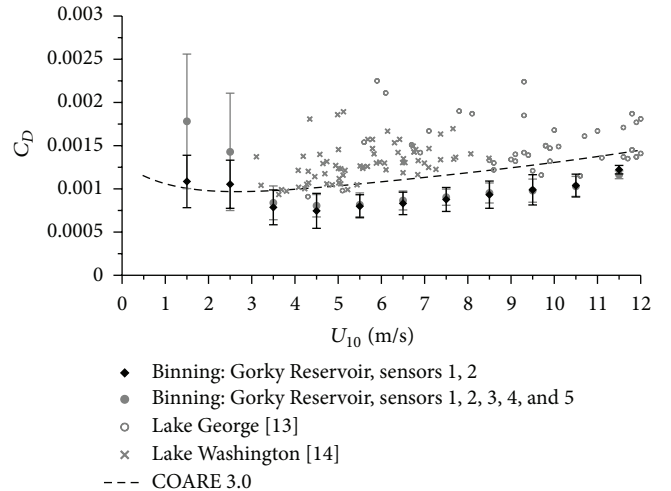


FIGURE 6: Comparison of retrieved dependence $C_D(U_{10})$ using two and five sensors: gray solid circles are the binning of the five-sensor data (the standard deviation as the error gates); black diamonds are the binning of the two-sensor data (the standard deviation as the error gates); gray circles are the results of the field experiment [13]; gray crosses are the results of the field experiment [14]; dashed line is the empiric oceanic parameterization COARE 3.0.

of drag coefficient differ slightly despite the small increase in the measurement error.

These results can be explained by the deviation of wind velocity profile from the logarithmic form. It may be caused by the stratification of the surface layer of the atmosphere and impact of the coastline as well as gustiness of the wind, because the lower part of the profile adapts more quickly to the changing conditions of waves, and the airflow parameters determine the momentum transfer from the wind to the waves exactly at the water-air boundary. Consequently, further analysis of the dependence $C_D(U_{10})$ was based on the measured data from sensors 1 and 2.

Throughout the 2012–2014 years, the dataset consisting of approximately 100 hours of recordings in the range of wind velocities 1–12 m/s for different fetch values ($L_{\text{fetch}} = 1\text{--}50$ km) and stratification conditions ($T_{\text{air}} - T_{\text{water}} = (-5) - 15^\circ\text{C}$) is obtained. The resulting dependence $C_D(U_{10})$ using two lower sensors is received and shown in Figure 7. The approximation of the obtained data is made by a function

$$C_D = 0.00124U_{10}^{-1} + 0.00034 + 0.000049U_{10}. \quad (14)$$

The result of binning of the wind speed data within a cell with size $\Delta U_{10} = 0.5$ m/s and the standard deviation as the error gates are shown in Figure 7. The dependence (14) is used below to adjust the wind input in WAVEWATCH III.

5. Tuning of WAVEWATCH III: Numerical Experiment

The tuning of WAVEWATCH III to the conditions of the Gorky Reservoir consists of the following factors. In the open code, the minimum value of a significant wave height H_S is adjusted in a number of blocks, where the lowest value of

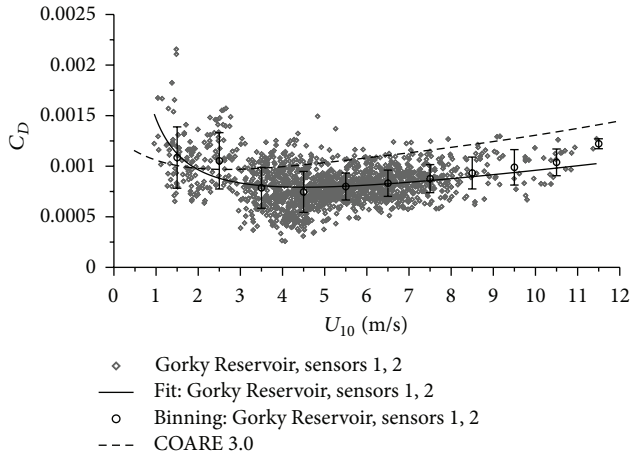


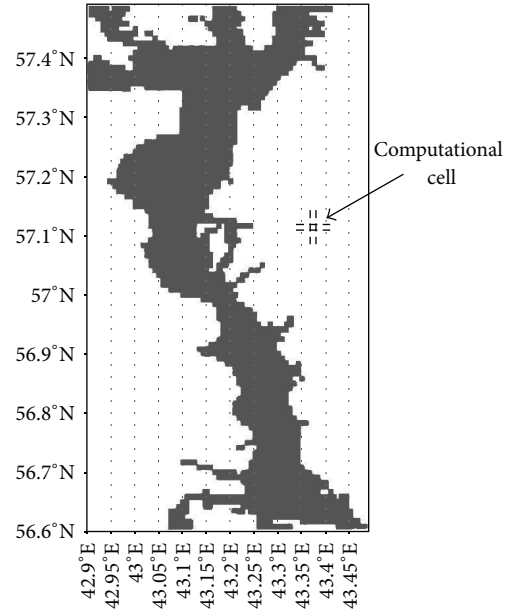
FIGURE 7: Detailed retrieved dependence $C_D(U_{10})$: gray diamonds denote the dependence received using two lower sensors; solid line is an approximation of the obtained data by a function $C_D = 0.00124 \cdot U_{10}^{-1} + 0.00034 + 0.000049 \cdot U_{10}$; black circles denote binning of the two-sensor data (the standard deviation as the error gates); dashed line is the empiric oceanic parameterization COARE 3.0.

H_S is directly indicated. For a description of the reservoir, the topographic grid of the Gorky Reservoir with dimensions 72×108 and increments of 0.00833° (which corresponds to approximately 800 m by 900 m for the considered latitudes) is used. The grid is taken from the NOAA data “Global Land One-Kilometer Base Elevation (GLOBE).” Topographic grid of Gorky Reservoir is shown in Figure 8. There is no reliable information about the bathymetry of the considered area, although the navigational maps show that the depth is big enough to consider an approximation of deep water. Thus, the constant depth of 9 m is taken.

The frequency range is changed to 0.2–4 Hz in accordance with the experimentally observed range, which is split in 31 frequencies in the simulation and is modeled by a logarithmic formula for the frequency growth

$$\sigma_N = (\delta)^{N-1} \sigma_1, \quad (15)$$

where the growth rate is determined to be $\delta = 1.1$ in accordance with the recommendations of [2]; 30 angular directions of the wave field are considered. The initial seeding is triggered and evolved in the wind. In practice, to simulate wind waves on the surface of the seas and oceans, the reanalysis data is typically used as a wind forcing. In the middle-sized inland waters, this approach is not applicable because of its too low spatial resolution (2.5°). In addition, in this area there are only two weather stations (Volga GMO, Yuryevets), but they are on the coast, and it was found out that the wind speed on the coast is different from those over the waters of the reservoir. In this regard, the magnitude and direction of the wind data are taken from the field experiment and are considered to be homogeneous over the whole water area of the reservoir. In fact, the wind field is expected to be heterogeneous, as such factors like the elongated shape of the reservoir and the high banks can lead to a significant spatial variability of the wind field. It should be noted that this



GrADS: COLA/IGES 2014-04-24-20:47

FIGURE 8: Topographical grid of Gorky Reservoir. Computational cell with a size of 0.00833° is shown.

assumption of the homogeneity of the wind forcing over the pond can be a source of errors in the numerical experiment.

As the wind above the reservoir is characterized by a strong mutability, the averaging of the wind speed in the experiment is performed in the interval of 15 minutes. Thus, the simulation is held with input data updated every 15 minutes, measured in field experiment: 10 m wind speed and direction, the water-air temperature difference. The comparison is made for the following output: 1D spectra elevations, significant wave height, and the average wave period. All data is obtained at the point corresponding to the point of observations and is averaged in the range of 15 minutes to match the similarity with the averaged data of the field experiment.

6. Adjusting of Wind Input Source Term in Tuned WAVEWATCH III

For the further tuning of WAVEWATCH III, a comparison of the used parameterizations of wind input is performed. For this, coefficients determining WAVEWATCH III parameterizations of wind input (C_D and β) are displayed at each step of the numerical simulation. Figure 9(a) shows the dependence $\beta(\sigma_{u_*}/g)$ for three considered parameterizations, results of numerical simulations for Tolman and Chalikov parameterizations, and theoretically estimated curves for parameterizations WAM 3 and WAM 4. Figure 9(b) shows the dependence $C_D(U_{10})$ of WAVEWATCH III and the proposed parameterization $C_D(U_{10})$ obtained as a result of field measurements (14). It can be seen that different parameterization of β and C_D used in WAVEWATCH III v.3.14 gives similar values in the conditions of middle-sized reservoirs ($\sigma_{u_*}/g = 0.1-0.15$, U_{10}

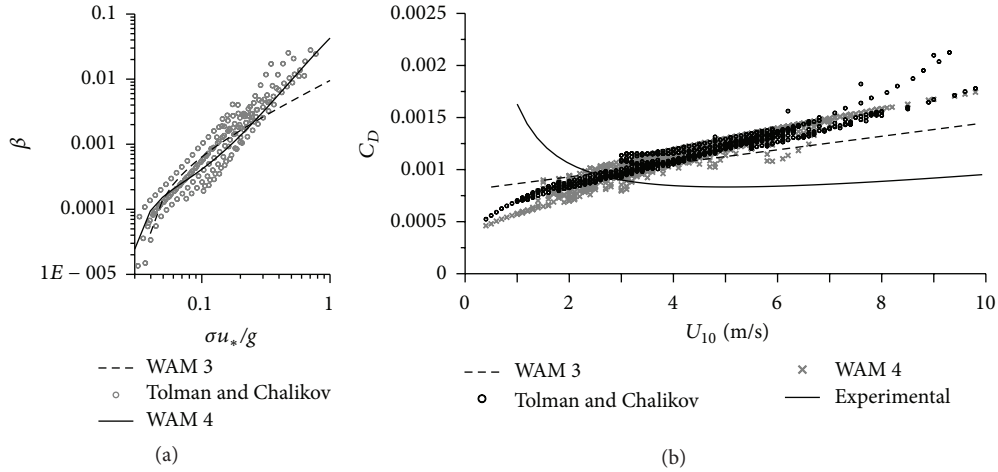


FIGURE 9: (a) Dependence of the wind-wave interaction coefficient on the dimensionless friction velocity for different parameterizations. (b) Dependence of the surface drag coefficient C_D on the wind speed U_{10} . WAM 3 is indicated by a dashed line, Tolman and Chalikov by circles, and WAM 4 by crosses.

= 1–10 m/s). At the same time, the proposed parameterization of C_D gives significantly lower values (on $\approx 50\%$) for moderate and strong wind speeds $U_{10} > 4$ m/s.

Then, wind-waves regime is studied for built-in parameterizations WAM 3, Tolman and Chalikov, and WAM 4. In the tuned WAVEWATCH III, we also used the adjusted wind input parameterization consisting of the use of the proposed experimental parameterization C_D within parameterizations WAM 3 and Tolman and Chalikov. As it was shown in Section 2, WAM 3 is based on the explicit formula, and Tolman and Chalikov is based on the implicit formula of $C_D(U_{10})$. These formulas are modified directly in the program code. Thus, instead of built-in parameterizations of C_D in the model, the new proposed parameterization (14) is used. Figures 10(a) and 10(b) show the results of the modeling and field measurements for the days 13.06.13 and 20.06.14, which are typical for the biggest part of the considered data. The lower plots show the measured values of the wind used in the simulation, and the plots on the top show a change for the retrieved values of H_S , obtained both from the field experiment and from the numerical experiments. In the model calculation, H_S is based on a formula

$$H_S = 4\sqrt{E}. \quad (16)$$

The same value gives the calculation of H_S in the experiment (7). As it can be seen from Figure 10, usually the values of the significant wave height in simulations with built-in parameterizations are overestimated. But it can be seen that the use of the proposed parameterization $C_D(U_{10})$ improves the agreement with the field experiment. The dependence $H_S(t)$ (Figure 10) shows that at the beginning of the time interval of the measurements (first 50 minutes) the wave regime is developing only, while the experimental values are already much higher. First of all, this is due to the fact that the wind prehistory for the simulations (before the start of the measurements) for both dates is taken from the weather stations, and, as it is mentioned in Section 5,

the wind speed on the coast is different from those over the waters of the reservoir. We also associate the difference between the simulation output and experimental values with the inaccuracy of wind forcing: due to the fact that the wind is set to be homogeneous, the waves that come from other parts of the reservoir are not large enough. To better match the results, inhomogeneous wind field is required.

Table 1 describes the evaluation of the difference in the applying of different parameterizations of wind input source term for two test dates: 13.06.13 and 20.06.14. It can be seen that WAM 3 typically overestimates the values of H_S compared with the experimental data for both dates, whereas the use of the proposed new C_D improves the accordance very well.

At the same time, Tolman and Chalikov parameterization underestimates the part of the values for 13.06.13, but the use of new C_D improves the total standard deviation (STD) for all the day of 13.06.13. For 20.06.14, the use of new C_D makes the underestimation of Tolman and Chalikov in the beginning of the time interval bigger, because it decreases the value of the energy entering the system (the new C_D lies lower than C_D in Tolman and Chalikov as it is shown in Figure 9(b)). This worsens the STD for Tolman and Chalikov with new C_D for 20.06.14. It should be mentioned that built-in Tolman and Chalikov source term performs well enough for the conditions of the middle-sized water body. It may be due to the particular properties of the dependence of C_D on U_{10} in Tolman and Chalikov parameterization (see Figure 9(b)). Tolman and Chalikov parameterization underestimates the growth rate at low wind speeds ($U_{10} < 3$ m/s) and overestimates it at higher wind speeds ($U_{10} > 4$ m/s) in comparison with the proposed new C_D in the adjusted WAM 3. Possibly, these effects compensate each other and give close results for the integral value of H_S . Nevertheless, new C_D is applied in the framework of this parameterization and shows different results for the dates of 13.06.13 and 20.06.14 (Table 1), but for the analysis of all

TABLE 1: Standard deviation of H_S .

	WAM 3 + new C_D	WAM 3	Tolman and Chalikov + new C_D	Tolman and Chalikov	WAM 4
13.06.13	0.28	0.36	0.19	0.23	0.32
20.06.14	0.23	0.41	0.25	0.20	0.20

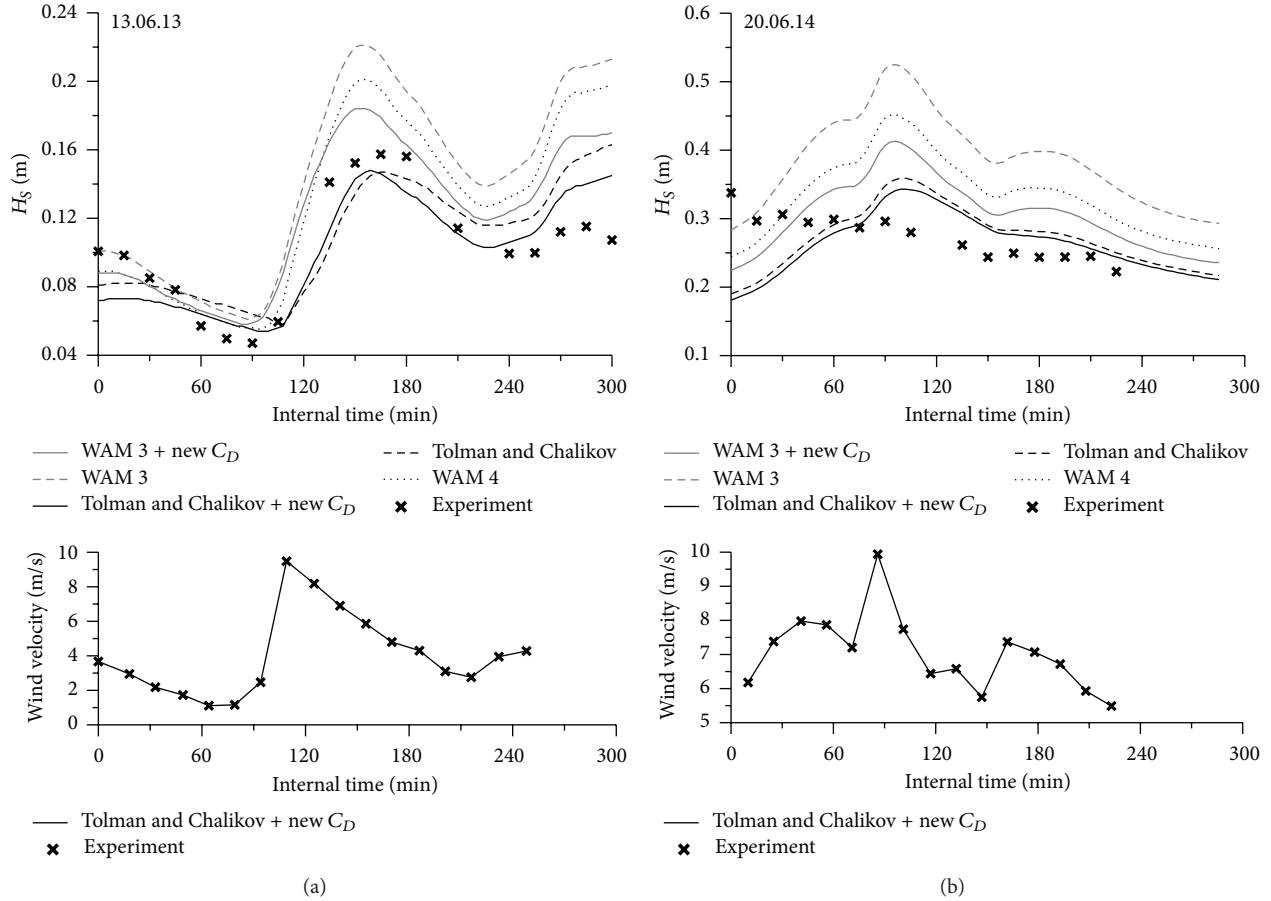


FIGURE 10: The upper graphs: dependence of H_S on time. Results of field experiments are marked by crosses, the simulated values of H_S for parameterizations WAM 3 (dark gray dashed line), WAM 3 with new C_D (dark gray solid line), Tolman and Chalikov (black dashed line), Tolman and Chalikov with new C_D (black solid line), and WAM 4 (long dotted line). The lower graphs: evolution of wind given by the field experiment, specified as input for WAVEWATCH III (a) 13.06.13, (b) 20.06.14.

the measured data with the simulation data it improves the coincidence (as shown in Figure 12(b)).

The resulting values of WAM 4 application are usually located between the results of WAM 3 and Tolman and Chalikov, and here in both cases the same situation is realized (the analysis of all data is shown in Figure 12(c)).

Figure 11 shows a comparison of the wave spectra at the point of measurements at a fixed time with the spectra obtained from a numerical experiment for built-in parameterizations WAM 3, Tolman and Chalikov, and WAM 4 and for the adjusted parameterizations WAM 3, Tolman and Chalikov with the new dependence $C_D(U_{10})$ as in formula (14). This improvement in the prediction of wave spectra is observed for the new parameterization $C_D(U_{10})$ for the biggest part of the considered data (Figure 11(a)). The spectra in the beginning of the time interval that correspond to

the situation in Figure 10, where the experimental values exceed the estimated values of H_S , are shown in Figure 11(b). However, along with improving the prediction of wind-wave characteristics, there is still a situation in which the simulated values of H_S are overestimated compared with the experimental values; this situation is reflected in the spectra in Figure 11(c).

For all of the considered experiments, a comparison of the integral characteristics (H_S and the mean wave period T_m) is performed. The mean wave period T_m is simulated using the following formula:

$$T_m = T_{m0,-1} = \left(\int_{f_{\min}}^{f_r} E(f) df \right)^{-1} \int_{f_{\min}}^{f_r} E(f) f^{-1} df. \quad (17)$$

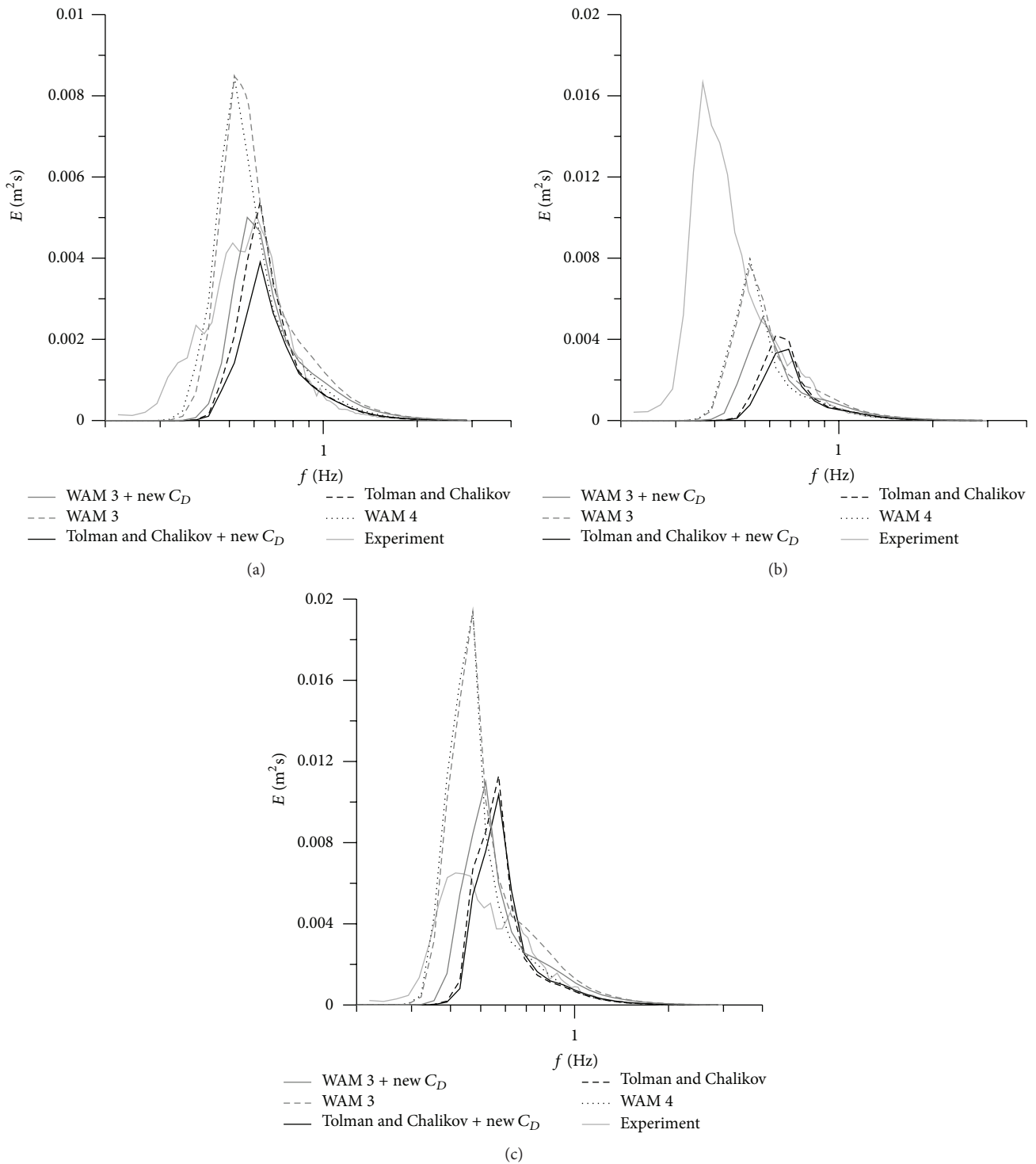


FIGURE 11: 1D wave spectra. The experimental spectrum is indicated by light-gray bold solid wide line, the simulated spectrum with the parameterizations WAM 3, gray dashed line, WAM 3 with the new C_D , gray solid line, Tolman and Chalikov, dark gray dashed line, Tolman and Chalikov with the new C_D , dark gray solid line, and WAM 4, a long dotted line. (a) The improved prediction of the wave spectra with the use of the new parameterization of C_D ; (b) spectra of the beginning of the time interval, where the spectra from the field experiment are higher than the spectra from the numerical experiment; (c) the spectra from the numerical experiment are higher than the spectra from the field experiment.

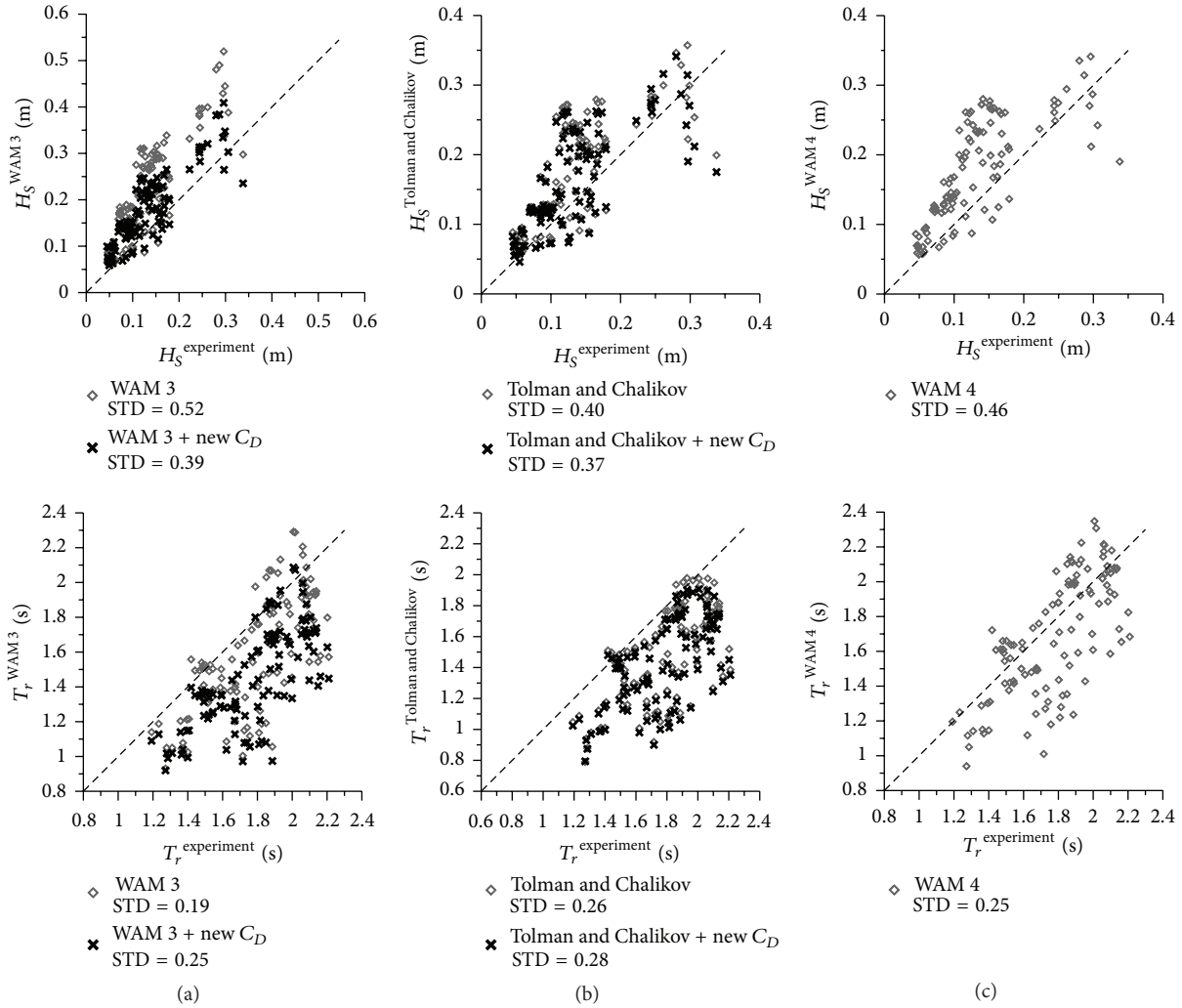


FIGURE 12: H_S (top graph) and T_m (bottom graph) in comparison with the data of field experiment for (a) parameterizations WAM 3 (diamonds) and WAM 3 with the new C_D (crosses), (b) parameterizations Tolman and Chalikov (diamonds) and Tolman and Chalikov with the new C_D (crosses), and (c) parameterization WAM 4 (diamonds).

On Figure 12, the x-axis represents the values obtained in the field experiments, and y-axis represents the results of the numerical simulations. On the top plots in Figure 12, for all the considered parameterizations (both built-in and with the use of a new parameterization), values of H_S in the output of the numerical simulation are compared with those obtained from the experiment. The lower plots are for the values of T_m . For all built-in parameterizations, the overestimation of the significant wave height and the underestimation of the mean wave period are typical, and the STD of H_S for WAM 3 is 52%, for Tolman and Chalikov is 40%, and for WAM 4 is 46%. The use of the new parameterization reduces the STD of H_S for WAM 3 from 52% to 39% and for Tolman and Chalikov from 40% to 37%. This is an expected result, as in the numerical experiment with the use of new parameterization of C_D , the wave growth increment is defined more precisely that means that the amount of energy entering the system is simulated more accurately.

However, the lower graphs in Figure 12 show that the prediction of mean wave periods has significant discrepancy with the measured ones, and the use of the new parameterization of $C_D(U_{10})$ does not make sufficient changes. Perhaps this is due to the fact that the adaptation of WAVEWATCH III to marine environment is reflected not only in the function of the wind input, but also in taking into account the specific parameters of numerical nonlinear scheme DIA [33, 34], because nonlinear processes are responsible for the redistribution of the energy received from the wind in the spectrum. WAVEWATCH III considers the wave characteristic of marine and ocean conditions, which have a lower slope compared to the waves on the middle-sized inland waters. The coefficients of proportionality in the scheme DIA are adjusted to the sea conditions. Steeper waves of middle-sized reservoir may require a different adjustment of parameters corresponding to a situation with stronger nonlinearity, which should lead to more rapid frequencies

downshift. Consequently, mean wave periods will decrease. At the same time, we can expect that such a tuning of the numerical nonlinear scheme should not affect the quality of the predictions of H_S , which indicates the amount of energy received by the system, but should lead to a better prediction of mean wave periods. This hypothesis will be tested in the subsequent numerical experiments.

7. Conclusions

The paper shows the tuning of WAVEWATCH III to the conditions of the middle-sized reservoir on the example of the Gorky Reservoir, which is specified in the model using real topographic grid NOAA "GLOBE." In carrying out the calculations, the default values of model parameters are modified on the basis of field measurements on the reservoir. In particular, the minimum value of significant wave height is adjusted and frequency range changed to 0.2–4 Hz. The initial seeding is developing under the influence of unsteady uniform wind given by the experiment. The wave field is simulated using both the built-in parameterizations of wind input adapted to the conditions of the open ocean and the parameterization using the new form of the surface drag coefficient (14), which is obtained from a series of field experiments.

Field experiments in the Gorky Reservoir show that the values of C_D in moderate and strong winds are on $\approx 50\%$ lower than those typical for the ocean conditions. In the course of the experiment, wave characteristics (frequency and wavenumber spectra, the mean wave period, and significant wave height) were obtained for different wind conditions. It is found out that the spectra have the asymptotic behavior similar to Phillips saturation spectrum. Field experiments in the Gorky Reservoir show that the values of C_D in moderate and strong winds are on $\approx 50\%$ lower than those typical for the ocean conditions.

The results of the numerical experiments are compared with the results obtained in the field experiments on the Gorky Reservoir. The use of the built-in parameterizations shows a significant overestimation of the simulated H_S compared with the experimental results. We interpret it by the overestimation of the turbulent wind stress (friction velocity u_*) and, accordingly, of the wind input. The use of the new parameterization $C_D(U_{10})$, based on field measurements on the reservoir, reduces the values of u_* and hence wind increment of surface waves. That improves the agreement in H_S from the field experiment and from the numerical simulation. Comparison of the simulation with built-in ocean parameterizations of the wind input overestimates values of the mean wave period T_m as well. At the same time, the adjustment of the wind input does not affect significantly the agreement of T_m values in the results of numerical simulation and in the field experiment. We interpret this by the fact that the nonlinear scheme is also adjusted to the conditions of seas and oceans, and we plan to make the adjustment of the parameters of the numerical nonlinear scheme DIA to the conditions of the middle-sized reservoir.

Another source of possible errors of numerical experiment should also be noted. Due to the lack of sufficient

experimental data, the wind speed is assumed to be uniform over the entire water area of the reservoir with the temporal variability defined from the experiment. In fact, nonuniform distribution of the wind is expected, as factors such as the elongated shape of the reservoir and the high banks can lead to a significant spatial variability of the scale with order of 1 km or less. The use of the wind from the reanalysis data is also impossible because of too low spatial resolution (2.5°). Taking into account the high spatial variability is a challenging problem. To solve it, it is planned to use the atmospheric models of high and ultrahigh spatial resolution (e.g., atmospheric model Weather Research & Forecasting (WRF) with block LES (Large Eddy Simulation)).

Conflict of Interests

The authors declare that there is no conflict of interests regarding the publication of this paper.

Acknowledgments

This work is supported by the Grant of the Government of the Russian Federation (Contract 11.G34.31.0048), President Grant for young scientists (MK-3550.2014.5), and RFBR (13-05-00865, 13-05-12093, 14-05-91767, 14-05-31343, 15-35-20953, and 15-45-02580). The field experiment is supported by Russian Science Foundation (Agreement no. 15-17-20009), and numerical simulations are partially supported by Russian Science Foundation (Agreement no. 14-17-00667).

References

- [1] K. Hunter, Ed., *Hydrodynamics of the Lakes*, CISM Courses and Lectures no. 286, International Centre for Mechanical Sciences, Udine, Italy, 1984.
- [2] H. Tolman and WAVEWATCH III Development Group, *User Manual and System Documentation of WAVEWATCH III Version 4.18*, Marine Modeling and Analysis Branch, Environmental Modeling Center, College Park, Md, USA, 2014.
- [3] S. A. Poddubnyi and E. V. Sukhova, *Modeling the Effect of Hydrodynamical and Anthropogenic Factors on Distribution of Hydrobionts in Reservoirs (User's Manual)*, Papanin Institute of Biology of Inland Waters, 2002.
- [4] E. N. Sutyryna, "The estimation of characteristics of the Bratskoye Reservoir wave regime," *Izvestiya Irkutskogo Gosudarstvennogo Universiteta*, vol. 4, pp. 216–226, 2011.
- [5] M. Newton-Matza, *Disasters and Tragic Events: An Encyclopedia of Catastrophes in American History*, ABC-CLIO, Santa Barbara, Calif, USA, 2014.
- [6] G. M. Jose-Henrique, A. Alves, H. L. Chawla et al., "The great lakes wave model at NOAA/NCEP: challenges and future developments," in *Proceedings of the 12th International Workshop on Wave Hindcasting and Forecasting*, Kohala Coast, Hawaii, USA, 2011.
- [7] J.-H. G. M. Alves, A. Chawla, H. L. Tolman, D. Schwab, G. Lang, and G. Mann, "The operational implementation of a Great Lakes wave forecasting system at NOAA/NCEP," *Weather and Forecasting*, vol. 29, no. 6, pp. 1473–1497, 2014.
- [8] <http://polar.ncep.noaa.gov/waves/viewer.shtml?-glw-latest-hs-grl->

- [9] SWAN Team, *SWAN—User Manual*, Environmental Fluid Mechanics Section, Delft University of Technology, Delft, The Netherlands, 2006.
- [10] L. J. Lopatoukhin, A. V. Boukhanovsky, E. S. Chernyshova, and S. V. Ivanov, “Hindcasting of wind and wave climate of seas around Russia,” in *Proceedings of the 8th International Workshop on Waves Hindcasting and Forecasting*, Oahu, Hawaii, USA, November 2004.
- [11] H. Gunter, S. Hasselmann, and P. A. E. M. Janssen, “The WAM model cycle 4,” Tech. Rep. 4, DKRZ WAM Model Documentation, Hamburg, Germany, 1992.
- [12] T. J. Hesser, M. A. Cialone, and M. E. Anderson, *Lake St. Clair: Storm Wave and Water Level Modeling*, The US Army Research and Development Center (ERDC), 2013.
- [13] A. V. Babanin and V. K. Makin, “Effects of wind trend and gustiness on the sea drag: lake George study,” *Journal of Geophysical Research*, vol. 113, no. 2, Article ID C02015, 2008.
- [14] S. S. Ataktürk and K. B. Katsaros, “Wind stress and surface waves observed on Lake Washington,” *Journal of Physical Oceanography*, vol. 29, no. 4, pp. 633–650, 1999.
- [15] H. L. Tolman, “A third-generation model for wind waves on slowly varying, unsteady, and inhomogeneous depths and currents,” *Journal of Physical Oceanography*, vol. 21, no. 6, pp. 782–797, 1991.
- [16] H. L. Tolman, “User manual and system documentation of WAVEWATCH III TM version 3.14,” Tech. Note 276, NOAA, NWS, NCEP, MMAB, 2009.
- [17] R. L. Snyder, F. W. Dobson, J. A. Elliott, and R. B. Long, “Array measurements of atmospheric pressure fluctuations above surface gravity waves,” *Journal of Fluid Mechanics*, vol. 102, pp. 1–59, 1981.
- [18] G. J. Komen, S. Hasselmann, and K. Hasselmann, “On the existence of a fully developed wind-sea spectrum,” *Journal of Physical Oceanography*, vol. 14, no. 8, pp. 1271–1285, 1984.
- [19] J. Wu, “Wind-stress coefficients over sea surface from breeze to hurricane,” *Journal of Geophysical Research*, vol. 87, no. 12, pp. 9704–9706, 1982.
- [20] H. L. Tolman and D. V. Chalikov, “Source terms in a third-generation wind-wave model,” *Journal of Physical Oceanography*, vol. 26, no. 11, pp. 2497–2518, 1996.
- [21] P. A. E. M. Janssen, *The Interaction of Ocean Waves and Wind*, Cambridge University Press, Cambridge, UK, 2004.
- [22] M. A. Donelan, W. M. Drennan, and A. K. Magnusson, “Non-stationary analysis of the directional properties of propagating waves,” *Journal of Physical Oceanography*, vol. 26, no. 9, pp. 1901–1914, 1996.
- [23] Y. I. Troitskaya, D. A. Sergeev, A. A. Kandaurov, G. A. Baidakov, M. A. Vdovin, and V. I. Kazakov, “Laboratory and theoretical modeling of air-sea momentum transfer under severe wind conditions,” *Journal of Geophysical Research: Oceans*, vol. 117, no. 6, Article ID C00J21, 2012.
- [24] O. M. Phillips, “Spectral and statistical properties of the equilibrium range in wind-generated gravity waves,” *Journal of Fluid Mechanics*, vol. 156, pp. 505–531, 1985.
- [25] P. Janssen, *The Interaction of Ocean Waves and Wind*, Cambridge University Press, Cambridge, UK, 2004.
- [26] O. G. Sutton, *Micrometeorology: A Study of Physical Processes in the Lowest Layers of the Earth’s Atmosphere*, McGraw-Hill, New York, NY, USA, 1953.
- [27] T. B. Benjamin, “Shearing flow over a wavy boundary,” *Journal of Fluid Mechanics*, vol. 6, pp. 161–205, 1959.
- [28] S. E. Belcher and J. C. R. Hunt, “Turbulent shear flow over slowly moving waves,” *Journal of Fluid Mechanics*, vol. 251, pp. 109–148, 1993.
- [29] WindSonic User Manual, Doc no. 1405-PS-0019, Issue 21, March 2013.
- [30] E. J. Hopfinger, J.-B. Flor, J.-M. Chomaz, and P. Bonneton, “Internal waves generated by a moving sphere and its wake in a stratified fluid,” *Experiments in Fluids*, vol. 11, no. 4, pp. 255–261, 1991.
- [31] G. R. Spedding, “The evolution of initially turbulent bluff-body wakes at high internal Froude number,” *Journal of Fluid Mechanics*, vol. 337, pp. 283–301, 1997.
- [32] C. W. Fairall, E. F. Bradley, J. E. Hare, A. A. Grachev, and J. B. Edson, “Bulk parameterization of air–sea fluxes: updates and verification for the COARE algorithm,” *Journal of Climate*, vol. 16, no. 4, pp. 571–591, 2003.
- [33] S. Hasselmann and K. Hasselmann, “Computations and parameterizations of the nonlinear energy transfer in a gravity-wave spectrum. Part I. A new method for efficient computations of the exact nonlinear transfer integral,” *Journal of Physical Oceanography*, vol. 15, no. 11, pp. 1369–1377, 1985.
- [34] S. Hasselmann, K. Hasselmann, J. H. Allender, and T. P. Barnett, “Computations and parameterizations of the nonlinear energy transfer in a gravity-wave spectrum. Part II: parameterizations of the nonlinear energy transfer for application in wave models,” *Journal of Physical Oceanography*, vol. 15, no. 11, pp. 1378–1391, 1985.

Research Article

Remote Sensing Observations of the Winter Yellow Sea Warm Current Invasion into the Bohai Sea, China

Jie Guo,¹ Hua Zhang,¹ Tingwei Cui,² Yijun He,³ Jie Zhang,² Kai Guo,¹
Chawei Hou,⁴ and Rongjie Liu²

¹Shandong Provincial Key Laboratory of Coastal Zone Environmental Processes, Yantai Institute of Coastal Zone Research, Chinese Academy of Sciences, No. 17 Chunhui Road, Laishan, Yantai 264003, China

²First Institute of Oceanography, SOA, No. 6 Xianxialing Road, Qingdao 266061, China

³School of Marine Sciences, Nanjing University of Information Science and Technology, No. 219 Ningliu Road, Nanjing, Jiangsu 210044, China

⁴Yantai Marine Environmental Monitoring Central Station, SOA, No. 16 Xihaiyang Beijie Road, Yantai 264006, China

Correspondence should be addressed to Jie Guo; jguo@yic.ac.cn

Received 6 August 2015; Revised 9 October 2015; Accepted 12 October 2015

Academic Editor: James Cleverly

Copyright © 2016 Jie Guo et al. This is an open access article distributed under the Creative Commons Attribution License, which permits unrestricted use, distribution, and reproduction in any medium, provided the original work is properly cited.

Using ASCAT, QuikSCAT, and MODIS data, we analyzed the sea surface wind field, temperature, salinity, and chlorophyll concentrations in the mixed zone between the Bohai Sea and Yellow Sea in the winter (the period of winter 2013 included December 2013 and January-February 2014) from 2002 to 2013. We found that the intrusion of the Yellow Sea Warm Current into the Bohai Sea occurred three times in the winters of 2007 (strongest), 2004, and 2013 (weakest) during this 12-year period. We present detailed validation of the intrusion in 2013. This study shows that the intrusion of the Yellow Sea Warm Current into the Bohai Sea occurred when the wind speed, sea surface temperature, and salinity were above (or close to) the multiyear average and the chlorophyll concentration was less than the multiyear average.

1. Introduction

The Yellow Sea Warm Current (YSWC) is a branch of the Tsushima Current, which both branch from the Kuroshio Current [1–3]. The YSWC originates in the area northeast of the East China Sea and south of the Jeju Island of Korea. It is the only source of sea water from the open sea entering the Yellow Sea and is characterized by high temperature, high salinity (SAL), and low dissolved oxygen content [4].

There are many important issues surrounding the YSWC. For example, existing high-resolution numerical simulations suggest that the path and intensity of the YSWC are altered by the wind [5–9]. Yuan et al. [8] showed that winter northerly winds could drive the YSWC north to flow across the Yellow Sea trough. Tang et al. [7] showed that the path of the YSWC had clear seasonal and interannual variations. Numerical calculations showed that the variations were closely related to the strength of the northerly wind. Model simulation by Song et al. [4] revealed clear 5-year variability in the YSWC and

found a south-north shifting that correlated with the zonal and meridional wind variability. In a strong wind situation, the YSWC intrudes further into the northern Yellow Sea. Using model simulation, Miu and Liu [10] found a northward flow along the northern Yellow Sea trough and assumed that it was the YSWC. The flow moves along the Yellow Sea trough against the wind, moving up from the deep area at the north of the Bohai Strait and extending to the central Bohai Sea. Shen and Mao [11] found that sea surface SAL of the eastern Bohai Sea reached a maximum in February and March every year.

From the review above, we found that it is not conclusive how and when the YSWC path enters the Bohai Strait. Furthermore, it is not clear whether the YSWC forms a persistent current into the Bohai Strait.

The Bohai Sea is an inland sea of China, with an average depth of about 18 m. The sea is rich in fishery resources, with busy industrial activities for ocean-shipping, petrochemical, and salt products [12]. The Bohai Strait is the only channel

TABLE 1: Remote sensing data used in this study.

Source	Resolution	Time	Purpose	Temporal resolution day	Products
ASCAT_L3	25 km	2007–2013	Wind field	2~3	C band
QuikSCAT_V4	25 km	2002–2006	Wind field	1~2	Ku band
MODIS_L3	9 km	2002–2013	SST	1~2	3.66–3.84 μm
MODIS_L3	9 km	2002–2013	CHL	1~2	405–420 μm
MODIS_L3	9 km	2002–2013	SAL	1~2	Monthly climatology remote sensing reflectance at 488 nm, 555 nm, and 667 nm

connecting the Bohai Sea to the open ocean, that is, the Yellow Sea. The Yellow Sea is a semiclosed shelf shallow sea (depth 70–100 m and average 44 m). There is a group of sand ridges located to the north of Bohai Strait [13, 14]. Surface observation data in Bohai Strait are not easily obtained, as waves whipped up by the wind roll turbulently in this area.

With the development of remote sensing technology, modern satellite data are frequently collected over the mixed zone between the Yellow Sea and Bohai Sea (Y-B) and are advantageous in monitoring the evolution of the YSWC path. Based on daily sea surface temperature (SST) of NOAA/AVHRR [15, 16], sea surface height (SSH) from AVISO, and the wind data recorded in the Chengshantou Station of China, Zhao et al. [17] identified two tongue-shaped branches of warm waters associated with the YSWC intrusion. Furthermore, statistical results revealed that these two branches were always present from 1981 to 2010. They found that the SSH was lower in the southern Yellow Sea than in the YSWC in the middle of September and from the end of February to early March. Starting in late March, the SSH was higher in the YSWC than in the southern Yellow Sea. Correlation analysis of the variation of the local SSH of the Yellow Sea indicated that the northwestern and northern branches of the YSWC were driven by relatively local SSH changes, caused by regional winds. They analyzed the characteristics of the YSWC using remote sensing data in combination with observational data; however, there was a lack of conclusive data on the SAL to analyze.

In a different area, Yuan et al. [18] studied the surface Kuroshio path in the Luzon Strait area using satellite ocean color, sea surface temperature, and altimeter data. The results suggested that the dominant path of the surface Kuroshio intrusion in the winter was a direct route from northeast of Luzon to southwest of Taiwan and then westward along the continental slope of the northern South China Sea.

All these issues are related to the YSWC intrusion into the Bohai Strait, which can be investigated using remote sensing ocean color and active microwave data. Many observations have indicated that the Kuroshio loop current is primarily a winter phenomenon and to date its occurrence in summer has not been frequently observed [19–21]. Winter is therefore the best season to observe the YSWC [17]. Further, the development of remote sensing technology provides a great possibility of studying the regional characteristics of the YSWC. Research on the YSWC invasion into the Bohai Sea

will significantly affect research on its ecological environment and the survival of fisheries spawning grounds. Its invasion clearly related to climate change.

In this study, we investigated the winter YSWC path in the mixed zone Y-B by remote sensing data based on wind field (atmospheric pressure changes cause sea surface wind field) and SST variations, with factor analyses of SAL, chlorophyll concentration (CHL), northerly wind days, and high wind days. We study that if remote sensing data show the intrusion of YSWC into the Bohai Sea, how to form decision criteria by remote sensing data and how to use the in situ data validate the criterion.

2. Materials and Methods

We used remote sensing data from the winter of 2013 as a case study to analyze and validate the in situ and cross section observational data. The sea surface wind field, temperature, SAL, CHL, wind scale, and high wind days were used to analyze characteristics of the mixed zone between the Bohai Sea and Yellow Sea in winters using remote sensing data.

2.1. Data Collection. The primary satellite data (Table 1) used to study the YSWC intrusion into the Bohai Sea in the winter was sea surface wind field data. Data were obtained from ASCAT_L3 daily average data on a global grid of about 25 km resolution (<ftp://ftp.ifremer.fr/ifremer/cersat/products/gridded/MWF/L3/ASCAT/Daily/>) and QuikSCAT_V4 daily average data in the Ku band on a global grid of about 25 km resolution (<http://www.remss.com/missions/qscat>). To reduce the cloudiness of the MODIS data, the monthly averaged sea surface SST and CHL data from MODIS_L3/Terra at 9 km resolution were used in this study (<http://oceancolor.gsfc.nasa.gov/cgi/l3>). The period of winter 2013 included December 2013 and January–February 2014. Scatterometer wind had an accuracy of less than 1 m/s [22, 23].

2.2. Methods. We computed the monthly average for all parameters. Validation data were from in situ and cross section observational data from ships. The SAL-retrieving algorithm for this study is from Qing et al. [24]. The model was recalibrated based on remote sensing reflectance data derived from MERIS and from in situ SAL data, yielding a root mean square error (RMSE) in modeled SAL of 1.31 psu (relative to in situ data). This recalibrated model was applied to MODIS

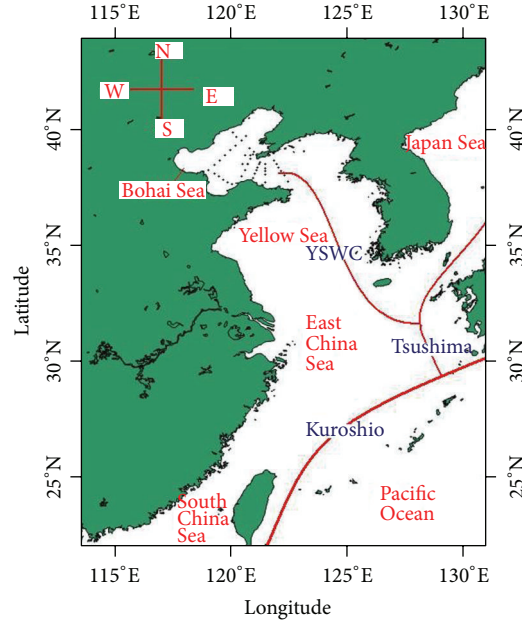


FIGURE 1: Study area (with symbol display area) sketch map.

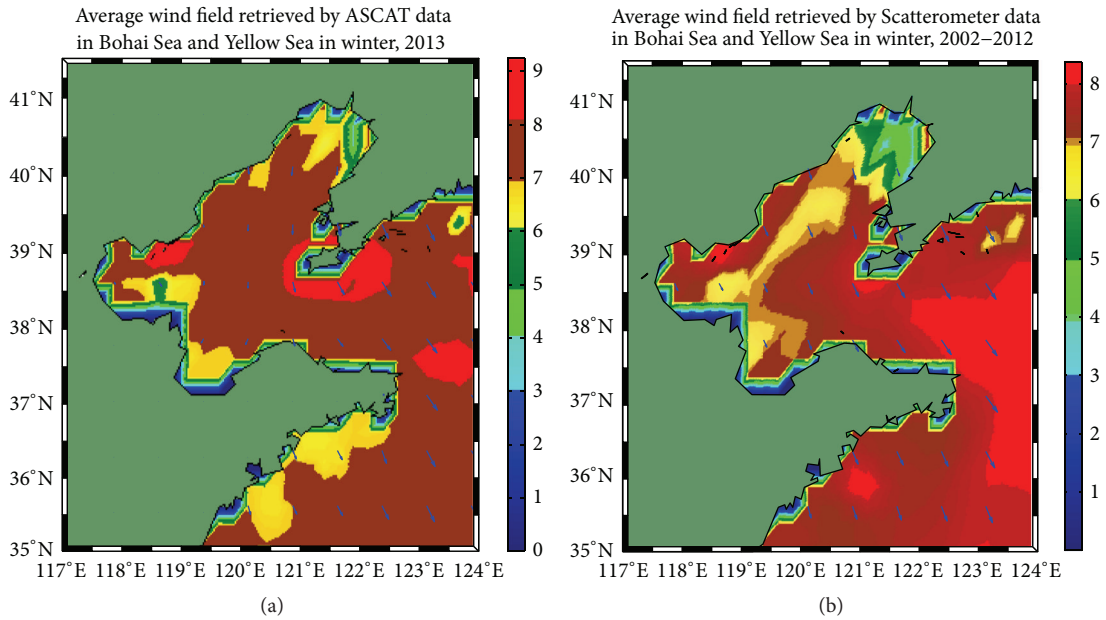


FIGURE 2: The average wind field retrieved by Scatterometer data in Y-B in winter 2013 (a) and 2002–2012 (b) (unit: m/s).

data following a linear correction for SAL in the mixed zone Y-B:

$$\lg(\text{SAL}) = 7.8 \times R_{rs}(488) - 11.325 \times R_{rs}(555) + 2.183 \times R_{rs}(667) + 1.53. \quad (1)$$

With winter remote sensing data from nearly 12 years, from 2002 to 2013, we analyzed the characteristics of the entry of the YSWC into the Bohai Sea, in the study area (Figure 1, spans 37.5–39°N/120–124°E in Y-B to avoid the land).

3. Results and Discussion

3.1. Wind Field Inversion of Y-B Mixed Zone from ASCAT Data. Wind field data were obtained from ASCAT_L3 data and displayed in Table 1. There were 90 wind field data points retrieved from ASCAT data, in the mixed zone, Y-B. In winter 2013, the average wind speed was 7.83 m/s (Figure 2(a)) compared with the average value of 7.71 m/s for 2002–2012 (Figure 2(b)). The wind speeds (2002–2012) were a fusion of ASCAT (2007–2012) and QuikSCAT (2002–2006) data, through Kriging interpolation in Figure 2(b). In winter 2013,

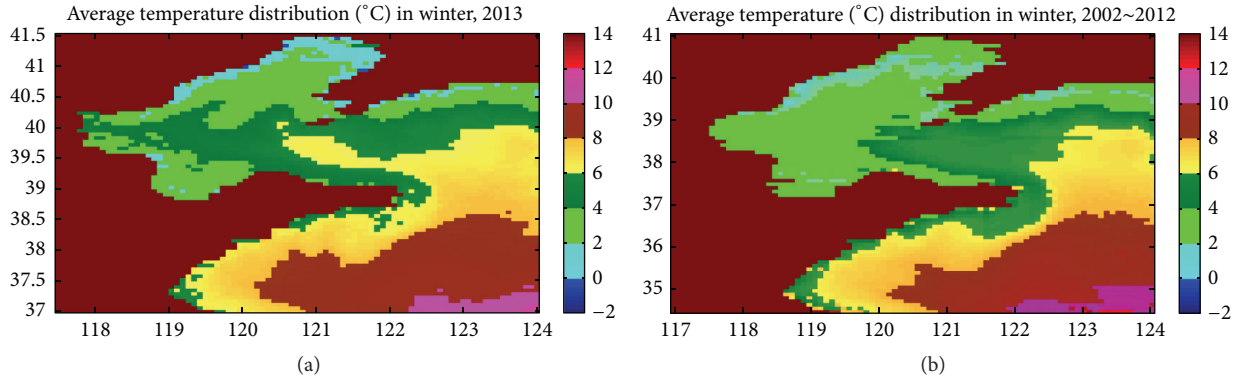


FIGURE 3: Average SST distribution in winter 2013 (a) and 2002–2012 (b).

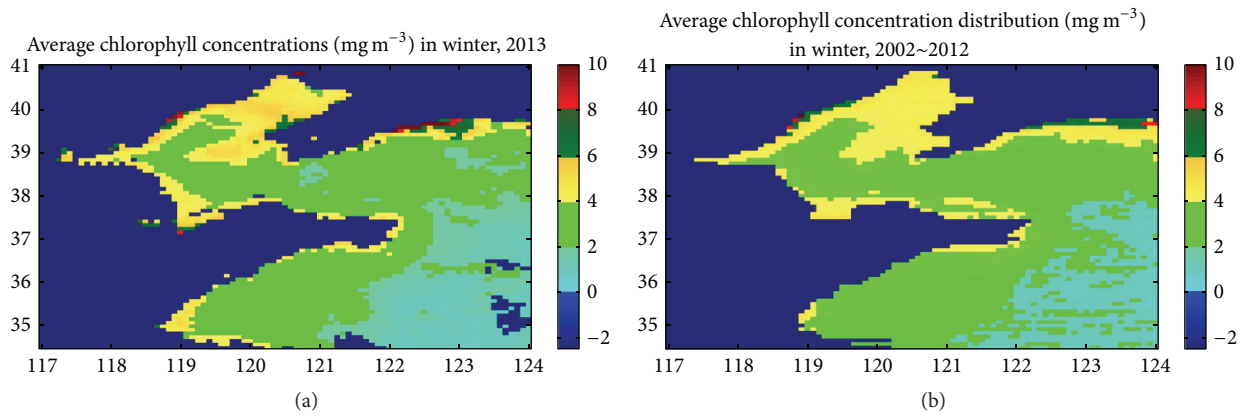


FIGURE 4: Average CHL distribution in winter 2013 (a) and 2002–2012 (b).

the numbers of windy days were defined on the Beaufort scale 1-2, 2-3, 3-4, 4-5, 5-6, and 6-7, with 1, 12, 28, 24, 19, and 6 days, respectively (Table 2). On the Beaufort scale, a wind with average maximum speed above level 6 (≥ 10.8 m/s) for 10 min is termed a high wind and above level 8 (≥ 17.2 m/s) is a strong wind [25].

Table 2 shows the number of days with each of the different wind directions: east (E) (occurring in 2 days), south (S), west (W), north (N), NNE, NNW, SSW, SSE, NWW, WSW, ESE, and NEE. We found that northerly winds occurred in 55 days (61%) in winter 2013.

3.2. SST Inversion Revealed by MODIS Data. The retrieved SST from MODIS_L3 monthly average data in winters of 2013 and 2002–2012 showed that temperature varied from 4°C to 8°C in the study region. There were 174 SST data points retrieved from MODIS_L3 data in the mixed zone Y-B. The average temperature was 7.23°C in winter 2013 (Figure 3(a)), which was higher than the average value of 6.71°C (Figure 3(b)) from winter of 2002–2012.

3.3. CHL Inversion from MODIS Data. The CHL distribution retrieved from MODIS_L3 monthly average data in winters of 2013 and 2002–2012 varied from 0 to 4 mg/m³. There were 428 CHL data points retrieved from MODIS_L3 data in the mixed

TABLE 2: Characteristics of wind field at Y-B mixed zone in winter 2013.

Wind scale	Days (90)	Wind_dir	Days (64)	Wind_dir	Days (26)
1~2	1	E	2	SSW	6
2~3	12	S	5	SSE	8
3~4	28	W	9	ESE	3
4~5	24	N	10	WSW	2
5~6	19	NNE	15	NWW	6
6~7	6	NNW	23	NEE	1

zone Y-B. The average CHL in winter 2013 was 3.02 mg/m³ (Figure 4(a)) and 3.06 mg/m³ for 2002–2012 (Figure 4(b)). There was no more variation in CHL in 2013 than in 2002–2012.

3.4. Salinity Inversion from MODIS. MODIS_L3 observations and inversion SAL from formula (1) showed that the SAL ranged from 31.03 to 32.93 psu in the winter of 2013 (Figure 5(a)). There were 779 SAL data points retrieved from MODIS_L3 data in the mixed zone Y-B. In the study region, the averaged value ranged from 28.97 to 32.82 psu (Figure 5(b)) in 2002–2012.

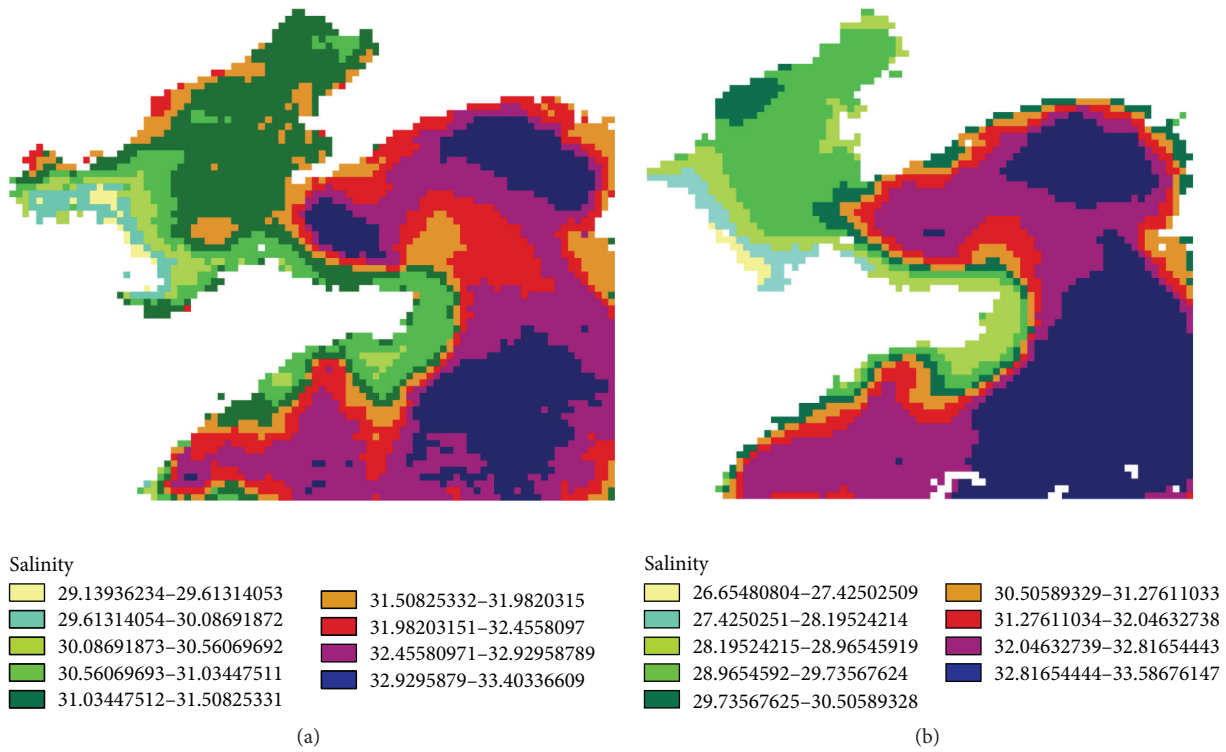


FIGURE 5: Average SAL distribution in winter 2013 (a) and 2002–2012 (b).

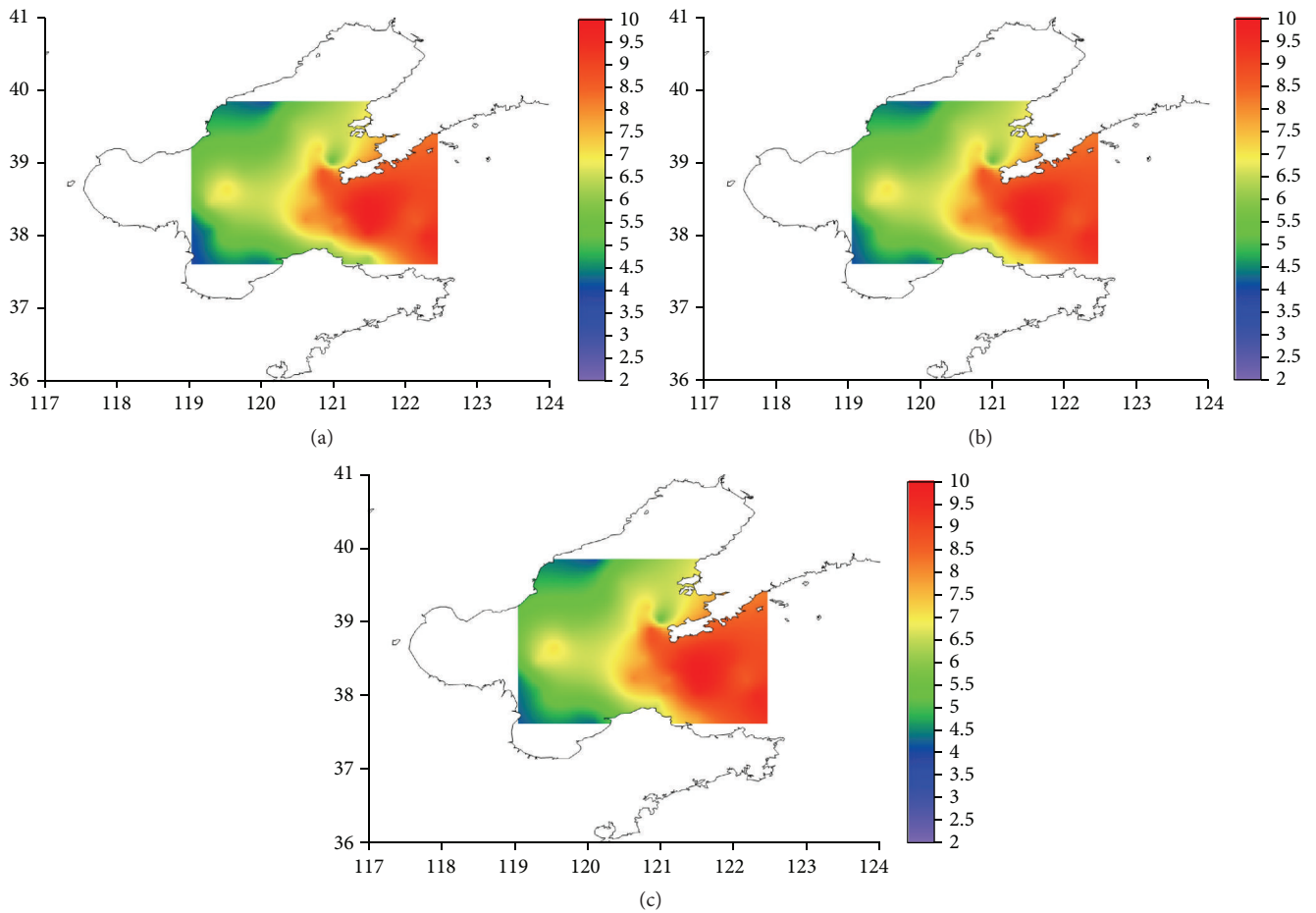


FIGURE 6: The SST data from 42 cross section stations in Y-B on December 17–24, 2013: (a) sea surface; (b) 10 m; (c) sea bottom (unit: °C).

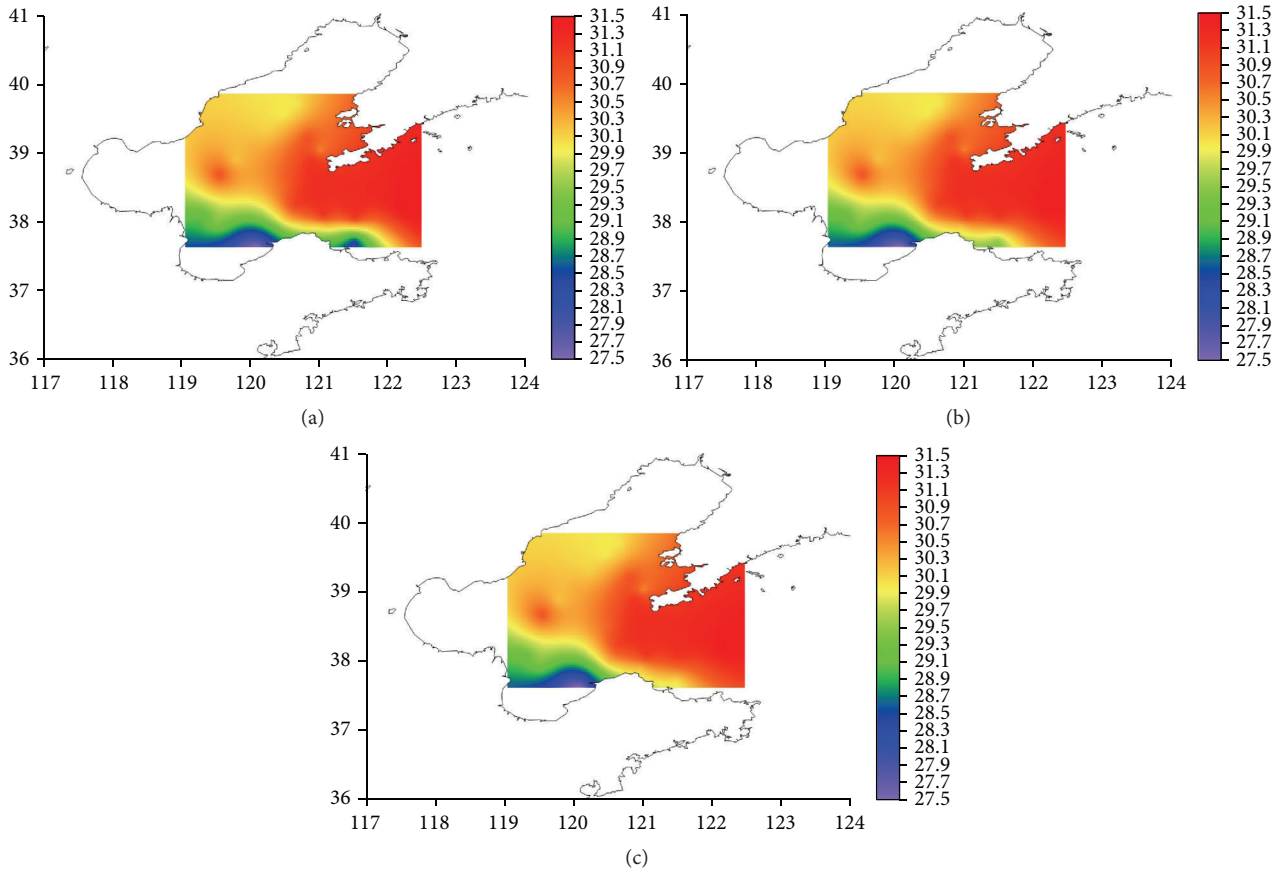


FIGURE 7: The SAL data from 42 cross section stations in Y-B on December 17–24, 2013: (a) sea surface; (b) 10 m; (c) sea bottom (unit: psu).

TABLE 3: Characteristics of the Y-B mixed zone in winter of 2002–2013.

Year	Winter days	Northerly wind days	High wind days	SST (°C)	SAL (psu)	CHL (mg/m ³)	V (m/s)	V _{dir} (°)
2002	89	68	29	6.16	31.51	2.44	7.49	159.01
2003	90	64	32	7.22	31.4	3.23	7.66	130.02
2004	89	67	32	7.71	31.46	2.79	8.18	163.20
2005	89	70	31	6.29	31.61	3.34	7.8	163.05
2006	90	64	23	7.81	31.3	2.66	6.82	152.35
2007	86	59	19	7.32	31.68	3.1	8.01	245.32
2008	87	53	26	7.03	31.35	3.63	7.97	213.69
2009	86	56	28	5.59	31.17	2.31	7.76	221.77
2010	88	55	34	6.15	30.98	3.49	8.3	230.12
2011	90	62	24	7.01	31.34	3.33	7.48	242.85
2012	90	53	18	5.51	31.19	3.3	7.30	215.06
2013	90	53	6	7.23	31.43	3.02	7.83	208.37

3.5. *The In Situ and Cross Section Observation Data Analysis in Winter 2013.* We analyzed the in situ and cross section observational SST and SAL data measured by shipboard CTD collected at the 42 stations shown in Figure 1 (+ symbol display site). These observations were made in Y-B on December 17–24, 2013, at depths of 0 m and 10 m and at the bottom (Figures 6 and 7).

As shown in Figure 6, the SST data came from the sea surface (Figure 6(a)), from 10 m water depth (Figure 6(b)), and

at the bottom (Figure 6(c)). The SAL data came from the sea surface (Figure 7(a)), 10 m water depth (Figure 7(b)), and the bottom (Figure 7(c)).

3.6. *Results.* Through the aforementioned remote sensing inversion average data for years contrast, we found that, in winter 2013, winds were mostly northerly (Table 2). The average wind speeds of the two periods were similar, only 0.12 m/s higher in 2013 than in 2002–2012, with an RMSE of

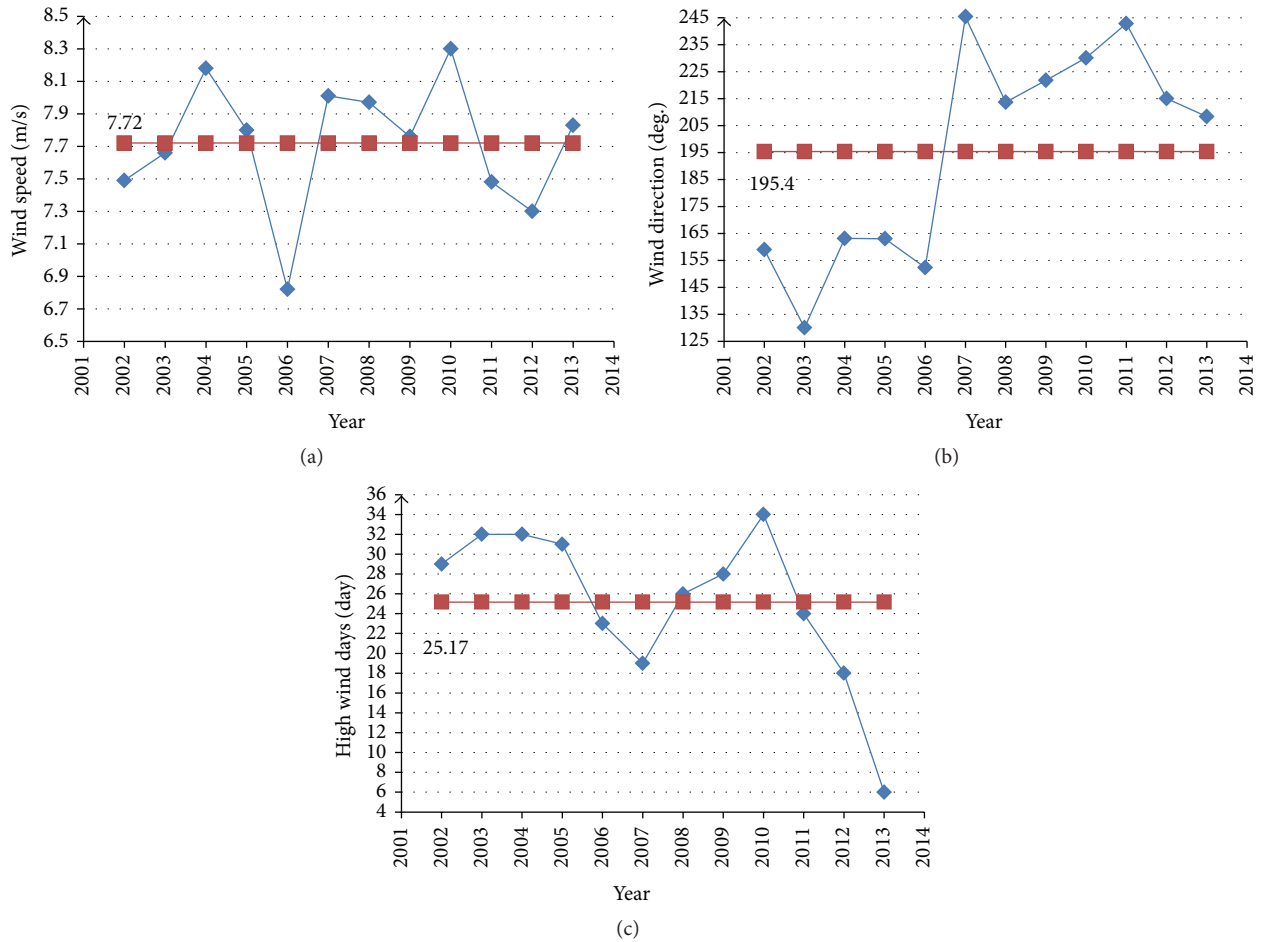


FIGURE 8: Average wind field parameters in winter between 2002 and 2013. (a) V : wind speed; (b) V_{dir} : wind direction; (c) high wind days.

0.26 m/s. On average high wind days were 2 days shorter in winter 2013 compared with 2002–2012, which had an average of 8.97 days. However, the average SST was 0.52°C in 2013, which was much higher than the average of 2002–2012; the RMSE was 1.85°C . The average CHL in the mixed zone in winter 2013 was similar to the average from 2002 to 2012, only 0.04 mg/m^3 lower in 2013 than in 2002–2012; the RMSE was 0.59 mg/m^3 . Figure 4 shows a low average CHL at $0\text{--}2\text{ mg/m}^3$ near the mixing zone in winter 2013, which is not existent in the previous decade to see Figure 4(b). The average SAL in winter 2013 was 32.01 and 31.29 psu in 2002–2012 (see Figure 5); RMSE was 1.84 psu. Thus, we hypothesized that the YSWC entered the Bohai Sea in winter 2013.

From in situ and cross section observational data, we found that a warm water mass (SST: $7\text{--}10^{\circ}\text{C}$; SAL: 30.1–31.5 psu) invaded the Bohai Sea from the Yellow Sea on December 17–24, 2013, at all depths. We found that, in December 2013, the SAL and SST from observational data did not vary greatly between different depths. Because of the shallowness of the research area and the wind and wave mixing in winter, the region formed a homogeneous mixed layer across different depths of seawater in Y-B, which confirms the winter 2013 remote sensing analysis. The YSWC invaded the Bohai Sea in winter 2013.

3.7. Discussion. To enable an understanding of the movement of the YSWC into the Bohai Sea, it is important to establish decision criteria by remote sensing data.

The YSWC is characterized by high temperature, high SAL, and low dissolved oxygen content. Figures 8(a), 8(b), 8(c), 9(a), 9(b), and 9(c) show that the average V , average V_{dir} , average high wind days, average SST, average SAL, and average CHL over 12 winters were 7.72 m/s, 195.4° , 25.17 days, 6.76°C , 31.37 psu, and 3.05 mg/m^3 , respectively. Table 3 shows that northerly winds dominated in the mixed zone Y-B in the winters of 2002–2013. There are no laws to follow from the average high wind days.

We found that the average V , average SST, and average SAL in winter 2013, retrieved by remote sensing data, were higher than the 12-year average. High wind days and average CHL were lower than the 12-year average (Table 4). The northerly winds dominated in winter 2013. By combining in situ, cross section observation and remote sensing data analysis, we found that the movement of the YSWC into the Bohai Sea is caused by positive anomalies of northerly wind speeds, SST, and SAL and a negative anomaly of CHL over multiyear average in the mixed zone Y-B.

According to the above criteria, the average SST in winter did not conform to the conditions in 2002, 2005, 2008, 2009,

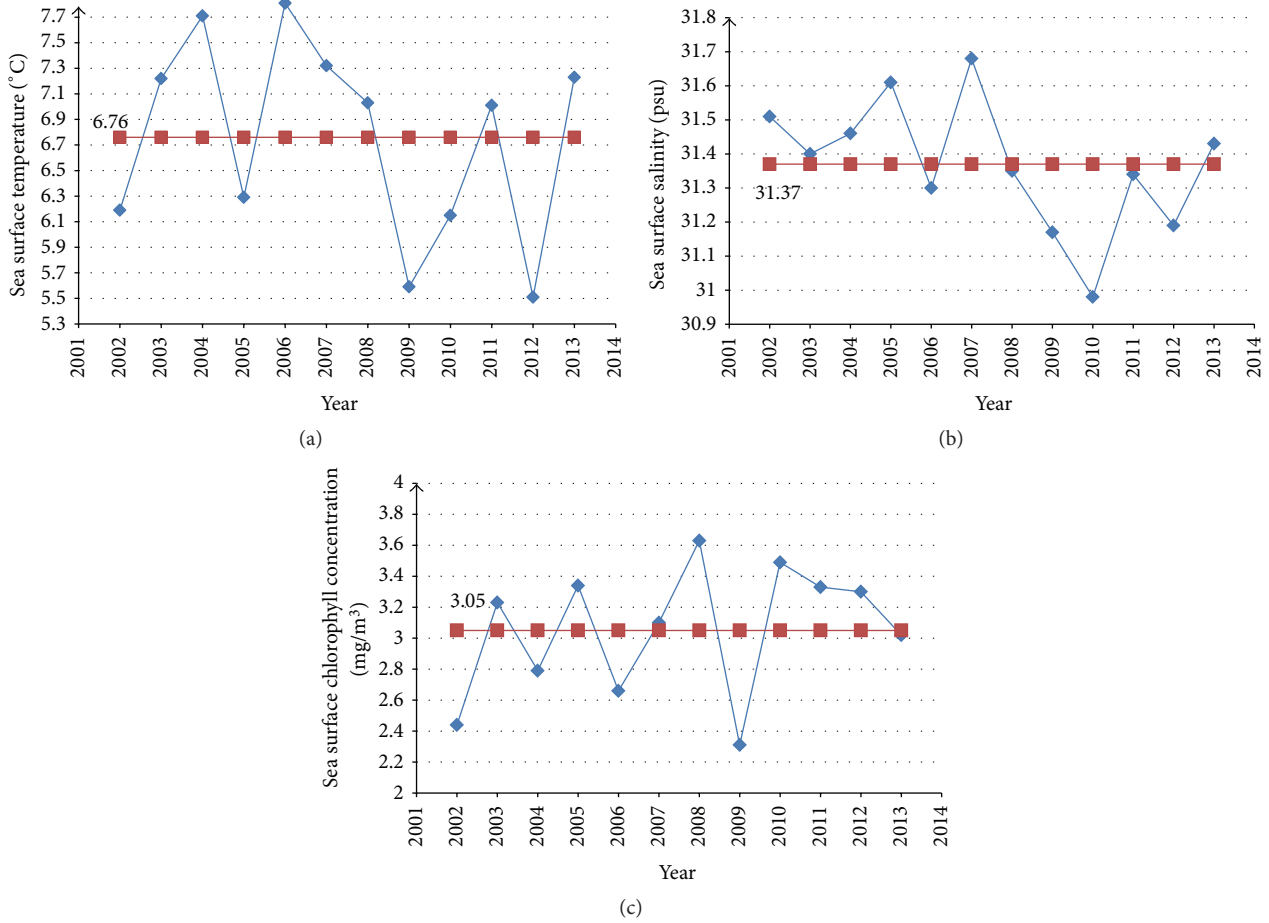


FIGURE 9: Average SST, SAL, and CHL in winter between 2002 and 2013. (a) Average SST; (b) average SAL; (c) average CHL.

TABLE 4: Analysis of characteristics of the movement of the YSWC into the Bohai Sea.

Year	SST >6.76°C	SAL >31.37 psu	CHL <3.05 mg/m ³	V >7.72 m/s	High wind days (day)
2002		✓	✓		
2003	✓	✓			
2004	✓	✓	✓	✓	32
2005		✓		✓	
2006	✓		✓		
2007	✓	✓	Nearby (3.1)	✓	19
2008		✓		✓	
2009			✓	✓	
2010				✓	
2011	✓				
2012					
2013	✓	✓	✓	✓	6

2010, and 2012. The average SAL in winter did not conform to the conditions in 2006, 2009, 2010, 2011, and 2012. The average CHL in winter did not conform to the conditions in 2003, 2005, 2008, 2010, 2011, and 2012. The average wind speed in winter did not conform to conditions in 2002, 2003, 2006, 2011, and 2012 (see Tables 3 and 4).

4. Conclusions

In winters of 2004, 2007, and 2013, when northerly winds dominated, the average wind speeds were 8.18 m/s, 8.01 m/s, and 7.83 m/s, respectively, which were all greater than the 12-year average (7.72 m/s); the SAL and SST were higher than

the 12-year average (6.76°C and 31.37 psu), while the CHL was less than the 12-year average (3.05 mg/m³, the average CHL is close to this value in winter 2007). The YSWC intrusion happened in 2007, 2004, and 2013, ranked by the intrusion strength. This conclusion was validated by the in situ and cross section observational data from winter 2013. We conclude that the YSWC intrusion into the Bohai Sea occurred when the wind speed, sea surface temperature, and SAL were above (or close to) the multiyear average and the CHL was less than (or close to) the multiyear average. This finding agrees with the model simulation results published in the literature [4, 7, 8, 17].

The study area is fully mixed in the winter owing to the wind field and ocean currents, and thus it is the ideal season to observe the intrusion of the YSWC into the Bohai Sea, by means of remote sensing; this conclusion is the same as Zhao et al. [17]. Therefore, the conclusions obtained from remote sensing data in this study are reasonable in this area, in the winter.

We also found that the YSWC intrusion into the Bohai Sea did not happen every year and was closely related to the wind field.

Future work shall increase in situ and cross section observational data from the study area and continue to verify the conclusions from remote sensing data. We will focus on the conditions and mechanism of the YSWC intrusion into the Bohai Sea during the autumn and winter and expand the study area to the north Yellow Sea and the Kuroshio area.

Conflict of Interests

The authors declare that there is no conflict of interests regarding the publication of this paper.

Acknowledgments

This project is financially supported by the “Strategic Priority Research Program” of the Chinese Academy of Sciences (no. XDA01020304) and by the National Natural Science Foundation of China (no. 41176160 and no. 4141101049). In addition, the authors thank ECMWF, EUMETSAT, KNMI, IFREMER/CERSAT, GODIVA, NOAA, Météo-France, NDBC, O&SI SAF, PMEL, and the UK Met Office for the courtesy of providing buoy, numerical, and satellite data used for daily ASCAT data production, evaluation, and validation. MODIS data were provided by NASA. Helpful advice from Dr. Xiaofeng Li NOAA is greatly appreciated.

References

- [1] B. X. Gran, “The main biographic features of shallow water in the Yellow and East China Seas,” *Journal of Oceanography of Huanghai and Bohai Seas*, vol. 3, no. 4, pp. 1–10, 1985.
- [2] H. Titanium, “Beginning of the Kuroshio,” in *Kuroshio: Its Physical Aspects*, H. Stommel and K. Yoshida, Eds., pp. 129–163, University of Tokyo Press, Tokyo, Japan, 1972.
- [3] D. Song, X. Bao, X. Wang, L. Xu, X. Lin, and D. Wu, “The inter-annual variability of the Yellow Sea warm current surface axis and its influencing factors,” *Chinese Journal of Oceanology and Limnology*, vol. 27, no. 3, pp. 607–613, 2009.
- [4] X. Song, X. Lin, and Y. Wang, “The variability of the Yellow Sea warm current axis in winter and its possible reason,” *Periodical of Ocean University of China*, vol. 39, supplement, pp. 259–266, 2009.
- [5] G. Liu, W. Sun, K. Lei, and W. Jiang, “A numerical study of circulation in the Huanghai Sea and East China Sea: numerical simulation of barotropic circulation,” *Journal of Ocean University of Qingdao*, vol. 32, no. 1, pp. 1–8, 2002.
- [6] A. C. Mask, J. J. O’Brien, and R. Preller, “Wind-driven effects on the Yellow Sea warm current,” *Journal of Geophysical Research: Oceans*, vol. 103, no. 13, Article ID 1998JC900007, pp. 30713–30729, 1998.
- [7] Y. Tang, E. Zou, and H. Lie, “On the origin and path of the Huanghai warm current during winter and early spring,” *Acta Oceanologica Sinica*, vol. 23, no. 1, pp. 1–12, 2001.
- [8] Y. Yuan, J. Su, and J. Zhao, “A single layer model of the continental shelf circulation in the East China Sea,” *Acta Oceanologica Sinica*, vol. 4, no. 1, pp. 2–11, 1982.
- [9] Y. Zhu and G. Fang, “Shelf and shallow water circulation of a three-dimensional barotropic model and its application in the Bohai Sea, Yellow sea and East China Sea,” *Acta Oceanologica Sinica*, vol. 16, no. 6, pp. 11–26, 1994.
- [10] J. B. Miu and X. Q. Liu, “The north Yellow sea and Bohai Sea in winter circulation dynamics numerical experiments,” *Acta Oceanologica Sinica*, vol. 11, no. 1, pp. 15–22, 1989.
- [11] H. Shen and H. Mao, “Basic hydrogeological characteristics of the Bohai Sea and the Yellow Sea of the western north,” *Bulletin of Marine Science*, vol. 1, no. 1, pp. 1–22, 1964.
- [12] J. Guo, X. Liu, and Q. Xie, “Characteristics of the Bohai Sea oil spill and its impact on the Bohai Sea ecosystem,” *Chinese Science Bulletin*, vol. 58, no. 19, pp. 2276–2281, 2013.
- [13] X. Li, C. Li, Q. Xu, and W. G. Pichel, “Sea surface manifestation of along-tidal-channel underwater ridges imaged by SAR,” *IEEE Transactions on Geoscience and Remote Sensing*, vol. 47, no. 8, pp. 2467–2477, 2009.
- [14] W. Shi, M. Wang, X. Li, and W. G. Pichel, “Ocean sand ridge signatures in the Bohai Sea observed by satellite ocean color and synthetic aperture radar measurements,” *Remote Sensing of Environment*, vol. 115, no. 8, pp. 1926–1934, 2011.
- [15] X. Li, W. Pichel, E. Maturi, P. Clemente-Colón, and J. Sapper, “Deriving the operational nonlinear multichannel sea surface temperature algorithm coefficients for NOAA-15 AVHRR/3,” *International Journal of Remote Sensing*, vol. 22, no. 4, pp. 699–704, 2001.
- [16] X. Li, W. Pichel, P. Clemente-Colon, V. Kransnopolsky, and J. Sapper, “Validation of coastal sea and lake surface temperature measurements derived from NOAA/AVHRR data,” *International Journal of Remote Sensing*, vol. 22, no. 7, pp. 1285–1303, 2001.
- [17] S. Zhao, F. Yu, X. Y. Diao, and G. C. Si, “The path and mechanism of the Yellow Sea warm current,” *Marine Sciences*, vol. 35, no. 11, pp. 73–80, 2011.
- [18] D. L. Yuan, W. Q. Han, and D. X. Hu, “Surface Kuroshio path in the Luzon Strait area derived from satellite remote sensing data,” *Journal of Geophysical Research*, vol. 111, no. C11, pp. 63–79, 2006.
- [19] L. R. Centurioni, P. P. Niiler, and D.-K. Lee, “Observations of inflow of Philippine sea surface water into the South China Sea through the Luzon strait,” *Journal of Physical Oceanography*, vol. 34, no. 1, pp. 113–121, 2004.

- [20] A. Farris and M. Wimbush, "Wind-induced Kuroshio intrusion into the South China Sea," *Journal of Oceanography*, vol. 52, no. 6, pp. 771–784, 1996.
- [21] J. Wang and C. S. Chern, "The warm-core eddy in the Northern South China Sea: I. Preliminary observations on the warm-core eddy," *Acta Oceanographica Taiwanica*, vol. 18, pp. 92–103, 1987.
- [22] X. Yang, X. Li, Q. Zheng, X. Gu, W. G. Pichel, and Z. Li, "Comparison of ocean-surface winds retrieved from quikscat scatterometer and radarsat-1 SAR in offshore waters of the U.S. West Coast," *IEEE Geoscience and Remote Sensing Letters*, vol. 8, no. 1, pp. 163–167, 2011.
- [23] X. Yang, X. Li, W. G. Pichel, and Z. Li, "Comparison of ocean surface winds from ENVISAT ASAR, MetOp ASCAT scatterometer, buoy measurements, and NOGAPS model," *IEEE Transactions on Geoscience and Remote Sensing*, vol. 49, no. 12, pp. 4743–4750, 2011.
- [24] S. Qing, J. Zhang, T. Cui, and Y. Bao, "Retrieval of sea surface salinity with MERIS and MODIS data in the Bohai Sea," *Remote Sensing of Environment*, vol. 136, pp. 117–125, 2013.
- [25] Y. Li, H. Chang, and Q. Wu, "Study of the characteristic and difference between sea and land wind of Bohai," *Plateau Meteorology*, vol. 32, no. 1, pp. 298–304, 2013.

Research Article

Analysis of the Global Swell and Wind Sea Energy Distribution Using WAVEWATCH III

Kaiwen Zheng,¹ Jian Sun,¹ Changlong Guan,¹ and Weizeng Shao²

¹Physical Oceanography Laboratory, Ocean University of China, 238 Songling Road, Qingdao 266100, China

²Zhejiang Ocean University, Zhoushan 316000, China

Correspondence should be addressed to Jian Sun; sunjian77@ouc.edu.cn

Received 21 August 2015; Revised 3 November 2015; Accepted 26 November 2015

Academic Editor: Xiaofeng Li

Copyright © 2016 Kaiwen Zheng et al. This is an open access article distributed under the Creative Commons Attribution License, which permits unrestricted use, distribution, and reproduction in any medium, provided the original work is properly cited.

Over the past several decades, an increasing number of studies have focused on the global view of swell and wind sea climate. However, our understanding of wind sea and swell is still incomplete as is the lack of an integrated description for all the wave components. In this paper, the European Centre for Medium-Range Weather Forecasts (ECMWF) Era-medium wind data is used to run the WAVEWATCH III model and the global wave fields in 2010 are reproduced. Using the spectra energy partition (SEP) method, two-dimensional wave spectra were separated and detailed information for the components of wind sea and swell was obtained. We found that the highest seasonal mean energy of swell and wind sea are distributed in the respective winter hemispheres. In most seas, swell carries a large part of the wave energy with W_s being higher than 50%. Compared to swell, the global distribution of wind sea energy is highly affected by the seasons. We also established a link between inverse wave age and the ratio of swell energy to total wave energy. This study aims to improve our understanding of surface wave energy composition and thus the parameterization of global-scale wind-wave interaction and air-sea momentum flux.

1. Introduction

Ocean surface gravity waves are the medium that transfers energy across the air-sea surface. The energy value is enormous. It was estimated by Wang and Huang [1] that the global wind energy input for the formation of surface waves is 60 TW. This enormous energy has different destinations. Some portion is transported into the subsurface ocean, playing a major role in regulating the general circulation of the ocean [2]. Some portion dissipates with tides, coastal surges, and others. Some portion is even transported back to the atmosphere through air-sea interaction. From results obtained during several sea expeditions, Grachev and Fairall (2001) [3] found that, in the equatorial west Pacific Ocean, upward energy and momentum transfer occurs about 10% of the time.

Surface gravity waves are classified into two categories, wind sea waves and swells. Wind seas and swells have completely different characteristic features. Wind seas are locally generated, are of short wavelength, are more chaotic,

and travel more slowly than surface wind. They require energy from wind to grow [4]. In contrast, swells are usually generated remotely by storms, are of long wavelength, have a smoother appearance, and can propagate thousands of kilometers across the ocean, without extracting energy from wind. In every area of the ocean, the sea state is mixed, with the components of both wind seas and swells composed together. The lack of knowledge of mixed wave energy composition limits the understanding of air-sea energy exchange. Since sea surface roughness is due mainly to surface gravity waves, the presence of swells and wind seas is a key factor in parameterizing the drag coefficient [5, 6]. Moreover, for the study of global-scale wind-wave interaction and air-sea momentum flux, isolating wind seas and swells from mixed waves is also meaningful.

In recent years, researchers have used various techniques and methods to study the spatial and seasonal distribution of swell and wind sea energy. Barstow (1996) [7] and Young (1999) [8] used satellite altimetry and wave models to study the distribution. This study focuses on the wave parameters

of significant wave height (SWH) and mean wave period (MWP). However, these two parameters cannot adequately describe the components of ocean waves, as even two fields with completely the same SWH and MVP may vary considerably in detail [9]. Gulev and Hasse (1998) [10] presented a global distribution of SWH, wind sea, and swell heights covering a period of more than 40 years from voluntary observing ships (VOS). Liu et al. (2002) [11] analyzed the temporal and spatial variation of northern Pacific Ocean wave fields covering a period from 1950 to 1995, using visual wave observations from meteorological observation ships. These studies used observers' subjective standard to classify wind seas and swells, and so the accuracy of the separation result is limited. On the basis of satellite data including wind speed and SWH, Chen et al. (2002) [12] used the wind-wave relation for fully developed seas given by Pierson and Moskowitz (1964) [13] to identify swells or wind seas and published a spatial and seasonal pattern of dominant swell and wind sea zones. As mentioned by Chen et al. (2002) [12], this standard can only be expected to be meaningful from a statistical point of view. Model reanalysis data can provide global wave information, with an improvement of the model's simulation ability, and more and more studies are using reanalysis data to study the global wave energy distribution. Zhang et al. (2011) [14] used wind speed, SWH, MWP, and mean wave direction (MWD) from the ECMWF Re-Analysis (ERA-40) data to analyze the global distribution of swell. Semedo et al. (2011) [9], using the 45 yr ECMWF Re-Analysis (ERA-40) data, studied the detailed global climatology of wind sea and swell properties. Although the ECMWF Re-Analysis (ERA-40) data is reliable, downloading detailed spectral information is limited.

Spectral partitioning is an effective way to isolate wind seas and swells from mixed waves [15, 16]. The SEP (spectra energy partition) method given by Hanson and Jensen (2004) [17] has proved to be valid and was transplanted into the WAVEWATCH III model in 2006 [18]. In this study, we used the year of 2010 ECMWF Era-Interim wind data to run the WAVEWATCH III model and to reproduce the global wave fields. Based on the directional spectrum, all the detailed parameters of wind seas and swells were extracted from the mixed waves. Using the result, we analyzed the spatial and seasonal distribution of wind sea and swell energy. NDBC (National Data Buoy Center) buoy data is also used in this study to examine the model output and calculate inverse wave age.

Section 2 describes the SEP method and some settings of running the WAVEWATCH III model. In this section, the examination results between model output and NDBC records are also displayed. We separated buoy directional spectra and obtained spectral parameters. We tried to establish the relationship between inverse wave age and W_s (swell energy proportion to total wave energy) and the result is discussed in Section 3. The 2010 spatial and seasonal distribution of wind sea and swell energy of global wave fields is also presented in Section 3. In Section 3, two indicators, W_s (the swell energy proportion to the total wave energy) and P_s (swell probability), are calculated. Using W_s , we found some distinctive areas with high values of wind sea or swell energy. The

conclusions and suggestions for further study are presented in Section 4.

2. Data and Methodology

2.1. The Spectra Energy Partition (SEP) Method. The SEP method originates from the digital image processing watershed algorithm [19] and was first used by Hanson and Jensen (2004) to separate a two-dimensional wave spectrum. Basically with this method, if the two-dimensional surface wave spectrum is inverted, spectral peaks become catchments and watershed lines or partition boundaries can be determined using the watershed algorithm. Then wind seas and swells are identified using a wave age criterion between the various components of its wind speed and direction. This method has proved to be highly accurate and was transformed to an efficient FORTRAN routine by Hanson et al. (2006) [18] for use in the WAVEWATCH III model.

2.2. Model Settings. The latest WAVEWATCH III official version 4.18 is used in this paper. The wind field is the 10 m wind speed from the ECWMF ERA-Interim datasets which are regularly gridded and cover from 75°N to 75°S and 180°W to 180°E, with 0.25° resolution. The time period was from 1 December 2009 to 31 December 2010 with a 6-hour interval. The water depth field was processed by the Gridgen 3.0 packet according to the NGDC (National Geophysical Data Center) ETOPO 1 data; resolution is 0.5° × 0.5°. The domain ranges from 75°N to 75°S and from 180°W to 180°E. Source terms for energy spectra in the model are set to default. The model integrates the spectrum to a cut-off frequency f_{hf} , and above this frequency a parametric tail is applied. The boundary condition is cyclical. The other option settings are 36 directions, and 24 discrete wavenumbers (0.0412~0.4060 Hz, 2.4~24.7 s). The model output is two-dimensional (2D) wave energy spectra obtained at each grid point with a time period from 1 January, 2010, to 31 December, 2010, with a 6-hour interval (365 * 4). It is important to point out that the ERA-Interim datasets are derived from reanalysis which is different from this paper's output. Reanalysis is a process by which model information and observations of many different sorts are combined in an optimal way to produce a consistent, global best estimate of the various atmospheric, wave, and oceanographic parameters. ERA-Interim uses altimeter wave height observations to constrain the wave spectra predicted by the WAM wave model. All of the ocean wave parameters including significant wave height were extracted from each dimensional spectrum. Also, there are some physical and numerical differences between the WAM and WW3 models.

2.3. Examination Results. Temporal correlation statistical analyses between model output and observed records are a commonly used comparison method to evaluate a model's simulation ability. With this method, Hanson et al. (2006) [18] used a series of nondirectional and directional wave spectra buoy data to quantify the ability of numerical wave models to reproduce measured wave components of height, period, and direction. In this paper, the SWH of total waves obtained from the WAVEWATCH III model output were compared against

the NDBC buoy data using temporal correlation analyses. The temporal resolution of the NDBC real-time spectra data is 1h, and to ensure statistical significance, only data of more than 8000 records in 2010 were used. We chose 27 buoys over a time period of 1 February 2010 to 31 December 2010 for our comparison. All the location information for these buoys is input into the model. To save space, only the results from four typical stations are presented here: Station 42003 (in the open ocean), Station 41013 (nearshore), Station 42020 (wind sea dominated for most of the year), and Station 42014 (swell dominated for most of the year). In order to quantify the comparison result, we calculated the correlation coefficient, bias, and root-mean-square (RMS) error between the model output and buoy records. It should be noted that the model's input (wind) is different from the NDBC buoy data. The 10 m wind speed used to run the model in this paper is the ERA-Interim reanalysis data, whereas the input data for the NDBC buoy is real-time wind data. Jung et al. (2004) [20] compared the analysis products from ERA-Interim with various observation-only data products and found that the differences between ERA-Interim and real-time data are generally small. So the difference between these two wind inputs could be ignored. The results are shown in Figure 1, and all the NDBC directional wave stations used in this study are listed in Table 1. We can see that the significant wave height produced by the model shows a strong temporal correlation with real-time data from NDBC observations. The absolute value of significant wave height produced by the model was also shown to correspond well to the NDBC observations.

2.4. Separate Buoy Spectrum Data. In this paper, we extracted the w3partmd.ftn file which directly performs spectral partitioning from the WAVEWATCH III source programs and separates all the buoy two-dimensional spectra. A series of wave parameters were used to calculate the inverse wave age and its corresponding W_s ($W_s = E_{swell}/E_{total}$). We intended to establish the relationship between these two parameters with the application of 27 buoys containing direction spectra records in 2010. We eventually investigated more than 20000 records using the high temporal resolution NDBC buoy data. More details are discussed in Section 3.

3. Results

3.1. Spatial and Seasonal Distribution of Wind Sea and Swell Energy. The SWH is related to the mean variance of the sea surface elevation (m_0):

$$SWH = H_s = 4.04\sqrt{m_0} = 4.04\sqrt{\iint f^0 F(f, \theta) df d\theta}, \quad (1)$$

where m_0 is the zeroth moment, f is the frequency, θ is the propagation direction, and $F(f, \theta)$ is the dimensional spectrum which describes the surface wave energy. Therefore the spatial and seasonal distribution of wave energy can be studied by SWH. The seasonal maps of SWH (total, wind sea, and swell) are shown in Figures 2 and 3. The highest seasonal mean energy of wind sea and swell is found in

TABLE 1: The NDBC directional wave stations used in this study.

Station ID	Latitude and longitude	Depth (m)
41013	33.48°N 77.58°W	57
42001	25.86°N 89.67°W	3246
42002	25.17°N 94.42°W	320
42003	25.01°N 85.91°W	3164
42007	30.09°N 88.77°W	13
42019	27.91°N 95.36°W	84
42020	26.95°N 96.70°W	88
42035	29.25°N 94.41°W	16
42036	28.51°N 84.51°W	53
42039	28.80°N 86.06°W	295
42040	29.21°N 88.20°W	238
44014	36.61°N 74.84°W	48
44025	40.25°N 73.17°W	40
45001	48.07°N 87.78°W	165
45003	45.35°N 82.84°W	137
45005	41.68°N 82.40°W	15
45007	42.68°N 87.03°W	165
45012	43.62°N 77.41°W	145
46028	35.74°N 21.89°W	1112
46029	46.12°N 24.51°W	140
46041	47.34°N 124.75°W	130
46042	36.75°N 122.42°W	1920
46069	33.65°N 120.20°W	1005
46086	32.50°N 118.00°W	1857
46087	48.49°N 124.73°W	37
46088	48.33°N 123.17°W	106
51028	0.02°S 153.87°W	4572

the extratropical areas. In the northern hemisphere, wave energy is concentrated in the northern Pacific and northern Atlantic Oceans. In the southern hemisphere, wave energy is continuously distributed along the south westerlies. In DJF (December, January, and February), the values of both wind sea and swell energy in the northern hemisphere are higher than in the southern hemisphere. By contrast in JJA (June, July, and August), the values of both wind sea and swell energy in the southern hemisphere are higher. This is dependent on the seasonal change of wind speed in the westerly sea storm areas. Because, on the one hand, wind sea is strongly aligned with the wind, strong westerly winds produce strong wind sea waves. On the other hand, although swell exists almost everywhere in the global ocean, the westerly sea storm areas in respective hemispheres are the main source areas of swell [21]. Seasonal mean wind speed in the north westerlies reaches a maximum in DJF and then gradually decreases in MAM (March, April, and May) and reaches a minimum in JJA, while, in the southern westerlies, the maximum appears in JJA and the minimum appears in DJF. So the highest seasonal mean energy of swell and wind sea is distributed in the respective winter hemispheres. The total wave energy in the Arabian Sea is different from the northern hemisphere overall trend being higher in summer

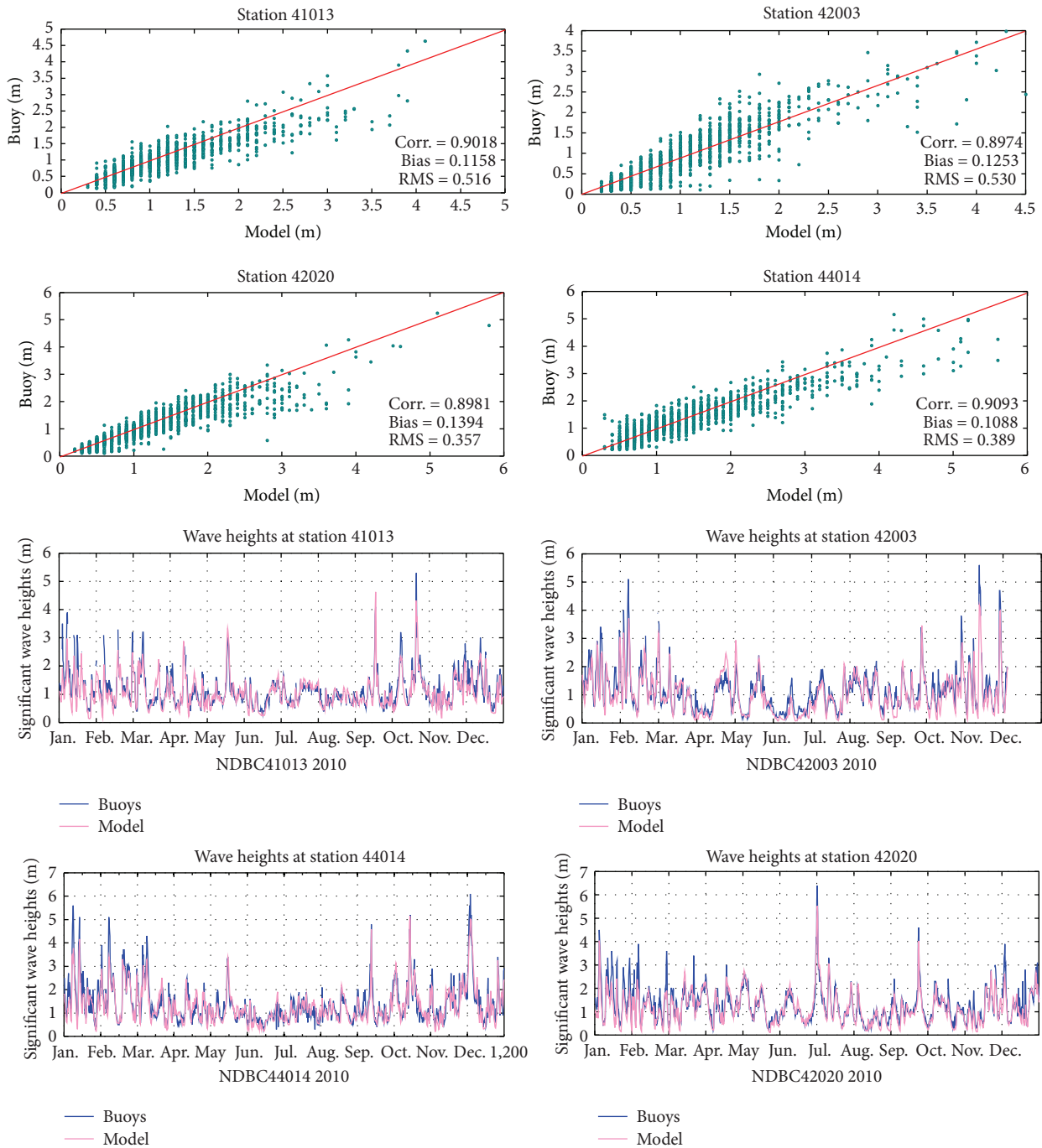


FIGURE 1: The comparison results between model output and buoy records.

than in winter. That is because strong summer monsoons produce a lot of energy to generate wind sea waves, while winter monsoons are much weaker. The maximum for both wind sea and swell energy over the whole year is found in the southern Indian Ocean areas because they are influenced by the southwesterly winds.

Table 2 shows the regional distribution of wind sea energy. When the three main oceans are compared, the Pacific Ocean accounts for the largest proportion of the whole year's total wind sea energy (53.27%), followed by

the Atlantic Ocean (30.57%) and the Indian Ocean (16.15%). Table 3 shows the regional distribution of swell energy. The Pacific Ocean accounts for the largest proportion (67.74%), followed by the Atlantic Ocean (28.9%) and the Indian Ocean (13.37%). These two proportions for wind sea energy and swell energy are similar and relate to ocean area. The area of the global ocean is $3.61 \times 10^8 \text{ km}^2$, with the Pacific accounting for 42.8%, the Atlantic Ocean for 24.1%, and the Indian Ocean for 19.6%. Compared with swell energy, the regional distribution of wind sea energy is highly affected by the

TABLE 2: The regional distribution of wind sea energy.

Regions	MAM	JJA	SON	DJF	Total
Northern Pacific Ocean	15.36%	5.67%	10.96%	23.69%	13.19%
Southern Pacific Ocean	40.91%	43.18%	43.62%	31.46%	40.08%
Northern Atlantic Ocean	7.44%	3.26%	7.77%	16.74%	8.27%
Southern Atlantic Ocean	22.45%	24.76%	22.28%	18.77%	22.30%
Indian Ocean	14.55%	23.14%	15.37%	9.34%	16.15%

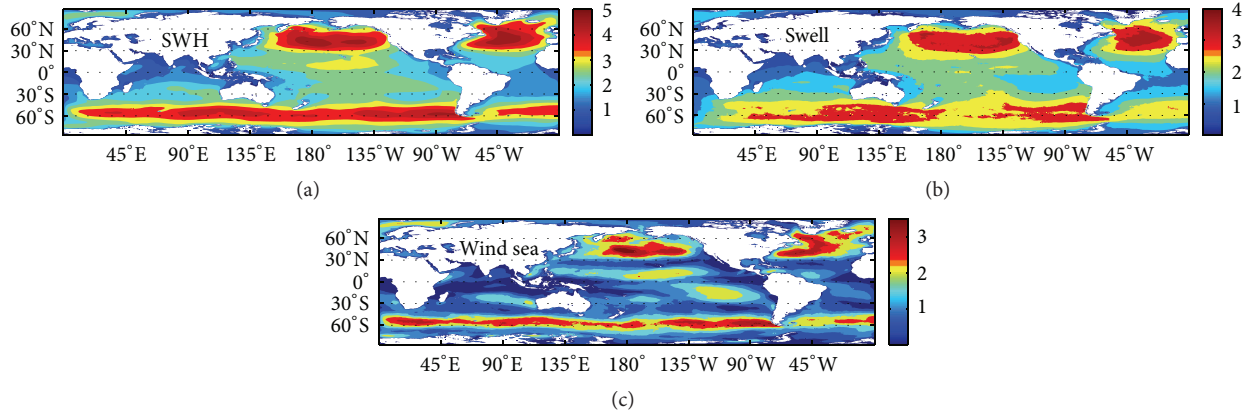


FIGURE 2: Seasonal averages for DJF of (a) SWH (m), (b) wave height of swell (m), and (c) wave height of wind sea (m).

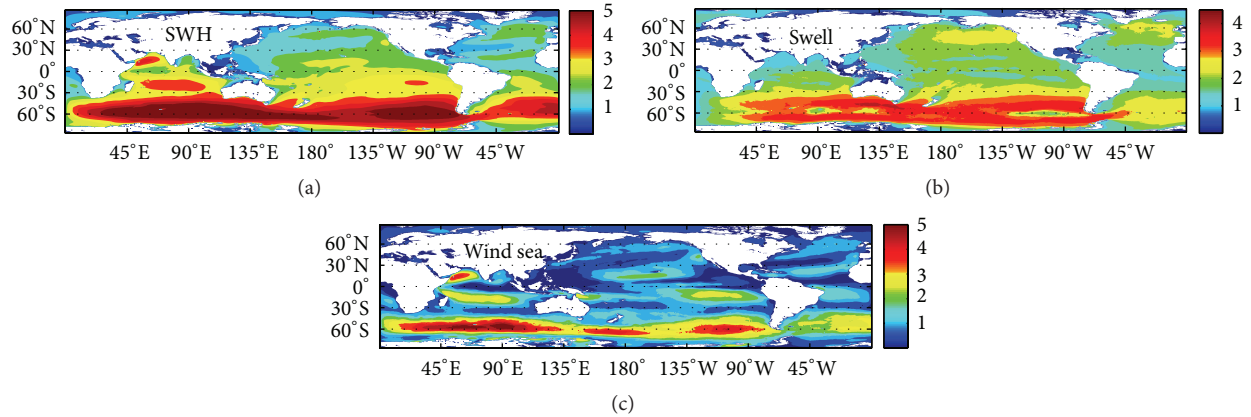


FIGURE 3: Seasonal averages for JJA of (a) SWH (m), (b) wave height of swell (m), and (c) wave height of wind sea (m).

seasons. In JJA, wind sea energy in the northern Pacific Ocean only accounts for 5.67% of all global wind sea energy, while, in DJF, it increases to 26.69%. Dramatic seasonal change also occurs in the northern Atlantic and the Indian Ocean. The Indian summer monsoon is much stronger than the winter monsoon, which means that wind sea energy accounts for 23.14% of all the global wind sea energy in JJA but this percentage reduces to 9.34% in DJF. Clearly, the regional distribution of swell energy shows much stronger seasonal stability than that of wind sea energy.

3.2. *Energy Content of the Wind Sea and Swell Fields.* The DJF and JJA global distribution of the proportion of swell energy to total wave energy ($W_s = E_{swell}/E_{total}$) is shown in Figure 4. Swell carries a large part of the wave energy

with W_s being higher than 50% in most seas. The value of W_s shows obvious zonal banded distribution. High W_s values (over 90%) show low seasonality and occur in the calm belt near the equator and subtropical high pressure belts near 30°N and 30°S. However the spatial distribution of low W_s (50%~60%) is highly affected by the seasons. In DJF, it is in the northern westerlies controlled areas and, in JJA, it is along with the southern westerly belt. W_s is lower along the eastern continental coasts (<50%) but increases to 90% in most of the western coasts which relate to wave transport and reflects swell energy reinforcement on the western continental coasts.

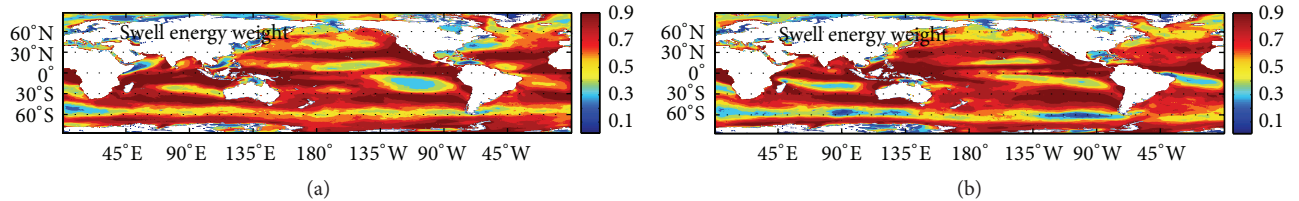
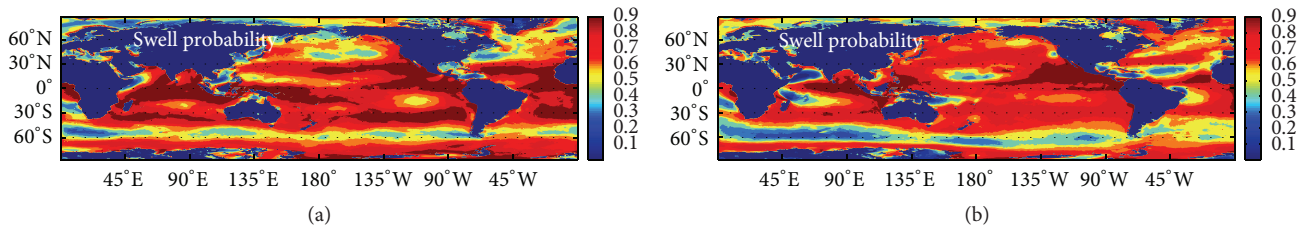
3.3. *Swell Probability.* Chen et al. (2002) [12] used the wind-wave relation for fully developed seas [22] to classify swells

TABLE 3: The regional distribution of swell energy.

Regions	MAM	JJA	SON	DJF	Total
Northern Pacific Ocean	14.74%	15.20%	13.99%	17.60%	14.86%
Southern Pacific Ocean	44.14%	40.14%	43.96%	37.21%	42.88%
Northern Atlantic Ocean	6.65%	6.18%	7.48%	18.47%	7.74%
Southern Atlantic Ocean	21.00%	24.31%	20.82%	16.99%	21.16%
Indian Ocean	13.45%	13.16%	13.75%	9.73%	13.37%

TABLE 4: Seasonal variations of the swell probability (P_s).

Regions	MAM	JJA	SON	DJF	Total
Northern Pacific Ocean	84.15%	90.84%	85.84%	79.16%	85.04%
Southern Pacific Ocean	93.50%	87.79%	86.59%	88.61%	84.01%
Northern Atlantic Ocean	87.07%	90.23%	83.41%	80.01%	88.73%
Southern Atlantic Ocean	86.65%	82.43%	80.00%	83.99%	88.19%
Indian Ocean	94.99%	85.36%	87.05%	91.66%	92.95%
Global	84.23%	84.57%	88.93%	86.91%	87.85%

FIGURE 4: Global distributions of the swell energy proportion to the total wave energy (W_s) for (a) DJF and (b) JJA.FIGURE 5: Global distributions of the swell probability (P_s) for (a) DJF and (b) JJA.

from wind waves. At a given location, they defined the sea state as swell if the SWH was greater than the value predicted by the wind-wave relation, while the sea state was considered as a growing sea in cases where the SWH was less than the predicted value. They also introduced a probability index, P_s , to quantify the frequencies of swell occurrences. In fact, the “swells” and “growing sea” mentioned by Chen et al. (2002) are a sea state of mixed seas (composed of wind sea and swell) and a sea state of pure wind sea. In this paper, we calculate the swell probability by redefining the sea state as swell if W_s is greater than 0% and the sea state as a growing sea if W_s is 0%. Results are shown in Figure 5 and the detailed values are shown in Table 4.

Compared with the results calculated by Chen et al. (2002) [12], P_s in this paper is more concrete. Obviously, swell exists almost everywhere and every moment in the global

wave fields. In particular, at low latitudes, swells exist all the time with P_s higher than 95%. Chen et al. (2002) [12] defined these areas with extremely high P_s values as “swell pools.” In fact, the location of the swell pools changes with the season. In JJA, there were two swell pools located in the tropical and subtropical areas in the northern Indian Ocean and eastern Pacific Ocean, while, in DJF, the swell pool in the Indian Ocean expanded and filled most of the northern Indian Ocean. There were also some tongue-shaped swell pools located in the low latitude areas in the eastern Pacific and Atlantic Ocean. The global P_s shows little seasonality and always remains at around 85%. When the three main oceans are compared, the Indian Ocean has the highest swell probability (92.95%), followed by the Atlantic Ocean (88.60%) and the Pacific Ocean (84.54%).

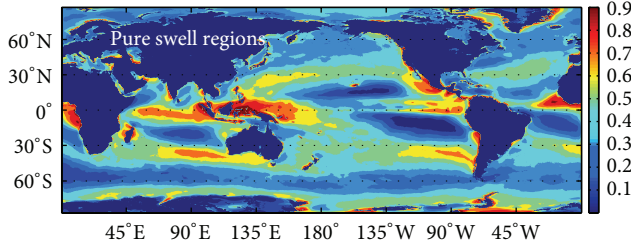


FIGURE 6: The distribution and frequency of occurrences of pure swell areas.

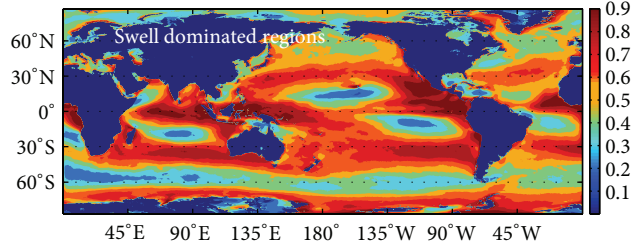


FIGURE 7: The distribution and frequency of occurrences of swell dominated areas (for 2010 whole year).

3.4. Frequency of Occurrences of High Swell (Wind Sea) Energy Areas. There are some distinctive areas in the global wave fields which are dominated by either high or low values of swell or wind sea energy. In this paper, we try to find these distinctive areas and analyze their frequency of occurrence. Firstly, we define four types of distinctive areas as pure wind sea area, wind sea dominated area, swell dominated area, and pure swell area. Since we have calculated W_s of each grid, we use a similar statistical method proposed by Hanley et al. (2010) [23] to calculate the results. A variable is defined as 1 if W_s is 0% (pure wind sea area) and 0 otherwise. Taking an average of the fraction of time ($365 * 4$) we get the frequency of occurrence of the pure wind sea area in the world ocean. The same method is used to find the other three types of distinctive areas, but W_s of them are all different. W_s of pure swell area is 100%, the swell dominated area is from 50% to 100%, and the wind sea dominated area is from 0% to 50%.

We found that pure wind sea grids were scattered implying that pure wind sea regions are very rare in the world's ocean wave fields. Some small pure wind sea areas may exist in closed or semiclosed seas but they were not found in our study. As shown in Figure 6, two pure swell regions with frequency of occurrence over 90% were found in nearby regions of Indonesia and nearby regions of Cape Verde in the east of the African continent. The annual mean significant wave height of these areas was about 1 to 1.5 meters with little wave energy. Figure 7 shows that there are four swell dominated areas with frequency of occurrence close to 100%. These are in the coast waters off Indonesia, in the northern Indian Ocean, in the equatorial waters in the west of central America and Africa, and a tongue-shaped region near the western boundary of central South America. Three of these swell dominated areas are in the same location with "swell pools" identified by Chen et al. (2002) [12]. Regions

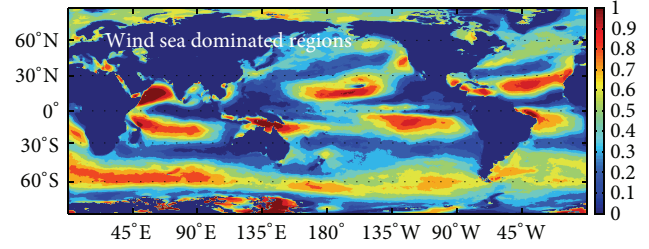


FIGURE 8: The distribution and frequency of occurrences of wind sea dominated areas (for June, July, and August).

which occur in the western coast of each continent also have a very high frequency of over 85.7% swell domination. Swell dominated areas with high frequency are far away from the swell generation regions (the westerly sea storm areas in the south Pacific, south Atlantic, and the southern Indian Ocean) but are close to the regions with low wind speed. The distribution of wind sea dominated areas showed strong seasonality and only occur in June, July, and August, so only these three months are shown in Figure 8. Wind sea dominated areas occur most frequently (over 90%) in the southern westerlies controlled regions. Three wind sea dominated areas occur frequently (over 80%) in a region near the east of Australia (affected by the southeast trade winds in the northern hemisphere), the Arabian sea (affected by the Indian summer monsoon), and mid-latitude regions in northern Pacific and northern Atlantic Ocean (affected by the southwest trade winds in the northern hemisphere). This is in agreement with Chen et al. (2002) [12] who found that wind seas are most common in the mid-latitude storm tracks.

3.5. The Link between Inverse Wave Age and W_s . The wave age concept, originally defined by Pierson and Moskowitz (1964) [13], is the traditional parameter to classify swells from wind sea waves. Hasselmann (1988) [22] used inverse wave age as an identifier to show the predominance of swell or wind sea: the wind sea components dominate when the value of the inverse wave age is larger than 0.83, and the swell prevails when the value of the inverse wave age is less than 0.15. It seems that the value of the inverse wave age in part reflects the presence of swell and wind sea. Now using the SEP method, we can separate the two-dimensional spectrum of any sea state and get all of its wave parameters. The inverse wave age and W_s can be calculated and the links between these two criteria can be established. In this paper the inverse wave age β is defined as

$$\beta = \frac{U \cos \theta}{C_p} = \frac{U \cos \theta 2\pi}{gT_p}, \quad (2)$$

where C_p and T_p are the phase velocity and period of total waves, U is 10 m wind speed, and θ is the relative angle between the wind and the waves. All of the wave parameters are calculated using the SEP method introduced in Section 2. Results are shown in Figure 9. We can draw a conclusion that the overall trend is that W_s decreases with an improvement of the inverse wave age. The wind sea energy will occur only

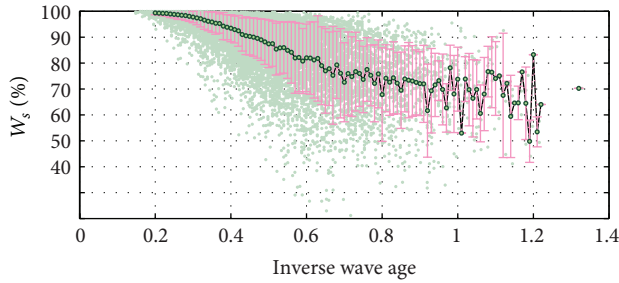


FIGURE 9: Relationship between inverse wave age and W_s .

if the value of the inverse wave age exceeds 0.18. We tried to draw a fitting curve between these two parameters but as the W_s values of most points were greater than 0.5, the curve became fluctuating when the value of the inverse wave age exceeded 0.8. The W_s value covering from 0 to 0.5 should be the subject of future research.

4. Conclusions

In this paper, we used the ECMWF Era-Interim wind data to run the WAVEWATCH III model and reproduced the global wave fields in 2010. After separating wind sea and swell from mixed waves, we studied the spatial and seasonal distribution of swell and wind sea energy. We found that the highest seasonal mean energy of swell and wind sea is distributed in the respective winter hemispheres, along the westerly storm areas. We calculated two commonly used indicators, W_s (the swell energy proportion to the total wave energy) and S_p (swell probability), of the global wave fields and found that swell energy accounts for a larger proportion of the total wave energy in most areas. The value of W_s shows obvious zonal banded distribution. High W_s values occur along the calm belt near the equator and subtropical high pressure belt near 30°N and 30°S . The W_s value is much lower along the eastern continental coasts than the western coasts which reflects the swell reinforcement on the western continental coasts. We also found some distinctive areas which are dominated by high values of swell or wind sea and calculated their frequency of occurrence. Data from 27 NDBC buoys were used to examine the model output. Based on the SEP method, we separated buoy directional spectra and obtained detailed spectral parameters to calculate the inverse wave age and W_s . We found that the value of inverse wave age improves when W_s declines and wind sea energy appears only if the value of the inverse wave age exceeds 0.18.

Despite the use of different wind datasets and different sea-swell separation criteria, there is a good agreement with previous studies. Using a wave model is the most effective way to get a sufficiently long spectral description of the wave field. This study is a meaningful attempt to isolate wind sea and swell characteristics by spectral partitioning. In further research, a longer time series of the global wave fields should be reproduced which will more reliably reflect the seasonal change of swell or wind sea energy distribution. In addition, SWAN is better than WAVEWATCH in shallow water wave

field simulation [24], so nested operation of these two models should be applied in further studies.

Conflict of Interests

The authors declare that there is no conflict of interests regarding the publication of this paper.

Acknowledgments

This study is supported by the National Natural Science Foundation of China (no. 41376010) and Zhejiang Provincial Natural Science Foundation of China under Grant no. LQ14D060001. The supports from the National Natural Science Foundation of China are appreciated (Grant nos. 41276010 and U1406401).

References

- [1] W. Wang and R. X. Huang, "Wind energy input to the surface waves," *Journal of Physical Oceanography*, vol. 34, no. 5, pp. 1276–1280, 2004.
- [2] R. X. Huang and W. Wang, "Decadal variability of wind energy input to the world ocean," *Deep-Sea Research II*, vol. 34, pp. 31–41, 2006.
- [3] A. A. Grachev and C. W. Fairall, "Upward momentum transfer in the marine boundary layer," *Journal of Physical Oceanography*, vol. 31, no. 7, pp. 1698–1711, 2001.
- [4] P. A. E. M. Janssen, "Wave-induced stress and the drag of air flow over sea waves," *Journal of Physical Oceanography*, vol. 19, no. 6, pp. 745–754, 1989.
- [5] M. A. Donelan, W. M. Drennan, and K. B. Katsaros, "The air-sea momentum flux in conditions of wind sea and swell," *Journal of Physical Oceanography*, vol. 27, no. 10, pp. 2087–2099, 1997.
- [6] C. Guan and L. Guan, "On the linear parameterization of drag coefficient over sea surface," *Journal of Physical Oceanography*, vol. 34, no. 12, pp. 2847–2851, 2004.
- [7] S. F. Barstow, *World Wave Atlas*, AVISO Newsletter no. 4, AVISO, Ramonville-Saint-Agne, France, 1996.
- [8] I. R. Young, "Seasonal variability of the global ocean wind and wave climate," *International Journal of Climatology*, vol. 19, no. 9, pp. 931–950, 1999.
- [9] A. Semedo, K. Sušelj, A. Rutgersson, and A. Sterl, "A global view on the wind sea and swell climate and variability from ERA-40," *Journal of Climate*, vol. 24, no. 5, pp. 1461–1479, 2011.
- [10] S. K. Gulev and L. Hasse, "North Atlantic wind waves and wind stress fields from voluntary observing ship data," *Journal of Physical Oceanography*, vol. 28, no. 6, pp. 1107–1130, 1998.
- [11] J. F. Liu, W. Jiang, M. G. Yu et al., "An analysis on annual variation of monthly mean sea wave fields in North Pacific Ocean," *Journal of Tropical Oceanography*, vol. 21, no. 3, pp. 364–69, 2002 (Chinese).
- [12] G. Chen, B. Chapron, R. Ezraty, and D. Vandemark, "A global view of swell and wind sea climate in the ocean by satellite altimeter and scatterometer," *Journal of Atmospheric and Oceanic Technology*, vol. 19, no. 11, pp. 1849–1859, 2002.
- [13] W. J. Pierson and L. Moskowitz, "A proposed spectral form for fully developed wind seas based on the similarity theory of S. A. Kitaigorodskii," *Journal of Geophysical Research*, vol. 69, no. 24, pp. 5181–5190, 1964.

- [14] J. Zhang, W. Wang, and C. Guan, "Analysis of the global swell distributions using ECMWF Re-analyses wind wave data," *Journal of Ocean University of China*, vol. 10, no. 4, pp. 325–330, 2011.
- [15] T. W. Gerling, "Partitioning sequences and arrays of directional wave spectra into component wave systems," *Journal of Atmospheric and Oceanic Technology*, vol. 9, no. 4, pp. 444–458, 1992.
- [16] J. L. Hanson and O. M. Phillips, "Automated analysis of ocean surface directional wave spectra," *Journal of Atmospheric and Oceanic Technology*, vol. 18, no. 2, pp. 277–293, 2001.
- [17] J. L. Hanson and R. E. Jensen, "Wave system diagnostics for numerical wave models," in *Proceedings of the 8th International Workshop on Wave Hindcasting and Forecasting*, Technical Report no. 29, WMO/TD-no. 1319, Joint WMO/IOC Technical Commission for Oceanography and Marine Meteorology, Oahu, Hawaii, USA, November 2004.
- [18] J. L. Hanson, B. Tracy, H. Tolman, and D. Scott, "Pacific hindcast performance evaluation of three numerical wave models," in *Proceedings of the 9th International Workshop on Wave Hindcasting and Forecasting*, Victoria, Canada, September 2006.
- [19] L. Vincent and P. Soille, "Watersheds in digital spaces: an efficient algorithm based on immersion simulations," *IEEE Transactions on Pattern Analysis and Machine Intelligence*, vol. 13, no. 6, pp. 583–598, 1991.
- [20] T. Jung, E. Klinker, and S. M. Uppala, "Reanalysis and reforecast of three major European storms of the twentieth century using the ECMWF forecasting system. Part I. Analyses and deterministic forecasts," *Meteorological Applications*, vol. 11, no. 4, pp. 343–361, 2004.
- [21] J.-H. G. M. Alves, "Numerical modeling of ocean swell contributions to the global wind-wave climate," *Ocean Modelling*, vol. 11, no. 1-2, pp. 98–122, 2006.
- [22] S. Hasselmann, "The WAM model—a third generation ocean wave prediction model," *Journal of Physical Oceanography*, vol. 18, no. 12, pp. 1775–1810, 1988.
- [23] K. E. Hanley, S. E. Belcher, and P. P. Sullivan, "A global climatology of wind-wave interaction," *Journal of Physical Oceanography*, vol. 40, no. 6, pp. 1263–1282, 2010.
- [24] N. Booij, R. C. Ris, and L. H. Holthuijsen, "A third-generation wave model for coastal regions: I. Model description and validation," *Journal of Geophysical Research C: Oceans*, vol. 104, no. 4, pp. 7649–7666, 1999.

Research Article

Impacts of Model Bias on the Climate Change Signal and Effects of Weighted Ensembles of Regional Climate Model Simulations: A Case Study over Southern Québec, Canada

Hyung-Il Eum,¹ Philippe Gachon,² and René Laprise²

¹APEC Climate Center (APCC), 12 Centum 7-ro, Haeundae-gu, Busan 612-020, Republic of Korea

²Étude et Simulation du Climat à l'Échelle Régionale (ESCCER), University of Québec at Montreal, 201 Président Kennedy Avenue, Montréal, QC, Canada H2X 3Y7

Correspondence should be addressed to Hyung-Il Eum; hieum01@apcc21.org

Received 19 August 2015; Revised 27 October 2015; Accepted 17 November 2015

Academic Editor: Xiaofeng Li

Copyright © 2016 Hyung-Il Eum et al. This is an open access article distributed under the Creative Commons Attribution License, which permits unrestricted use, distribution, and reproduction in any medium, provided the original work is properly cited.

This study examined the impact of model biases on climate change signals for daily precipitation and for minimum and maximum temperatures. Through the use of multiple climate scenarios from 12 regional climate model simulations, the ensemble mean, and three synthetic simulations generated by a weighting procedure, we investigated intermodel seasonal climate change signals between current and future periods, for both median and extreme precipitation/temperature values. A significant dependence of seasonal climate change signals on the model biases over southern Québec in Canada was detected for temperatures, but not for precipitation. This suggests that the regional temperature change signal is affected by local processes. Seasonally, model bias affects future mean and extreme values in winter and summer. In addition, potentially large increases in future extremes of temperature and precipitation values were projected. For three synthetic scenarios, systematically less bias and a narrow range of mean change for all variables were projected compared to those of climate model simulations. In addition, synthetic scenarios were found to better capture the spatial variability of extreme cold temperatures than the ensemble mean scenario. These results indicate that the synthetic scenarios have greater potential to reduce the uncertainty of future climate projections and capture the spatial variability of extreme climate events.

1. Introduction

Climate change has significant effects on the natural (e.g., hydrologic systems) and social components (e.g., urban development) of regional systems [1, 2]. Changes in extreme weather and climate events have particularly significant impacts and are among the most serious challenges for all human societies. In recent decades, an unprecedented number of extreme climate events have occurred, such as unusually hot days and nights, fewer unusually cold days and nights, and fewer frost days [3], while heavy rainfall has also become more frequent and intense [4]. In addition, more extreme and frequent floods and droughts are anticipated in the future [5, 6]. All of these factors exert a major influence at regional scales, potentially increasing the risk of disaster for both human and environmental systems. Therefore or, feasible

plausible regional climate scenarios are necessary to efficiently adapt to climate change and to mitigate the risk of disaster, especially when extreme weather and high impact climatic events are concerned. Confidence in projecting changes in the direction and magnitude of climate extremes depends on many factors, for example, the type of extreme, the region, and season, the amount and quality of observational data, the understanding of underlying processes, and the reliability of model simulations, especially at the regional scale [6].

Recently, numerous regional climate models (RCMs) have provided regionalized climate information to assess the hydrologic and environmental as well as the social and economic impacts of climate change (see the recent CORDEX initiative organized by the World Climate Research Program, <http://www.cordex.org/>). These RCMs are nested in atmosphere-ocean global climate models (AOGCMs) or

global-scale reanalysis products. Because RCMs incorporate higher-resolution surface forcings (i.e., topography, land-sea contrast, land surface conditions, and other parameters), a large range of climate responses has been detected in previous studies, depending on the combination of RCMs/AOGCMs [7–9]. In particular, the reported temperature responses of the RCMs during winter are extremely variable due to snow-albedo feedbacks that are quasiabsent in AOGCMs as a result of their coarse horizontal resolution [10, 11]. The high and variable spatial resolutions of RCMs may therefore result in higher spatial and temporal variability in climate responses compared with those from AOGCMs, which also means potentially higher uncertainty in climate simulations derived from both RCMs and AOGCMs when changes in regional surface conditions are considered [12, 13].

An accurate assessment of confidence in future regional scale climate models from all available RCMs is essential to identify sources of uncertainty and thereby prevent erroneous analysis in climate change impact studies at regional scales [14, 15]. Therefore, it is crucial to systematically assess the dependence of projected regional climate change signals on model bias at regional scales [16]. The presence of this dependence may be an important issue when applying an ensemble scheme to consider the uncertainty in combined multimodel simulations with weighting procedures, as the main assumption behind an ensemble scheme is that the climate responses (e.g., model bias) in a model during the past provide robust guidance on the likelihood of future responses.

In addition, we need to investigate a range of climate change signals to estimate the variability of multi-RCM/AOGCM projections. The results of several carefully controlled comparison studies have been reported by the European Prediction of Regional Scenarios and Uncertainties for Defining European Climate Change Risks and Effects (PRUDENCE) [17], the ENSEMBLES project over the whole European region [8], and the recent North American Regional Climate Change Assessment Program (NARCCAP) [18]. These studies evaluated the accuracy of RCMs by comparing regional climate simulations with historical observed data and estimated the uncertainty of projected climate scenarios over all study regions (i.e., over Europe and the USA). In these studies, changes in mean values between the current and future periods were investigated to assess the uncertainty of future climate conditions as an indigenous response of RCM/AOGCM combinations to emission scenarios. To extend these studies to southern Québec (Canada), we investigate a range of spatial and temporal changes in meteorological variables (i.e., daily precipitation and minimum and maximum temperatures (T_{\min} and T_{\max})) under one Special Report on Emissions Scenarios (SRES) emission scenario (A2). We compare climate change signals estimated by differences in both extreme (e.g., 90th percentile of daily precipitation, and the 10th and 90th percentiles of daily T_{\min} and T_{\max}) and median (50th percentile) values between the reference (1971–1995) and future (2041–2065) RCM/AOGCM simulations.

A model-performance-based weighting scheme was successfully applied, and it demonstrated that model weighting might improve the average skill of climate projections [2, 19–21]. Eum et al. [2, 22] applied a comprehensive weighting

method that takes into account the skill of both RCMs and AOGCMs based on RCM/AOGCM performance. These studies formulated a cumulative density function (CDF) using a comprehensive weighting method based on the performance of RCM/AOGCM and RCM/Reanalysis combinations. Using a Monte Carlo simulation (MCS) technique, synthetic future scenarios were generated based on the CDFs and were compared with twelve RCM/AOGCM simulations and the ensemble mean to consider a range of climate change signals for each meteorological variable. More details are provided in [2]. As in the previous studies, we use twelve RCMs, the ensemble mean, and five synthetic future scenarios to investigate the intermodel correlation of changes in bias and the range of climate change signals. The focus of this study is on the following three factors: (1) the dependence of projected climate change signals on model bias at the regional scale; (2) a comparison of the performance of RCM/AOGCM simulations and their synthetic scenarios; and (3) a comparison of seasonal climate change signals for each RCM/AOGCM and synthetic scenario, considering the median and extreme values.

The next section of the paper provides a description of the RCM/AOGCM simulation and scenarios generated based on weighting factors. The study area and reference-gridded observed datasets are presented in the subsequent section. The results section presents an intermodel correlation of the bias and climate change signal with the range of extreme and median values of climate change signals for each season and subregion within the study basin. In the summary and discussion section, we discuss our results and offer a general conclusion regarding the climate signals developed over the study area.

2. RCM/AOGCM Simulations and Synthetic Scenarios

This study used twelve RCM/AOGCM combinations released from NARCCAP (<http://www.narccap.ucar.edu>) and from the Data Access and Integration (DAI) project of Environment Canada (recently renamed the Canadian Climate Data and Scenarios portal, ccds-dscc.ec.gc.ca/). Table 1 presents the different versions of the Canadian Regional Climate Model (CRCM) [23, 24] according to initialization and domains at 45 km horizontal resolution provided by the Climate Scenarios and Services Group at Ouranos. CRCM4.1.1 has a smaller domain over Quebec (QC domain, 112×88 grid points) than other CRCMs, which incorporate a large domain covering North America (AMNO, 201×193 grid points).

NARCCAP released multiple high-resolution regional climate scenarios driven by multiple AOGCMs forced with the A2 emission scenario (e.g., [25]). In this study, we used multiple RCMs such as the CRCM4.2.0 and the Experimental Climate Prediction Version 2 (ECP2), MM5-PSU/NCAR mesoscale model (MM5I), Weather Research and Forecasting Models by US groups (WRF), Regional Climate Model version 3 (RegCM3), and Hadley Regional Model 3 (HRM3) by European groups. ARPEGE (Action de Recherche Petite Echelle Grande Echelle) was developed by Meteo France to

TABLE 1: Description of RCM/AOGCM combinations used in this study.

Number	RCM	Driven by	Time window	Modeling center/source
1	CRCM4.2.3 (aet)	CGCM3 4th member	1963–2001	Ouranos/University of Quebec at Montreal (UQAM)/Environment Canada
2	CRCM4.2.3 (aev)	CGCM3 5th member	2041–2070	
3	CRCM4.1.1 (QC domain)	CGCM3 4th member	1968–2000 2041–2070	
4	CRCM4.2.0	CGCM3 4th member	1968–2000 2041–2070	
5	RCM3		1968–2000 2041–2065	
6	CRCM4.2.0		1968–1998 2041–2070	
7	MM5I	CCSM	1968–1999 2041–2070	NARCCAP (http://www.narccap.ucar.edu/)
8	WRFG		1968–1999 2041–2070	
9	RCM3	GFDL	1968–2000 2041–2070	
10	ECP2		1968–2001 2041–2070	
11	HRM3	HadCM3	1968–2000 2041–2070	
12	ARPEGE	ARPEGE	1961–2001 2041–2070	Ouranos/Météo-France

simulate the European climate [26], and the Climate Scenarios and Services Group at Ouranos produced a regional climate simulation over North America.

Five driving AOGCMs were used in this study: (1) the NCAR Community Climate System Model: CCSM [27]; (2) the third Canadian Global Climate Model: CGCM3 [28]; (3) the Geophysical Fluid Dynamics Laboratory: GFDL [29]; (4) the Hadley Centre Coupled Model, version 3: HadCM3 [30]; and (5) the ARPEGE global model version 3 [31]. Note that not all RCMs incorporated the five driving AOGCM simulations due to the limited RCM/AOGCM data pool. For example, HRM3 is driven only by HadCM3, and GFDL is used in RCM3 and ECP2 simulations (see Table 1). However, this study includes an identical CRCM version (CRCM4.2.0) with different driving AOGCM conditions (CGCM3 and CCSM), which enabled us to assess the effects of different boundary forcings according to the variability in RCM/AOGCM simulations.

Eum et al. [2] suggested the following comprehensive weighting factor that comprises the RCM and AOGCM weighting factors and a multiplication factor:

$$W_k = w_i^{\text{RCM}} \times w_j^{\text{AOGCM}} \quad w = \prod_m f_m^{n_m}, \quad (1)$$

where W_k is the comprehensive weighting factor of the k th RCM/AOGCM combination; w_i^{RCM} is a weighting factor for the i th RCM calculated from the performance of RCM/Reanalysis data; w_j^{AOGCM} is a weighting factor of the j th AOGCM estimated from the average performance of RCM simulations driven by the same AOGCM; and w is a combined weighting

factor [8] consisting of a performance metric $m(f_m)$ and an exponent n_m . This study evaluated five performance metrics: relative absolute mean error, annual variability, spatial pattern, extreme events, and multidecadal trend [2]. If reanalysis data was used instead of an AOGCM in the comprehensive weighting factor, we assumed that w_j^{AOGCM} would be 1.0 because the reanalysis data forced by observed data through state-of-the-art assimilation techniques, for example, National Centers for Environmental Prediction/National Center for Atmospheric Research (NCEP/NCAR) [32] and European Centre for Medium-Range Weather Forecasts (ECMWF-ERA40) [33], can be considered as near-best-fit models, although some biases still exist. The exponent n_m represents the relative importance of the performance metrics and may significantly affect the performance of the weighting factor. Eum et al. [2] used the differential evolution (DE) optimization scheme [34] to determine an optimal relative importance and then compared it with the equal relative importance considering the skills of RCMs and AOGCMs, which were referred to as DE (RCM/AOGCM) and EQ (RCM/AOGCM), respectively. More details on the weighting factor and its use can be found in [2].

Using the CDFs formulated with DE (RCM/AOGCM) and EQ (RCM/AOGCM) and simple equal probability (SEP) that assigned equal weighting to all RCMs, we generated synthetic scenarios with the MCS technique over the common time windows given in Table 1: hindcast (25 years from 1971 to 1995) and future (25 years from 2041 to 2065). In addition, we used an ensemble mean scenario that simply averaged the simulations from all RCM/AOGCMs. Therefore, this study

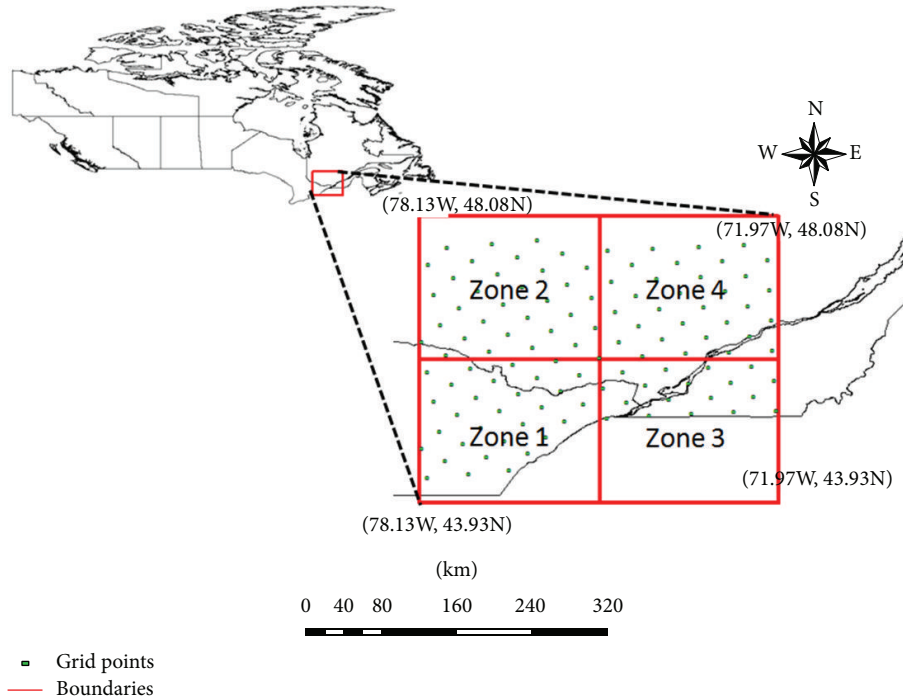


FIGURE 1: Study area over Québec and Ontario Provinces, Canada.

investigated the climate signals from 16 simulations (i.e., 12 RCM/AOGCM simulations and four synthetic scenarios).

3. Application

3.1. Study Area. As a follow-up case study of previous climate change studies [2, 22], we selected the Southern Quebec and Ontario regions in Canada bounded by 43.93–48.08°N and 71.97–78.13°W (Figure 1). This area, which is covered by 113 grid points on the CRCM 45-km polar stereographic (PS) grid, was divided into four subzones to investigate the spatial variability of model performance, as significant differences across these subzones were obtained from the RCM runs for both the current and the future simulated periods [2].

The reference-gridded observed datasets of [35] were used to calculate model bias at each grid point. The gridded data sets provided a daily time series of precipitation and temperature (T_{\min} and T_{\max}) derived from a Canada-wide spatial model (~10-km gridded climate dataset) using data from Environment Canada's 7,514 stations from 1961 to 2003; the number of stations active for a given year ranged from 2,000 to 3,000 for precipitation and from 1,500 to 2,200 for temperature. All gridded climate data (all RCMs given in Table 1, as well as the gridded observed data of [35]) were interpolated to the CRCM 45 km PS grid to facilitate comparison of model performances (see [22]).

3.2. Bias and Climate Change Signal. We calculated the bias and climate change signals for all climate scenarios at each grid point and then aggregated them over the four subregions to analyze the relation between bias and climate change signals for each subregion. Bias was calculated from

the differences between simulated and gridded observed data [35], and the climate change signal was calculated by the difference between the mean and extreme values for the future (2041–2065) and the reference (1971–1995) periods from RCM/AOGCMs or synthetic simulations. The variables considered were daily precipitation, T_{\min} , and T_{\max} , which are key input data for environmental and hydrologic modeling. The analysis was conducted on the median and extremes, that is, the 90th percentile of daily precipitation, the 10th and 90th percentiles of daily T_{\min} and T_{\max} , and the 50th percentiles of all variables.

4. Results and Discussion

4.1. Correlation between Bias and the Climate Change Signal. Figures 2 and 3 show spatial maps of the bias and the climate change signal for the three variables (mean values averaged over the 12 RCM/AOGCM simulations) during summer and winter, respectively. These maps were initially used to examine whether a regional pattern of bias versus signal characteristics existed within the study area. For precipitation, there was a considerable negative relationship between bias and climate change signal in the study area. Grid points where high biases were identified, in particular over the southeast area, projected a low climate change signal in precipitation. In summer, for both T_{\min} and T_{\max} , a general cold bias was apparent over the whole region and was more pronounced in the south along the St. Lawrence valley and in the east. These large biases generally corresponded to the location of small climate change signals, with larger signals found in the southwestern region. These results may have been induced by

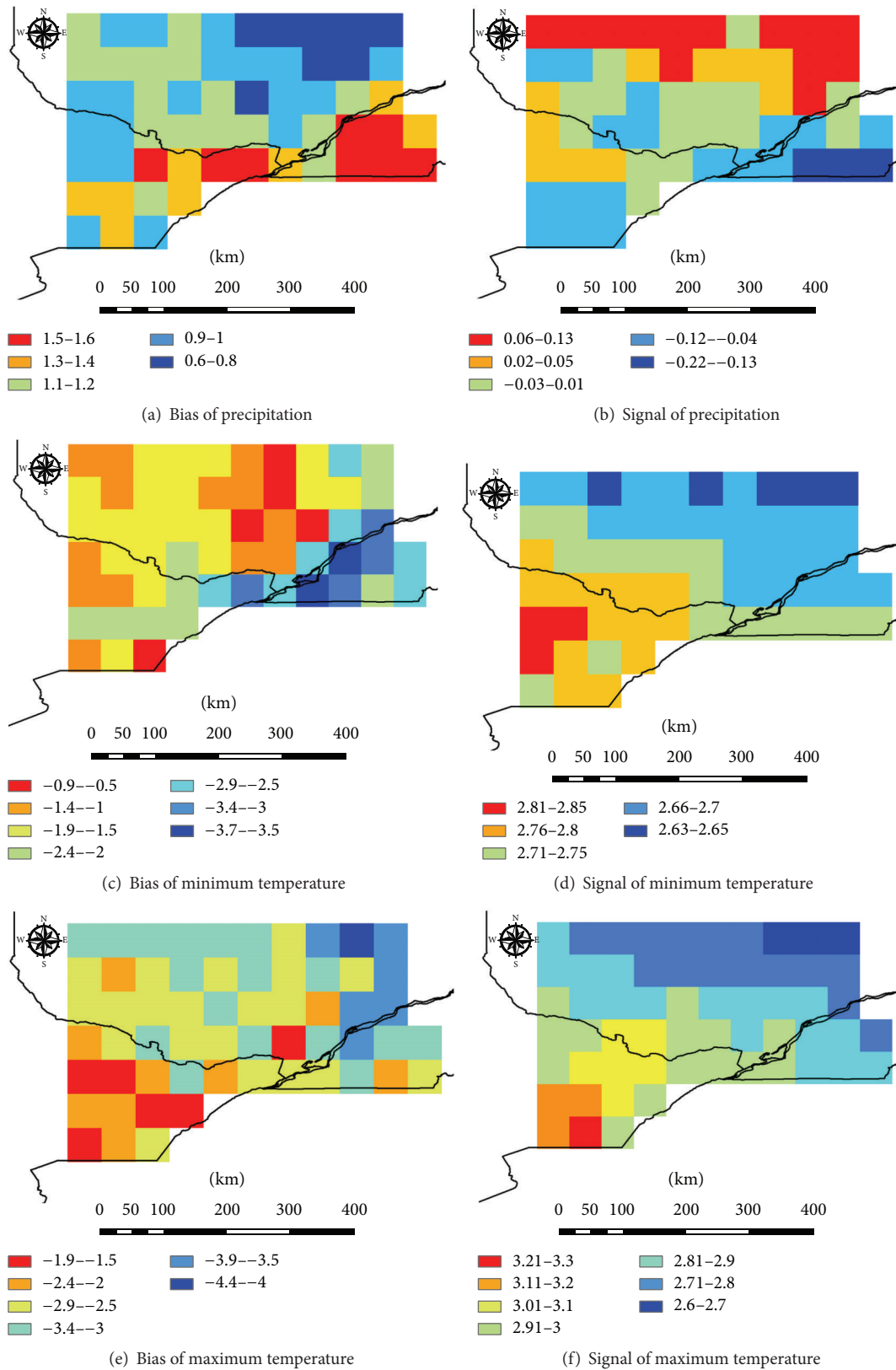


FIGURE 2: Spatial map of intermodel biases and climate change signals averaged for all RCM/AOGCMs' simulations during summer season for precipitation (in mm/d) and minimum and maximum temperatures (in °C).

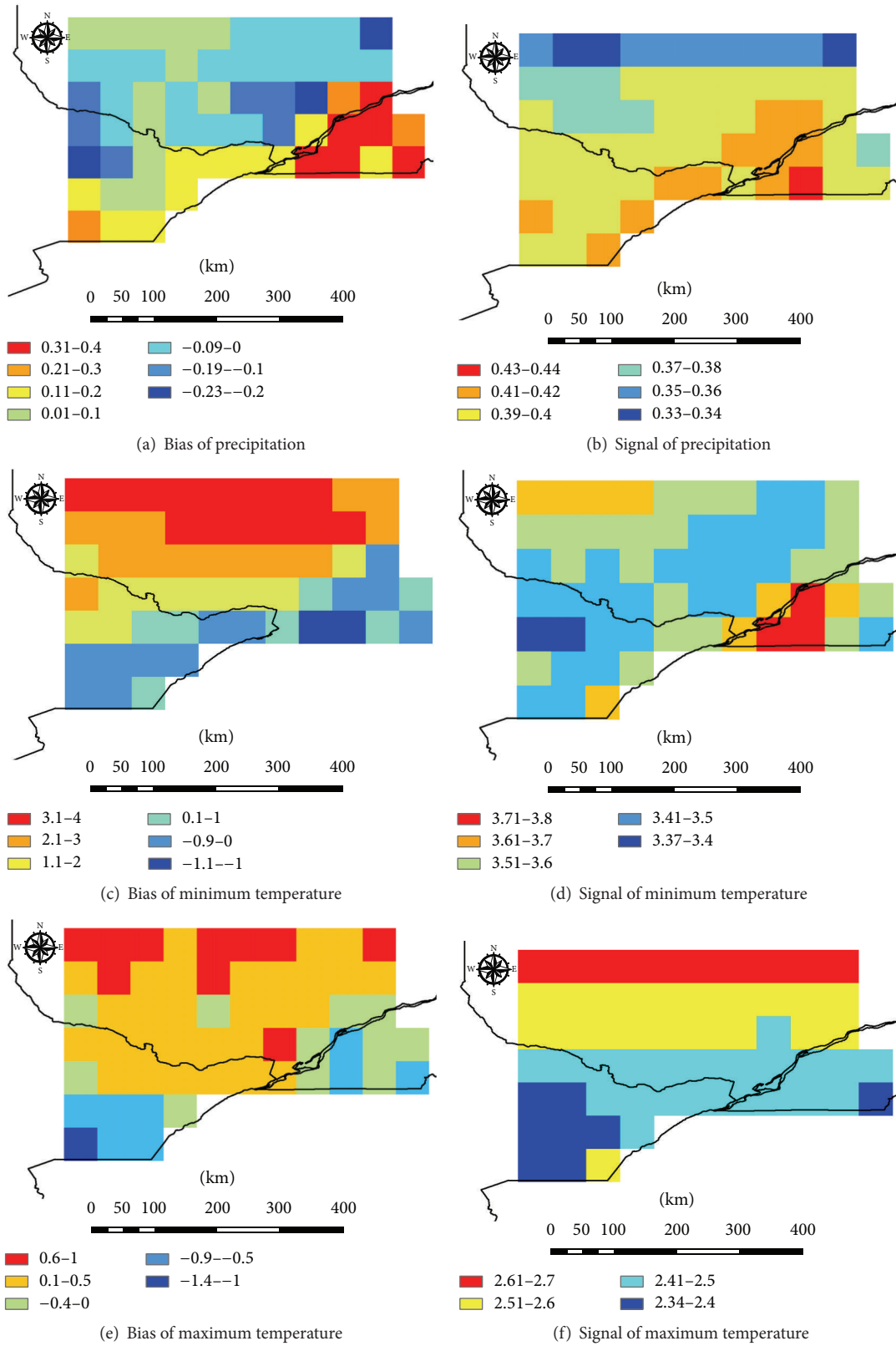


FIGURE 3: Same as Figure 2 but for the winter season.

TABLE 2: Intermodel correlation between simulated change and bias for seasonal mean precipitation and temperatures. Precipitation (PPT), T_{\min} , and T_{\max} represent precipitation, minimum temperature, and maximum temperature, respectively. Bold font in correlation coefficient represents the case in which the intermodel correlation is significant at the 90% confidence level (absolute values above |0.497|). Each subregion or zone (from 1 to 4) represents each subarea (SW, NW, SE, and NE, resp.) defined in Figure 1.

Zone	Season	Mean change versus bias			90th percentile change versus Bias			10th percentile change versus bias	
		PPT (mm/d)	T_{\min} ($^{\circ}$ C)	T_{\max} ($^{\circ}$ C)	PPT (mm/d)	T_{\min} ($^{\circ}$ C)	T_{\max} ($^{\circ}$ C)	T_{\min} ($^{\circ}$ C)	T_{\max} ($^{\circ}$ C)
1	Spring	0.55	-0.53	0.42	0.36	-0.01	-0.36	-0.62	-0.64
	Summer	-0.30	-0.87	-0.61	-0.09	-0.84	-0.76	-0.84	-0.80
	Autumn	0.18	-0.56	-0.18	-0.23	-0.33	-0.78	-0.76	-0.47
	Winter	-0.17	-0.86	-0.82	-0.10	-0.90	-0.33	-0.44	-0.57
2	Spring	0.64	-0.68	0.43	0.79	-0.08	-0.42	-0.61	-0.64
	Summer	-0.38	-0.88	-0.76	-0.18	-0.74	-0.71	-0.78	-0.87
	Autumn	-0.26	-0.67	-0.24	-0.38	-0.25	-0.51	-0.59	-0.54
	Winter	-0.35	-0.87	-0.85	-0.48	-0.91	-0.28	-0.46	-0.60
3	Spring	0.15	-0.65	-0.41	-0.32	-0.06	-0.33	-0.57	-0.47
	Summer	-0.50	-0.35	-0.19	-0.27	-0.75	-0.79	-0.80	-0.87
	Autumn	0.19	0.13	0.27	-0.11	-0.33	-0.71	-0.67	-0.54
	Winter	-0.21	-0.85	-0.83	-0.39	-0.89	-0.30	-0.45	-0.59
4	Spring	0.55	-0.72	0.28	0.48	-0.01	-0.38	-0.59	-0.51
	Summer	-0.37	-0.87	-0.76	-0.01	-0.77	-0.70	-0.76	-0.88
	Autumn	0.17	-0.58	-0.24	-0.04	-0.26	-0.46	-0.55	-0.49
	Winter	-0.33	-0.87	-0.87	-0.46	-0.91	-0.26	-0.44	-0.60

the relatively coarse-scale resolution, which may have caused some systematic errors over complex topography and heterogeneous surface conditions, especially in the south near the St. Lawrence valley. There may have been low level land and a river in a grid, but the RCM simulated climate conditions in the grid as either land or a river (also with a smoother topographic effect in the RCM compared to the real physiographic features), which may affect both biases and climate signals for all variables in the south near the St. Lawrence valley. Recent results over this area [36] and over Europe (e.g., over the UK in [37]) have revealed that the added value from higher-resolution models when modeling very fine local-mesoscale climate patterns over the inner domain, including the diurnal variations in temperature and winds and the effect of wind channeling (which affects the temperature advection), is crucial to decreasing the systematic biases in local climatology. In winter, warm biases for both T_{\min} and T_{\max} were found in the north, and cold biases were found in the southwest and southeast in summer. In such cases, the signals were slightly higher/lower in the north/south where warm/cold biases were apparent, along with a clear warming trend in T_{\min} (but not T_{\max}), which was not apparent in summer.

In addition to the intermodel averaged bias and climate change signals of mean values across the study area, bias defined by the spatially averaged differences between simulated and gridded observed data for each subregion was calculated for each RCM/AOGCM combination with regard to both the mean and the extreme of daily T_{\min} , T_{\max} , and precipitation. In this way, the corresponding mean spatial climate change signals were calculated. Using all of the RCM/AOGCM simulations, we calculated the intermodel Pearson's

correlation between the bias and climate change signals for each season and subzone (as presented in Figure 1). Table 2 shows the intermodel correlation between the simulated climate signal and bias for precipitation and temperature fields, with the bold font representing the cases where the intermodel correlation was significant at the 90% confidence level (i.e., above |0.497|). A significant correlation indicates that the model bias is linearly linked to the projected climate change signal of mean and extreme values for both a season and subregion. Note that the bias and the signal were calculated based on spatially averaged values over each subregion for each of the 12 AOGCM/AOGCM simulations, which provided 12 pairs of bias and signal values for the calculation of intermodel correlation.

For precipitation, only 4 of the 16 cases had a significant intermodel correlation between the mean change and bias in spring. In addition, only one case had a significant intermodel correlation at the 90th percentile in spring in subzone 2, indicating that the linear dependency of the climate change signal on the model bias for both mean and extreme values of precipitation was not significant, except in spring. These results suggest that the precipitation projections might be mainly affected by emission scenarios or large-scale boundary forcings from AOGCMs and by local effects such as topography and local convection and their systematic influences on spatial biases over most of the study area in spring. In other seasons, biases and forcing factors were randomly distributed, with no clear link between bias features and climate signals. This means that the large-scale flow from AOGCMs dominated the regional climate responses during most of the year, particularly over the Great Lakes/St.

Lawrence valley. This is also in line with a recent study over the same area [38], which showed that the largest source of uncertainty in summer or winter simulated (RCM) precipitation originated from the AOGCM selection, especially for heavy rainfall and along the St. Lawrence valley, which systematically exhibited a higher uncertainty value.

For T_{\min} , there were prominent negative correlations between the mean change and bias in 14 cases (87.5%), implying that the RCMs with a higher positive bias (overestimation of observed T_{\min} values) were likely to project a lower mean change and vice versa. Remarkably, the correlations between large extreme changes (i.e., 90th percentile of T_{\min}) and bias were mainly significant only for summer and winter in all subregions, whereas in most cases, the correlations of cold extreme changes (10th percentile of T_{\min}) with bias were significant except in winter. Such results indicate that the extreme minimum temperature (biases and climate change signals) for all seasons may be significantly and systematically affected by local or regional physical processes (e.g., topography and surface conditions), while depending mainly on the RCM/AOGCM sensitivity over the model domain rather than model bias for spring and autumn at the warm extreme (90th percentile) and for winter at the cold extreme (10th percentile). This also reflects the strong or systematic influences of surface conditions through spring to autumn both on the mean values of T_{\min} and on the cold extremes of T_{\min} from the proper diabatic fluxes, especially during thaw and frost periods in spring and autumn, and during the storage of heat within the soil in summer.

For T_{\max} , the correlation between the mean change and model bias was also significant only in summer and winter, whereas the correlation between the 90th percentile T_{\max} change and bias was significant mainly in summer and autumn (except for subzone 4). The relationship between bias and the climate change signal of the 90th percentile T_{\max} during winter was not significant because heat waves are a large-scale forcing derived from large-scale patterns such as the El Niño Southern Oscillation (ENSO), Pacific Decadal Oscillation (PDO), and blocking events over the eastern Pacific, among other climate phenomena (e.g., [39]). In winter, the warm extreme of the T_{\max} climate change signal was mainly affected by the boundary conditions of the AOGCMs, which provided large-scale patterns rather than systematic biases in RCMs. However, in 87.5% of all cases, there were significant negative correlations between the 10th percentile change and bias, suggesting a quasisystematic link between climate change signals and bias for the cold extreme of T_{\max} . In summary, during summer, climate change signals significantly depended on the model bias in all subzones for both mean seasonal T_{\min} and T_{\max} , as well as for their warm and cold extremes (i.e., their 10th and 90th percentiles). During winter, the situation was similar, although the dependence was only significant for the 10th percentile of T_{\max} and 90th percentile of T_{\min} climate change signals. In spring and autumn, the regional warm extreme (i.e., the 90th percentile) was affected mainly by the RCM/AOGCM sensitivity over the model domain, but it was still correlated with the bias for the cold extremes of T_{\max} and T_{\min} (10th percentiles). Hence, the dependence of moderate temperature changes on model

bias, that is, the mean change in T_{\min} and the 10th percentile change in T_{\max} , was significant in all seasons within the study area.

4.2. Comparison of RCM/AOGCM and Synthetic Simulation Performance. Figure 4 shows scatter plots of the intermodel and synthetic data mean changes versus bias for precipitation, T_{\min} , and T_{\max} . Because the differences in the relations between mean change and bias in all subzones were insignificant, the mean change and bias in Figure 4 were spatially averaged over the study area. Although we investigated the intermodel bias and mean changes for all seasons, only the results for summer and winter are shown here for brevity, as the majority of significant correlations (i.e., mean change versus bias) among model runs were found for these two seasons, as suggested in Table 2. All of the trend lines for both precipitation and temperature changes were in inverse proportion to bias, with a negative correlation. In addition, the four synthetic scenarios represented by red color (ensemble mean from 12 RCM/AOGCM simulations, DE (RCM/AOGCM), EQ (RCM/AOGCM), and SEP) systematically showed less bias and a narrow range of mean change and bias for all variables. CRCM423(AEV)-CGCM3 substantially overestimated the precipitation amount during both summer and winter. However, the effect of this large bias was not significant on the climate change signals, as reflected in Table 2. CRCM4.2.3 had a much lower bias when it was driven by the other members of the CGCM3 model group (i.e., AET simulation with the 4th CGCM3 member versus the AEV-5th CGCM3 member), indicating a substantial effect from members of the same AOGCM on RCM accuracy, as well as on the uncertainties in the climate change signal. For both T_{\min} and T_{\max} , most RCM/AOGCM simulations were underestimated in summer and overestimated in winter, suggesting that the RCM/AOGCM simulations considered in this study were systematically biased in both seasons. In particular, the HRM3-HadCM3 substantially underestimated both temperatures in summer but overestimated them in winter. In addition, the scatter plots in winter had steeper slopes, a wider range of biases, and higher R^2 values for the trend line compared with those in summer, indicating a stronger correlation between model bias and mean change in winter, with a higher uncertainty in T_{\min} projections in winter. The synthetic scenarios were also clearly less biased in winter with more consensual climate change signals, falling near the middle of the range of climate signals (i.e., reduced uncertainties from both DE and EQ simulated values) than the RCM/AOGCM raw outputs for all variables. In addition, DE (RCM/AOGCM) and EQ (RCM/AOGCM) projected higher climate change signals than the ensemble mean, especially for precipitation (and T_{\min} , to a lesser extent) because the performances of both synthetic scenarios depended on the accuracy of each RCM/AOGCM in the form of the weighting factor, whereas the ensemble mean projected a more conservative signal, which strongly depended on model run outliers and/or the spread of all simulated values.

Figures 5 and 6 show strong and systematic correlations between the cold extreme and warm extreme climate change signals of T_{\min}/T_{\max} and their corresponding biases for

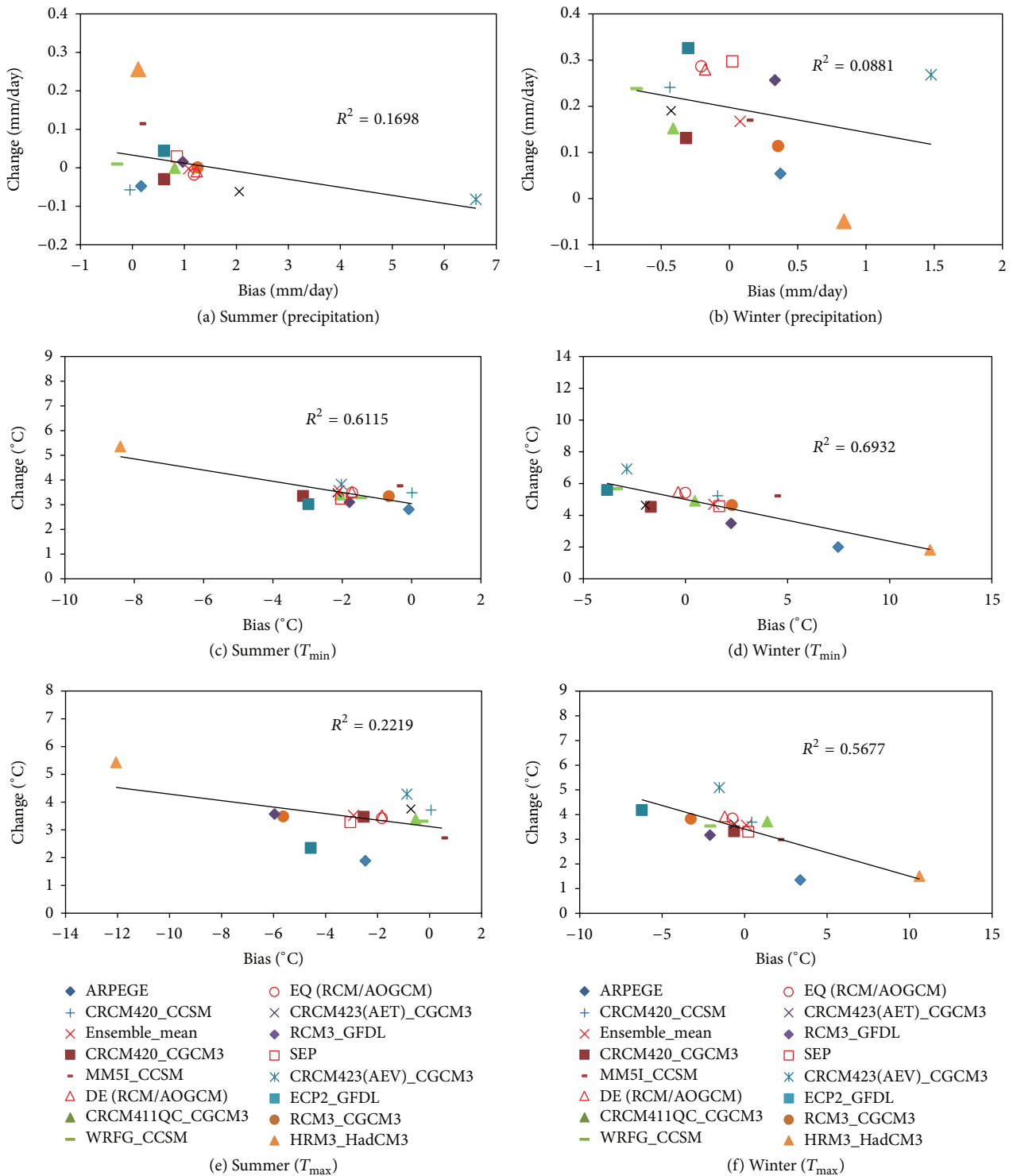


FIGURE 4: Seasonal (summer and winter, left and right panels, resp.) scatter plots of intermodel and synthetic data of mean change (y-axis) versus bias (x-axis) for the mean precipitation ((a) and (b) panels) and the minimum ((c) and (d) panels) and maximum ((e) and (f) panels) temperatures: all values are spatially averaged over the study area.

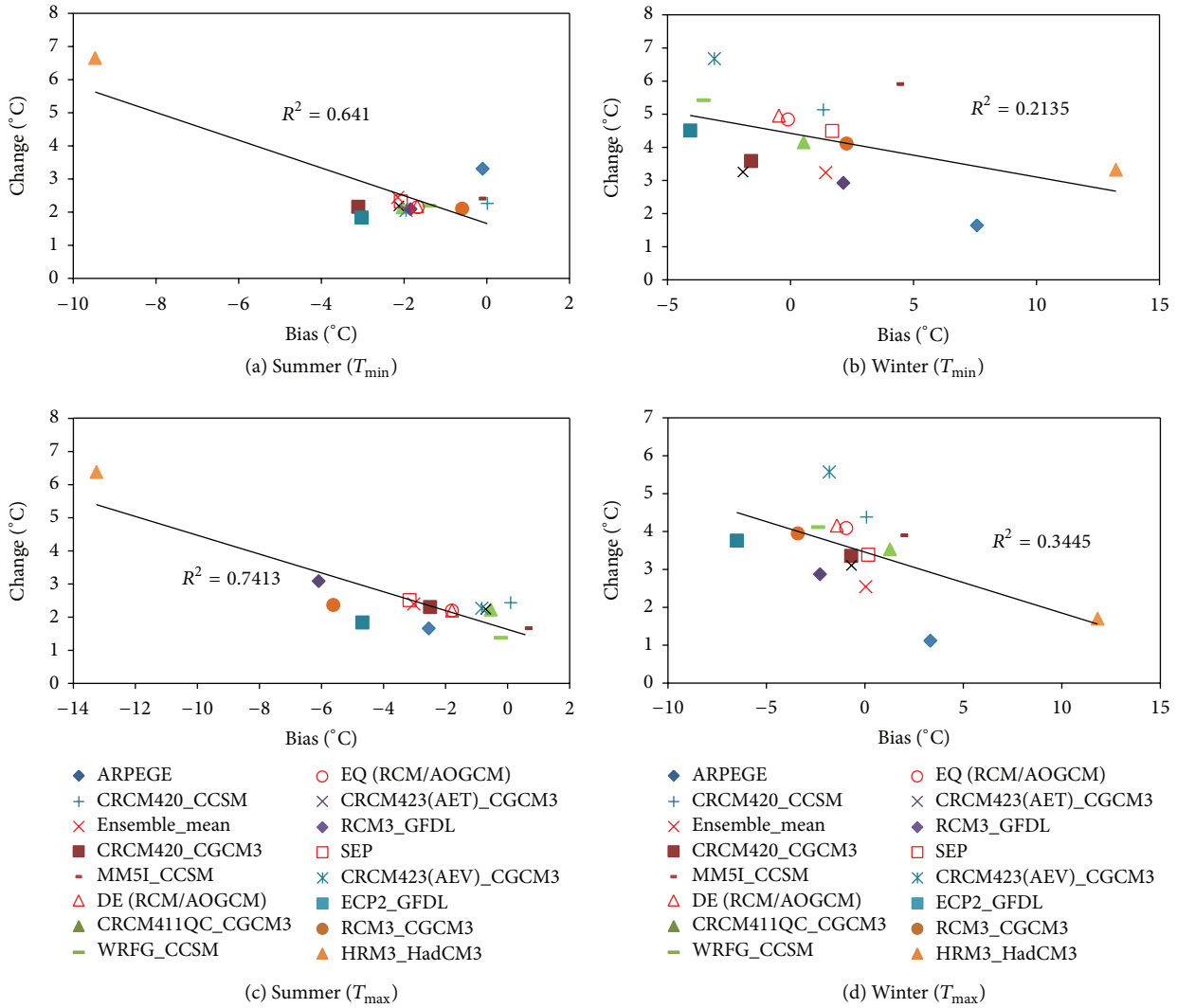


FIGURE 5: Same as Figure 4 but for the 10th percentile of T_{\min} and T_{\max} .

summer and winter, as suggested in Table 2. For T_{\min} , the correlation between the 10th percentile change and bias for winter was not significant, whereas the other cases, for example, 10th percentile for summer and 90th percentile changes for summer and winter, showed strong correlations. This suggests that the cold extreme T_{\min} in winter may be dominated by large-scale patterns rather than by the regional physical processes in RCMs. For T_{\max} , there were strong correlations, except for the 90th percentile change versus bias for winter. Furthermore, the dependence of the extreme temperature change to model bias in summer was much stronger than in winter, although the correlation between mean change and bias in winter was more significant for the warm extreme of T_{\min} . Model bias had a significant effect on the future mean and extremes of T_{\min} and T_{\max} , indicating that climate signals in mean values and various ranges of the extremes for both T_{\min} and T_{\max} were significantly and systematically affected by local physical processes such as topography and surface conditions, that is, sub-grid-scale processes. In addition,

as shown by the mean changes in Figure 4, the extreme temperature changes in the synthetic data had a narrower range and less bias as compared to the RCM/AOGCM simulations, as expected. This implies that the synthetic scenarios may reduce future climate variability among model runs (i.e., a lower level of uncertainty in the future climate) with improved skill. As noted for the mean precipitation and T_{\min} , the DE or EQ synthetic scenarios projected higher signals in the 10th percentile of T_{\min} and T_{\max} than those from the ensemble mean or SEP equivalent values in winter.

4.3. Comparison of Seasonal Climate Change Signals between Median and Extreme Values. As noted in the recent IPCC report [6], large changes in extreme values relative to the mean change are projected in the future. Therefore, we examined the climate change signals of extreme values (90th percentile for precipitation; 90th and 10th percentiles for both T_{\max} and T_{\min}) with respect to the median values to determine the respective rate of change among median/extreme values

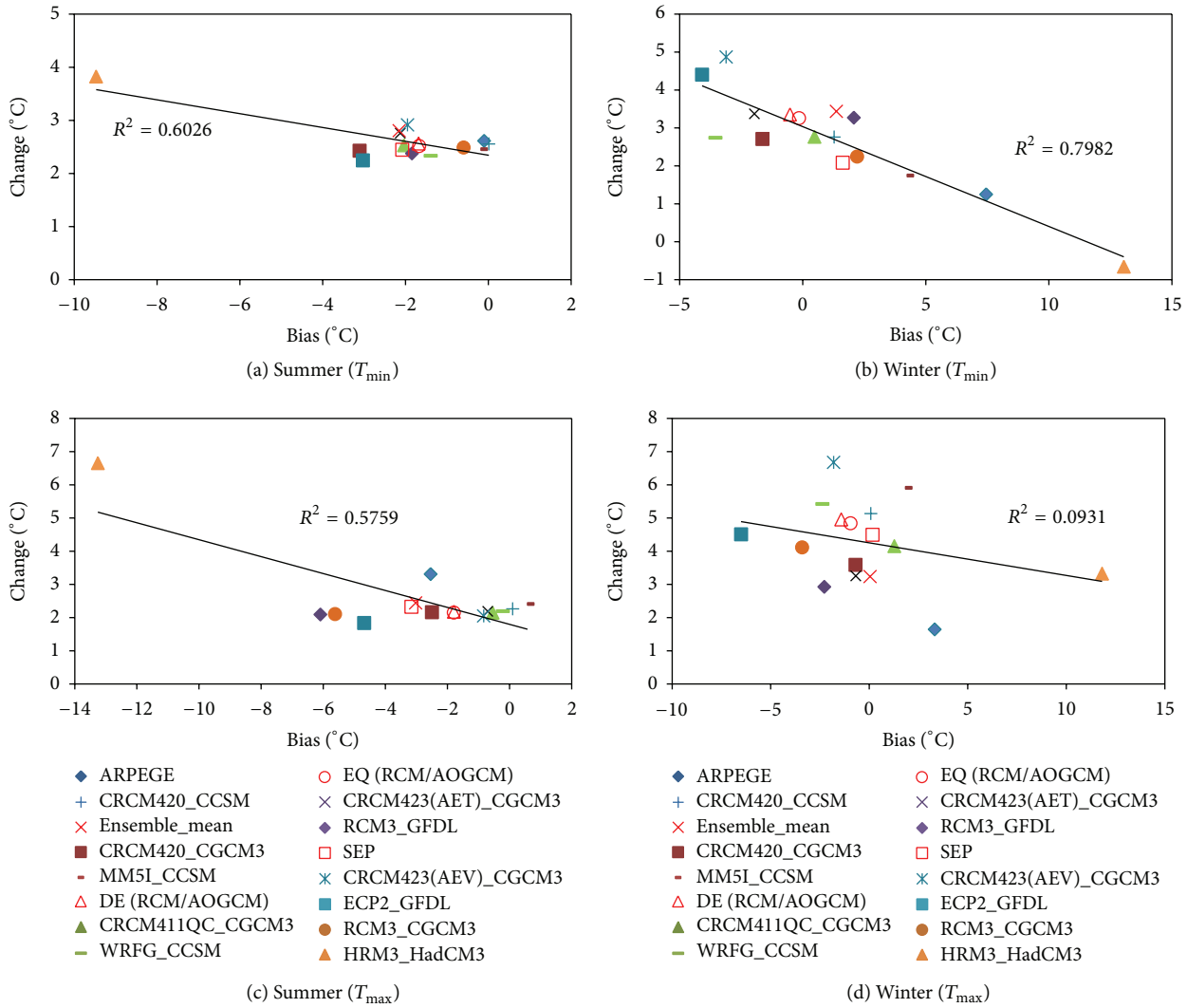


FIGURE 6: Same as Figure 4 but for the 90th percentile of T_{min} and T_{max} .

over the study region. Note that the signals were rescaled as percentages for precipitation and absolute values (i.e., °C) for T_{min} and T_{max} .

Figure 7 shows the seasonal (summer and winter) climate change signal of the models and synthetic data for the 50th (x -axis) and 90th percentile (y -axis) values over the study area. For precipitation change, most RCM/AOGCM simulations projected an increase in both extreme and median values in summer and winter. In most cases, the change in the 90th percentile was larger than that in the median values, especially in winter, when the 90th percentile changes were about twice as large as the 50th percentile changes. This suggests that the frequency of extreme precipitation events may increase more rapidly than the mean change in summer and winter in the future, mainly due to the effects of global warming that accelerates local convection, with an enhancement in humidity in the air and the recycling of water, reaching a higher intensity than that experienced over the historical period, as also noted in [2]. The range of changes

for the 12 RCM/AOGCM simulations was much wider than for the 2 synthetic simulations (DE (RCM/AOGCM) and EQ (RCM/AOGCM)), which incorporated weighting factors into the generation of future climate projections, enabling the more frequent selection of RCM/GCMs with a higher accuracy. In addition, the changes in the two synthetic climate scenarios were very similar to each other, which may indicate a reduction in future variability among models (or less pronounced uncertainty), with respect to raw RCM/AOGCM's simulations, as suggested in [2].

All of the simulations in this study projected an increase in the 50th and 90th percentile values for T_{min} , with a similar rate of changes in summer, that is, most points were located on the diagonal line. There was a small increase in the warm extreme (90th percentile) of T_{min} and T_{max} in winter. However, a quasisystematic higher increase in the warm extreme than in the median value of T_{max} was projected for summer, except in HRM3_HadCM3, which was an outlier among

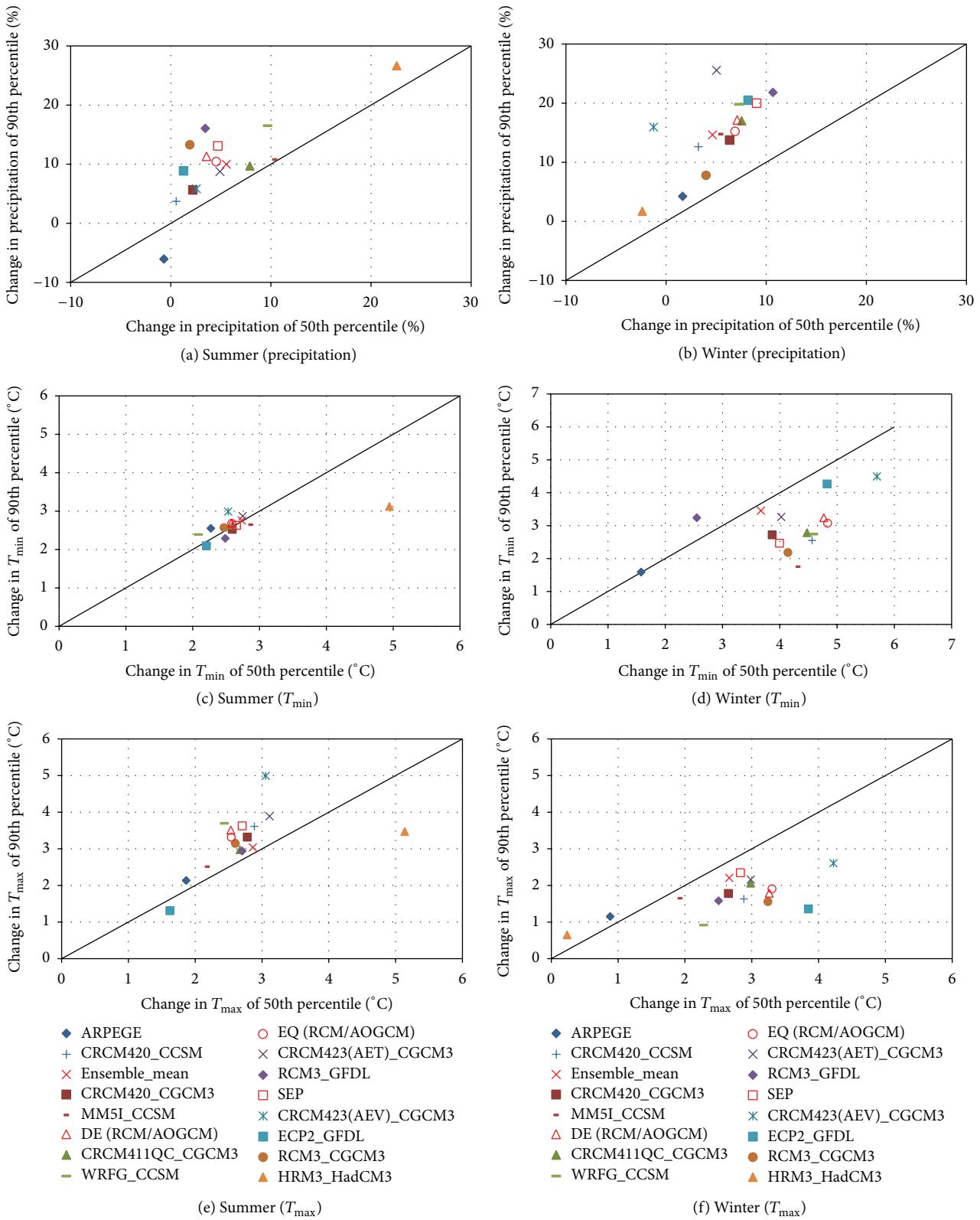


FIGURE 7: Seasonal (summer and winter, left and right panels, resp.) scatter plots of intermodel climate change signal of the 50th (x -axis) and 90th (y -axis) percentile values for precipitation ((a) and (b) panels) and minimum ((c) and (d) panels) and maximum ((e) and (f) panels) temperatures: all values are spatially averaged over the study area.

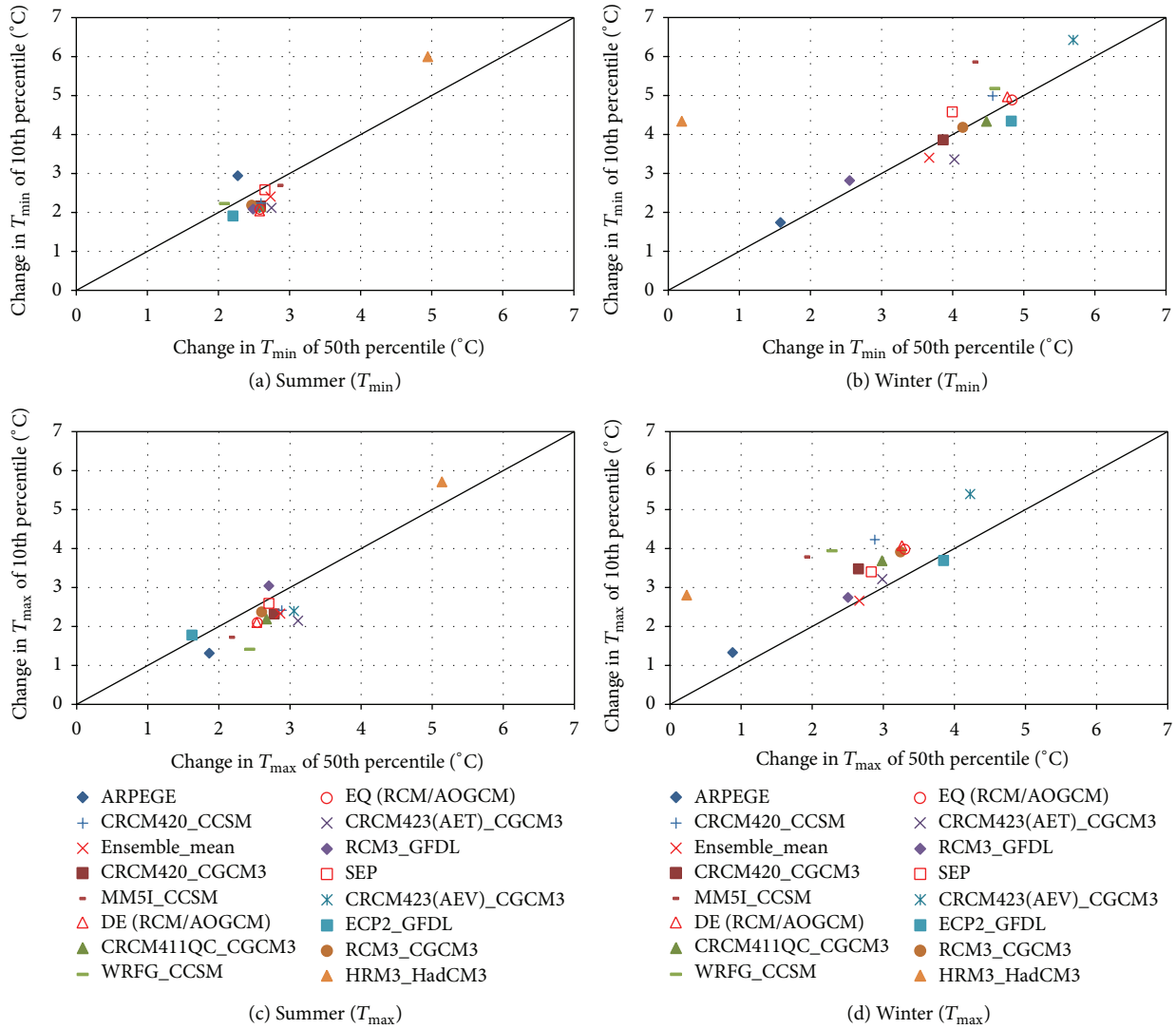


FIGURE 8: Same as Figure 7 but for the 50th (x-axis) and 10th (y-axis) percentile values of T_{\min} and T_{\max} .

the RCMs. These results indicate that global warming may affect the mean change more significantly than the extreme hot T_{\min} and T_{\max} in winter. However, the impacts of climate change on extreme temperature may depend on topographic complexity (e.g., mountainous regions; see the suggested warming amplification in high-elevation regions in [40] and dry or wet surface conditions). Consequently, the relative changes need to be investigated in a variety of regions with different physiographic features. Of the 12 RCM/AOGCM simulations, the HRM3_HadCM3 projected the greatest positive change in both the 50th and 90th percentile values for T_{\min} and the highest positive change in both 50th percentile values for T_{\max} , but negligible changes were projected in T_{\min} and T_{\max} for winter. The range of changes in T_{\min} for summer was much narrower (i.e., less uncertainty) than for winter. The change ratios for T_{\min} and T_{\max} in the four subzones were similar to each other, although for precipitation a larger change ratio was projected in the north (not shown here). This indicates that the spatial variability of T_{\min} and T_{\max}

changes was less pronounced than that for precipitation because these variables were generally more strongly affected by both large scale and regional scale forcings. As with the mean precipitation change, the range of changes for synthetic climate scenarios was narrower than that of the 12 RCM/AOGCM simulations. The DE and EQ scenarios produced higher median values of T_{\min} and T_{\max} in winter than ensemble mean values (i.e., less conservative in this last case).

Figure 8 shows the seasonal (summer and winter) climate change signals of T_{\min} and T_{\max} between the 50th (x-axis) and 10th (y-axis) percentiles for the models and synthetic climate scenarios. In contrast to the warm extremes T_{\min}/T_{\max} , the increase in the 10th percentile (mainly T_{\max}) for the winter was systematically higher than the increase in the 50th percentile in most cases. This indicates that future cold extremes of temperature may be considerably attenuated under climate change conditions. Remarkably, this was not reflected in the winter changes of the ensemble mean scenario, where the changes in the 10th and 50th percentiles for T_{\min} and T_{\max}

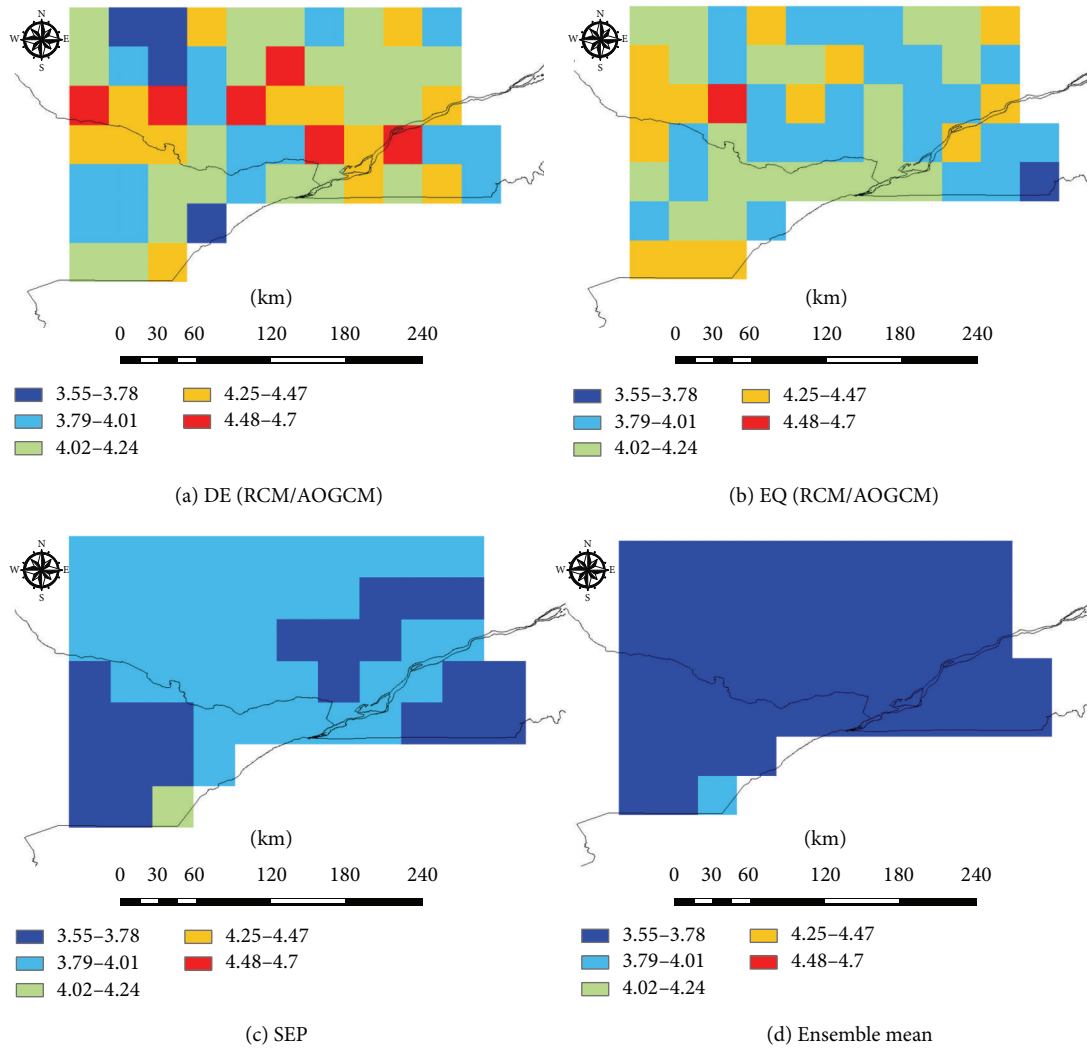


FIGURE 9: Climate change signal of the 10th percentile values at all grid points within the study area for T_{min} from DE (RCM/AOGCM), EQ (RCM/AOGCM), SEP, and the ensemble mean.

were systematically smaller than those of the DE, EQ, and SEP synthetic scenarios.

Figure 9 provides spatial maps of the 10th percentile T_{min} signal in winter to illustrate how well the synthetic scenarios capture a range of extreme cold projections. The range of climate change signals for the DE (RCM/AOGCM) and EQ (RCM/AOGCM) synthetic scenarios was much wider than that for SEP and the ensemble mean. The climate change signal of the ensemble mean was restricted to the 3.55–3.78°C range, with a smoothing pattern from the averaging process. In Figures 9(a) and 9(b), the areas in the north had relatively greater spatial variability in the 10th percentile T_{min} signal for winter, whereas Figures 9(c) and 9(d) show a less warm signal. This demonstrates that the synthetic scenarios better capture the spatial variability in cold extreme events from multiple RCM/AOGCM simulations than they do from the ensemble mean scenario, which may provide a more conservative change value because it simply averages all of the RCM/AOGCM simulations.

5. Summary and Concluding Remarks

This study investigated the relationship between climate change signals and biases for RCM/AOGCM simulations to assess the dependence of future projections on regional model biases for precipitation, T_{min} , and T_{max} over southern Québec (Canada). In addition, we compared 16 projections (i.e., 12 RCM/AOGCM’s simulations, the ensemble mean, and 3 synthetic simulations) and considered the median and extreme seasonal climate change signals.

For precipitation, among the 12 RCM/AOGCM combinations tested, we found that the linear dependence of the climate change signal on the model bias was not significant in most cases for either the mean or the extreme values, indicating that precipitation projection is mainly affected by emission scenarios or large-scale forcings in combination or in interaction with various local effects such as topography and local convection. However, for T_{min} and T_{max} , extreme temperature changes (e.g., the 10th and 90th

percentiles) for summer and winter depended significantly and systematically on the model bias, except for the warm extreme T_{\max} (90th percentile) and cold extreme T_{\min} (10th percentile) in winter. These results suggest that extreme hot and cold temperatures could be significantly affected by a large-scale forcing derived from boundary conditions, that is, the sensitivity of an RCM/AOGCMs, rather than systematic biases in the RCMs over the study area. In addition, the dependence of modest temperature changes (e.g., the mean change in T_{\min} and 10th percentile change of T_{\max}) on model bias was significant in all seasons in the study area. The correlation between model bias and mean change was stronger in winter than summer, while the dependence of extreme temperature changes (10th and 90th percentiles) on model bias was stronger in summer than winter. This means that projections of mean winter temperature and summer T_{\min}/T_{\max} extremes may be significantly affected by model bias (i.e., local physical processes) within the study area. Furthermore, the four synthetic scenarios (ensemble mean, DE (RCM/AOGCM), EQ (RCM/AOGCM), and SEP) generated by the MCS technique based on each RCM/AOGCM's skill displayed systematically less bias and a narrower range of mean change for all variables (less uncertainty) compared with raw RCM/AOGCM simulations.

Regarding the climate change signals of median and extreme values, the increased percentage of extremes (90th percentile) was larger than that of median values for precipitation due to the higher air temperature, which accelerated local convection and the water cycle, whereas the increase in the 90th percentile of both T_{\min} and T_{\max} changes was similar to that in the 50th percentile, except in summer, where the hottest temperatures were projected to increase more than the median T_{\max} values. This indicates that more extreme precipitation events and a larger increase in mean temperature may be expected during summer and winter in the future in southern Québec. Nevertheless, the increase in the 10th percentile of both T_{\min} and T_{\max} for winter was larger than that in the 50th percentile, indicating that future cold extremes may be attenuated or reduced by global warming. The range of changes in the signal for the 12 RCM/AOGCM simulations was much greater than the corresponding range for the synthetic scenarios. Furthermore, the changes in the 10th and 50th percentiles of T_{\min} and T_{\max} from the ensemble mean scenario for winter were systematically smaller than those of the synthetic scenarios. These results indicate that the consistency in climate projections may be significantly improved by incorporating the weighting factors assigned from RCM/AOGCM skill. Moreover, we found that the synthetic scenarios (i.e., DE, EQ, and SEP) might provide or develop spatial variability for cold extreme events, whereas the ensemble mean was likely to be too conservative due to the averaging of all RCM/AOGCM simulations.

Although a significant bias-signal correlation was detected for T_{\min} and T_{\max} in this study, a greater number of RCM/AOGCM combinations is required to confirm the effect of model bias introduced by the different skills of RCM/AOGCM combinations. As noted in previous studies [2, 6, 19, 38], when RCMs are forced with different boundary conditions from various AOGCMs, the systematic

biases of AOGCMs may affect the skill of RCM/AOGCM combinations. Even when RCMs were forced by a specific AOGCM, the bias patterns (not shown) differed from one RCM to another, implying a wider spread across the ensemble of RCMs [13, 19, 41]. Incorporating a larger pool of RCM/AOGCM's simulations, as undertaken in the recent the COordinated Regional climate Downscaling Experiment initiative (CORDEX; Giorgi et al. [42]; <http://wcrp-cordex.ipsl.jussieu.fr>), may provide a more comprehensive insight into the relationships between bias and climate change signals, especially for extreme values at the regional scale.

Conflict of Interests

The authors declare that there is no conflict of interests regarding the publication of this paper.

Acknowledgments

This research was made possible by a financial support from Québec's Ministère du Développement Économique, de l'Innovation et de l'Exportation (MDEIE), National Sciences and Engineering Research Council (NSERC) of Canada, and partially APEC Climate Center (APCC) and a grant (14AWMP-B082564-01) from Advanced Water Management Research Program funded by Ministry of Land, Infrastructure and Transport of the Korean government. The authors would like to acknowledge the Data Access and Integration (DAI, see <http://climat-quebec.qc.ca/CC-DEV/trunk/index.php/pages/dai>) Team for providing the data and technical support, in particular the help of Milka Radojevic in preparing the data. The DAI data download gateway is made possible through collaboration among the FQRNT-funded Global Environmental and Climate Change Centre (GEC3), the Adaptation and Impacts Research Section (AIRS) of Environment Canada, and the Drought Research Initiative (DRI). The CRCM time series data has been generated and supplied by Ouranos' Climate Simulations Team. We wish to thank the North American Regional Climate Change Assessment Program (NARCCAP) for providing the data used in this paper. NARCCAP is funded by the National Science Foundation (NSF), the U.S. Department of Energy (DoE), the National Oceanic and Atmospheric Administration (NOAA), and the U.S. Environmental Protection Agency Office of Research and Development (EPA).

References

- [1] A. F. Hamlet and D. P. Lettenmaier, "Effects of 20th century warming and climate variability on flood risk in the western US," *Water Resources Research*, vol. 43, no. 6, Article ID W06427, 2007.
- [2] H.-I. Eum, P. Gachon, and R. Laprise, "Developing a likely climate scenario from multiple regional climate model simulations with an optimal weighting factor," *Climate Dynamics*, vol. 43, no. 1-2, pp. 11-35, 2014.
- [3] L. A. Vincent, X. L. Wang, E. J. Milewska, H. Wan, F. Yang, and V. Swail, "A second generation of homogenized Canadian monthly surface air temperature for climate trend analysis," *Journal of*

- Geophysical Research: Atmospheres*, vol. 117, no. 17, Article ID D18110, 2012.
- [4] CCSP, *Weather and Climate Extremes in a Changing Climate*, NOAA's National Climate Data Center, Washington, DC, USA, 2008.
 - [5] B. R. Bonsal, R. Aider, P. Gachon, and S. Lapp, "An assessment of Canadian prairie drought: past, present, and future," *Climate Dynamics*, vol. 41, no. 2, pp. 501–516, 2013.
 - [6] IPCC, *Managing the Risks of Extreme Events and Disasters to Advance Climate Change Adaptation*, A Special Report of Working Groups I and II of the Intergovernmental Panel on Climate Change, Cambridge University Press, Cambridge, UK, 2012, edited by: C. B. Field, V. Barros, T. F. Stocker, D. Qin, D. J. Dokken, K. L. Ebi, M. D. Mastrandrea, K. J. Mach, G.-K. Plattner, S. K. Allen, M. Tignor, P. M.
 - [7] L. R. Leung and S. J. Ghan, "Pacific Northwest climate sensitivity simulated by a regional climate model driven by a GCM. Part II: $2\times\text{CO}_2$ simulations," *Journal of Climate*, vol. 12, no. 7, pp. 2031–2053, 1999.
 - [8] P. van der and J. F. B. Linden, *ENSEMBLES: Climate Change and its Impacts: Summary of Research and Results from the ENSEMBLES Project*, Met Office Hadley Centre, Exeter, UK, 2009.
 - [9] D. Jacob, A. Elizalde, A. Haensler et al., "Assessing the transferability of the regional climate model REMO to different coordinated regional climate downscaling experiment (CORDEX) regions," *Atmosphere*, vol. 3, no. 1, pp. 181–199, 2012.
 - [10] P. B. Duffy, R. W. Arritt, J. Coquard et al., "Simulations of present and future climates in the western United States with four nested regional climate models," *Journal of Climate*, vol. 19, no. 6, pp. 873–895, 2006.
 - [11] P. Gachon and Y. Dibike, "Temperature change signals in northern Canada: convergence of statistical downscaling results using two driving GCMs," *International Journal of Climatology*, vol. 27, no. 12, pp. 1623–1641, 2007.
 - [12] J. H. Christensen, T. R. Carter, M. Rummukainen, and G. Amanatidis, "Evaluating the performance and utility of regional climate models: the PRUDENCE project," *Climatic Change*, vol. 81, supplement 1, pp. 1–6, 2007.
 - [13] D. Jacob, J. Petersen, B. Eggert et al., "EURO-CORDEX: new high-resolution climate change projections for European impact research," *Regional Environmental Change*, vol. 14, no. 2, pp. 563–578, 2014.
 - [14] H. Visser, R. J. M. Folkert, J. Hoekstra, and J. J. de Wolff, "Identifying key sources of uncertainty in climate change projections," *Climatic Change*, vol. 45, no. 3–4, pp. 421–457, 2000.
 - [15] H. J. Fowler and M. Ekström, "Multi-model ensemble estimates of climate change impacts on UK seasonal precipitation extremes," *International Journal of Climatology*, vol. 29, no. 3, pp. 385–416, 2009.
 - [16] F. Giorgi and E. Coppola, "Does the model regional bias affect the projected regional climate change? An analysis of global model projections: a letter," *Climatic Change*, vol. 100, no. 3, pp. 787–795, 2010.
 - [17] J. H. Christensen, T. R. Carter, and F. Giorgi, "PRUDENCE employs new methods to assess european climate change," *Eos*, vol. 83, no. 13, p. 147, 2002.
 - [18] L. O. Mearns, W. J. Gutowski, R. Jones et al., "A regional climate change assessment program for North America," *EOS Transactions*, vol. 90, no. 36, pp. 311–312, 2012.
 - [19] J. H. Christensen, E. Kjellström, F. Giorgi, G. Lenderink, and M. Rummukainen, "Weight assignment in regional climate models," *Climate Research*, vol. 44, no. 2–3, pp. 179–194, 2010.
 - [20] E. Coppola, F. Giorgi, S. A. Rauscher, and C. Piani, "Model weighting based on mesoscale structures in precipitation and temperature in an ensemble of regional climate models," *Climate Research*, vol. 44, no. 2–3, pp. 121–134, 2010.
 - [21] J. Räisänen and J. S. Ylhäisi, "Can model weighting improve probabilistic projections of climate change?" *Climate Dynamics*, vol. 39, no. 7–8, pp. 1981–1998, 2012.
 - [22] H.-I. Eum, P. Gachon, R. Laprise, and T. Ouarda, "Evaluation of regional climate model simulations versus gridded observed and regional reanalysis products using a combined weighting scheme," *Climate Dynamics*, vol. 38, no. 7–8, pp. 1433–1457, 2012.
 - [23] D. Caya and R. Laprise, "A semi-implicit semi-Lagrangian regional climate model: the Canadian RCM," *Monthly Weather Review*, vol. 127, no. 2–3, pp. 341–362, 1999.
 - [24] R. Laprise, D. Caya, A. Frigon, and D. Paquin, "Current and perturbed climate as simulated by the second-generation Canadian Regional Climate Model (CRCM-II) over northwestern North America," *Climate Dynamics*, vol. 21, no. 5–6, pp. 405–421, 2003.
 - [25] N. Nakicenovic, J. Alcamo, G. Davis et al., *IPCC Special Report on Emissions Scenarios*, Cambridge University Press, Cambridge, UK, 2000.
 - [26] M. Déqué and J. P. Piedelièvre, "High resolution climate simulation over Europe," *Climate Dynamics*, vol. 11, no. 6, pp. 321–339, 1995.
 - [27] W. D. Collins, C. M. Bitz, M. L. Blackmon et al., "The Community Climate System Model version 3 (CCSM3)," *Journal of Climate*, vol. 19, no. 11, pp. 2122–2143, 2006.
 - [28] G. M. Flato and G. J. Boer, "Warming asymmetry in climate change simulations," *Geophysical Research Letters*, vol. 28, no. 1, pp. 195–198, 2001.
 - [29] T. L. Delworth, A. J. Broccoli, A. Rosati et al., "GFDL's CM2 global coupled climate models. Part I: formulation and simulation characteristics," *Journal of Climate*, vol. 19, pp. 643–674, 2006.
 - [30] C. Gordon, C. Cooper, C. A. Senior et al., "The simulation of SST, sea ice extents and ocean heat transports in a version of the Hadley Centre coupled model without flux adjustments," *Climate Dynamics*, vol. 16, no. 2–3, pp. 147–168, 2000.
 - [31] A.-L. Gibelin and M. Déqué, "Anthropogenic climate change over the Mediterranean region simulated by a global variable resolution model," *Climate Dynamics*, vol. 20, no. 4, pp. 327–339, 2003.
 - [32] E. Kalnay, M. Kanamitsu, R. Kistler et al., "The NCEP/NCAR 40-year reanalysis project," *Bulletin of the American Meteorological Society*, vol. 77, no. 3, pp. 437–471, 1996.
 - [33] S. M. Uppala, P. W. Kållberg, A. J. Simmons et al., "The ERA-40 re-analysis," *Quarterly Journal of the Royal Meteorological Society*, vol. 131, no. 612, pp. 2961–3012, 2005.
 - [34] K. V. Price, R. M. Storn, and J. A. Lampinen, *Differential Evolution: A Practical Approach to Global Optimization*, Springer, Berlin, Germany, 2005.
 - [35] M. F. Hutchinson, D. W. McKenney, K. Lawrence et al., "Development and testing of Canada-wide interpolated spatial models of daily minimum–maximum temperature and precipitation for 1961–2003," *Journal of Applied Meteorology and Climatology*, vol. 48, no. 4, pp. 725–741, 2009.
 - [36] M. Cholette, R. Laprise, and J. M. Thériault, "Perspectives for very high-resolution climate simulations with nested models:

- illustration of potential in simulating St. Lawrence River Valley channelling winds with the fifth-generation Canadian regional climate model,” *Climate*, vol. 3, no. 2, pp. 283–307, 2015.
- [37] C. Wang, R. Jones, M. Perry, C. Johnson, and P. Clark, “Using ultrahigh-resolution regional climate model to predict local climatology,” *Quarterly Journal of the Royal Meteorological Society*, vol. 139, no. 677, pp. 1964–1976, 2013.
- [38] P. Roy, P. Gachon, and R. Laprise, “Sensitivity of seasonal precipitation extremes to model configuration of the Canadian regional climate model over eastern Canada using historical simulations,” *Climate Dynamics*, vol. 43, no. 9, pp. 2431–2453, 2014.
- [39] J. H. Christensen, K. Krishna Kumar, E. Aldrian et al., “Climate phenomena and their relevance for future regional climate change,” in *Climate Change 2013: The Physical Science Basis. Contribution of Working Group I to the Fifth Assessment Report of the Intergovernmental Panel on Climate Change*, T. F. Stocker, D. Qin, G.-K. Plattner et al., Eds., Cambridge University Press, Cambridge, UK, 2013.
- [40] Q. Wang, X. Fan, and M. Wang, “Recent warming amplification over high elevation regions across the globe,” *Climate Dynamics*, vol. 43, no. 1-2, pp. 87–101, 2014.
- [41] C. Jacob, L. Bärring, O. B. Christensen et al., “An inter-comparison of regional climate models for Europe: model performance in present-day climate,” *Climatic Change*, vol. 81, supplement 1, pp. 31–52, 2007.
- [42] F. Giorgi, C. Jones, and G. R. Asrar, “Addressing climate information needs at the regional level: the CORDEX framework,” *WMO Bulletin*, vol. 58, no. 3, pp. 175–183, 2009.

Research Article

The Parameters Estimation for a PM_{2.5} Transport Model with the Adjoint Method

Daosheng Wang,¹ Ning Li,^{1,2} Youli Shen,^{1,3} and Xianqing Lv¹

¹Key Laboratory of Physical Oceanography, Ocean University of China, Ministry of Education, Qingdao 266100, China

²School of Science, Dalian Jiaotong University, Dalian 116028, China

³Beihai Marine Environmental Monitoring Center, Station of State Oceanic Administration, Beihai 536000, China

Correspondence should be addressed to Xianqing Lv; xqinglv@ouc.edu.cn

Received 19 April 2015; Accepted 13 September 2015

Academic Editor: Xiaofeng Li

Copyright © 2016 Daosheng Wang et al. This is an open access article distributed under the Creative Commons Attribution License, which permits unrestricted use, distribution, and reproduction in any medium, provided the original work is properly cited.

Based on the theory of inverse problem and data assimilation, the adjoint method is applied for the estimation of parameters including the initial condition (IC), the source and sink (SS) in a PM_{2.5} transport model. To reduce the ill-posedness of the inverse problem, an independent point scheme (IPS) is implemented during the estimation process. In twin experiments, both the prescribed IC and SS can be inverted successfully and better inversion results are obtained when the IPS is used than not, suggesting the feasibility and validity of the PM_{2.5} transport model as well as the IPS. In practical experiments, several inversion strategies are compared based on the simulation results of PM_{2.5} concentrations over China. It is found that IC and SS are better estimated with smaller difference between simulated results and observations, when IC and SS are inverted simultaneously than separately. And the simulated results can reproduce the temporal and spatial variation feature of the observed PM_{2.5} concentrations. On the basis of the numerical results, it is shown that the adjoint method and the IPS are the powerful way to improve the precision of the simulation of the PM_{2.5} concentrations.

1. Introduction

In China, a combination of rapid industrialization and high population density inevitably deteriorates the air pollution problems [1]. As the 2013 Report on the State of Environment in China shows, the number of hazy days is about 36, reaching a record high since 1961. In some areas the number is even up to 100. And when haze occurs, the PM_{2.5} (particles with aerodynamic diameters less than 2.5 μm) is usually reported as the principal pollutant. To control the haze pollution effectively and provide increased protection for public health, the Chinese government made the new ambient air quality standards in 2012 to which the PM_{2.5} standard was added. Naturally PM_{2.5} pollution has become a major concern in China in recent years, due to its possible impacts on health [2–6], visibility [7], and climate changes [8].

Numerical model is one of the most important ways to investigate PM_{2.5}. And many studies about PM modeling have been conducted using Eulerian box models (e.g., [9]), Lagrangian trajectory models (e.g., [10]), Lagrangian plume

models (e.g., [11]), and 3-dimensional Eulerian models (e.g., [12]). The aforementioned PM models have developed rapidly and become increasingly complex, and details about them are available in several recent review articles (e.g., [13–15]). However, there are several indeterminate factors in the simulation, such as primary PM [16–18], gas-phase chemistry [19, 20], and dry and wet deposition [21, 22]. McKeen et al. [21] evaluated seven PM_{2.5} forecast models using data collected during the ICARTT/NEAQS 2004 field campaign and found that the ensemble PM_{2.5} forecast, created by combining six separate forecasts with equal weighting, yielded the best possible forecast in terms of the statistical measures considered. And the ensemble forecast is also taken as the technique to improve forecasting skills in Zhang et al. [15]. In addition, Zhang et al. [15] indicated that the chemical data assimilation techniques could combine the predicting model with observations to improve the initial and boundary conditions as well as emissions and decrease inaccuracy in the predicting process. Furthermore, the inverse model using data assimilation could estimate the uncertain parameters in

the simulation process. Previous studies have demonstrated the effectiveness of various inverting modeling method to obtain spatial distribution of pollution emissions. For large fields, the 4-dimensional variational method (4D-Var) is chosen. Quélo et al. [23] proved its feasibility on real emission factor of NO_x. Black carbon emission over East Asia was estimated by Hakami et al. [24] using the adjoint STEM model. Yumimoto and Uno [25] applied 4D-Var to a chemical transport model and estimated carbon monoxide emissions over East Asia. Elbern et al. [26] carried out the large-scale inversions of the precursors of O₃, SO₂, NH₃, and so forth, over Europe. And the adjoint method has been applied to several chemical transport models [27–29]. In addition, the adjoint method has been used to study the PM_{2.5}. Henze et al. [30] used the adjoint of GEOS-Chem to do the inverse modeling and mapping US air quality influences of inorganic PM_{2.5} precursor emissions. The source attribution of PM_{2.5} pollution over North China was examined by Zhang et al. [31] using the adjoint method. Capps et al. [32] used the GEOS-Chem adjoint to reveal the relative contributions of global emissions to PM_{2.5} air quality attainment in the US.

But the parameters estimation is often ill-posed and beset by instability and nonuniqueness, particularly if the parameters are distributed in space and time domain [33–36]. The parameters in the general chemical transport model are often distributed complexly; even they are not understood fully. So reducing the number of control variables in the process of parameters estimation is a good way to increase the well-posedness of the inverse problem and improve the estimated results. In this paper, an independent point scheme (IPS) is employed in which a subset of the full grid points is chosen as the independent points and the parameters at the other grid points are obtained through interpolation of the values at the independent points.

In this paper, the parameters of a PM_{2.5} transport model are estimated using the adjoint method (i.e., 4D-Var) with the IPS and the PM_{2.5} concentrations are simulated over China. In Section 2, the adjoint PM_{2.5} transport model is constructed and the IPS is described. In Section 3, twin experiments are carried out to test the reasonability and feasibility of this model and verify the effectiveness of the IPS. Section 4 estimates the parameters using this model and simulates the PM_{2.5} over China. Section 5 summarizes the paper and provides some discussions.

2. Model

2.1. The PM_{2.5} Transport Model. Generally speaking, PM_{2.5} varies due to interactions among many processes including emissions (anthropogenic emission and natural dust production), transport (as well as convection-influenced dispersion and dilution), photochemical transformation (new particle speciation and production of secondary PM_{2.5}), and deposition (dry and wet), with meteorology playing an overarching role [37]. Hence the general PM_{2.5} model includes a rich description of the photochemical oxidant cycle and a chemical mechanism to simulate the formation of secondary PM_{2.5}, and the adjoint model is significantly difficult to build.

Just to verify the estimation ability of adjoint method and the superiority of IPS, we take the primary PM_{2.5} and secondary PM_{2.5} as a whole, calling it “source and sink” (SS) without considering the specific details. Considering that the observations are of ground level and the vertical meteorology environment is indeterminate, we establish a two-dimensional PM_{2.5} transport model in rectangular coordinates as follows:

$$\frac{\partial C}{\partial t} + u \frac{\partial C}{\partial x} + v \frac{\partial C}{\partial y} = \frac{\partial}{\partial x} \left(A_H \frac{\partial C}{\partial x} \right) + \frac{\partial}{\partial y} \left(A_H \frac{\partial C}{\partial y} \right) + S, \quad (1)$$

$$C(t^0, x, y) = C^0(x, y), \quad (2)$$

$$\frac{\partial C}{\partial t} = 0 \quad \text{on } \Gamma^{\text{IN}}, \quad (3)$$

$$\frac{\partial C}{\partial n} = 0 \quad \text{on } \Gamma^{\text{OUT}}. \quad (4)$$

Here C represents the PM_{2.5} concentration, u and v are the horizontal wind velocity in x -coordinate and y -coordinate, respectively, A_H is the horizontal diffusivity coefficient, and S is the SS. The model has the initial conditions (ICs) C^0 and is subject to constant boundary conditions at the inflow boundary Γ^{IN} and to no gradient boundary conditions at the outflow boundary Γ^{OUT} .

The finite difference scheme of (1) is as follows:

$$\begin{aligned} & \frac{C_{i,j}^{n+1} - C_{i,j}^n}{\Delta t} + u_{i,j}^n \frac{C_{uup}^n - C_{udn}^n}{\Delta x_j} + v_{i,j}^n \frac{C_{vup}^n - C_{vdn}^n}{\Delta y} \\ & = \frac{1}{\Delta x_j} \left((A_H)_{i+1,j} \left(\frac{C_{i+1,j}^n - C_{i,j}^n}{\Delta x_j} \right) \right. \\ & \quad \left. - (A_H)_{i,j} \left(\frac{C_{i,j}^n - C_{i-1,j}^n}{\Delta x_j} \right) \right) \\ & \quad + \frac{1}{\Delta y} \left((A_H)_{i,j+1} \left(\frac{C_{i,j+1}^n - C_{i,j}^n}{\Delta y} \right) \right. \\ & \quad \left. - (A_H)_{i,j} \left(\frac{C_{i,j}^n - C_{i,j-1}^n}{\Delta y} \right) \right) + S_{i,j}^n. \end{aligned} \quad (5)$$

Here, the upwind scheme is used in the advection term; that is,

$$\begin{aligned} C_{uup}^n &= C_{i,j}^n, \\ C_{udn}^n &= C_{i-1,j}^n, \\ & \quad \text{if } u_{i,j}^n > 0, \\ C_{uup}^n &= C_{i+1,j}^n, \\ C_{udn}^n &= C_{i,j}^n, \\ & \quad \text{if } u_{i,j}^n < 0. \end{aligned} \quad (6)$$

And it is similar for the term in y -coordinate.

With the IC, the SS, and the background value which is the constant in (3), the $PM_{2.5}$ transport model could be solved by a sequence of N time steps of length Δt in the discrete schemes (i.e., (5)).

2.2. The Adjoint Model. In order to construct the adjoint model, the cost function is defined as

$$J = \frac{1}{2} \int_{\Sigma} K (C - C_{\text{obs}})^2 d\sigma. \quad (7)$$

And based on the theory of Lagrangian multiplier method, the Lagrangian function is defined as

$$L = J + \int \left\{ p \times \left[\frac{\partial C}{\partial t} + u \frac{\partial C}{\partial x} + v \frac{\partial C}{\partial y} - \frac{\partial}{\partial x} \left(A_H \frac{\partial C}{\partial x} \right) - \frac{\partial}{\partial y} \left(A_H \frac{\partial C}{\partial y} \right) - S \right] \right\} d\Omega. \quad (8)$$

Here Σ is the set of the observations, C and C_{obs} are the simulated and observed $PM_{2.5}$ concentrations, respectively, p denotes the adjoint variable of C , and K is the weighting matrix and theoretically should be the inverse of observation error covariance matrix. Assuming the errors of the data are uncorrelated and equally weighted, K can be simplified [38], and in this study K is 1 if observations are available and 0 otherwise.

To let the cost function reach the minimum, we make the first-order derivatives of Lagrangian function with respect to all the variables and parameters be zero, as follows:

$$\frac{\partial L}{\partial p} = 0, \quad (9)$$

$$\frac{\partial L}{\partial C} = 0, \quad (10)$$

$$\frac{\partial L}{\partial A_H} = 0, \quad (11)$$

$$\frac{\partial L}{\partial S} = 0.$$

Actually (9) is (1). The adjoint equation can be derived from (10), which is in the following form:

$$\frac{\partial p}{\partial t} + u \frac{\partial p}{\partial x} + v \frac{\partial p}{\partial y} + \frac{\partial}{\partial x} \left(A_H \frac{\partial p}{\partial x} \right) + \frac{\partial}{\partial y} \left(A_H \frac{\partial p}{\partial y} \right) - K (C - C_{\text{obs}}) = 0. \quad (12)$$

Furthermore, the ICs and open boundary conditions are similar to (2)–(4).

The finite difference scheme of (12) is similar to (5), but it should be noted that the difference scheme of the advection term is opposite to (6) because the adjoint model is integrated backward.

From (11) and the difference scheme, the gradients of the cost function with respect to parameters including

the horizontal diffusivity coefficient, the SS, and IC could be obtained and displayed as follows:

$$\frac{\partial J}{\partial A_H} = - \left(\frac{\partial p}{\partial x} \frac{\partial C}{\partial x} + \frac{\partial p}{\partial y} \frac{\partial C}{\partial y} \right), \quad (13)$$

$$\frac{\partial J}{\partial S} = p, \quad (14)$$

$$\frac{\partial J}{\partial C^0} = \left(\frac{\partial p}{\partial t} \right)^0 + (\nabla \cdot \vec{V}p)^0 + (A_H \nabla^2 p)^0. \quad (15)$$

2.3. Independent Point Scheme. In oceanic and atmospheric studies, the adjoint method (i.e., 4D-Var) has been more and more widely implemented. However, the ill-posedness is normal if the parameters which are estimated are distributed in space or time domain, especially when the parameters are distributed complexly [36]. In this study the IC and the SS spatially vary and the SS also depends on the time. So the dimension of the estimated model parameters is large. Meanwhile, the observations are just obtained at a limited number of locations. Hence the ill-posedness problem is ineluctable.

An IPS is developed in this paper. In this scheme, some grid points are selected uniformly in the space domain as independent points at which the values of parameters are adjusted and the values at other points are obtained by the interpolation of the values at the independent points. It reduces the number of control variables so as to increase the well-posedness and ensure the continuity of variables which accords with the physical properties.

Let $vp_{i,j}$ be the value of parameters at the grid point (i, j) and let $vpip_{m,n}$ be the value of parameters at the independent point (m, n) . In this paper the vp is the value of IC or the SS. Then we have the relationship between vp and $vpip$:

$$vp_{i,j} = \sum_{m,n} \varphi_{i,j,m,n} * vpip_{m,n}, \quad (16)$$

where $\varphi_{i,j,m,n}$ is the coefficient of linear interpolation, as follows:

$$\varphi_{i,j,m,n} = \frac{W_{i,j,m,n}}{\sum_{m,n} W_{i,j,m,n}}. \quad (17)$$

$W_{i,j,m,n}$ is the weighted coefficient of the Cressman form [36]; that is,

$$W_{i,j,m,n} = \frac{R^2 - r_{i,j,m,n}^2}{R^2 + r_{i,j,m,n}^2}, \quad (18)$$

where R is the influence radius and $r_{i,j,m,n}$ is the distance between the two points.

The gradients of the cost function with respect to the independent parameters are as follows:

$$\frac{\partial J}{\partial vpip_{m,n}} = \sum_{i,j} \varphi_{i,j,m,n} \frac{\partial J}{\partial vp_{i,j}}. \quad (19)$$

Note that the partial derivative term in the right side of (19) is computed by (14) or (15).

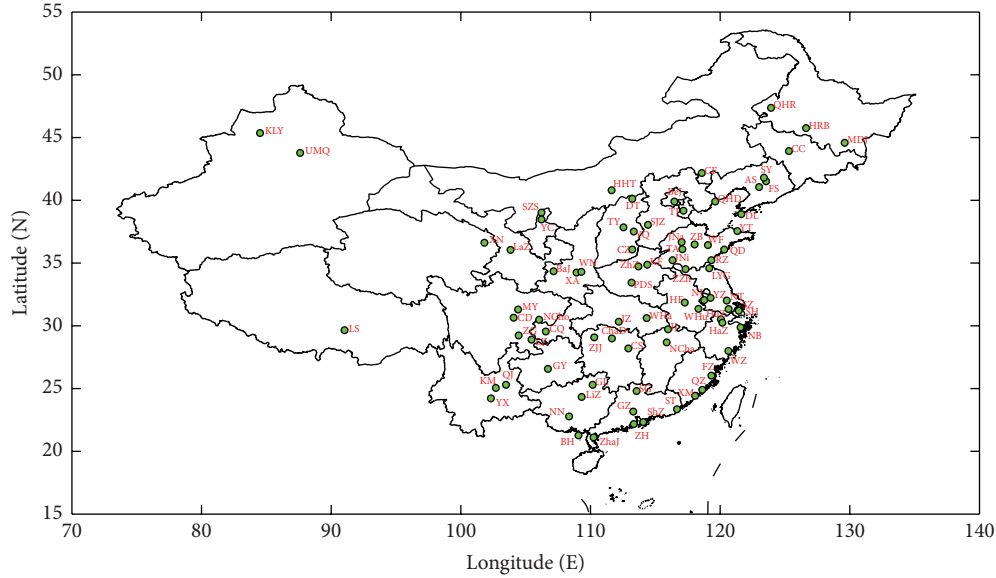


FIGURE 1: The computing area and locations of the 82 cities in which observations are available. Full names of these cities can be found in [37].

With the $PM_{2.5}$ transport model and corresponding adjoint model constructed, the $PM_{2.5}$ observations could be assimilated to optimize the parameters with IPS and improve the simulated results by repeating the following steps. (1) Run the $PM_{2.5}$ transport model with the given parameters. (2) The simulated $PM_{2.5}$ concentrations could be obtained, and the cost function can be calculated by (7) with the observations. (3) The adjoint model is run and the adjoint variable p can be obtained. (4) The gradients of the cost functions with respect to the parameters at the independent points could be calculated by (19). (5) The parameters at the independent points are adjusted by the typical steepest descent method with the gradients. (6) Then the parameters at other points are determined by the interpolation of the values at the independent points by (16).

2.4. Model Settings. The model is applied over a domain encompassing China (see Figure 1). The horizontal resolution for the model is $0.5^\circ \times 0.5^\circ$. The integral time step is 600 s and the assimilation window is 168 hours. Considering the actual $PM_{2.5}$ concentration and the air quality standards in China, the background value is set as $15.0 \mu\text{g}/\text{m}^3$ which is the constant boundary condition at the inflow boundary. The independent points are selected uniformly over each $2.5^\circ \times 2.5^\circ$ area and the influence radius of Cressman interpolation in IPS is 2.5° .

The records of $PM_{2.5}$ concentrations every two hours for 82 major Chinese cities which are shown in Figure 1 are used as observations in the present study. Elbern et al. [26] pointed out that the validity of the assimilation results can be shown satisfactorily by independent observations. So in this study, Jinan (JNa), Zhengzhou (ZhZ), Shenyang (SY), Quanzhou (QZ), Hangzhou (HaZ), Kunming (KM), Chengdu (CD), and Urumchi (UMQ) are selected as “checked cities,” in

which the observations are not assimilated and used for testing the assimilated results. And the other cities are seen as “assimilated cities,” in which the observations are assimilated. The wind data are derived from the National Centers for Environmental Prediction (NCEP) winds daily averaged for each 2.5° latitude by 2.5° longitude region.

3. Twin Experiments

It is well known that the SS and the IC are significant for the simulation of $PM_{2.5}$. As the SS is taken as a black box in our model, the inversion of the SS and IC is the vital part of the whole model. In this section, the ideal twin experiments (TEs) are carried out to verify the inversion ability of the adjoint model and test the reasonability and availability of the IPS.

3.1. Setup of Twin Experiments. The process of TE is designed as follows. First, a distribution of the SS (or IC) is prescribed and taken as “true values.” Then the $PM_{2.5}$ transport model is run using the “true values” and the simulated results recorded at grid points of “checked cities” and “assimilated cities” are taken as the “observations”; that is, only the spatiotemporal position of real observation is used and the value of observation is obtained by running the $PM_{2.5}$ transport model. Considering that the real observations contain noises, artificial random errors are added to the “observations” and the maximum percentage of random errors is 5%. Having obtained the “observations,” a guess value of SS (or IC) that is 0 in this work (or the background value for IC) is assigned to run the $PM_{2.5}$ transport model. Then the differences between simulated results and “observations” will drive the adjoint model. With the backward integration of the adjoint model and the calculation of the gradient, the SS

TABLE 1: The detailed settings of the 6 TEs.

Experiment	$K1^a$	$K2^a$	$K3^a$	$K4^a$	IPS
TE1	Figure 2(a)	0	Yes	No	Yes
TE2	Figure 2(a)	Figure 2(b)	No	Yes	Yes
TE3	Figure 3(a)	Figure 3(b)	Yes	Yes	Yes
TE4	Figure 2(a)	0	Yes	No	No
TE5	Figure 2(a)	Figure 2(b)	No	Yes	No
TE6	Figure 3(a)	Figure 3(b)	Yes	Yes	No

^a $K1$ and $K2$ are the distribution of the IC and the SS, respectively. $K3$ represents the case when the IC is inverted and $K4$ represents the case when the SS is inverted.

(or IC) are optimized. With the above procedures repeated, the SS (or IC) will get closer to the “true values” continually and the differences between the simulated results and the “observations” will be decreased simultaneously. The iteration of optimization will terminate when the number of iteration steps is equal to 300 exactly which is sufficient for this work.

Because there is no fixed trend of SS in real life, in TEs the SS varies only in space and keeps invariant at every time step. Considering the distribution and emission of $PM_{2.5}$ concentrations in China, six different TEs are designed which are described in Table 1.

3.2. Results of Twin Experiments. For inversion ability evaluation, the mean absolute errors (MAEs) between simulated results and “observations” in “checked cities” and “assimilated cities” and between the prescribed “true values” of SS (or IC) and the inverted values are calculated and shown in Table 2. It is calculated that the MAEs at “assimilated cities” decrease by 98.11% in TE1, 89.52% in TE2, 98.07% in TE3, 95.47% in TE4, 89.40% in TE5, and 95.34% in TE6. And the MAEs in “checked cities” decrease by 97.90% in TE1, 86.90% in TE2, 97.78% in TE3, 93.59% in TE4, 90.11% in TE5, and 92.68% in TE6. It is obvious that the “observations” have been assimilated well in all TEs from the MAEs. Comparing the MAEs in TE1 and TE4, it is found that the MAEs in TE1 are less than those in TE4, stating that the IPS could improve the simulated results. And the conclusion is also found from the other TEs.

The prescribed IC, SS, and the inversion results when they are inverted separately are shown in Figure 2. Although the MAEs in TE4 have shown that the $PM_{2.5}$ observations are assimilated well and the inverted IC is close to the prescribed one, from Figure 2(e) it is found that the inverted IC is inconsecutive and the characteristic of Figure 2(a) which is the prescribed value does not reappear. However, Figure 2(c) which is the inverted one with IPS reproduces the feature of Figure 2(a). In Figure 2(f), the SS cannot reflect the feature of the prescribed one. However, the inverted SS with IPS which is illustrated in Figure 2(d) has the same character of spatial distribution with Figure 2(b). It is concluded that the IPS can ensure the continuity of the inverted IC and the SS which accords with the prescribed one.

Figure 3 illustrates the prescribed IC, SS, and the inverted ones in TE3 and TE6. It is worth noting that the prescribed initial and SS have the overlapped area in space.

From Figure 3(e), it is found that the inverted IC without IPS is discontinuous and has different values in Shanxi and Jiangxi provinces. What is worse, the inverted SS without IPS in Figure 2(f) does not have the same pattern with Figure 2(b) and the values in Liaoning province are greater than the prescribed ones. In fact, the pattern of the inverted SS in TE6 is more close to the pattern of the prescribed IC, rather than the prescribed SS, and it is ascribed to the ill-posedness of the inverse problem. But the inverted IC and SS with IPS reproduce the prescribed ones well. It is shown that the IPS can increase the well-posedness of the inverse problem. In addition, the prescribed IC and SS can be inverted successfully with IPS no matter separately or simultaneously.

4. Practical Experiments

4.1. Setup of Practical Experiments. In order to find the best way to invert the IC and the SS in practice, several practical experiments (PEs) are carried out. In PEs, both the position and the values of observations are used, which is different from TEs. It is noted that in this section the observations during 18 to 24 May 2014 are assimilated to invert the SS and the IC, that is, the $PM_{2.5}$ concentrations at 18 May 0:00.

In the adjoint model, there are several modes to invert the IC and the SS. To get the best simulation results, ten different modes are compared in the PEs, which are described as follows. In PE1, the SS and the IC are inverted simultaneously with 300 optimization iteration steps using IPS. In PE2, only the SS is inverted with 300 optimization iteration steps using IPS. In PE3, only the IC is inverted with 300 optimization iteration steps using IPS. In PE4, the SS is inverted firstly with 150 optimization iteration steps and the IC is inverted subsequently with 150 optimization iteration steps using IPS. In PE5, the IC is inverted firstly with 150 optimization iteration steps and the SS is inverted subsequently with 150 optimization iteration steps using IPS. PE6–PE10 are corresponding to PE1–PE5 without using IPS.

4.2. Results and Analysis of Practical Experiments. Table 3 gives the error statistics for PEs. It could be found that in PE1 the cost function which is normalized by its initial values at the first iteration step reaches the minimum value and the MAE between simulated values and observations in “assimilated cities” is the smallest of the PEs using IPS. At the same time, in PE6 which is the corresponding one without IPS those evaluation indexes are the smallest of PEs without IPS. It is shown that when the IC and the SS are inverted simultaneously with or without IPS, the effect of the data assimilation is the best.

In addition, the normalized cost functions and the MAE between simulated values and observations in “assimilated cities” in the PEs without IPS are less than those in the corresponding ones with IPS, but the MAE between simulated values and observations in “checked cities” is greater than that in the corresponding ones with IPS. It may be stated that, in the PEs without IPS, the simulated results are optimized just in the “assimilated cities” where the observations are

TABLE 2: Error statistics of twin experiments before and after assimilation.

Experiment	J_{300}/J_1^a	$K1^a$ ($\mu\text{g}/\text{m}^3$)		$K2^a$ ($\mu\text{g}/\text{m}^3$)		$K3^a$ ($\mu\text{g}/\text{m}^3$)		$K4^a$ ($10^{-6} \mu\text{g}/\text{m}^3/\text{s}$)	
		Before	After	Before	After	Before	After	Before	After
TE1	0.00042	31.79	0.60	25.87	0.54	6.33	1.20	—	—
TE2	0.00931	7.80	0.82	5.60	0.73	—	—	3.16	1.04
TE3	0.00043	38.45	0.74	30.46	0.68	6.33	1.26	3.16	0.81
TE4	0.00357	31.79	1.44	25.87	1.66	6.33	2.80	—	—
TE5	0.00968	7.80	0.83	7.80	0.77	—	—	3.16	1.28
TE6	0.00316	38.45	1.79	30.46	2.23	6.33	3.19	3.16	3.47

^a J_{300} is the final value of cost function and J_1 is the initial value of cost function. $K1$ and $K2$ are the MAEs between simulated values and “observations” in “assimilated cities” and “checked cities,” respectively. $K3$ and $K4$ are the MAEs between prescribed and inverted IC and SS, respectively.

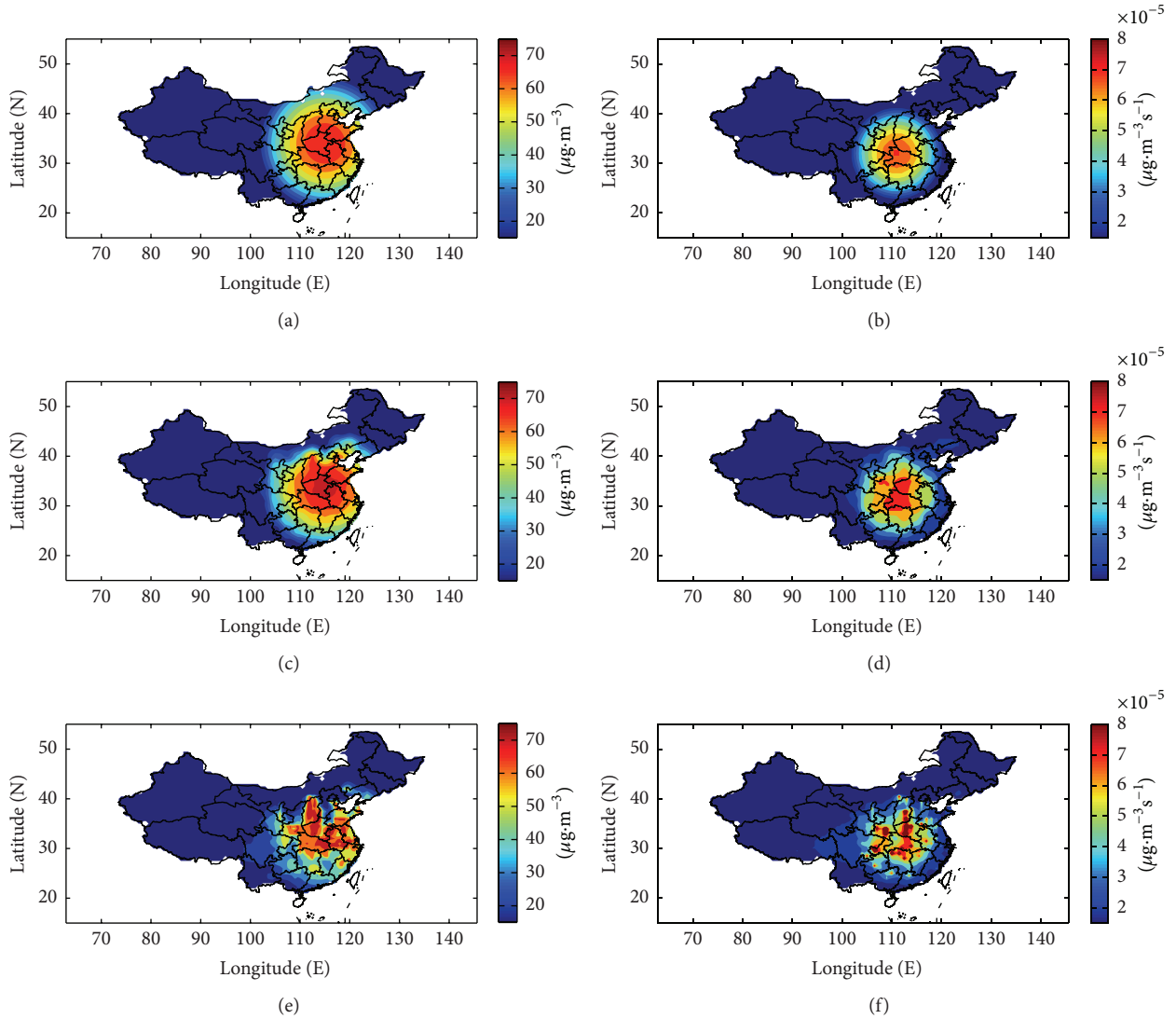


FIGURE 2: (a) The prescribed IC, (b) the prescribed SS, (c) the inverted IC in TE1, (d) the inverted SS in TE2, (e) the inverted IC in TE4, and (f) the inverted SS in TE5.

assimilated. To verify this, four cities, including Zhanjiang (Zha), Jingzhou (JZ), Hangzhou (HaZ), and Chengdu (CD), are selected to compare the time-varying $\text{PM}_{2.5}$ concentrations. The four cities are representative, because the MAE between simulated results and observations in Zhanjiang is

the smallest of the “assimilated cities” and that in Jingzhou is the largest; Hangzhou and Chengdu are major cities of the “checked cities.” The time-varying $\text{PM}_{2.5}$ concentrations of the four cities in the PEs are shown in Figure 4. The results in Zhanjiang and Jingzhou indicate that all PEs could capture

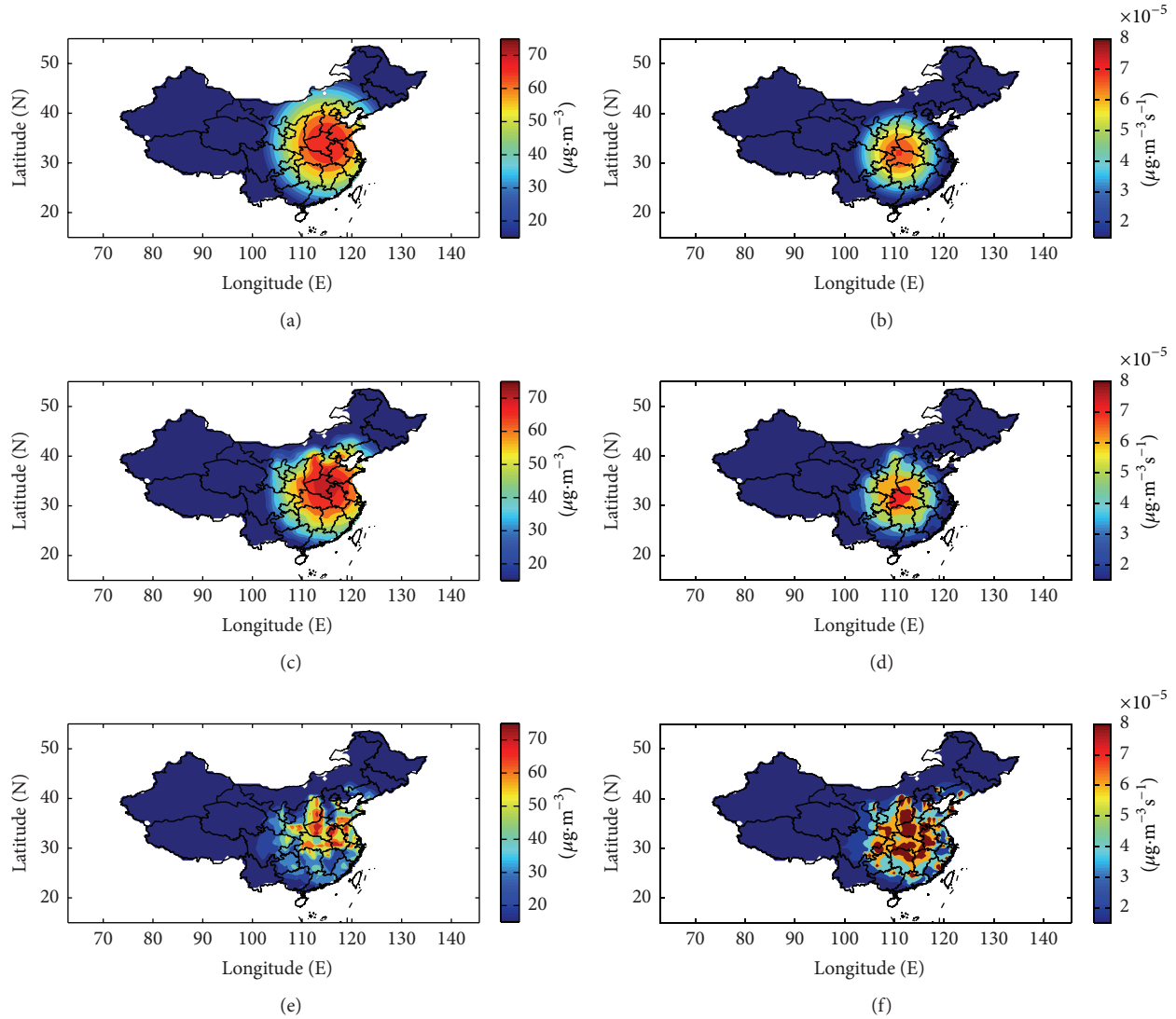


FIGURE 3: (a) The prescribed IC which is the same as that in Figure 2(a), (b) the prescribed SS which is the same as that in Figure 2(b), (c) the inverted IC in TE3, (d) the inverted SS in TE3, (e) the inverted IC in TE6, and (f) the inverted SS in TE6.

the variation trend of $PM_{2.5}$ concentrations, except PE3 and PE8. In detail, it is found that the simulated results in the PEs without IPS are more close to the observations than those with IPS. However, in Hangzhou and Chengdu, it is obvious that the simulated results in the PEs with IPS except PE3 could show the variation character of $PM_{2.5}$ observations well, and the simulated results in the PEs without IPS are bad. The results in the four representative cities agree with the aforementioned inference. In fact, the “assimilated cities” are in a minority, and the cities in which there are no observations may gain more attention. So the simulated results in the PEs with IPS are more reasonable and believable. With the MAEs in Table 3 and Figure 4, it is concluded that the best simulated result is gained in PE1 in which the IC and SS are inverted simultaneously using IPS.

The IC is important for the simulation of $PM_{2.5}$. To compare the IC obtained from different modes, the observations at the initial time are shown in Figure 5. The $PM_{2.5}$ concentrations are larger than $120 \mu g/m^3$ in Chengdu (CD), Wuhu (WHu), Nanjing (NJ), and Yangzhou (YZ), while

TABLE 3: Error statistics of practical experiments before and after assimilation.

Experiment	J_{300}/J_1^a	$K1^a$ ($\mu g/m^3$)		$K2^a$ ($\mu g/m^3$)		$K3^a$ ($\mu g/m^3$)	
		Before	After	Before	After	Before	After
PE1	0.12434	41.26	12.31	41.85	17.38	40.50	15.22
PE2	0.13007	41.26	12.63	41.85	17.79	40.50	40.50
PE3	0.38750	41.26	24.54	41.85	21.52	40.50	18.94
PE4	0.15637	41.26	14.13	41.85	18.04	40.50	36.35
PE5	0.14755	41.26	13.62	41.85	17.29	40.50	18.44
PE6	0.08964	41.26	10.42	41.85	18.21	40.50	13.56
PE7	0.10516	41.26	11.33	41.85	19.36	40.50	40.50
PE8	0.36593	41.26	23.20	41.85	23.27	40.50	14.78
PE9	0.15294	41.26	14.12	41.85	20.09	40.50	24.42
PE10	0.13889	41.26	13.24	41.85	18.11	40.50	14.95

^a J_{300} is the final value of cost function and J_1 is the initial value of cost function. $K1$ and $K2$ are the MAEs between simulated values and observations in “assimilated cities” and “checked cities,” respectively. $K3$ is the MAEs between the observations and simulated results in all the cities at the initial time.

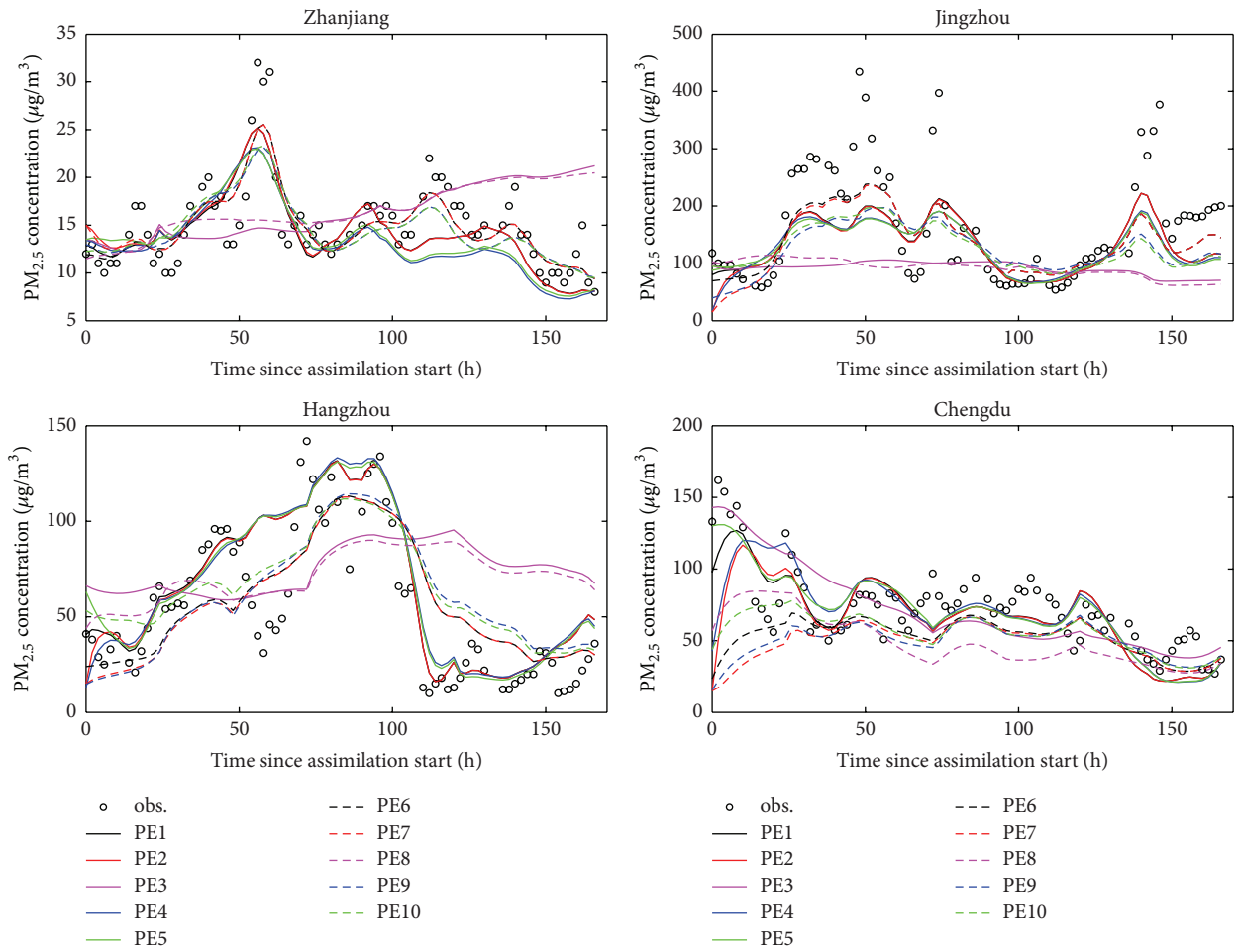


FIGURE 4: The time-varying PM_{2.5} concentrations of four representative cities.

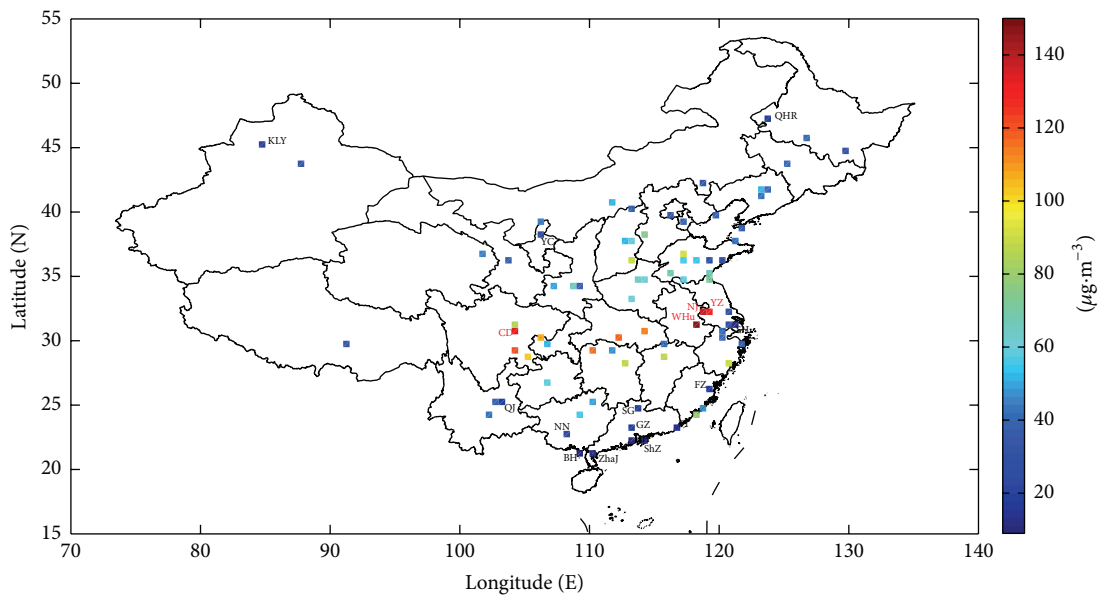


FIGURE 5: The observations at 18 May 0:00.

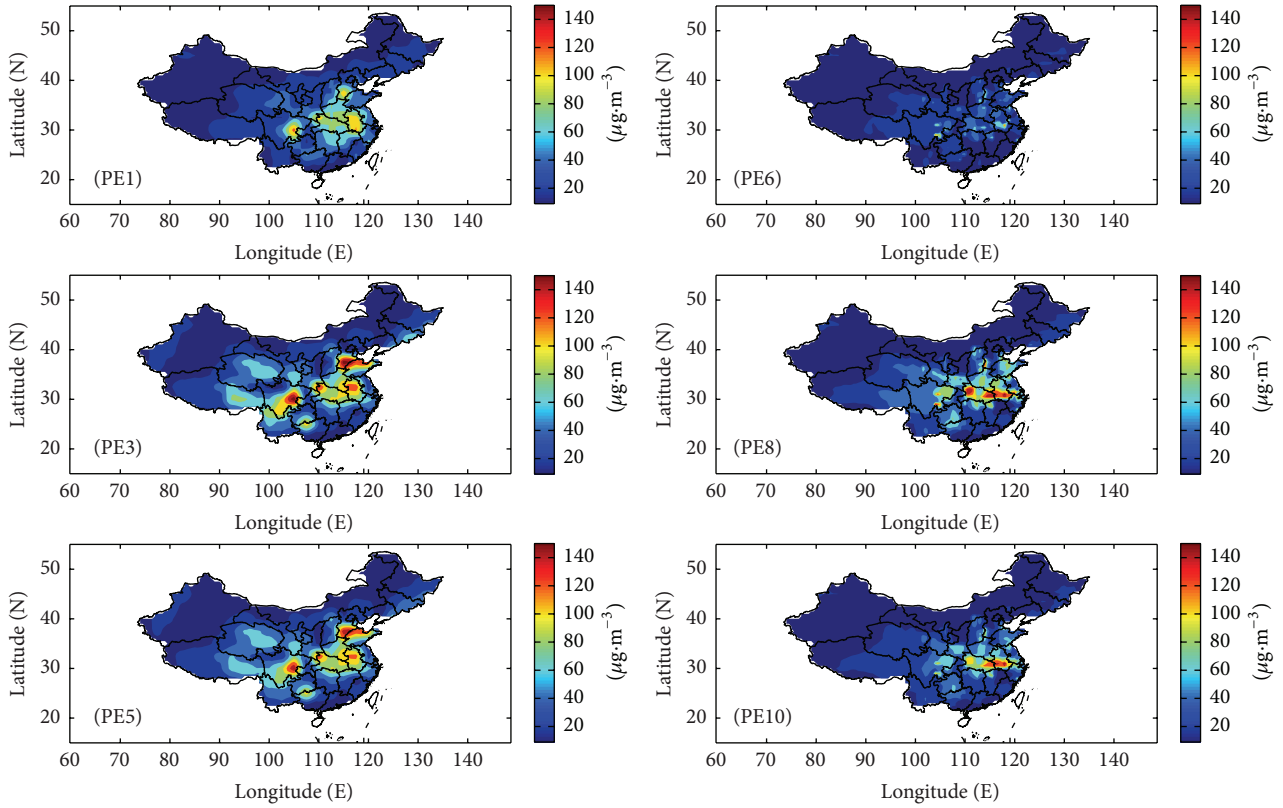


FIGURE 6: The IC obtained in PEs.

the value is less than $30 \mu\text{g}/\text{m}^3$ in the other cities whose names are marked in Figure 5. The ICs obtained from PEs in which the IC is inverted are exhibited in Figure 6. It is obvious that the inverted ICs got in the PEs without IPS are discontinuous in several areas, especially in PE6; there are several extrema at the grid points where the observations are assimilated. So it is indicated that in the PEs without IPS just the observations are assimilated fully and the inverted ICs do not accord with the physical properties. In PE3 and PE5 the $\text{PM}_{2.5}$ concentrations in Tianjin and Shandong province are larger than $140 \mu\text{g}/\text{m}^3$ where the observations are about $90 \mu\text{g}/\text{m}^3$ and the simulated results are different obviously with the observations in Nanjing, Yangzhou, and Wuhu. In PE1, the inverted IC conforms to the spatial distribution characteristics of the observations and the MAE between the inversion results and observations is the minimum. So the inverted IC in PE1 is the best one.

From the analysis above, it is obvious that the simulated results and inverted IC in PE1 are the best. So the inverted SS in PE1 will be investigated. The SS at the current time step will affect the $\text{PM}_{2.5}$ concentrations at the next time step and there should be correlation between them. The correlation coefficients between the $\text{PM}_{2.5}$ observations and the corresponding SS are calculated in all cities. The mean values of $\text{PM}_{2.5}$ concentrations during assimilation window and the value of correlation coefficient in all cities are shown in Figure 7. From Figure 7, the following conclusions can be deduced. Firstly, the mean values of $\text{PM}_{2.5}$ concentrations are

larger in northwest China which is covered by desert and in middle China where the emission of $\text{PM}_{2.5}$ is enormous. And the mean values are smaller in southeast China where precipitation is rich. Secondly, the correlation coefficient is positive in most cities. With the setting of the PE1, the convection and diffusion would not play roles in just one time step. Therefore, the SS at the current time step will determine the change of the $\text{PM}_{2.5}$ concentrations at the next time step. It is accordant with the fact and proves that the inverted SS in PE1 is roughly reasonable.

For detailed model performance evaluation in PE1, regression statistics along with two measures of bias, the mean bias (MB) and the normalized mean bias (NMB), and two measures of error, the root mean square error (RMSE) and normalized mean error (NME) [14], are calculated. The mean values of MB and RMSE in PE1 are $0.70 \mu\text{g}/\text{m}^3$ and $20.58 \mu\text{g}/\text{m}^3$, respectively, and those for NMB and NME are 1.26% and 23.08%, respectively. Furthermore, the mean value of all the observations is $55.62 \mu\text{g}/\text{m}^3$ and that of the simulated results is $56.32 \mu\text{g}/\text{m}^3$, and the correlation coefficient between the observations and simulated results is 0.85. In detail, the scatterplot of Figure 8(a) indicates that the model captured a majority (95.4%) of observations with a factor of 2 and underestimated the observations in the high $\text{PM}_{2.5}$ concentration range. Since Tapered Element Oscillating Microbalance analyzers (TEOMs, which are commonly used in the EPA-China's air quality monitoring network) measurements for $\text{PM}_{2.5}$ should be considered as lower limits because of

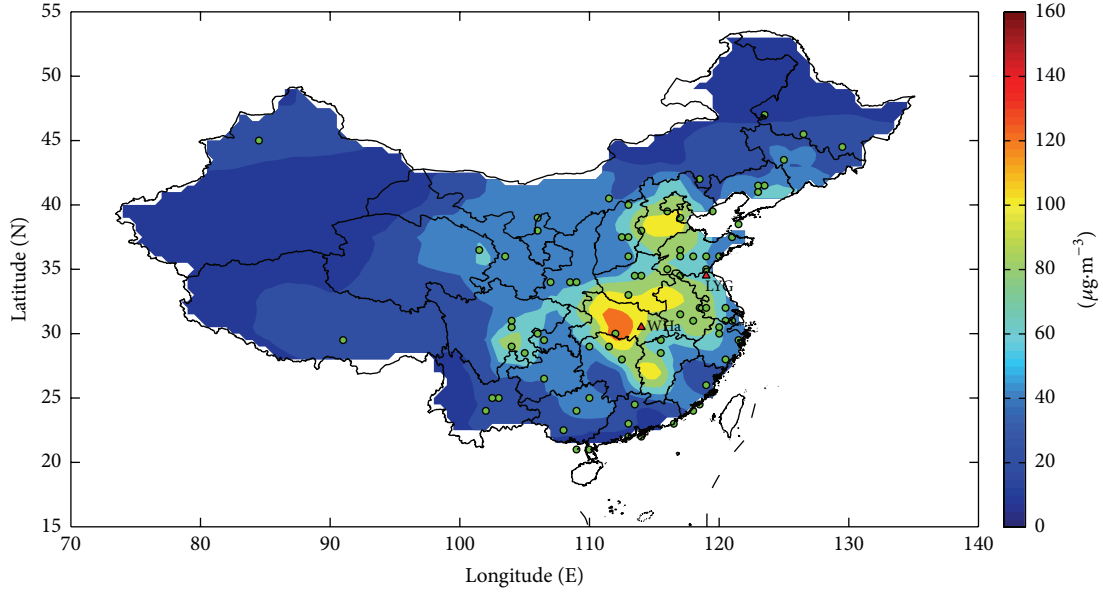


FIGURE 7: The mean field of $PM_{2.5}$ concentrations ($\mu\text{g}/\text{m}^3$), where “o” represents that in this city the correlation coefficient is positive and “ Δ ” represents that the correlation coefficient is negative in this city.

volatilization of soluble organic carbon species in the drying stages of the measurement [12, 37, 39], the undersimulation is likely to be more severe than this evaluation suggests. In order to investigate the model’s performance over time, the values of mean $PM_{2.5}$ concentrations, NMB, NME, and correlation coefficients are calculated (spatial averages) and plotted as a time series (Figure 8(b)). It is noted that there are no observations at several hours. As can be seen, the mean values of observations and simulated results are almost equal and have the same time-varying trend. In addition, it is found that the mean $PM_{2.5}$ concentrations vary analogously every day and the values reach the minimum every afternoon. The NMB values range from -14.25% to 18.41% . The NME values are approximate to 23.08% which is the NME value of all the observations and it proved that the model is steady during the time. Spatially, the model estimates observed $PM_{2.5}$ well in most areas (74.39%) where the NME value is less than 0.25 . Moreover, in 7 cities the absolute value of NMB is larger than 0.25 and only Quanzhou (QZ) and Urumchi (UMQ) are the “checked cities.” It indicates that the model can simulate good results in the cities where the observations are not assimilated through the data assimilation. Therefore, whether in terms of time or space, even on the whole, this model simulates the $PM_{2.5}$ concentrations well through estimating the IC and the SS simultaneously using IPS.

4.3. Discussion. To further indicate that the adjoint method and the IPS can improve the precision of the simulation of the $PM_{2.5}$ concentrations, the $PM_{2.5}$ concentrations over China are simulated during 10 to 16 December 2014. It is in different season and different meteorological conditions with the previous PEs and the other conditions are the same. As before, ten same modes numbered as NPE1 to NPE10 are compared. The error statistics for NPEs are shown in

TABLE 4: Error statistics of NPEs before and after assimilation.

Experiment	J_{300}/J_1^a	$K1^a$ ($\mu\text{g}/\text{m}^3$)		$K2^a$ ($\mu\text{g}/\text{m}^3$)		$K3^a$ ($\mu\text{g}/\text{m}^3$)	
		Before	After	Before	After	Before	After
NPE1	0.11399	46.47	13.41	52.63	26.16	53.06	23.57
NPE2	0.14117	46.47	14.22	52.63	25.90	53.06	53.06
NPE3	0.39897	46.47	27.38	52.63	35.58	53.06	30.03
NPE4	0.16400	46.47	15.88	52.63	26.39	53.06	47.60
NPE5	0.14558	46.47	15.24	52.63	25.95	53.06	29.46
NPE6	0.14179	46.47	15.20	52.63	31.07	53.06	25.92
NPE7	0.18743	46.47	16.59	52.63	31.92	53.06	53.06
NPE8	0.43091	46.47	28.32	52.63	37.98	53.06	23.74
NPE9	0.22616	46.47	19.41	52.63	33.24	53.06	37.10
NPE10	0.21780	46.47	19.17	52.63	33.33	53.06	30.51

^a J_{300} is the final value of cost function and J_1 is the initial value of cost function. $K1$ and $K2$ are the MAEs between simulated values and observations in “assimilated cities” and “checked cities,” respectively. $K3$ is the MAEs between the observations and simulated results in all the cities at the initial time.

Table 4. It is found that when the IPS is used, the effect of the data assimilation and the simulation results are better. As the $PM_{2.5}$ concentrations in winter are larger and the differences in concentration are steeper than spring, the MAEs are slightly larger than those of PEs aforementioned. In addition, it is proved that the inverted IC and SS are reasonable and the simulated results are the best in NPE1 using the same way aforementioned, which is not shown in this part.

5. Summary and Discussion

To estimate the parameters and simulate the $PM_{2.5}$ concentrations over China, a $PM_{2.5}$ adjoint model is set up in this paper.

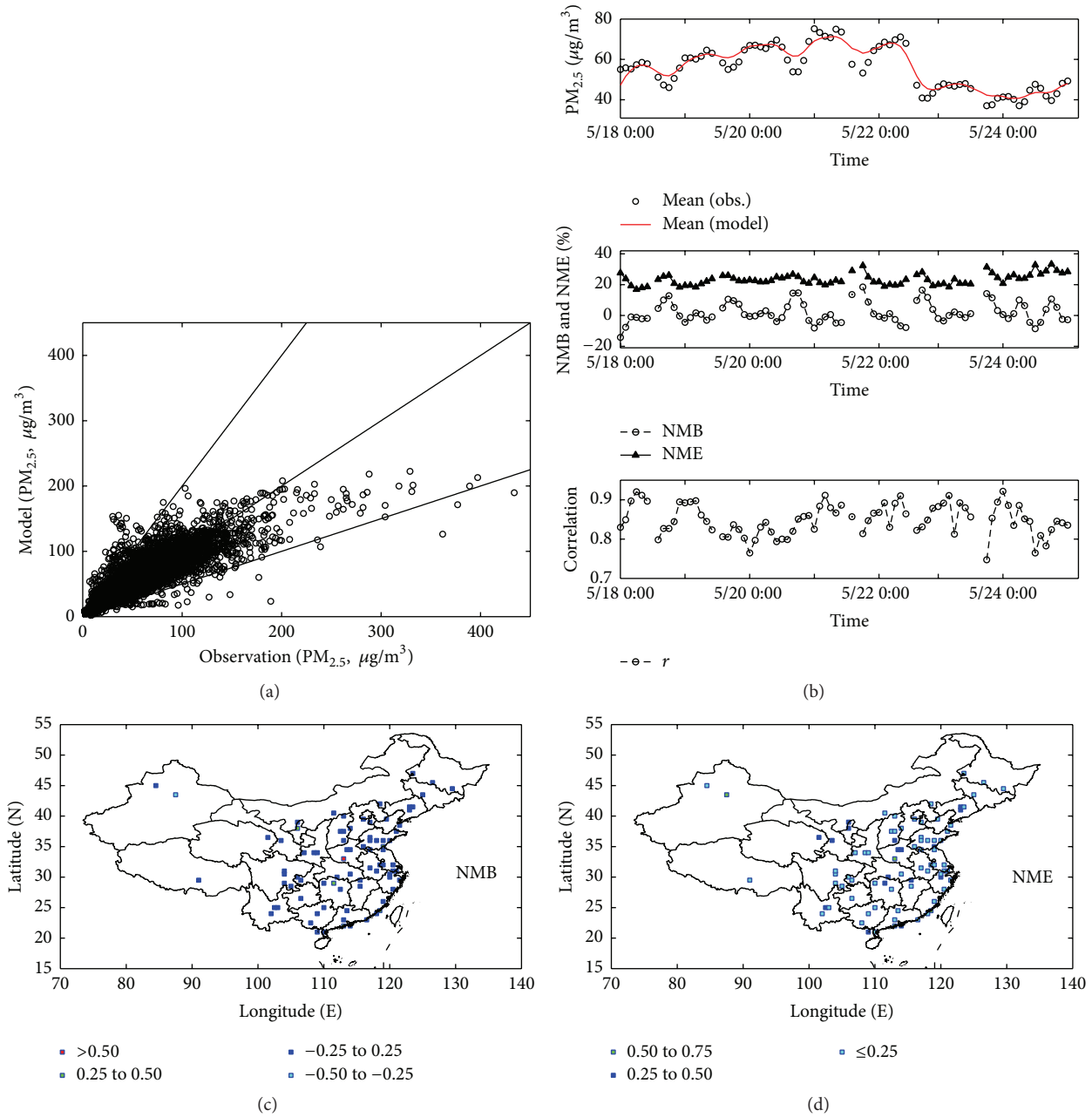


FIGURE 8: Comparison of the modeled and observed $PM_{2.5}$ concentrations in PE1: (a) scatterplot ($\mu g/m^3$) (the 1:2, 1:1, and 2:1 lines are shown for reference), (b) temporal variation of spatial mean, NMB, NME, and correlation, and spatial distribution of (c) NMB and (d) NME.

In this model, the IC and the SS are estimated by assimilating the observations with the adjoint method. In addition, an IPS is used in the estimation to decrease the ill-posedness of the inversion problem. Through TEs, the inversion ability of the adjoint model is verified and the effectiveness of the IPS is shown. In PEs, the IC and the SS are estimated in ten different modes. The simulated results indicate that when they are estimated simultaneously with IPS in PE1, the best results are obtained. In PE1 the inverted IC is better than that of other PEs, and the SS is accordant with the fact. In detail, the $PM_{2.5}$ concentrations in four representative cities

have the same trend with the observations. The simulated results in PE1 show that the model is able to capture a majority (95.4%) of $PM_{2.5}$ observations within a factor of 2, with NMB and NME of 1.26% and 23.08%, respectively. And whether in time or space domain, even on the whole, the $PM_{2.5}$ concentrations are simulated well in PE1. To further explain the conclusions in PEs, the NPEs are done in winter. And the same conclusions are obtained.

The $PM_{2.5}$ transport model in this paper is simple and the complex multiphase chemical pathways are lumped into a single term, SS. It is obvious that the SS is circumscribed

because the primary $PM_{2.5}$ is not obtained from direct emission observations and the chemical mechanism that simulates the formation of secondary $PM_{2.5}$ is not considered. However, the $PM_{2.5}$ concentrations over China are simulated well by estimating the IC and the SS using the adjoint method with IPS. It is shown that the adjoint method is a powerful way to estimate the parameters in the models and improve the simulated results by assimilating the observations. The adjoint method has a bright prospect in the atmospheric pollutants simulation and forecast model. In addition, the IPS presented in this paper is an effective method to decrease the ill-posedness of inverse problem and further improve the precision of parameters estimation and simulated results. In further studies, the selection of independent points in space will be optimized and the independent points will be even selected over time.

Conflict of Interests

The authors declare that there is no conflict of interests regarding the publication of this paper.

Acknowledgments

Partial support for this research was provided by the Natural Science Foundation of Shandong Province of China through Grant ZR2014DM017, the State Ministry of Science and Technology of China through Grant 2013AA122803, the National Natural Science Foundation of China through Grants 41371496 and 41206001, and Beijing Environment Foundation for Young Talents.

References

- [1] F. K. Duan, K. B. He, Y. L. Ma et al., "Concentration and chemical characteristics of $PM_{2.5}$ in Beijing, China: 2001-2002," *Science of the Total Environment*, vol. 355, no. 1-3, pp. 264-275, 2006.
- [2] C.-M. Wong, N. Vichit-Vadkan, H. Kan et al., "Public Health and Air Pollution in Asia (PAPA): a multicity study of short-term effects of air pollution on mortality," *Environmental Health Perspectives*, vol. 116, no. 9, pp. 1195-1202, 2008.
- [3] H. Kan, S. J. London, G. Chen et al., "Season, sex, age, and education as modifiers of the effects of outdoor air pollution on daily mortality in Shanghai, China: the Public Health and Air Pollution in Asia (PAPA) Study," *Environmental Health Perspectives*, vol. 116, no. 9, pp. 1183-1188, 2008.
- [4] A. Millman, D. Tang, and F. P. Perera, "Air pollution threatens the health of children in China," *Pediatrics*, vol. 122, no. 3, pp. 620-628, 2008.
- [5] S. Jayachandran, "Air quality and early-life mortality evidence from Indonesia's wildfires," *Journal of Human Resources*, vol. 44, no. 4, pp. 916-954, 2009.
- [6] K. Zhang, H. Wan, B. Wang, M. Zhang, J. Feichter, and X. Liu, "Tropospheric aerosol size distributions simulated by three online global aerosol models using the M7 microphysics module," *Atmospheric Chemistry and Physics*, vol. 10, no. 13, pp. 6409-6434, 2010.
- [7] K. Okada, M. Ikegami, Y. Zaizen, Y. Makino, J. B. Jensen, and J. L. Gras, "The mixture state of individual aerosol particles in the 1997 Indonesian haze episode," *Journal of Aerosol Science*, vol. 32, no. 11, pp. 1269-1279, 2001.
- [8] B. L. Zhuang, L. Liu, F. H. Shen, T. J. Wang, and Y. Han, "Semidirect radiative forcing of internal mixed black carbon cloud droplet and its regional climatic effect over China," *Journal of Geophysical Research D: Atmospheres*, vol. 115, no. 7, 1984.
- [9] B. K. Pun and C. Seigneur, "Sensitivity of particulate matter nitrate formation to precursor emissions in the California San Joaquin Valley," *Environmental Science & Technology*, vol. 35, no. 14, pp. 2979-2987, 2001.
- [10] M. J. Kleeman, G. R. Cass, and A. Eldering, "Modeling the air-borne particle complex as a source-oriented external mixture," *Journal of Geophysical Research: Atmospheres*, vol. 102, no. 17, pp. 21355-21372, 1997.
- [11] A. B. Hudischewskyj and C. Seigneur, "Mathematical modeling of the chemistry and physics of aerosols in plumes," *Environmental Science & Technology*, vol. 23, no. 4, pp. 413-421, 1989.
- [12] S. Yu, R. Mathur, K. Schere et al., "Evaluation of real-time $PM_{2.5}$ forecasts and process analysis for $PM_{2.5}$ formation over the eastern United States using the Eta-CMAQ forecast model during the 2004 ICARTT study," *Journal of Geophysical Research: Atmospheres*, vol. 113, no. 6, Article ID D06204, 2008.
- [13] C. Seigneur, "Current status of air quality models for particulate matter," *Journal of the Air & Waste Management Association*, vol. 51, no. 11, pp. 1508-1521, 2001.
- [14] Y. Zhang, M. Bocquet, V. Mallet, C. Seigneur, and A. Baklanov, "Real-time air quality forecasting, part I: history, techniques, and current status," *Atmospheric Environment*, vol. 60, pp. 632-655, 2012.
- [15] Y. Zhang, M. Bocquet, V. Mallet, C. Seigneur, and A. Baklanov, "Real-time air quality forecasting, part II: state of the science, current research needs, and future prospects," *Atmospheric Environment*, vol. 60, pp. 656-676, 2012.
- [16] A. M. M. Manders, M. Schaap, and R. Hoogerbrugge, "Testing the capability of the chemistry transport model LOTOS-EUROS to forecast PM_{10} levels in the Netherlands," *Atmospheric Environment*, vol. 43, no. 26, pp. 4050-4059, 2009.
- [17] M. Shrivastava, J. Fast, R. Easter et al., "Modeling organic aerosols in a megacity: comparison of simple and complex representations of the volatility basis set approach," *Atmospheric Chemistry and Physics*, vol. 11, no. 13, pp. 6639-6662, 2011.
- [18] M.-T. Chuang, Y. Zhang, and D. Kang, "Application of WRF/Chem-MADRID for real-time air quality forecasting over the Southeastern United States," *Atmospheric Environment*, vol. 45, no. 34, pp. 6241-6250, 2011.
- [19] J. Chen, J. Vaughan, J. Avise, S. O'Neill, and B. Lamb, "Enhancement and evaluation of the AIRPACT ozone and $PM_{2.5}$ forecast system for the Pacific Northwest," *Journal of Geophysical Research: Atmospheres*, vol. 113, no. 14, 2008.
- [20] C. Cai, C. Hogrefe, P. Katsafados et al., "Performance evaluation of an air quality forecast modeling system for a summer and winter season—photochemical oxidants and their precursors," *Atmospheric Environment*, vol. 42, no. 37, pp. 8585-8599, 2008.
- [21] S. A. McKeen, S. H. Chung, J. Wilczak et al., "Evaluation of several $PM_{2.5}$ forecast models using data collected during the ICARTT/NEAQS 2004 field study," *Journal of Geophysical Research: Atmospheres*, vol. 112, no. 10, Article ID D10S20, 2007.
- [22] C. Hogrefe, W. Hao, K. Civerolo et al., "Daily simulation of ozone and fine particulates over New York State: findings and challenges," *Journal of Applied Meteorology and Climatology*, vol. 46, no. 7, pp. 961-979, 2007.

- [23] D. Quélo, V. Mallet, and B. Sportisse, “Inverse modeling of NO_x emissions at regional scale over northern France: preliminary investigation of the second-order sensitivity,” *Journal of Geophysical Research: Atmospheres*, vol. 110, no. 24, Article ID D24310, 2005.
- [24] A. Hakami, D. K. Henze, J. H. Seinfeld et al., “Adjoint inverse modeling of black carbon during the Asian Pacific regional aerosol characterization experiment,” *Journal of Geophysical Research: Atmospheres*, vol. 110, no. 14, pp. 1–17, 2005.
- [25] K. Yumimoto and I. Uno, “Adjoint inverse modeling of CO emissions over Eastern Asia using four-dimensional variational data assimilation,” *Atmospheric Environment*, vol. 40, no. 35, pp. 6836–6845, 2006.
- [26] H. Elbern, A. Strunk, H. Schmidt, and O. Talagrand, “Emission rate and chemical state estimation by 4-dimensional variational inversion,” *Atmospheric Chemistry and Physics*, vol. 7, no. 14, pp. 3749–3769, 2007.
- [27] A. Sandu, W. Liao, G. R. Carmichael, D. K. Henze, and J. H. Seinfeld, “Inverse modeling of aerosol dynamics using adjoints: theoretical and numerical considerations,” *Aerosol Science and Technology*, vol. 39, no. 8, pp. 677–694, 2005.
- [28] K. Nester and H.-J. Panitz, “Sensitivity analysis by the adjoint chemistry transport model DRAIS for an episode in the Berlin Ozone (BERLIOZ) experiment,” *Atmospheric Chemistry and Physics*, vol. 6, no. 8, pp. 2091–2106, 2006.
- [29] T. Stavroukou and J.-F. Müller, “Grid-based versus big region approach for inverting CO emissions using Measurement of Pollution in the Troposphere (MOPITT) data,” *Journal of Geophysical Research: Atmospheres*, vol. 111, no. 15, Article ID D15304, 2006.
- [30] D. K. Henze, J. H. Seinfeld, and D. T. Shindell, “Inverse modeling and mapping US air quality influences of inorganic PM_{2.5} precursor emissions using the adjoint of GEOS-Chem,” *Atmospheric Chemistry and Physics*, vol. 9, no. 16, pp. 5877–5903, 2009.
- [31] L. Zhang, L. Liu, Y. Zhao et al., “Source attribution of PM_{2.5} pollution over North China using the adjoint method,” in *Proceedings of the American Geophysical Union Fall Meeting Abstracts*, vol. 1, p. 4, May 2014.
- [32] S. Capps, D. K. Henze, A. G. Russell et al., “Quantifying relative contributions of global emissions to PM_{2.5} air quality attainment in the US,” in *Proceedings of the American Geophysical Union Meeting Abstracts*, vol. 1, San Francisco, Calif, USA, December 2008.
- [33] W. W.-G. Yeh, “Review of parameter identification procedures in groundwater hydrology: the inverse problem,” *Water Resources Research*, vol. 22, no. 2, pp. 95–108, 1986.
- [34] D. S. Ullman and R. E. Wilson, “Model parameter estimation from data assimilation modeling: temporal and spatial variability of the bottom drag coefficient,” *Journal of Geophysical Research: Oceans*, vol. 103, no. 3, pp. 5531–5549, 1998.
- [35] A. W. Heemink, E. E. A. Mouthaan, M. R. T. Roest, E. A. H. Vollebregt, K. B. Robaczewska, and M. Verlaan, “Inverse 3D shallow water flow modelling of the continental shelf,” *Continental Shelf Research*, vol. 22, no. 3, pp. 465–484, 2002.
- [36] J. Zhang and Y. P. Wang, “A method for inversion of periodic open boundary conditions in two-dimensional tidal models,” *Computer Methods in Applied Mechanics and Engineering*, vol. 275, pp. 20–38, 2014.
- [37] W. J. Qu, R. Arimoto, X. Y. Zhang et al., “Spatial distribution and interannual variation of surface PM₁₀ concentrations over eighty-six Chinese cities,” *Atmospheric Chemistry and Physics*, vol. 10, no. 12, pp. 5641–5662, 2010.
- [38] L. Yu and J. J. O’Brien, “On the initial condition in parameter estimation,” *Journal of Physical Oceanography*, vol. 22, no. 11, pp. 1361–1364, 1992.
- [39] B. D. Grover, M. Kleinman, N. L. Eatough et al., “Measurement of total PM_{2.5} mass (nonvolatile plus semivolatile) with the Filter Dynamic Measurement System tapered element oscillating microbalance monitor,” *Journal of Geophysical Research: Atmospheres*, vol. 110, no. 7, Article ID D07S03, 2005.

Research Article

Climatological Features of Korea-Landfalling Tropical Cyclones

Jae-Won Choi,¹ Yumi Cha,² Hae-Dong Kim,³ and Sung-Dae Kang⁴

¹National Institute of Meteorological Research, Jeju 63568, Republic of Korea

²National Typhoon Center, Korea Meteorological Administration, Jeju 63614, Republic of Korea

³Department of Global Environment, Keimyung University, Daegu 42601, Republic of Korea

⁴Green Simulation, Co., Ltd., SK HUB-SKY, 1523 Jungangdae-ro, Dongrae-gu, Busan 46227, Republic of Korea

Correspondence should be addressed to Hae-Dong Kim; khd@kmu.ac.kr

Received 6 July 2015; Accepted 24 August 2015

Academic Editor: Xiaofeng Li

Copyright © 2016 Jae-Won Choi et al. This is an open access article distributed under the Creative Commons Attribution License, which permits unrestricted use, distribution, and reproduction in any medium, provided the original work is properly cited.

The present study analyzed the interdecadal variation by applying the statistical change-point analysis to the frequency of the tropical cyclone (TC) that landed in the Korean Peninsula (KP) for the recent 54 years (1951 to 2004) and performed cluster classification of the Korea-landfall TC tracks using a Fuzzy Clustering Method (FCM). First, in the interdecadal variation analysis, frequency of TC that landed in the KP was largely categorized into three periods: high frequency period from 1951 to 1965, low frequency period from 1966 to 1985, and high frequency period from 1986 to 2004. The cluster analysis result of the Korea-landfall TC tracks produced the optimum number of clusters as four. In more detail, Cluster A refers to a pattern of landing in the southern coast in the KP starting from East China Sea followed by heading north while Cluster B refers to a pattern of landing in the west coast of the Korean Peninsula, also starting from East China Sea followed by heading north. Cluster C refers to a pattern of landing in the southern region of the west coast in the KP moving from mainland China while Cluster D refers to a pattern of landing in the mid-north region of the west coast in the Korean Peninsula, also moving from mainland China.

1. Introduction

Although many studies on tropical cyclone (TC) that affected the Korean Peninsula have been conducted [1, 2], few studies have been done on TC that landed in the Korean Peninsula. As a study on TC that landed in the Korean Peninsula, Choi and Kim [3] analyzed interannual and interdecadal variation of frequency of TC, track of TC, and intensity of TC, which landed in the Korean Peninsula for recent 54 years (1951 to 2004), and conducted analysis of large-scale atmospheric circulations with regard to causes of variation of the Korean Peninsula landed TC activity. Choi et al. [4] also performed cluster analysis on TCs that landed in the Korean Peninsula for recent 54 years using a Fuzzy Clustering Method and analyzed large-scale atmospheric circulations of the TC track characteristics for each cluster.

Furthermore, Park and Moon [5] analyzed TCs that affected the Korean Peninsula, starting from the tropical and subtropical western North Pacific, climatologically, and

studied the characteristics of rainfall due to TC in relation to the track or kinetic energy. Lee et al. [6] analyzed the central pressure and the maximum sustained wind speed statistically about all the TCs that approached mid-latitude regions in East Asia and affected the Korean Peninsula for 30 years from 1960 to 1989 thereby classifying the typhoons according to their movement characteristic and presenting the large-atmospheric circulations characteristics of the representative case for each category. Kim et al. [7] analyzed the long-term change of TCs using data obtained from 1951 to 2001, proposing the location and intensity of the subtropical western North Pacific high (SWNPH) among the large-scale atmospheric circulations as the most influential factors that affected the course of TC, and studied how the variation of the large-scale atmospheric circulations influenced the TC track that affected the Korean Peninsula. As other studies on TC in relation to its damage, Yoo and Jung [8] presented the damage caused by typhoon “Saomai” and “Prapiroon,” which affected the Korean Peninsula in 2000, and compared them with other

typhoons that had similar tracks in the past. Furthermore, Park et al. [1] categorized the TC track that affected the Korean Peninsula into 7 types and showed that typhoons that affected Korea via China and via Japan accounted for 24.6% and 22.9%, respectively. That is, they claimed that about 50% of TCs that affected the Korean Peninsula approached Korea via the neighboring countries.

TC is one of the major weather phenomena that incurs human casualties and property damage as it passes through the Korean Peninsula and the surrounding regions mainly in June to September, and intensity of typhoon and hurricane has been intensified more and more [9, 10]. Weather phenomena that incurred the most damage in Korea for the last 10 years (1998 to 2007) are heavy rainfall and TC, which account for 97% of entire human casualties and 89% of property damage. In particular, property damage and human casualties caused by TCs that landed in Korea were 53% and 40% [11]. A study on current status analysis of meteorological disasters that occurred in Korea from 1987 to 2003 [12] showed that 2002 had the largest damage due to Typhoon Rusa (0215), about 6.1153 trillion Korean Won (KRW), followed by 2003 of 4.38321 trillion KRW due to Typhoon Maemi (0314). In addition, Kwon et al. [13] presented that the damage caused by typhoon ‘‘Rusa’’ accounted for 0.9% of GDP in Korea, which was considerably high compared to the recent economic growth rate. As described above, TCs that landed in Korea caused much damage and incurred economic loss greatly so that many studies on TCs have been conducted. Therefore, the present study also examines the characteristics of the Korea-landfall TC activity in order to reduce property damage and human casualties caused by the TCs that landed in the Korean Peninsula every year.

This paper is organized as follows. In Section 2, data and analysis method are introduced. In Section 3, interannual and interdecadal variation of the Korea-landfall TC activity are analyzed. In Section 4, cluster analysis is performed with the Korea-landfall TC track and analysis of the TC activity on each classified cluster is conducted. Finally, in Section 5, conclusion is presented.

2. Data and Methods

2.1. Data. The TC data in this study was obtained from the best-track of TC provided by Regional Specialized Meteorological Center- (RSMC-) Tokyo Typhoon Center. This data consists of TC name, latitude and longitude location of TC, TC central pressure, and TC maximum sustained wind speed (MSWS), which were observed in every 6 hours for 54 years from 1951 to 2004. TC is generally classified into four classes by the criteria of MSWS: Tropical Depression (TD: $MSWS < 17 \text{ m s}^{-1}$), Tropical Storm (TS: $17 \text{ m s}^{-1} \leq MSWS \leq 24 \text{ m s}^{-1}$), Severe Tropical Storm (STS: $25 \text{ m s}^{-1} \leq MSWS \leq 32 \text{ m s}^{-1}$), and Typhoon (TY: $MSWS \geq 33 \text{ m s}^{-1}$). Along with the four classes of TC above, this study included extratropical cyclone which was transformed from TC for analysis. This was because such extratropical cyclone also incurred great damage on property and human in the mid-latitude regions in East Asia.

Moreover, this study also used the variables of geopotential height (gpm) data from National Centers for Environmental Prediction-National Center for Atmospheric Research (NCEP-NCAR) reanalysis [14, 15]. This NCEP-NCAR reanalysis data consisted of spatial resolution such as latitude and longitude $2.5^\circ \times 2.5^\circ$ and 17 vertical layers.

2.2. Methods. In order to detect the significant climate regime shift of the Korea-landfall TC frequency, this study performed statistical change-point analysis used by Ho et al. [16]. This statistical method is known to be effective in finding the significant climate regime shift objectively from time series data such as TC frequency. More information about this statistical method can be found in Elsner et al. [17] and Chu [18].

As one of the indexes applied to the statistical change-point analysis, Accumulated Cyclone Energy (ACE) was calculated [19]:

$$\text{Accumulated Cyclone Energy (ACE)} = \sum \frac{V^2}{10^4}. \quad (1)$$

The ACE is calculated by summing the squares of the MSWS (V) of greater than every TS at 6-hour intervals on all the KP landfalling TCs for each corresponding decade. The numbers are usually divided by 10,000 to make them more manageable. The unit of ACE is 10^4 kt^2 and for use as an index, the unit is assumed.

This study used the Student’s t -test to determine significance [20]. In case that two independent time series follow a t distribution and their time averages are denoted as \bar{x}_1 and \bar{x}_2 , respectively, the test statistic is given by

$$t = \frac{\bar{x}_1 - \bar{x}_2}{(s_1^2/n_1 + s_2^2/n_2)^{1/2}}, \quad (2)$$

where S_1 and S_2 are standard deviations and n_1 and n_2 are numbers of the two time series, respectively. From the above formula, if the absolute value of t is greater than threshold values with a level of significance, the null hypothesis would be rejected at the α ($\times 100$)% significance level.

In this study, TC life time was defined as a stage from formation to decay observed in every 6 hours in the best-track data from RSMC-Tokyo Typhoon Center. TC recurring location was defined as a location where direction of TC was changed from northwest movement to northeast movement.

3. Interannual and Interdecadal Variations

3.1. Change-Point Analysis. Figure 1 shows total Korea-landfall TC frequency (TDET) and Korea-landfall TC frequency (TSTY) having intensity above TS, Accumulated Cyclone Energy (ACE) for TCs having intensity above TS, and Total Moving Distance (TMD) during the TC life. Overall, all the four indexes showed high values until the mid-1960s while showing low values from the late 1960s till the mid-1980s and high values again after the late 1980s. In addition to tropical cyclones, it is also of interest to investigate whether there is any change-point in the SST records or

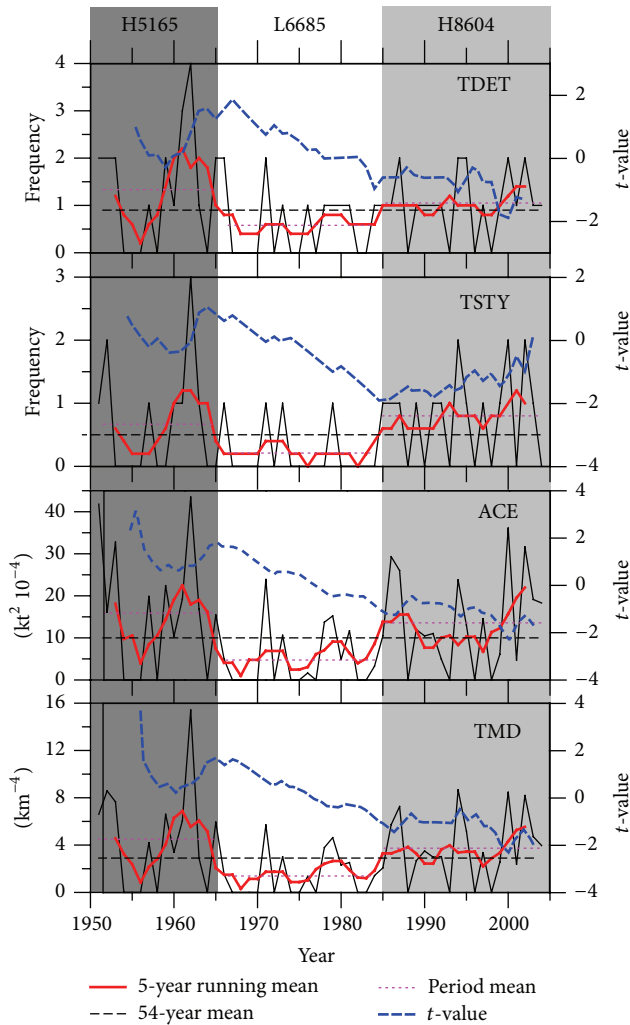


FIGURE 1: Decadal variation related to a Korea-landfall TC activity. Indices in order from an upper-most side are the total TC frequency (F-TDEC), the TC frequency with intensity greater than tropical storm (TS) (F-TSTY), Accumulated Cyclone Energy (ACE) of TC with intensity greater than TS, and total moving distance (TMD) for the TC lifetime, respectively. The periods of H5165, L6685, and H8604 indicate the first high frequency period for 1951–1965, the low frequency period for 1966–1985, and the second high frequency period for 1986–2004 defined by *t*-value (thick blue line) of the statistical change-point analysis. The thick red, black dashed, and red dotted lines denote 5-year running mean, 54-year mean, and each period mean, respectively.

typhoon passage frequency series. Because these variables do not follow a Poisson distribution, we use a different method to detect climate regime shifts in the temperature or passage frequency series: using a log-linear regression model in which a step function is expressed as an independent variable. If the estimated slope is at least twice as large as its standard error, one may reject the null hypothesis (i.e., the slope being zero) at the 5% significance level. Therefore, this study conducted statistical change-point analysis in order to determine whether climate regime shift existed in the four

indexes for the recent 54 years. The analysis results showed that the climate regime shift existed in 1965 and 1985 as shown in the figure. It meant that, in the four variables, high values existed from 1951 to 1965, low values from 1966 to 1985, and high values again from 1986 to 2004. Therefore, in this study, interdecadal variation of the Korea-landfall TC frequency was categorized into high frequency of 1951–1965 (hereafter referred to as H5165), low frequency period of 1966–1985 (hereafter referred to as L6685), and high frequency period of 1986–2004 (hereafter referred to as H8604).

3.2. TC Intensity. TC frequency and TC intensity for the three periods defined above were examined (see Figure 2). First, the number of the total Korea-landfall TC frequencies during the recent 54 years was 51, and 30 TCs, which accounted for 60% of them, had landed in Korea with intensity above TS (see Figure 2(a)). The total Korea-landfall TC frequencies for the three periods of H5165, L6685, and H8604 were 20 TCs, 11 TCs, and 20 TCs, showing that total Korea-landfall TC frequency in the high frequency period was almost twice the number in the low frequency period. However, TC frequency that landed in Korea with more than TS intensity in the two high frequency periods showed that H5165 had 10 TCs while H8604 had 15 TCs, indicating that more intensified TCs landed in Korea recently. In the L6685 period, only 4 TCs that landed in Korea had more than TS intensity. Regarding TC intensity, when TC landed in Korea, the climatological mean of the TC central pressure was analyzed as 985.1 hPa (see Figure 2(b)). The averages of TC central pressure in the three periods of H5165, L6685, and H8604 were 987.8 hPa, 993.5 hPa, and 977.8 hPa, indicating that recent landed TCs had more intensity. Regarding TC lifetime, the H8604 period had the longest life time as 13.3 days (see Figure 2(c)).

This high frequency of TC with strong intensity which recently landed in the Korean Peninsula can be found in 5-year variation of the case where TCs with TD intensity landed in Korea and the case where TCs with above TS intensity landed in Korea (see Figure 3). Frequency of TC with TD intensity that landed in Korea decreased gradually during the recent 54 years whereas frequency of TC with strong intensity above TS that landed in Korea increased rapidly since the late 1980s.

3.3. TC Track. The Korea-landfalling TC track for the three periods was analyzed (see Figure 4). During the H5165 period, TCs landed mainly in the mid-north region in the west coast, while, during the L6685 period, TCs landed mainly in the southern region of the west coast. During the H8604 period, TCs landed in the southern region of the west coast and the south coast mainly. That is, TC's landfalling showed a pattern that landfalling location moved from the west sea to the south sea more and more in recent activities. Therefore, this study analyzed the regression mean track for the three periods to determine the average movement during the three periods (thick solid line). As shown in the figure, during H5165 period, TC landed in the central region of the west coast, during the L6685 period, the southern region of the west coast, and during the H8604 period, the

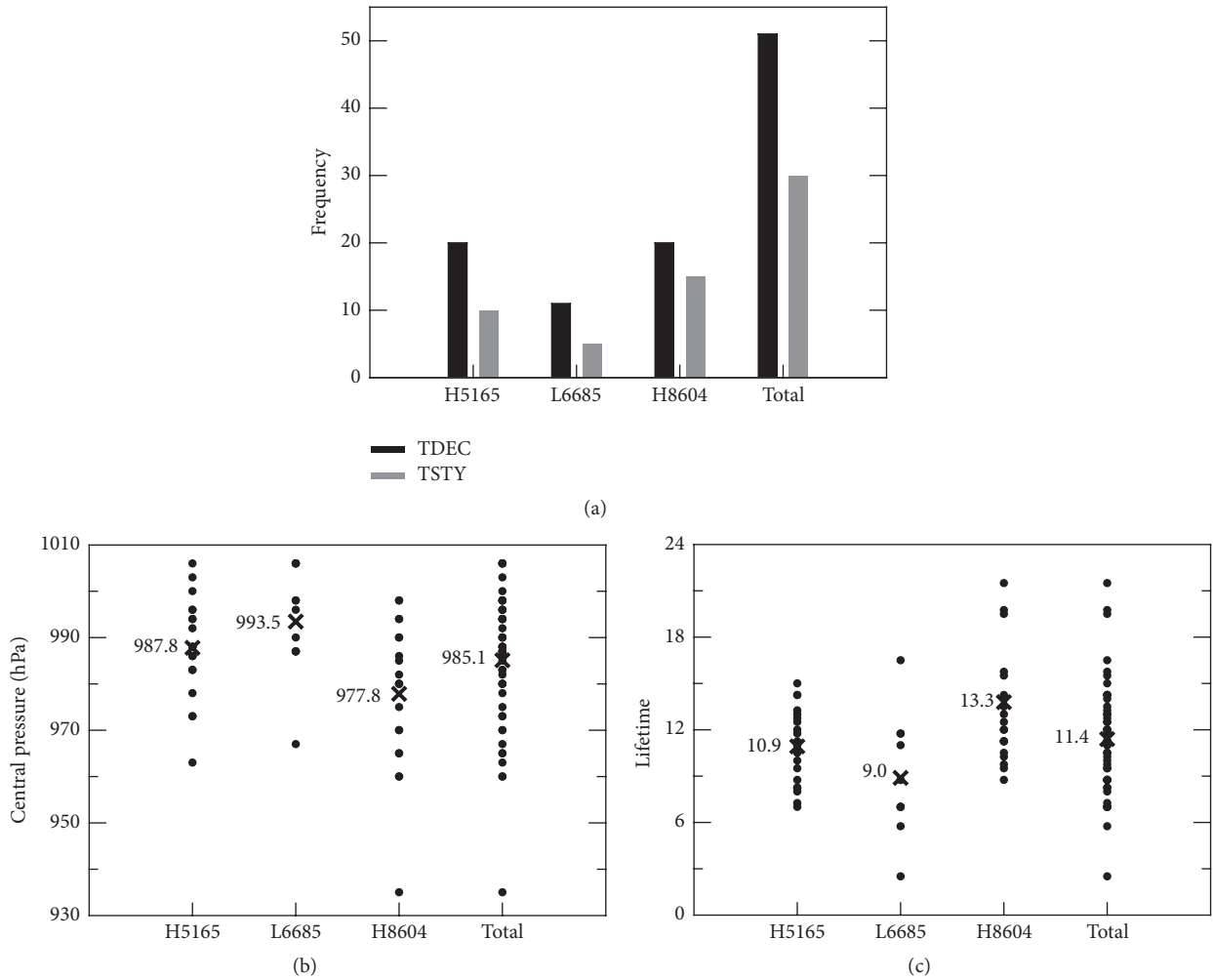


FIGURE 2: The (a) frequency, (b) central pressure at landfall, and (c) lifetime of the Korea-landfall TC in each period. × marks in central pressure and lifetime denote averages in each period.

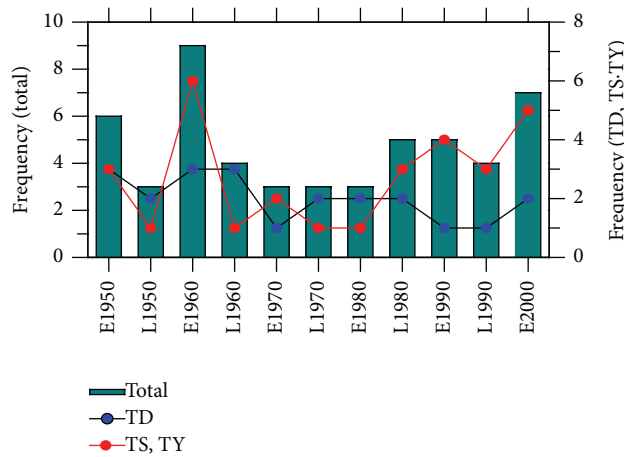


FIGURE 3: 5-year variation of the landfall frequency of Korea-landfall TCs. The bar and blue and red lines denote a 5-year total frequency, a TD and extratropically transitioned cyclone frequency, and a TS and TY frequency, respectively. Capital E and L denote “early” and “late,” respectively.

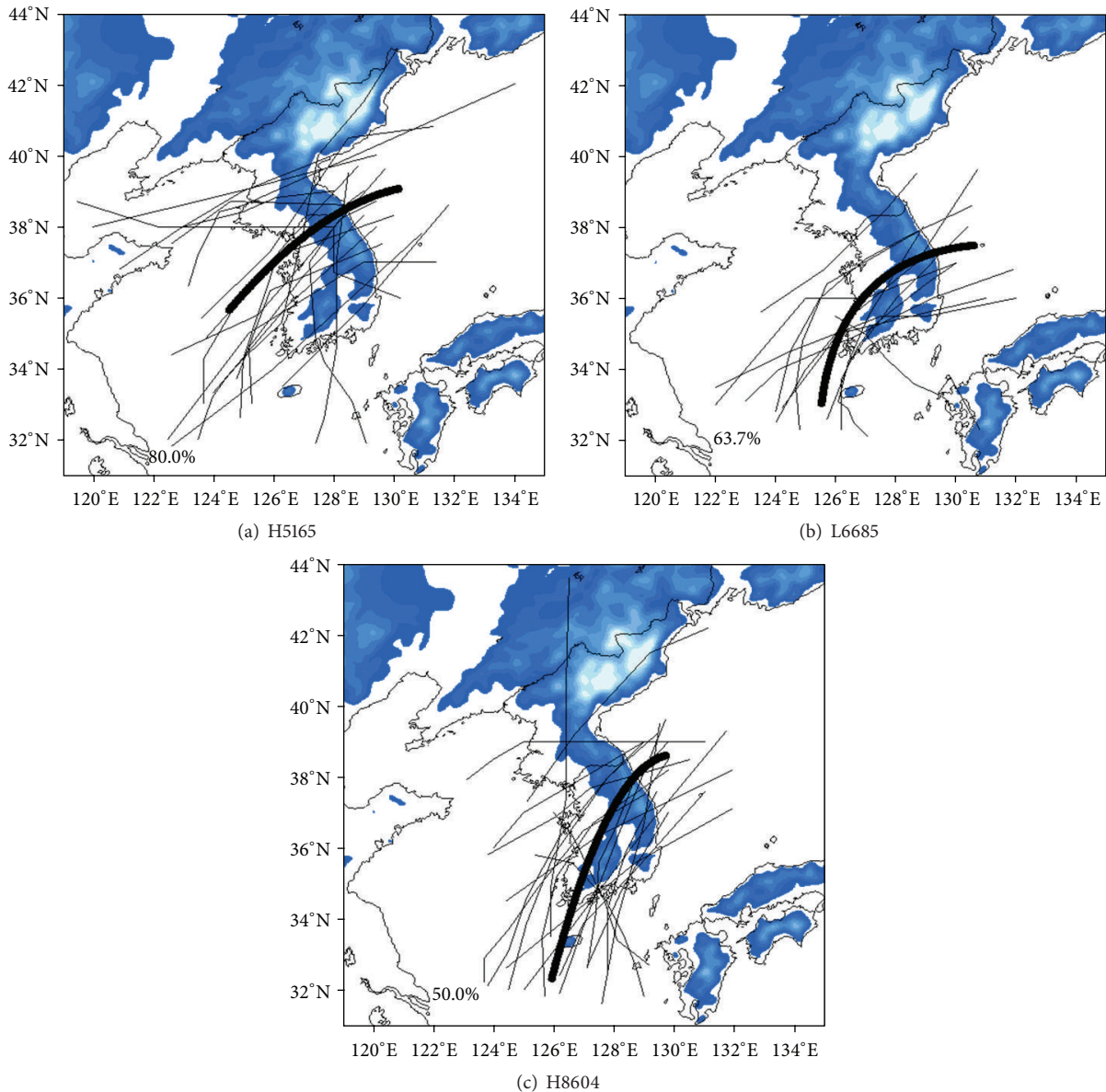


FIGURE 4: Landfalling (left) of a Korea-landfall TC for the periods of (a) H5165, (b) L6685, and (c) H8604. The thick lines denote the mean regression tracks and the number in the lower-left corner denotes the ratio of the landfalling TC frequency at the west coast of Korea to the total TC frequency in each period. Shaded areas indicate topography higher than 200 m.

western region of the south coast mainly. Therefore, the Korea-landfall TC track has been changed to move easterly more for 54 years.

This trend of change in the Korea-landfall TC track was also found in 10-year variation (see Figure 5). The mean regression track analyzed in every 10 years showed that the Korea-landfall location was moved easterly more and more in recent years.

This study also examined the TC full-track variation for the three periods (see Figure 6). The important point of this analysis was to find out the change in TCs frequency that passed through mainland China before they landed in Korea.

During the H5165 period, 12 TCs out of 20 TCs (60.0%) had passed through the inland of mainland China before they landed in Korea, while, during the L6685 period, 4 TCs out of 11 TCs (36.4%) and, during the H8604 period, only 6 TCs out of 20 TCs (30.0%) had passed the heart of mainland China, indicating that more and more TCs had not passed through the heart of mainland China but via the east coast of China before they landed in the Korean Peninsula in recent years. Therefore, the reason for the strong intensity of TC that landed in Korea recently was due to obtaining sufficient energy from the sea as they moved over the sea rather than via mainland China prior to Korea-landfall.

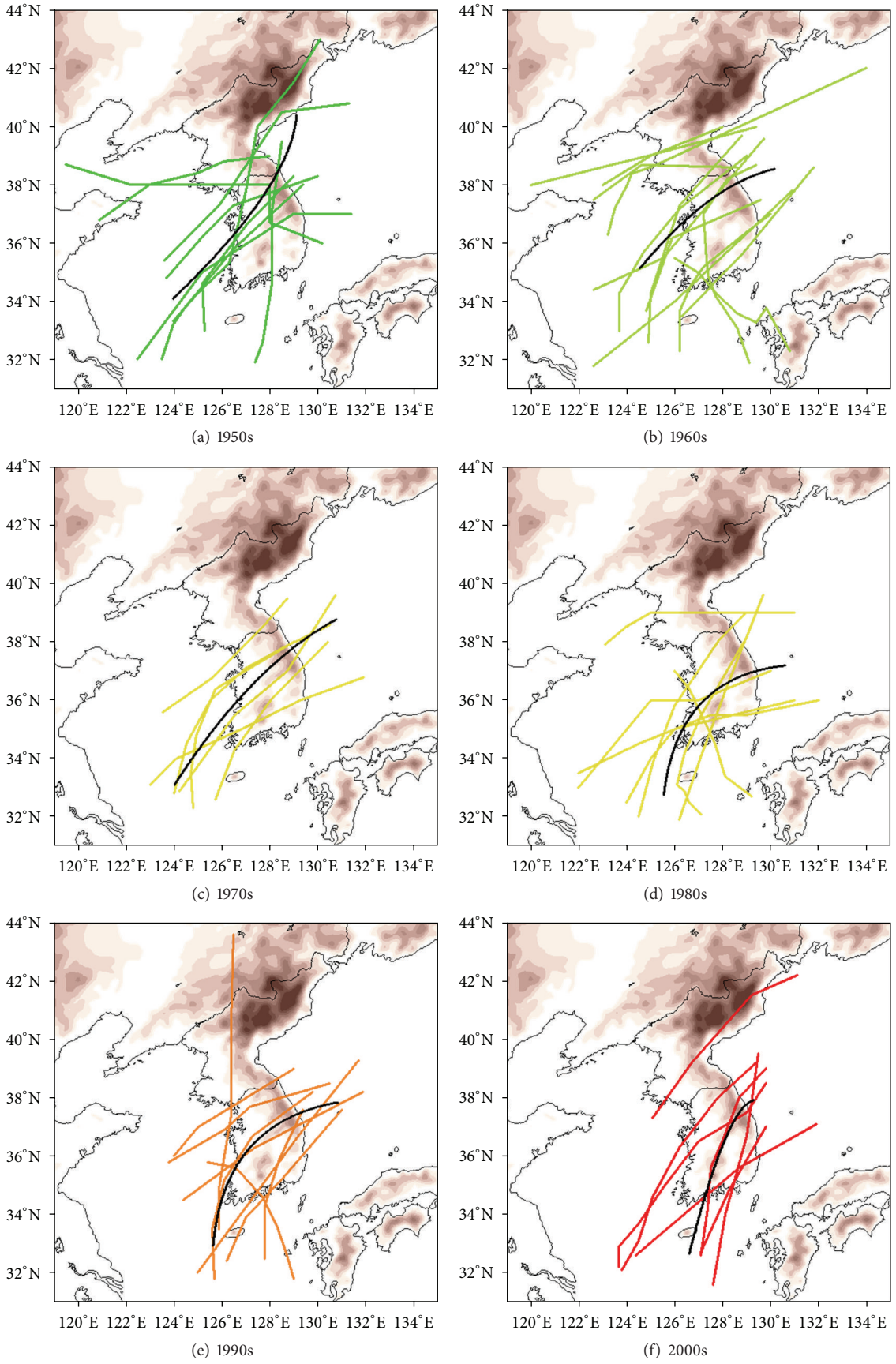


FIGURE 5: Continued.

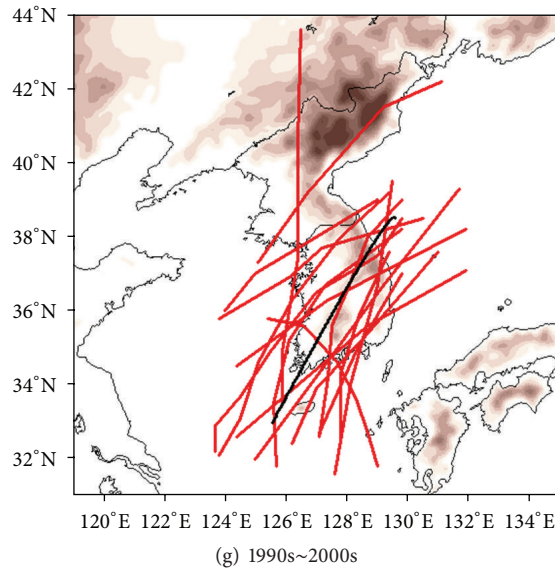


FIGURE 5: Decadal variation of the landfalling track of Korea-landfall TCs. Thick black lines denote regression mean tracks. Shaded areas indicate topography higher than 200 m.

Such variation trend of the Korea-landfall TC full-track can be seen in the 10-year variation (see Figure 7). Prior to the 1980s, high frequency of TCs via mainland China before landing in Korea was found but, since the 1990s, this was decreased rapidly.

3.4. Large-Scale Atmospheric Condition. In order to determine the cause of the Korea-landfall TC intensity and TC track variations during the three periods, averaged 500 hPa geopotential height over the three periods was examined (see Figure 8). The ridge of the SWNPH (brown solid line) was developed westerly up to mainland China during the H5165 and L6685 periods whereas it was retreated easterly up to the southwest sea in Japan. Accordingly, the Korea-landfall TC track displayed a characteristic of moving easterly in recent years and frequency of TCs via mainland China before Korea-landfall decreased more and more in recent years. Such variation trend of the Korea-landfall TC full-track influenced the intensity of TCs upon Korea-landfall. Moreover, development of the SWNPH in the east-west direction also influenced the TC recurving location so that recurving occurred largely in mainland China during the H5165 and L6685 periods whereas recurving occurred mainly in East China Sea during the H8604 period (dots in Figure 8).

4. Classification of TC Tracks

4.1. Fuzzy Clustering. This study introduced a Fuzzy Clustering Method (FCM) to conduct cluster analysis for Korea-landfall TC tracks. This analysis method is different compared to the Classical Clustering Method (CCM). For example, assuming that TC genesis location is classified into four clusters as shown in Figure 9 and object 1 (TC 1) is located

between A and C groups, cluster analysis may generate errors due to object 1 which is ambiguous for cluster classification in CCM. On the contrary, the FCM can show the probability of object 1 on group that object 1 may belong so that it helps an analyzer to decide whether object 1 is removed from analysis or included to other groups. More information regarding the FCM can be found in studies of Kim et al. [21] and Kim et al. [22]. Therefore, in this study, we briefly explain the FCM as follows: applying vector empirical orthogonal function (EOF) analysis to the latitude-longitude center position of the Korea-landfall TCs, the principal components (PCs) corresponding to each TC track are obtained. These PCs imply the eigen-characteristics of each track. Using the PCs, a dissimilarity index between the tracks is constructed. Then, fuzzy clustering analysis is performed using the dissimilarity index as an input of the algorithm. The optimal cluster number is determined by examining the silhouette coefficient [23]. Although the silhouette coefficient in this study was the largest in the third cluster, the fourth cluster was consistent with our current study course and was selected.

4.2. Patterns of TC Tracks. By performing the FCM, silhouette coefficient is produced, which can determine the optimal number of clusters (see Figure 10). The higher the silhouette coefficient is, the more optimal the number of clusters is. As shown in the figure, the result indicated three clusters as the optimal cluster number but this study selected four clusters as the optimal cluster number due to the following reasons. Figure 11 shows the Korea-landfall TC tracks when dividing the cluster into three. Overall, the cluster seemed well classified according to the landfall location. In case of Cluster 1, TCs showed a pattern of moving northerly from East China Sea to landing in the south and west sea in the

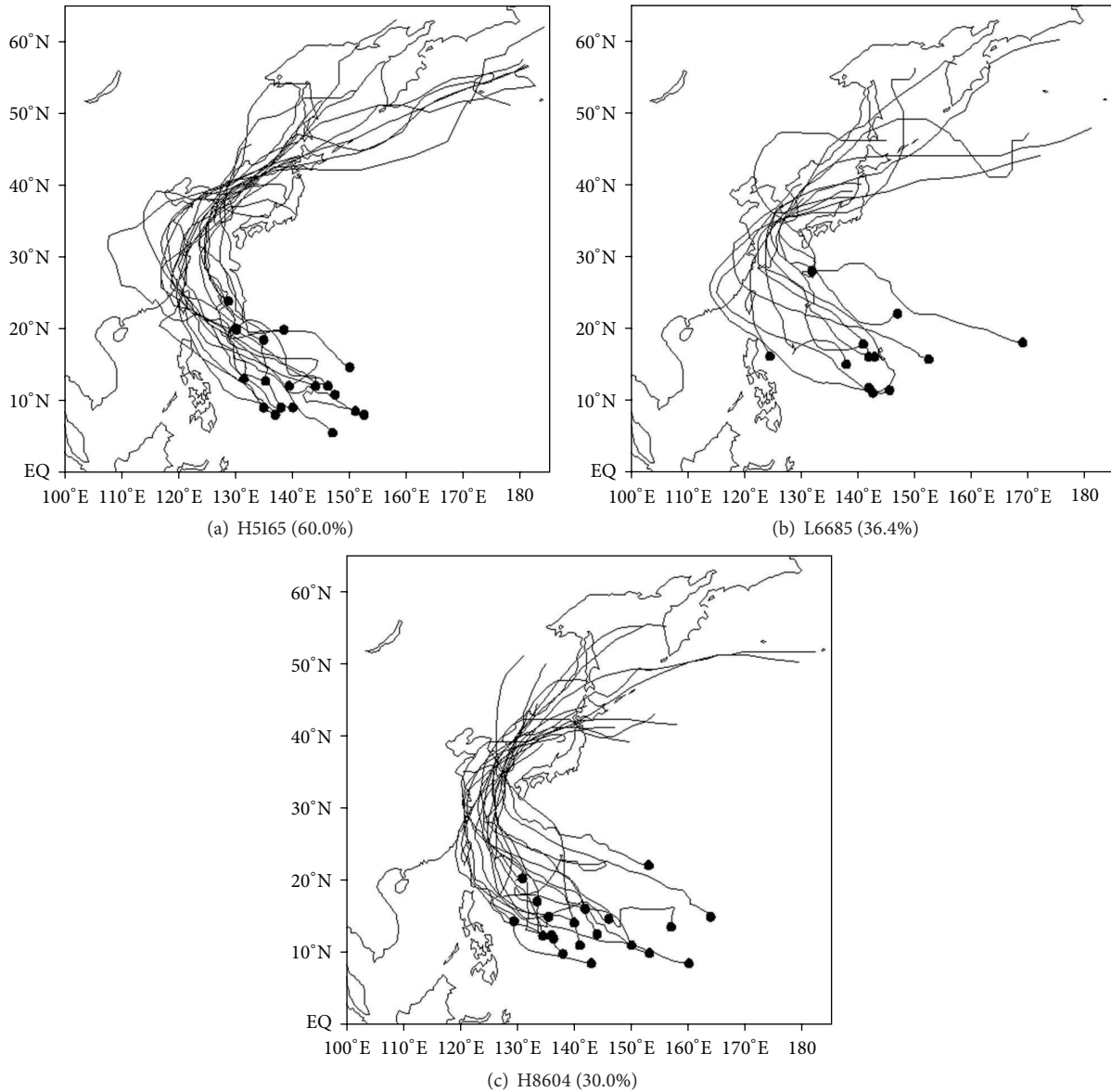


FIGURE 6: Full-tracks of a Korea-landfall TC for the periods of (a) H5165, (b) L6685, and (c) H8604. Dots are the genesis location of the Korea-landfall TC and the number in the upper-left corner denotes the ratio of a TC passage frequency over mainland China to the total TC frequency in each period.

Korean Peninsula. In case of Cluster 2, TCs showed a pattern of moving from mainland China to landing in the southern region of the west coast in the Korean Peninsula. In case of Cluster 3, TCs also showed a strong tendency to moving from mainland China to landing in the mid-north region of the west coast in the Korean Peninsula. However, the result of cluster analysis revealed that Cluster 1 included too many objects (TCs) compared to Cluster 2 and Cluster 3 clearly.

Therefore, this study classified the Korea-landfall TC tracks using four clusters (see Figure 12). As a result, Cluster 1 in Figure 11 was named as Cluster A and Cluster B while Cluster 2 and Cluster 3 changed their name to Cluster C and Cluster D, respectively. That is, Cluster 1 was divided into two clusters (Cluster A and Cluster B). Accordingly, the

number of objects (TCs) in each cluster was now distributed somewhat evenly. Thus, although the silhouette coefficient proposed three clusters as the optimal cluster number, this study selected four clusters as the optimal number of clusters due to the above reason. The study of the characteristics of TC track in each cluster showed that Cluster A showed a pattern of moving northerly from East China Sea to landing in the south coast of the Korean Peninsula (see Figure 12(a)) while Cluster B also showed a pattern of moving northerly from East China Sea to landing in the west coast in the Korean Peninsula (see Figure 12(b)). Cluster C showed a pattern of moving from mainland China to landing in the southern region of the west coast in the Korean Peninsula (see Figure 12(c)), while Cluster D also showed a pattern

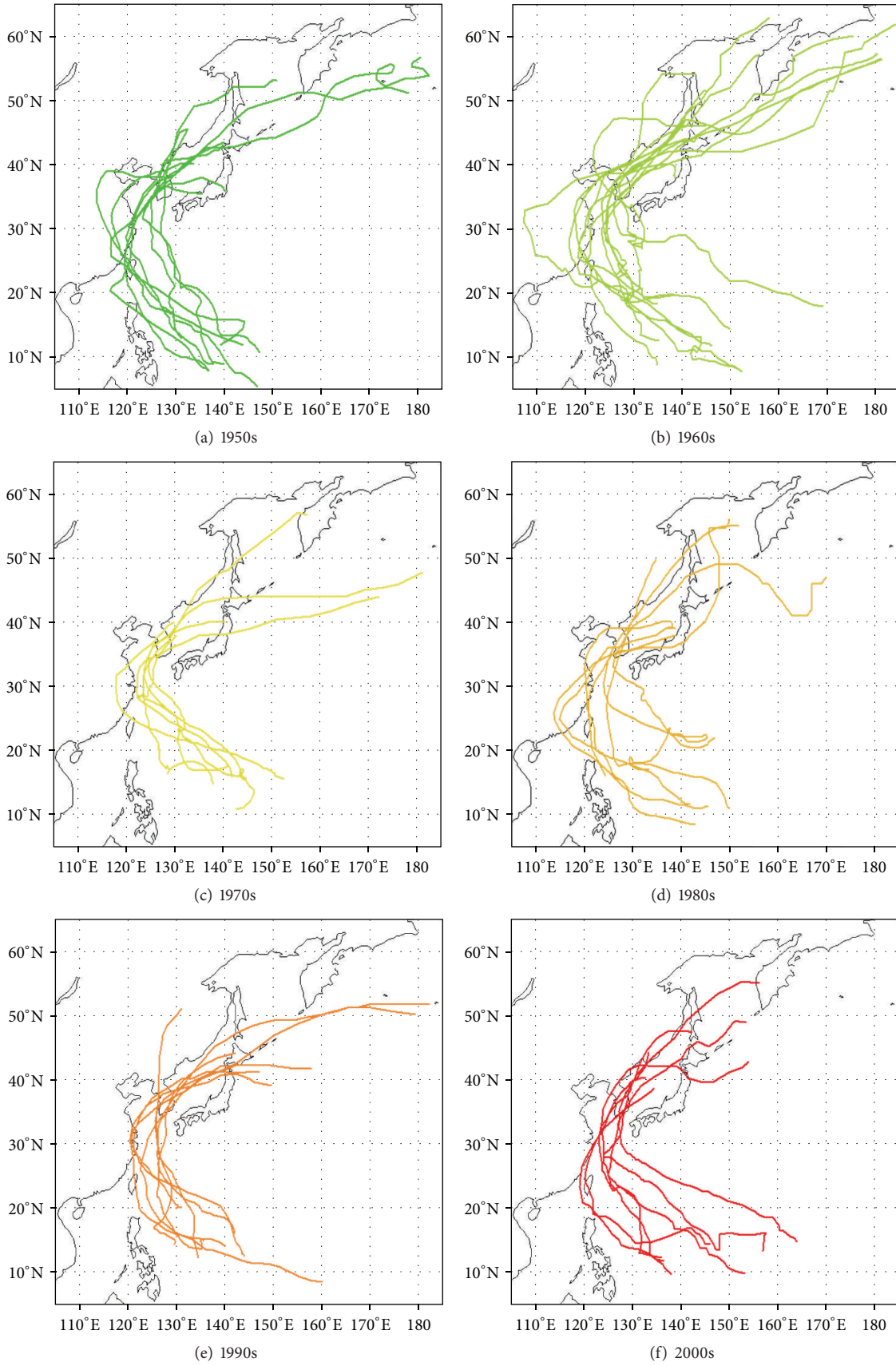


FIGURE 7: Continued.

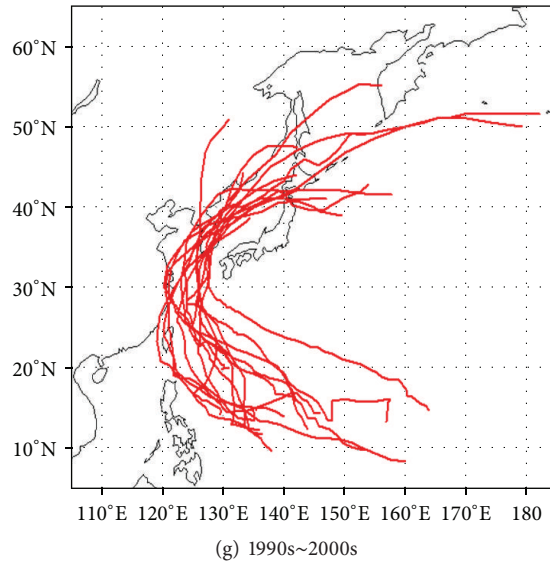


FIGURE 7: Same as Figure 5, but for TC full-track.

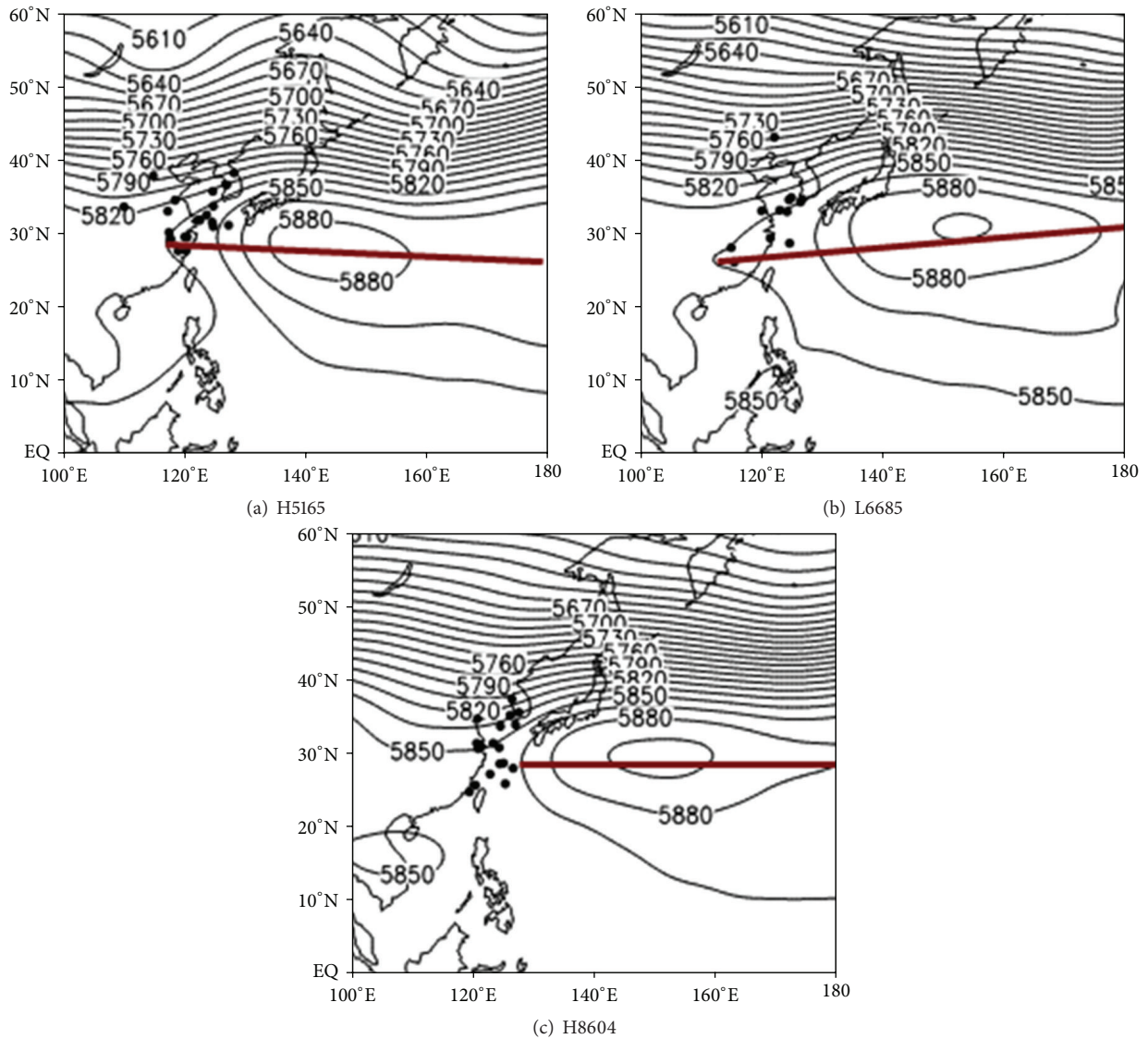


FIGURE 8: Composites of geopotential heights at 500 hPa for the periods of (a) H5165, (b) L6685, and (c) H8604. Dots denote recurring locations of TCs. Brown solid lines denote ridges of WNPH.

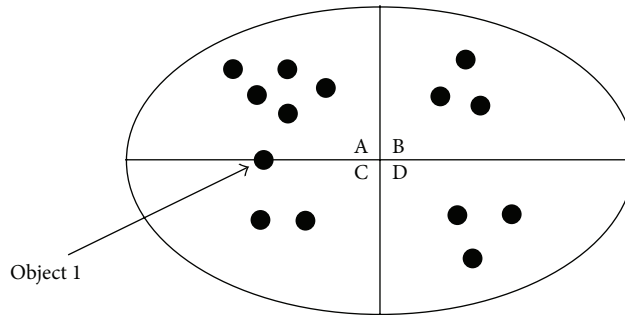


FIGURE 9: Example for the explanation of Fuzzy Clustering Method. Dots denote TC genesis locations in Areas A, B, C, and D.

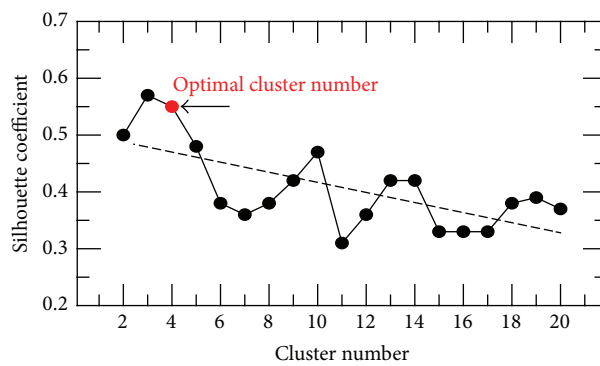


FIGURE 10: Silhouette coefficient (solid line with dots) at each cluster number using the Fuzzy Clustering Method (FCM) and its trend (dashed line). In this study, the optimal cluster number (red circle) was selected as four clusters.

of moving from mainland China to landing in the mid-north region of the west coast in the Korean Peninsula (see Figure 12(d)). The four clusters above could be classified largely into two groups: one is a pattern via mainland China before landing in Korea and the other is a pattern of moving northerly from East China Sea.

This study analyzed the Korea-landfall TC full-track based on the four clusters (see Figure 13). Any of TCs in Cluster A and Cluster B, which moved northerly from East China Sea, did not pass through mainland China whereas many TCs in Cluster C and Cluster D, which showed a pattern of moving from mainland China, showed a tendency of passing through mainland China prior to Korea-landfall.

As analyzed earlier, passing through mainland China prior to Korea-landfall could influence intensity of Korea-landfall TCs. Therefore, this study analyzed 5-year variation of Korea-landfall TC frequency as it divided TCs into Cluster A and Cluster B (hereafter referred to as C-AB), which did not pass through mainland China before landing in Korea and Cluster C and Cluster D (hereafter referred to as C-CD), which passed through mainland China (see Figure 14). C-CD, which passed through mainland China, showed decreasing frequency more and more in recent years (blue bar graph) whereas C-AB, which did not pass through mainland China,

showed a trend of increasing frequency more and more in recent years (red bar graph). This result is well matched with the previous analysis that more and more Korea-landfall TCs do not pass through mainland China in recent years. Therefore, intensity of TCs in C-AB, which did not pass through mainland China, may have higher possibility of strong intensity than C-CD.

5. Summary

The present study analyzed the interdecadal variation by applying the statistical change-point analysis to the frequency of TC that landed in the Korean Peninsula for the recent 54 years (1951 to 2004) and performed cluster classification of the Korea-landfall TC tracks using a Fuzzy Clustering Method (FCM).

First, in the interdecadal variation analysis, frequency of TC that landed in the Korean peninsula was largely categorized into three periods: high frequency period (H5165) from 1951 to 1965, low frequency period (L6685) from 1966 to 1985, and high frequency period (H8604) from 1986 to 2004. The pattern of the Korea-landfall TC track in the three periods showed that TC in the H5165 period landed in the mid-north region of the west coast in the Korean

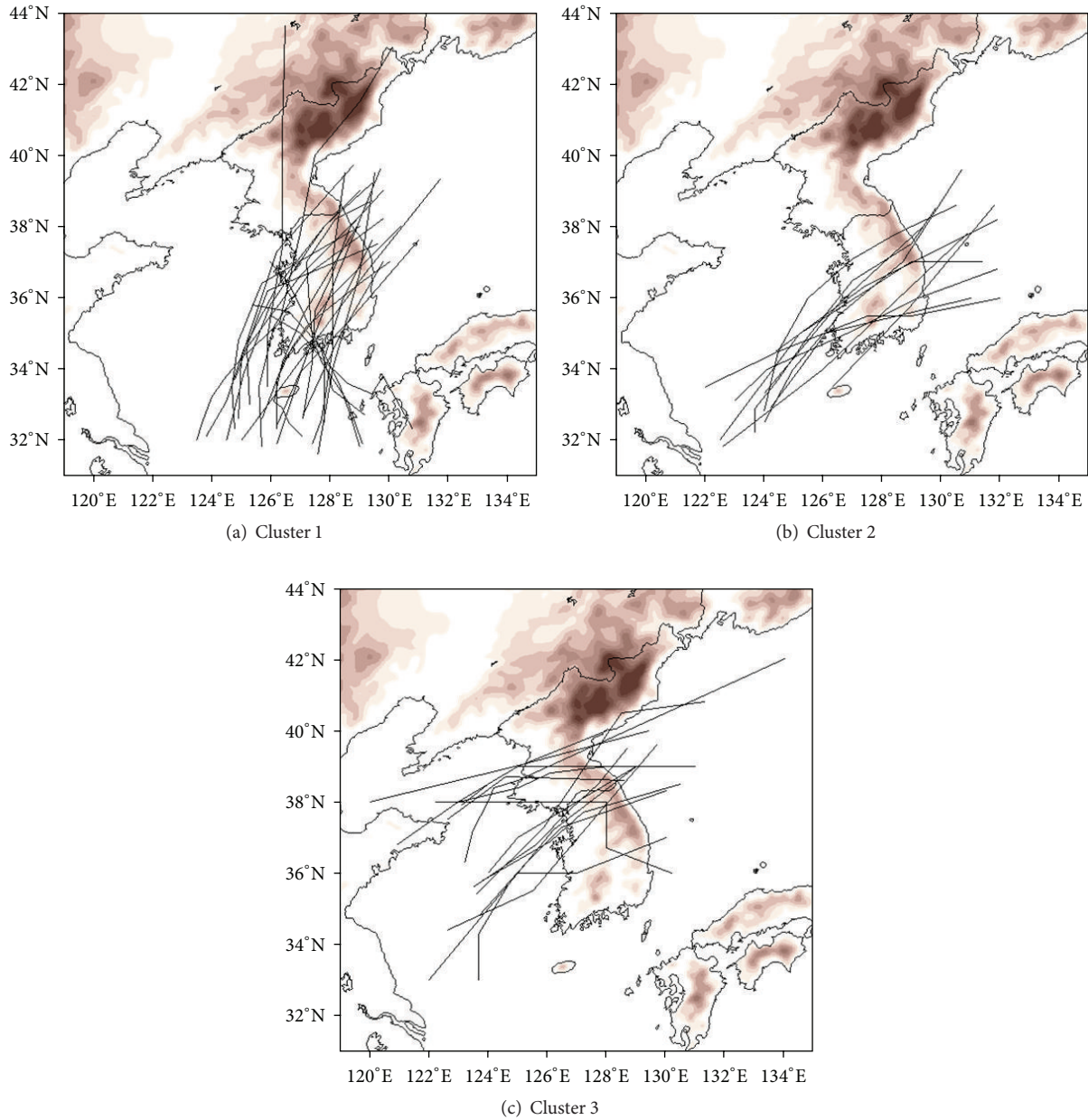


FIGURE 11: Landfalling tracks of Korea-landfall TCs classified into three clusters. Shaded area indicates topography higher than 200 m above the sea level.

Peninsula, TC in the L6685 period landed in the southern region of the west coast, and TC in the H8604 period landed in the southern region of the west coast and the south coast. This meant that the Korea-landfall location of TCs tended to move easterly gradually. This tendency of moving easterly of Korea-landfall location was also analyzed in 10-year variation of the Korea-landfall TC track. The result of the Korea-landfall TC full-track analysis during the three periods showed that frequency of TC, which passed through mainland China before landing in the Korean Peninsula, has decreased. Therefore, intensity of TCs during the H8604

period, which has the lowest frequency of passing through mainland China, was the strongest.

Silhouette coefficient, which was produced by the cluster analysis result on the Korea-landfall TC tracks, suggested three clusters as the optimal cluster number. However, the number of objects (TCs) in Cluster 1, which moved northerly from East China Sea and landed in the southern region of the west coast and south coast in the Korean Peninsula, was significantly larger than the number of objects in Cluster 2, which moved from mainland China and landed in the southern region of the west coast in the Korean Peninsula,

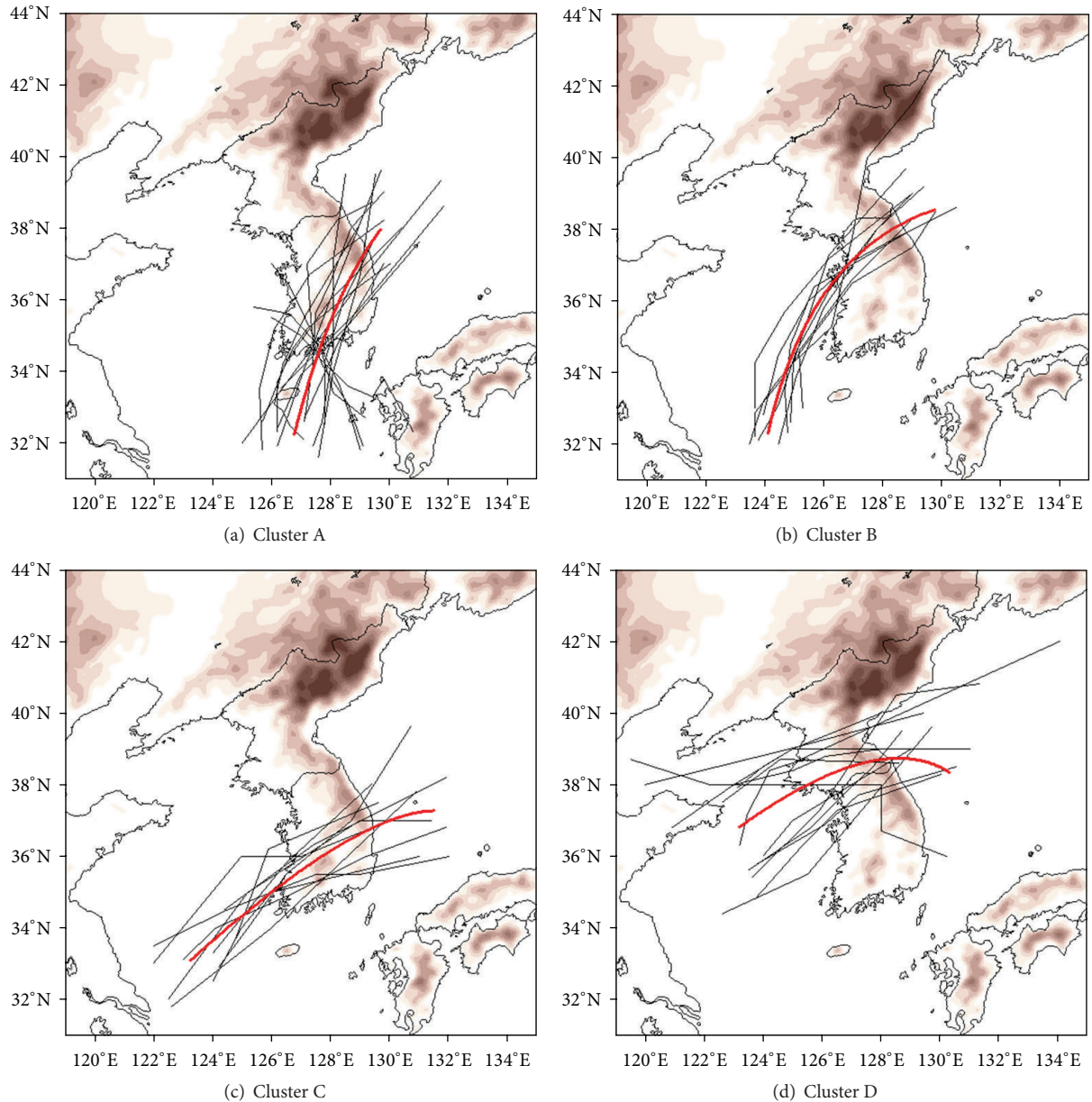


FIGURE 12: Same as Figure 11, but for four clusters. Thick red lines denote mean regression tracks. Shaded area indicates topography higher than 200 m above the sea level.

or the number of objects in Cluster 3, which also moved from mainland China and landed in the mid-north region of the west coast in the Korean Peninsula. Accordingly, 4 clusters were selected as the optimum number of clusters. Cluster 1 in the three clusters was divided into Cluster A, which moved northerly from East China Sea and landed in the south coast in the Korean Peninsula, and Cluster B, which also moved northerly from East China Sea and landed in the west coast in the Korean Peninsula, while Cluster 2 and Cluster 3 were named as Cluster C and Cluster D, respectively. Therefore, the divided four clusters were classified largely into two groups: one is a pattern showing moving northerly from

East China Sea prior to landing in Korea and the other is a pattern of moving from mainland China before landing in Korea. In Clusters A and B (C-AB), which start TCs from East China Sea followed by heading north, there were no TC that passed through mainland China before it landed in the Korean Peninsula whereas many TCs that passed through mainland China were found in Clusters C and D (C-CD). The 5-year variation of TC frequency between the two groups showed that TC frequency of C-AB group, which do not pass through mainland China, has increased more and more until recently, which is related to the strengthening of intensity of TC that landed recently in the Korean Peninsula.

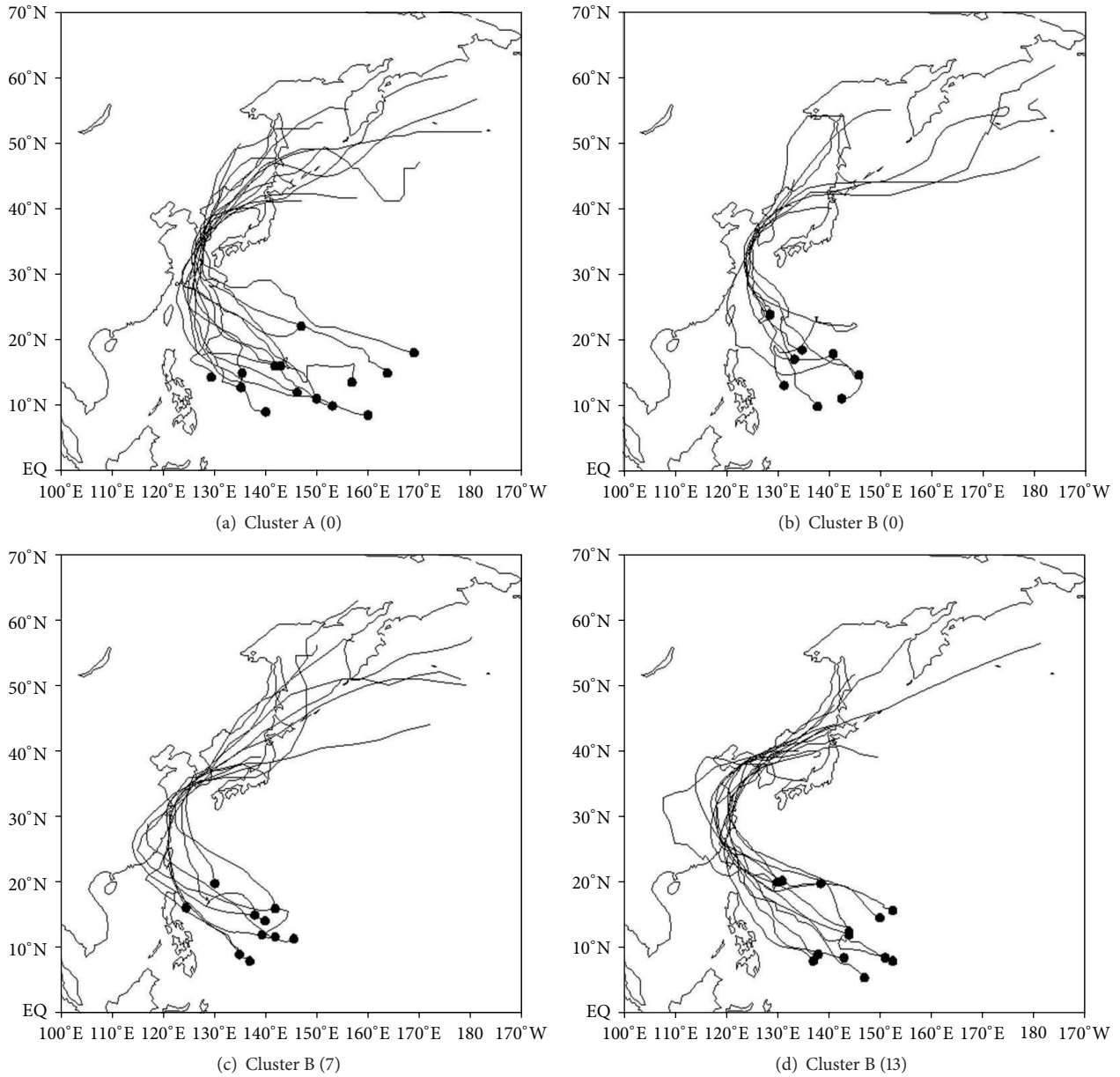


FIGURE 13: Same as Figure 12 but for the full-track. Small solid dots denote each TC genesis location of Korea-landfall TCs, respectively. The numbers in the parentheses represent TC frequencies without passing through mainland China.

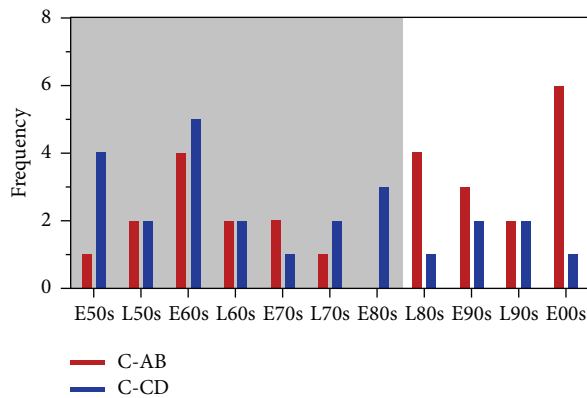


FIGURE 14: 5-year variation of the landfalling frequency of C-AB and C-CD of Korea-landfall TCs. The E and L characters mean “early” and “late,” respectively. For example, E50s (L50s) denotes early (late) 1950s.

Conflict of Interests

The authors declare that there is no conflict of interests regarding the publication of this paper.

Acknowledgments

This work (15-2-40-41) was supported by Researcher Program through grant funded by the DEGEC. The authors thank Dr. Joo-Hong Kim of Seoul National University for providing the program of fuzzy clustering analysis.

References

- [1] J. K. Park, B. S. Kim, W. S. Jung, E. B. Kim, and D. G. Lee, "Change in statistical characteristics of typhoon affecting the Korean Peninsula," *Atmosphere*, vol. 16, pp. 1–17, 2006.
- [2] K. S. Choi and T. R. Kim, "Regime shift of the early 1980s in the characteristics of the tropical cyclone affecting Korea," *Journal of Korean Earth Science Society*, vol. 32, no. 5, pp. 453–460, 2011.
- [3] K. S. Choi and B. J. Kim, "Climatological characteristics of tropical cyclones making landfall over the Korean Peninsula," *Asia-Pacific Journal of Atmospheric Sciences*, vol. 43, pp. 97–109, 2007.
- [4] K.-S. Choi, B.-J. Kim, C.-Y. Choi, and J.-C. Nam, "Cluster analysis of tropical cyclones making landfall on the Korean Peninsula," *Advances in Atmospheric Sciences*, vol. 26, no. 2, pp. 202–210, 2009.
- [5] J. K. Park and S. E. Moon, "The climatological characteristics of typhoon visit to Korea," *Journal of the Korean Meteorological Society*, vol. 31, pp. 139–147, 1995.
- [6] D. K. Lee, D. E. Jang, and T. K. Wee, "Typhoons approaching Korea, 1960–1989 part I: statistics and synoptic overview," *Journal of the Korean Meteorological Society*, vol. 28, pp. 133–147, 1992.
- [7] H.-S. Kim, C.-H. Ho, J.-H. Kim, and P.-S. Chu, "Track-pattern-based model for seasonal prediction of tropical cyclone activity in the western North Pacific," *Journal of Climate*, vol. 25, no. 13, pp. 4660–4678, 2012.
- [8] S. A. Yoo and J. S. Jung, "Investigation on typhoon affecting Korean Peninsula in 2000," *Journal of the Korean Meteorological Society*, vol. 10, pp. 302–304, 2000.
- [9] K. Emanuel, "Increasing destructiveness of tropical cyclones over the past 30 years," *Nature*, vol. 436, no. 7051, pp. 686–688, 2005.
- [10] P. J. Webster, G. J. Holland, J. A. Curry, and H.-R. Chang, "Changes in tropical cyclone number, duration, and intensity in a warming environment," *Science*, vol. 309, no. 5742, pp. 1844–1846, 2005.
- [11] K. Y. Park, "Meteorological disaster and measures," *Meteorological Specialist*, vol. 41, pp. 36–43, 2008.
- [12] J. K. Park, E. S. Chang, and H. J. Choi, "Analysis on meteorological disaster in Korean Peninsula," *Journal of the Korean Environmental Society*, vol. 14, pp. 613–619, 2005.
- [13] W. T. Kwon, K. O. Boo, and I. H. Heo, "Climatological characteristics for 10 years in Korean Peninsula," *Journal of Korea Water Resources Society*, vol. 8, pp. 278–280, 2007.
- [14] E. Kalnay, M. Kanamitsu, R. Kistler et al., "The NCEP/NCAR 40-year reanalysis project," *Bulletin of the American Meteorological Society*, vol. 77, no. 3, pp. 437–471, 1996.
- [15] R. Kistler, W. Collins, S. Saha, and et al., "The NCEP/NCAR 50-year reanalysis," *Bulletin of the American Meteorological Society*, vol. 82, no. 2, pp. 247–267, 2001.
- [16] C.-H. Ho, J.-J. Baik, J.-H. Kim, D.-Y. Gong, and C.-H. Sui, "Interdecadal changes in summertime typhoon tracks," *Journal of Climate*, vol. 17, no. 9, pp. 1767–1776, 2004.
- [17] J. B. Elsner, T. Jagger, and X.-F. Niu, "Changes in the rates of North Atlantic major hurricane activity during the 20th century," *Geophysical Research Letters*, vol. 27, no. 12, pp. 1743–1746, 2000.
- [18] P.-S. Chu, "Large-scale circulation features associated with decadal variations of tropical cyclone activity over the central North Pacific," *Journal of Climate*, vol. 15, no. 18, pp. 2678–2689, 2002.
- [19] G. D. Bell, M. S. Halpert, R. C. Schnell et al., "Climate assessment for 1999," *Bulletin of the American Meteorological Society*, vol. 81, pp. 1–50, 2000.
- [20] D. S. Wilks, *Statistical Methods in the Atmospheric Sciences*, Academic Press, 1995.
- [21] H.-S. Kim, J.-H. Kim, C.-H. Ho, and P.-S. Chu, "Pattern classification of typhoon tracks using the fuzzy c-means clustering method," *Journal of Climate*, vol. 24, no. 2, pp. 488–508, 2011.
- [22] J. H. Kim, C. H. Ho, and J. J. Baik, "Study on typhoon around Korean Peninsula during the period from 1951 to 2001," *Journal of the Korean Meteorological Society*, vol. 12, pp. 436–439, 2002.
- [23] L. Kaufman and P. J. Rousseeuw, *Finding Groups in Data*, Wiley-Interscience, 1990.

Research Article

Latitudinal Change of Tropical Cyclone Maximum Intensity in the Western North Pacific

Jae-Won Choi,¹ Yumi Cha,² Hae-Dong Kim,³ and Sung-Dae Kang⁴

¹National Institute of Meteorological Research, Jeju, Republic of Korea

²National Typhoon Center, Korea Meteorological Administration, Jeju, Republic of Korea

³Department of Global Environment, Keimyung University, Daegu, Republic of Korea

⁴Green Simulation, Co., Ltd., SK HUB-SKY, 1523 Jungangdae-ro, Dongrae-gu, 102-3004 Busan, Republic of Korea

Correspondence should be addressed to Hae-Dong Kim; khd@kmu.ac.kr

Received 6 July 2015; Revised 23 July 2015; Accepted 29 July 2015

Academic Editor: Xiaofeng Li

Copyright © 2016 Jae-Won Choi et al. This is an open access article distributed under the Creative Commons Attribution License, which permits unrestricted use, distribution, and reproduction in any medium, provided the original work is properly cited.

This study obtained the latitude where tropical cyclones (TCs) show maximum intensity and applied statistical change-point analysis on the time series data of the average annual values. The analysis results found that the latitude of the TC maximum intensity increased from 1999. To investigate the reason behind this phenomenon, the difference of the average latitude between 1999 and 2013 and the average between 1977 and 1998 was analyzed. In a difference of 500 hPa streamline between the two periods, anomalous anticyclonic circulations were strong in 30°–50°N, while anomalous monsoon trough was located in the north of South China Sea. This anomalous monsoon trough was extended eastward to 145°E. Middle-latitude region in East Asia is affected by the anomalous southeasterlies due to these anomalous anticyclonic circulations and anomalous monsoon trough. These anomalous southeasterlies play a role of anomalous steering flows that make the TCs heading toward region in East Asia middle latitude. As a result, TCs during 1999–2013 had higher latitude of the maximum intensity compared to the TCs during 1977–1998.

1. Introduction

The number of tropical cyclones generated in the western North Pacific is about 30 cyclones every year, which is relatively more than TCs generated in other oceans (Indian Ocean, Eastern Pacific, and western North Pacific). Most of them are landed on a number of East Asia nations including Korea that are adjacent to the western North Pacific, thereby resulting in economic damage and casualties enormously. In particular, TC intensity has a positive correlation with damages it causes so that a large number of studies have been conducted on the variation of the western North Pacific TC intensity over the past few years. Some studies including Emanuel [1] showed that as the sea surface temperature in the western North Pacific increased in recent years TC intensity has also been strengthened.

In the Western Pacific region, a large amount of property damages and casualties has occurred every year due to tropical cyclones (TCs) generated in the tropical and subtropical

western North Pacific. In Japan, 10 TCs were landed in 2004, which was still recorded the highest year that is not broken [2]. In Korea, Typhoon Rusa was landed in 2002, pouring the maximum accumulated rainfall of 870.5 mm in Gangneung, which was the all-time record high up until now in Korea [3]. In Taiwan, Typhoon Morakot was landed in 2009, pouring rainfall in one day that was equivalent to an annual amount of accumulated rainfall [4]. In the Philippines, about 10 TCs were landed every year, which revealed the highest TC frequency in East Asia [5]. In particular, super Typhoon “Haiyen” struck the Leyte province located in the middle of the Philippines in November 8, 2013, which was the largest TC ever recorded in the Philippines. The maximum sustained wind speed of the TC was recorded as 379 km per hour, which was 1.5 times stronger than “Maemi” the worst TC ever recorded in Korea and even worse than “Katrina” in the USA. “Haiyen” caused a large number of casualties as well as property damage as 6 m high tidal waves with storing wind swept over the middle of the Philippines. Although it is not

confirmed yet, the number of deaths and missing caused by the TC was over 5,000 and victims over 4 million suffered from interruption of electricity and water supply as well as food shortage. In particular, about 95% of Tacloban city was completely destroyed and changed into a huge landfill [6, 7].

However, it is difficult to make a conclusion definitely regarding the increase of TC intensity due to the lack of reliable long-term observation data with respect to the variation of TC intensity [8]. This is because TCs are affected by various factors other than sea surface temperature such as vertical wind shear and lower-level relative vorticity in addition to inaccuracies of the TC observation data [9]. Nonetheless, recently published studies reported that frequency of strong TCs that had more than category 4, their duration, and their intensity have increased since 2000s and many researchers view that this phenomenon is due to the effect of global warming caused by fossil fuel emission [10]. Chu and Clark [11] also proved that the recent increase of influence by TCs with strong intensity was also found in the central Pacific noticeably. In general, global warming due to the greenhouse effect has been accepted as the reason for such increase of TC frequency and intensity in recent years.

Recently, Kamahori et al. [12] emphasized that it was necessary to be prepared for TCs with strong intensity since intense TC days have increased steadily for the recent 30 years. Similar to the above study result, Elsner et al. [13] also reported that all TC basins except for South Pacific Ocean basin experienced increased intensity of strong TCs. In particular, they proved that such increase was more evident in North Atlantic and North Indian Ocean basins.

In contrast with the above results, there are other studies that claim that TC intensity has become weakened. Landsea et al. [14] emphasized that intense hurricane frequency has decreased in the Atlantic Ocean over the last 50 years. Ho et al. [15] also proved through statistical change-point analysis that TC annual frequency and TC intensity have decreased in the East China Sea since the mid-1970s while the declining trend was more evident near the Philippines. As an extension of a study by Chan and Shi [16], Chan [17] fitted TC intensity data in Northwest Pacific, which was updated up to the early 2000s, with a second-order polynomial equation and proved that there has rather been decreased trend TC intensity since the mid-1990s. Such decreasing trend in TC intensity has also been observed in the South China Sea for the past 40 years [18].

It is also found that there are studies claiming that there has been no trend change in TC intensity. Lighthill [19] showed that there has been no significant change in TC intensity in North Atlantic, Northeast, and Northwest Pacific basins. Klotzbach [20] also mentioned that there has been no increasing trend in accumulated cyclone energy (ACE) in each TC basin over the last 20 years (1990–2006) except for minor increase of ACE in categories 4-5 hurricanes. Bove et al. [21] also discovered that there was no increasing trend in hurricane intensity landed on the Gulf of Mexico over the past century.

Recent study result also showed that latitudes that showed TC maximum intensity have been globally moved northerly [22, 23]. They pointed out that the reason for the northerly

shift was related to northerly shift of tropic regions due to global warming. However, their study also did not provide large-scale environments for the clear reason for the recent northerly latitude shift of TC maximum intensity. Thus, the present study aims to determine whether recent northerly latitude shift of TC maximum intensity is found and to analyze large-scale environments for this shift.

Section 2 in the present study introduces data and analysis method, while Section 3 presents statistical change-point analysis with respect to the latitude change of TC maximum intensity. Section 4 analyzes large-scale environments for the latitude change of TC maximum intensity between the periods before and after 1999. Section 5 concludes this study.

2. Data and Methodology

2.1. Data. The TC data in this study was obtained from the best-track of TC provided by Regional Specialized Meteorological Center- (RSMC-) Tokyo Typhoon Center. This data consists of TC name, latitude and longitude location of TC, TC central pressure, and TC maximum sustained wind speed (MSWS), which were observed in every 6 hours for 35 years from 1977 to 2013. TC is generally classified into four classes by the criteria of MSWS as follows: Tropical Depression (TD, $MSWS < 17 \text{ m s}^{-1}$), Tropical Storm (TS, $17 \text{ m s}^{-1} \leq MSWS \leq 24 \text{ m s}^{-1}$), Severe Tropical Storm (STS, $25 \text{ m s}^{-1} \leq MSWS \leq 32 \text{ m s}^{-1}$), and Typhoon (TY, $MSWS \geq 33 \text{ m s}^{-1}$). Along with the four classes of TC above, this study included extratropical cyclone, which was transformed from TC for analysis. This was because such extratropical cyclone also incurred great damage on property and human in the mid-latitude regions in East Asia.

Moreover, this study also used the variables of geopotential height (gpm), zonal and meridional winds (m s^{-1}), relative humidity (%), and air temperature ($^{\circ}\text{C}$) data from National Centers for Environmental Prediction-National Center for Atmospheric Research (NCEP-NCAR) reanalysis in 1977 to 2013 [24, 25]. This NCEP-NCAR reanalysis data consisted of spatial resolution such as latitude and longitude $2.5^{\circ} \times 2.5^{\circ}$ and 17 vertical levels (relative humidity is 16 vertical levels).

Also, the National Oceanic and Atmospheric Administration (NOAA) interpolated outgoing longwave radiation (OLR) data retrieved from the NOAA satellite series are available starting from June 1974 from NOAA's Climate Diagnosis Center (CDC). However, the data are incomplete, with a missing period from March to December of 1978. Detailed information about this OLR data can be found on the CDC website (<http://www.cdc.noaa.gov/>) and in the study by Liebmann and Smith [26].

The NOAA extended reconstructed monthly sea surface temperature (SST) [27], available from the same organization, was also used. The data have a horizontal resolution of $2.0^{\circ} \times 2.0^{\circ}$ latitude-longitude and are available for the period of 1854 to the present day.

2.2. Methodology. To calculate the TC passage frequency, each position of a TC is binned into a $5^{\circ} \times 5^{\circ}$ grid box, and a TC is only counted once, although it may enter the same grid

box several times [28]. The TC genesis frequency is calculated by the same method as for the TC passage frequency. The range of the latitudes/longitudes where the TCs are analyzed is 0–70°N and 95°–185°E.

This study used Student's t -test to determine significance [29]. In case that two independent time series follow t distribution and their time averages are denoted as \bar{x}_1 and \bar{x}_2 , respectively, the test statistic is given by

$$t = \frac{\bar{x}_1 - \bar{x}_2}{(s_1^2/n_1 + s_2^2/n_2)^{1/2}}, \quad (1)$$

where s_1 and s_2 are standard deviations and n_1 and n_2 are numbers of the two time series, respectively. From the above formula, if the absolute value of t is greater than threshold values with a level of significance, the null hypothesis would be rejected at the α ($\times 100$)% significance level.

With a trend change, statistical change-point analysis was conducted to determine whether climate regime shift existed in the time series of 35 years. Because this variable does not follow Poisson distribution, we use a different method to detect climate regime shifts in the temperature or TC frequency series: using a log-linear regression model in which a step function is expressed as an independent variable. If the estimated slope is at least twice as large as its standard error, one may reject the null hypothesis (i.e., the slope being zero) at the 5% significance level. The details of this method are well described in studies of Elsner et al. [30], Chu [31], and Ho et al. [15]. Once statistical change-point analysis is conducted, t value is produced for every year. If absolute value of t value is the largest, it means that the corresponding year had a climate regime shift.

The vertical wind shear (VWS) to diagnose the large-scale condition is calculated as follows:

$$VWS = \sqrt{(u_{200-850})^2 + (v_{200-850})^2}. \quad (2)$$

Here, u and v indicate the zonal and meridional flows, respectively, and 200 and 850 represent 200 hPa and 850 hPa levels, respectively [32].

This study analyzes TCs in summer season which is defined as July–September. This is because two-thirds of TCs generated over the year are concentrated in these three months.

3. Analysis of Climate Regime Shift on Latitude Change of TC Maximum Intensity

Figure 1 shows a time series of annually averaged latitude of TC maximum intensity after finding all latitudes of TC maximum intensity using the maximum sustained wind speed in the RSMC best track at the interval of six hours. Overall, latitudes of TC maximum intensity shifted northerly (light face dashed line) showing clear interannual and interdecadal variations. Therefore, statistical change-point analysis was conducted with regard to this time series to determine whether climate regime shift existed. The result showed that t value maintained a certain trend until 1999, followed by showing an increasing trend (dotted line). Therefore,

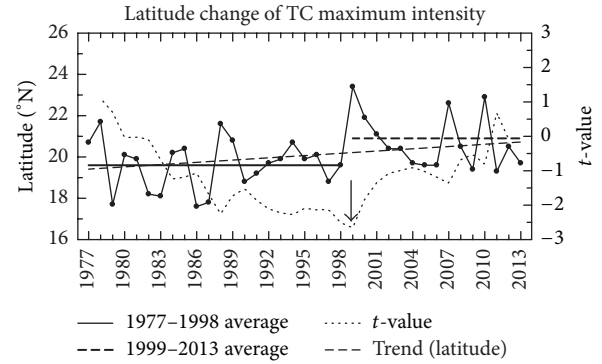


FIGURE 1: Time series of latitude of tropical cyclone (TC) maximum intensity averaged for all TCs in each year (solid line with dot) and its trend (light face dashed line). Thick solid and bold dashed lines denote averages for 1977–1998 and for 1999–2013, respectively. Arrow denotes change-point year in time series of latitude of tropical cyclone (TC) maximum intensity.

a climate regime shift year was set to 1999 in terms of latitude change of TC maximum intensity for the recent 37 years (arrow mark). The average latitude of TC maximum intensity over the years of 1977–1998 was 19.6°N (thick solid line), while that of 1999–2013 was 21.2°N (bold dashed line), indicating a about 1.6°N latitude difference between two periods. Assuming that 1° is equivalent to 100 km, a latitude shift of TC maximum intensity for the recent 37 years means 160 km northerly shift. Here, a latitude difference between two periods is statistically significant with 95% confidence level. To determine the reason for the recent latitude shift of TC maximum intensity, a difference of means between 1999–2013 and 1977–1998 was analyzed.

4. Differences between 1999–2013 and 1977–1998

4.1. TC Activity. The present study investigated differences of TC activity between two periods (see Figure 2). The TC activity in this study refers to TC genesis frequency and TC passage frequency. With respect to the TC genesis frequency, TCs in 1999–2013 were generated more in a northwest region of the tropical and subtropical western North Pacific than TCs in 1977–1998 (see Figure 2(a)). The data of TC average genesis locations during the two periods showed that 1999–2013 was 16.8°N, 135.1°E while 1977–1998 was 14.9°N, 144.5°E, confirming that recent TCs were generated further in a northwest region of the tropical and subtropical western North Pacific than previous TCs. Here, differences of both TC average genesis latitude and TC average genesis longitude between the two periods were statistically significant with 95% confidence level. Accordingly, northerly latitude shift of not only TC maximum intensity but also TC genesis location was found in recent TCs through the data.

There was a clear difference of TC track pattern between two periods with respect to TC passage frequency (see Figure 2(b)). The TC track over the years of 1977–1998 showed two patterns. A first pattern is a TC track that was generated

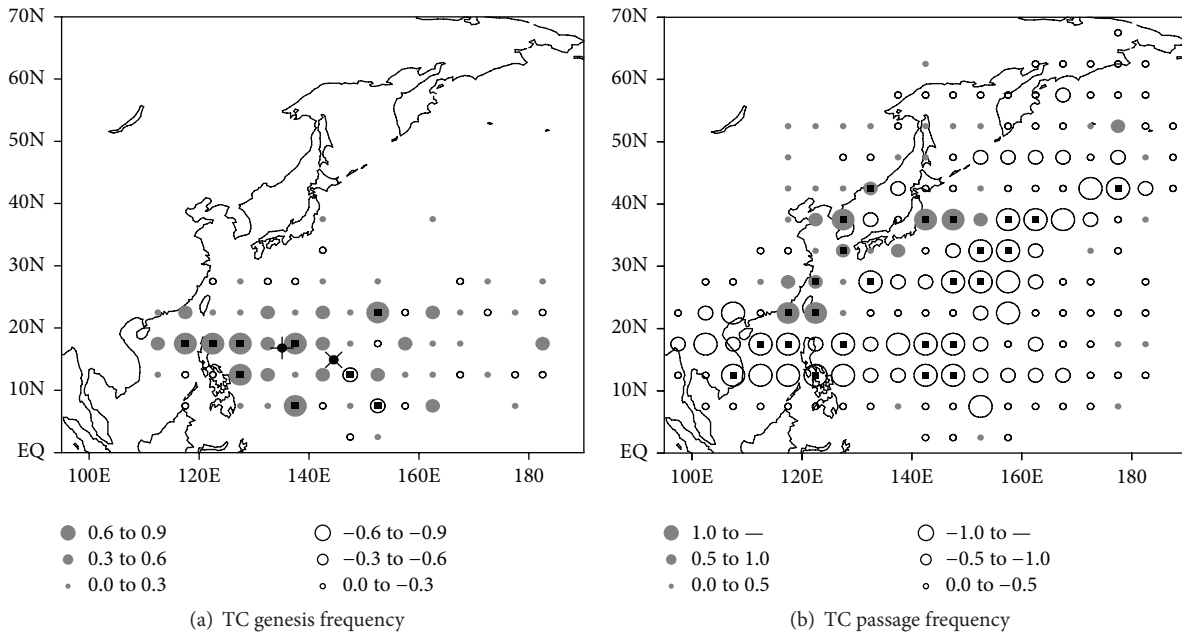


FIGURE 2: Geographical distributions of difference in (a) TC genesis frequency and (b) TC passage frequency between the periods of 1999–2013 and 1977–1998 in each $5^\circ \times 5^\circ$ grid area. Small box inside circles indicate that differences are significant at the 95% confidence level.

in a distant sea in the east of the Philippines and moved via the Philippines and the South China Sea towards the Indochina Peninsula to the west. A second pattern is a TC track that moved northerly from a distant sea in the east of the Philippines towards a distant sea in the east of Japan. During 1999 to 2013, a TC track showed a pattern that moved to the mid-latitude in East Asia mostly. Therefore, these patterns showed that TCs in 1999–2013 tended to move further to the high latitude than TCs in 1977–1998. That is, TC maximum intensity is likely to be found more in high latitudes in 1999–2013 than 1977–1998. In this regard, Wang and Chan [33] also showed that intensity of TCs that moved toward the mid-latitude region in East Asia was much stronger than that of TCs that moved westerly toward the Indochina Peninsula or toward a distant sea in the east of Japan. They stressed that this strong intensity can be obtained because sufficient energy can be gotten from the sea while TCs moved toward the mid-latitude in East Asia.

4.2. Large-Scale Environments. This study analyzed a difference of large-scale environments between two periods to determine the reason of the latitude shift of TC maximum intensity in recent years. In the difference of 500 hPa streamline between two periods, anomalous anticyclonic circulations were strengthened in 30–50N, whereas anomalous monsoon trough was placed in the northern water of the South China Sea, which was extended to the east up to 145E (see Figure 3(a)). Therefore, as analyzed previously, TCs in 1999–2013 could be generated in much higher latitudes than TCs in 1977–1998. In addition, anomalous anticyclonic circulations were strengthened in the east of the anomalous monsoon trough. Therefore, a mid-latitude region in East

Asia was affected by the anomalous anticyclonic circulations and anomalous monsoon trough. This anomalous southeasterlies played a role in anomalous steering flows that directed TCs toward the mid-latitude in East Asia. Accordingly, as analyzed previously, anomalous pressure systems were formed in the mid-latitude region in East Asia that could affect TCs in 1999–2013 more than TCs in 1977–1998, which resulted in northerly latitude shift of TC maximum intensity in 1999–2013.

A difference of 850 hPa streamline between two periods was also similar to a difference of 500 hPa streamline between two periods (see Figure 3(b)). Anomalous anticyclonic circulations were strengthened in the mid-latitude of the analysis area, while anomalous monsoon trough was placed near Taiwan. In addition, anomalous southeasterlies were strengthened from the southeastern sea in the tropical and subtropical western North Pacific to the mid-latitude in East Asia.

A difference of OLR between two periods was studied (see Figure 4(a)). The smaller the OLR is, the stronger the convective activity is. Positive anomaly was strengthened in regions to the north of 25N, while negative anomaly was strengthened in regions to the south of 25N. This means that convective activity in 1999–2013 was strengthened more in the tropical and subtropical western North Pacific than in 1977–1998. Furthermore, the center of the negative anomaly was located in subtropical regions (10–20N) rather than tropical regions, while the northern boundary of the negative anomaly was located up to the southwestern sea in Japan. Such results can be one of the factors that cause the northerly latitude shift of TC maximum intensity in recent years. In addition, as analyzed in the above, it was found that suitable

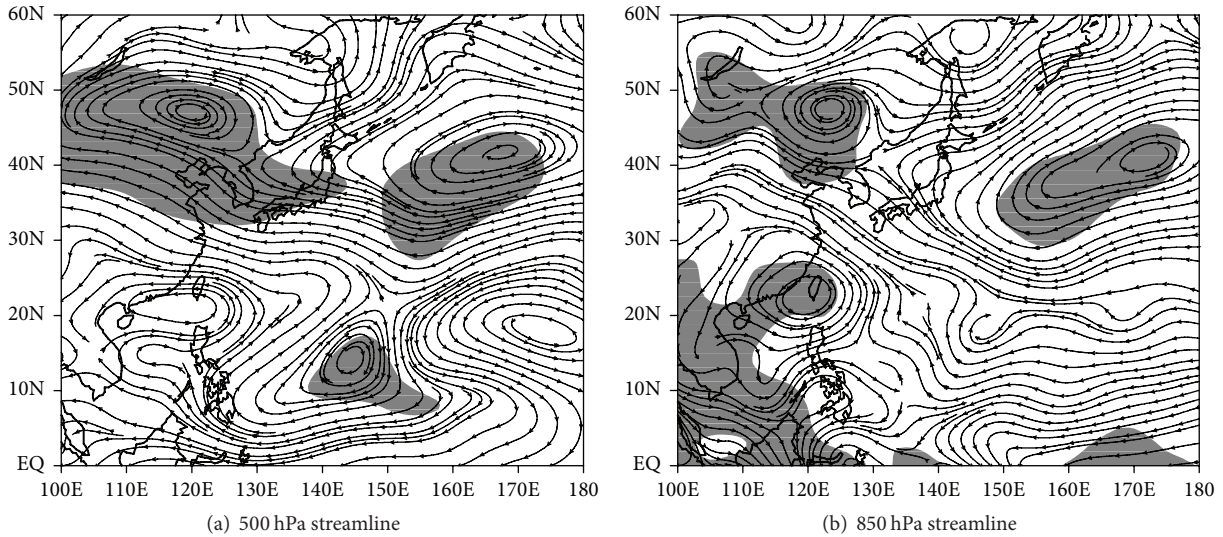


FIGURE 3: Differences in (a) 500 hPa and (b) 850 hPa streamline between the periods of 1999–2013 and 1977–1998. Shaded areas indicate that differences are significant at the 95% confidence level.

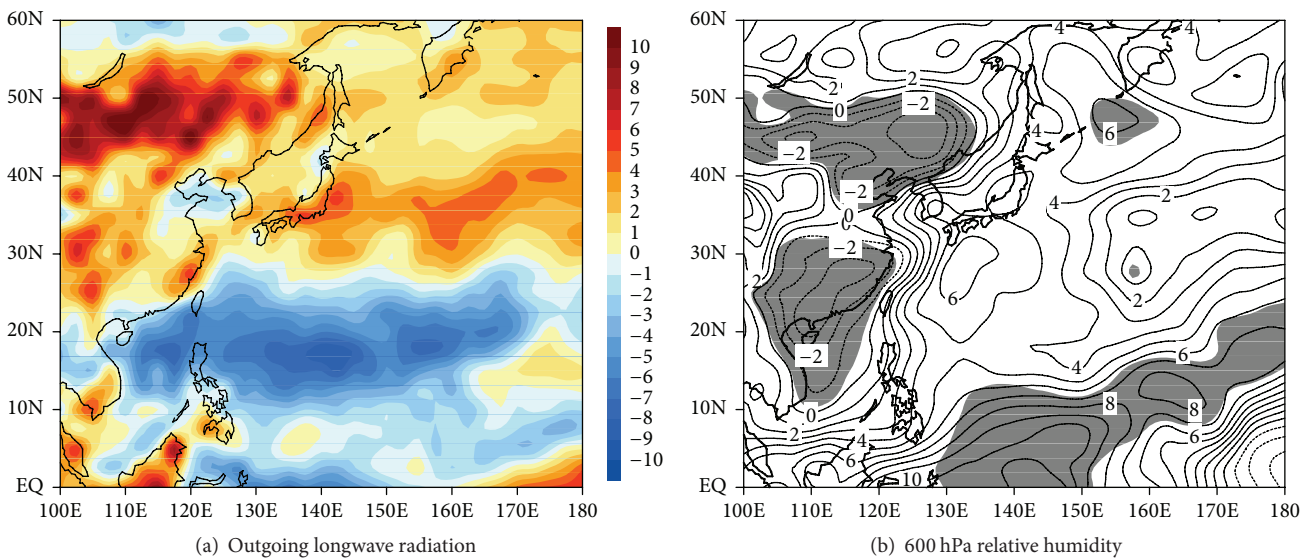


FIGURE 4: Same as in Figure 3, but for (a) outgoing longwave radiation (OLR) and (b) 600 hPa relative humidity. In (b), contour interval is 1% and shaded areas are significant at the 95% confidence level.

environments were formed so that TCs in 1999–2013 were generated further to the northern seas than TCs in 1977–1998 did.

Furthermore, this study analyzed a difference of 600 hPa relative humidity between two periods (see Figure 4(b)). Negative anomaly was strengthened in East Asia continent, while positive anomaly was strengthened in the western North Pacific. Although the center of positive anomaly was located in the southeastern seas in the tropical western North Pacific, considerable anomaly values were also found in the southwestern sea in Japan. Therefore, these analysis results can also be one of the factors that cause the northerly latitude shift of TC maximum intensity in recent years.

Furthermore, this study analyzed a difference of 850 hPa air temperature between two periods (see Figure 5(a)). In all of the analysis regions, warm anomaly was found. A magnitude of warm anomaly was higher in the western North Pacific than in East Asia continent. This result can also be one of the factors that cause the northerly latitude shift of TC maximum intensity in recent years.

A difference of 850 hPa relative vorticity between two periods was also analyzed (see Figure 5(b)). Positive anomaly was located in 20–30N, whereas negative anomaly was strengthened in tropical regions. This means that not only environments where TCs in 1999–2013 could be generated more frequently in higher latitude than TCs in 1977–1998

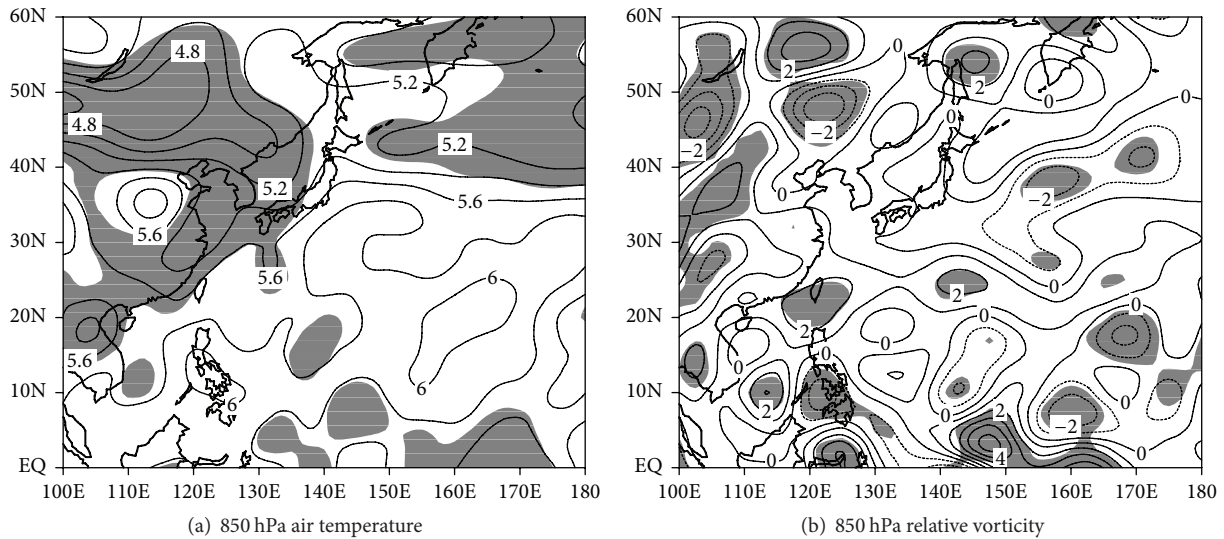


FIGURE 5: Same as in Figure 3, but for (a) 850 hPa air temperature and (b) 850 hPa relative vorticity. Contour intervals are 0.2°C for 850 hPa air temperature and $1 \times 10^{-6} \text{ s}^{-1}$ for 850 hPa relative vorticity. Shaded areas are significant at the 95% confidence level.

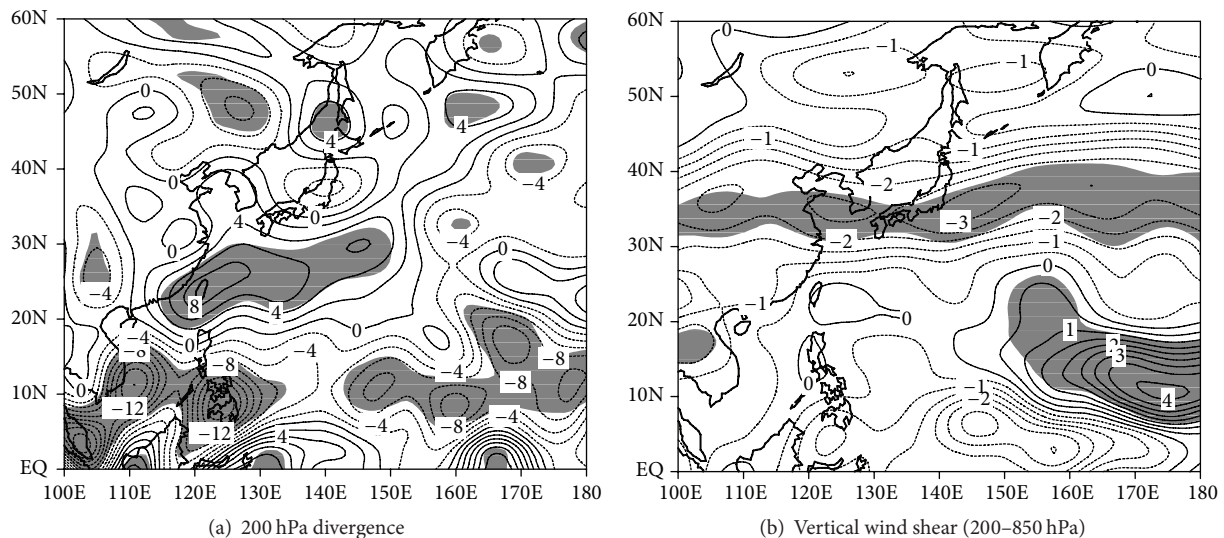


FIGURE 6: Same as in Figure 3, but for (a) 200 hPa divergence and (b) vertical wind shear between 200 hPa and 850 hPa. Contour intervals are 2 ms^{-1} for 200 hPa divergence and 0.5 ms^{-1} for vertical wind shear between 200 hPa and 850 hPa. Shaded areas are significant at the 95% confidence level.

were formed but also can be a factor that results in more northerly latitude shift of TC maximum intensity in recent years.

This study also analyzed a difference of 200 hPa divergence between two periods (see Figure 6(a)). Negative anomaly was strengthened in the south of 20°N , whereas positive anomaly was strengthened in $20\text{--}30^{\circ}\text{N}$ (from Taiwan to the southern sea in Japan). This meant that anomalous convergence was strengthened in the upper atmosphere of the south to 20°N , thereby forming anomalous downward flows, whereas anomalous divergence was strengthened in the upper atmosphere in $20\text{--}30^{\circ}\text{N}$, thereby forming anomalous upward flows. Such result means that not only environments

where TCs in 1999–2013 could be generated more frequently in higher latitude than TCs in 1977–1998 were formed but also can be a factor that results in more northerly latitude shift of TC maximum intensity in recent years.

200–850 hPa vertical wind shear could also influence TC genesis and TC intensification. Therefore, this study analyzed a difference of 200–850 hPa vertical wind shear between two periods (see Figure 6(b)). Except for eastern seas in the subtropical western North Pacific, most regions in the analysis areas showed negative anomaly. This meant that an atmospheric structure, which was advantageous to strengthening of TC genesis and TC intensity, was formed because structures of the upper and lower troposphere layers

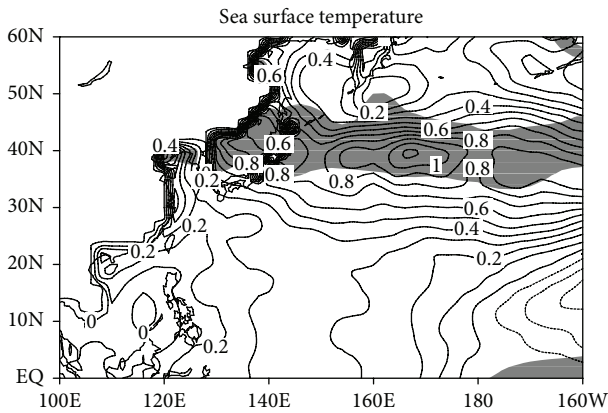


FIGURE 7: Same as in Figure 3, but for sea surface temperature. Contour interval is 0.1°C . Shaded areas are significant at the 95% confidence level.

were stabilized as values of 200–850 hPa vertical wind shear became smaller. In particular, the largest negative anomaly was shown in the mid-latitude zone. Therefore, this result can be one of the factors that cause the northerly latitude shift of TC maximum intensity in recent years.

SST can also be a factor that can influence TC genesis and TC intensity. Thus, a difference of SST between two periods was analyzed in this study (see Figure 7). Warm anomaly was found in all waters in the analysis regions except for eastern seas in the tropical western Pacific. In particular, a center of warm anomaly was located in the sea in the mid-latitude. Therefore, even if TCs can move to the seas in the mid-latitude, strong TC intensity can be maintained by the warm SST anomaly. Therefore, this result can also be one of the factors that cause the northerly latitude shift of TC maximum intensity in recent years.

5. Summary and Conclusion

The present study obtained latitudes when tropical cyclones (TCs) had maximum intensity and applied statistical change-point analysis to the averaged time series of yearly data. The analysis result showed that latitudes of the maximum intensity of TCs have increased since 1999. Then, to determine the reason for this increase, we have analyzed a difference of the means between period of 1999–2013 and 1977–1988.

First, with respect to the TC genesis frequency, TCs during 1999 to 2013 were generated more frequently in the northwest waters in the tropical and subtropical western North Pacific than TCs during 1977 to 1998. Accordingly, northerly latitude shift of not only TC maximum intensity but also TC genesis location was found in the data.

There was also a big difference of TC tracks between two periods. TCs over the period 1977–1998 showed a northward track trend generated mostly from the distant sea in the east of the Philippines via the mainland of the Philippines and South China Sea to the west toward Indochina or from the distant sea in the east of the Philippines to the distance sea in the east of Japan. On the contrary, TCS over the period

of 1999–2013 showed a northward move pattern to the mid-latitude region in East Asia mostly. Therefore TCs over the period of 1999–2013 tended to move to much higher latitudes than TCs over the period of 1977–1998, which also resulted in high possibility of TC maximum intensity occurred in higher latitudes during the former period than during the latter period.

In the difference of 500 hPa streamline between two periods, anomalous anticyclonic circulations were strengthened in 30–50N whereas anomalous monsoon trough was placed in the north of the South China Sea, which was extended to the east up to 145E. Therefore, TCs in 1999–2013 could be generated in much higher latitudes than TCs in 1977–1998. Furthermore, the mid-latitude in East Asia was affected by the anomalous southeasterlies due to the above anomalous anticyclonic circulations and anomalous monsoon trough and the anomalous southeasterlies played a role in anomalous steering flows that directed TCS to the mid-latitude regions in East Asia, which made TCs in 1999–2013 to have more influence in the mid-latitude region in East Asia than TCs in 1977–1998 did. Because of this, the former period had to shift latitudes of TC maximum intensity northerly.

A difference of OLR between two periods showed that a center of the negative anomaly was located in subtropical region rather than in tropical regions, while the northern boundary of the negative anomaly was moved up to the southern sea of Japan. In addition, a difference of 600 hPa relative humidity showed that positive anomaly was strengthened in the southern seas of Japan, which not only made TCs in 1999–2013 to be generated in higher latitudes but also shifted latitudes of TC maximum intensity further to the north.

Furthermore, analysis result with regard to a difference of 850 hPa air temperature between two periods showed warm anomaly in most of the analysis regions, while 850 hPa relative vorticity showed that positive anomaly was strengthened in 20–30N rather than tropical regions, thereby shifting latitudes of TCs in 1999–2013 of maximum intensity further to the north.

Analysis result on a difference of 200 hPa divergence between two periods showed that positive anomaly was strengthened from regions near Taiwan to the southern seas of Japan, which meant that anomalous upward flows were formed over these latitudes. These results hinted that not only TCs in 1999–2013 could be generated in higher latitudes but also latitudes of TC maximum intensity could be shifted further to the north than TCs in 1977–1998 could.

Furthermore, analysis results on a difference of 200–850 hPa vertical wind shear between two periods showed that negative anomaly was shown in most analysis regions. Analysis on a difference of SST also showed that the highest warm anomaly was shown in the mid-latitude in East Asia, which could be one of the factors that can shift latitudes of TC maximum intensity further to the north in recent years.

The present study simply analyzed reasons for the shift on latitude change of TC maximum intensity in recent years. For the future study, such reasons found in this study will be verified through regional climate models.

Conflict of Interests

The authors declare that there is no conflict of interests regarding the publication of this paper.

Acknowledgment

This work (15-2-40-41) was supported by Research Program funded by the DEGEC.

References

- [1] K. Emanuel, "Increasing destructiveness of tropical cyclones over the past 30 years," *Nature*, vol. 436, no. 7051, pp. 686–688, 2005.
- [2] J. H. Kim, C. H. Ho, and C. H. Sui, "Circulation features associated with the record-breaking typhoon landfall on Japan in 2004," *Geophysical Research Letters*, vol. 32, no. 14, 2005.
- [3] S. K. Park and E. H. Lee, "Synoptic features of orographically enhanced heavy rainfall on the east coast of Korea associated with Typhoon Rusa (2002)," *Geophysical Research Letters*, vol. 34, no. 2, Article ID L02803, 2007.
- [4] C. J. Pan, K. Krishna Reddy, H. C. Lai, and S. S. Yang, "Role of mixed precipitating cloud systems on the typhoon rainfall," *Annales Geophysicae*, vol. 28, no. 1, pp. 11–16, 2010.
- [5] B. Lyon and S. J. Camargo, "The seasonally-varying influence of ENSO on rainfall and tropical cyclone activity in the Philippines," *Climate Dynamics*, vol. 32, no. 1, pp. 125–141, 2009.
- [6] W. J. Yang and W. H. Yi, "Safety evaluation of masonry buildings for tsunamis," *Journal of Korean Society of Hazard Mitigation*, vol. 13, no. 6, pp. 45–49, 2013.
- [7] National Climatic Data Center (NOAA), *State of the Climate: Hurricanes and Tropical Storms for Annual 2013*, National Climatic Data Center (NOAA), Asheville, NC, USA, 2013.
- [8] C. W. Landsea, "Counting Atlantic tropical cyclones back to 1900," *EOS*, vol. 88, pp. 197–208, 2007.
- [9] D. S. R. Park, C. H. Ho, J. H. Kim, and H. S. Kim, "Strong landfall typhoons in Korea and Japan in a recent decade," *Journal of Geophysical Research*, vol. 116, no. D7, 2011.
- [10] P. J. Webster, G. J. Holland, J. A. Curry, and H. R. Chang, "Changes in tropical cyclone number, duration, and intensity in a warming environment," *Science*, vol. 309, no. 5742, pp. 1844–1846, 2005.
- [11] P.-S. Chu and J. D. Clark, "Decadal variations of tropical cyclone activity over the central north pacific," *Bulletin of the American Meteorological Society*, vol. 80, no. 9, pp. 1875–1881, 1999.
- [12] H. Kamahori, N. Yamazaki, N. Mannoji, and K. Takahashi, "Variability in intense tropical cyclone days in the western North Pacific," *SOLA*, vol. 2, pp. 104–107, 2006.
- [13] J. B. Elsner, J. P. Kossin, and T. H. Jagger, "The increasing intensity of the strongest tropical cyclones," *Nature*, vol. 455, no. 7209, pp. 92–95, 2008.
- [14] C. W. Landsea, N. Nicholls, W. M. Gray, and L. A. Avila, "Downward trends in the frequency of intense Atlantic hurricanes during the past five decades," *Geophysical Research Letters*, vol. 23, no. 13, pp. 1697–1700, 1996.
- [15] C.-H. Ho, J.-J. Baik, J.-H. Kim, D.-Y. Gong, and C.-H. Sui, "Interdecadal changes in summertime typhoon tracks," *Journal of Climate*, vol. 17, no. 9, pp. 1767–1776, 2004.
- [16] J. C. L. Chan and J.-E. Shi, "Long-term trends and interannual variability in tropical cyclone activity over the western North Pacific," *Geophysical Research Letters*, vol. 23, no. 20, pp. 2765–2767, 1996.
- [17] J. C. L. Chan, "Interannual and interdecadal variations of tropical cyclone activity over the western North Pacific," *Meteorology and Atmospheric Physics*, vol. 89, no. 1, pp. 143–152, 2005.
- [18] A. Z.-C. Goh and J. C. L. Chan, "Interannual and interdecadal variations of tropical cyclone activity in the South China Sea," *International Journal of Climatology*, vol. 30, no. 6, pp. 827–843, 2010.
- [19] J. Lighthill, "Global climate change and tropical cyclones," *Bulletin American Meteorological Society*, vol. 75, no. 11, pp. 2147–2157, 1994.
- [20] P. J. Klotzbach, "Trends in global tropical cyclone activity over the past twenty years," *Geophysical Research Letters*, vol. 33, no. 10, Article ID L10805, 2006.
- [21] M. C. Bove, D. F. Zierden, and J. J. O'Brien, "Are Gulf landfalling hurricanes getting stronger?" *Bulletin of the American Meteorological Society*, vol. 79, no. 7, pp. 1327–1328, 1998.
- [22] J. P. Kossin, K. A. Emanuel, and G. A. Vecchi, "The poleward migration of the location of tropical cyclone maximum intensity," *Nature*, vol. 509, no. 7500, pp. 349–352, 2014.
- [23] K. Choi, K. Park, J. Kim, and B. Kim, "Synoptic analysis on the trend of northward movement of tropical cyclone with maximum intensity," *Journal of the Korean earth science society*, vol. 36, no. 2, pp. 171–180, 2015.
- [24] E. Kalnay, M. Kanamitsu, R. Kistler et al., "The NCEP/NCAR 40-year reanalysis project," *Bulletin of the American Meteorological Society*, vol. 77, no. 3, pp. 437–471, 1996.
- [25] R. Kistler, "The NCEP/NCAR 50-year reanalysis," *Bulletin of the American Meteorological Society*, vol. 82, pp. 247–267, 2001.
- [26] B. Liebmann and C. A. Smith, "Description of a complete (interpolated) outgoing longwave radiation dataset," *Bulletin of the American Meteorological Society*, vol. 77, pp. 1275–1277, 1996.
- [27] R. W. Reynolds, N. A. Rayner, T. M. Smith, D. C. Stokes, and W. Wang, "An improved in situ and satellite SST analysis for climate," *Journal of Climate*, vol. 15, no. 13, pp. 1609–1625, 2002.
- [28] C.-H. Ho, J.-H. Kim, H.-S. Kim, C.-H. Sui, and D.-Y. Gong, "Possible influence of the Antarctic oscillation on tropical cyclone activity in the Western North Pacific," *Journal of Geophysical Research*, vol. 110, Article ID D19104, 2005.
- [29] D. S. Wilks, *Statistical Methods in the Atmospheric Sciences*, Academic Press, New York, NY, USA, 1995.
- [30] J. B. Elsner, T. H. Jagger, and X.-F. Niu, "Changes in the rates of North Atlantic major hurricane activity during the 20th century," *Geophysical Research Letters*, vol. 27, no. 12, pp. 1743–1746, 2000.
- [31] P.-S. Chu, "Large-scale circulation features associated with decadal variations of tropical cyclone activity over the central North Pacific," *Journal of Climate*, vol. 15, no. 18, pp. 2678–2689, 2002.
- [32] M. T. Wingo and D. J. Cecil, "Effects of vertical wind shear on tropical cyclone precipitation," *Monthly Weather Review*, vol. 138, no. 3, pp. 645–662, 2010.
- [33] B. Wang and J. C. L. Chan, "How strong ENSO events affect tropical storm activity over the western North Pacific," *Journal of Climate*, vol. 15, no. 13, pp. 1643–1658, 2002.

Research Article

A Semianalytical Model Using MODIS Data to Estimate Cell Density of Red Tide Algae (*Aureococcus anophagefferens*)

Lingling Jiang,¹ Lin Wang,² Xinyu Zhang,³ Yanlong Chen,² and Deqi Xiong¹

¹College of Environmental Science and Engineering, Dalian Maritime University, No. 1 Linghai Road, Dalian 116026, China

²National Marine Environmental Monitoring Center, No. 42 Linghe Road, Dalian 116023, China

³Navigation College, Dalian Maritime University, No. 1 Linghai Road, Dalian 116026, China

Correspondence should be addressed to Lingling Jiang; jll5@163.com

Received 21 April 2015; Accepted 8 July 2015

Academic Editor: Xiaofeng Li

Copyright © 2016 Lingling Jiang et al. This is an open access article distributed under the Creative Commons Attribution License, which permits unrestricted use, distribution, and reproduction in any medium, provided the original work is properly cited.

A multiband and a single-band semianalytical model were developed to predict algae cell density distribution. The models were based on cell density (N) dependent parameterizations of the spectral backscattering coefficients, $b_b(\lambda)$, obtained from *in situ* measurements. There was a strong relationship between $b_b(\lambda)$ and N , with a minimum regression coefficient of 0.97 at 488 nm and a maximum value of 0.98 at other bands. The cell density calculated by the multiband inversion model was similar to the field measurements of the coastal waters (the average relative error was only 8.9%), but it could not accurately discern the red tide from mixed pixels, and this led to overestimation of the area affected by the red tide. While the single-band inversion model is less precise than the former model in the high chlorophyll water, it could eliminate the impact of the suspended sediments and make more accurate estimates of the red tide area. We concluded that the two models both have advantages and disadvantages; these methods lay the foundation for developing a remote sensing forecasting system for red tides.

1. Introduction

Red tides are always observed in coastal waters all over the world. They not only harm marine fisheries and aquaculture, deteriorate the marine environment, and affect the coastal tourist industry, but also cause human health problems [1, 2]. Monitoring the blooms and forecasting their development and movement are an important prerequisite for mitigating the impacts of such harmful algal blooms. Remote sensing has become an effective means of regularly monitoring algae blooms due to their synoptic and repetitive satellite coverage [3–8].

Most present efforts to detect and monitor red tides are based on chlorophyll *a* concentrations [9–14]. And the algorithms mainly include blue-to-green ratio algorithms and sensitivity of fluorescence algorithms [15–17]. The blue-to-green ratio algorithm was designed according to algal spectral properties in visible bands. It provides reasonable estimates of chlorophyll concentrations in Case I Water, in which chlorophyll is the optically dominant constituent [18].

However, the algorithm is not robust in Case II Water, in which colored dissolved organic matter (CDOM) and/or suspended sediment are present. These constituents increase the absorption of blue bands and influence the spectral ratio of reflectance [19–22], resulting in erroneously high estimates of chlorophyll concentrations and misidentifying the sample as red tide water [13, 23, 24]. To reduce the error arising from the influence of CDOM, the chlorophyll fluorescent method was based on positive correlation between fluorescence line height (FLH) and chlorophyll concentrations. This became the new standard of measuring chlorophyll concentrations in Case II Water. The FLH measurements were estimated using band triplets included in Medium Resolution Imaging Spectrometer (MERIS) and Moderate Resolution Imaging Spectrometer (MODIS) sensors. The method was widely used by researchers [12, 25, 26], who have found that fluorescence was useful for separating true pigment concentrations from the strong influence of CDOM effects. However, the MODIS FLH approach uses a simple radiance peak of 678 nm compared with the bottom line of 667 and 748 nm and is less sensitive to

high concentrations of suspended sediment due to increasing interactions between chlorophyll and the sediment [13, 27]. Otherwise, the relationship between FLH and chlorophyll concentration is not consistent for the different red tide alga and a negative correlation was found among some algae [28]. Thus, identification of blooms remains out of reach with these data. Recently, some approaches have been developed to monitor red tides based on optical closure relationships, such as using semianalytical and model-based approaches to measure apparent optical properties (AOPs) and the relevant inherent optical properties (IOPs) of seawater [29–31]. The cell density of a specific alga is the primary factor used to discern red tides in field monitoring and this value is determined by cell size. The pigment type and proportional size vary between algae species and so chlorophyll concentrations cannot be used to correctly identify red tides.

Algal spectral backscattering provides useful information because it is a function of algal size and refractive indices. Under normal conditions, oceanic particle size distributions appear dispersed; however, a distinctive feature of blooms is a high concentration of less dispersed distribution cells (with uniform cell diameters) that have unique backscattering spectra and might drastically alter ocean color. Thus, we used the available cell density information for a continuous and systematic study of algal blooms. We tested a combined analysis that uses simple spectral properties and band ratio to detect algal blooms with high accuracy using MODIS spectral data. The purpose of this study was to (1) identify the spectral characteristics of red tides (specifically *Aureococcus anophagefferens* blooms) based on backscattering coefficients, radiance, and cell density; (2) build a cell density remote sensing inversion model according to the MODIS data; (3) map areas of red tide by using the model; and (4) validate the new model using *in situ* data and addressing sources of error that limit the potential utility of satellite ocean color data for predicting red tides.

2. Formulation of the Reflectance Model

Remote sensing of ocean color relies on detecting the light signal that leaves the water surface and reaches a sensor on board a satellite. Ocean remote sensing reflectance, R_{rs} , is defined as the ratio of water-leaving radiance to downwelling irradiance, measured just above the sea surface, and it is dependent on the backscattering and absorption properties of seawater and the angular distribution of light within the ocean. Using radiative transfer theory, R_{rs} can be expressed as follows [32, 33]:

$$R_{rs}(\lambda, 0^+) = \frac{t^2}{n^2} \frac{f}{Q(\lambda)} \frac{b_b(\lambda)}{a(\lambda) + b_b(\lambda)}, \quad (1)$$

where $b_b(\lambda)$ is the total backscattering coefficient; $a(\lambda)$ is the total absorption coefficient of the seawater; t is the transmittance across the air-sea interface; n is the index of refraction of seawater; f is an empirical factor that is a function of the solar zenith angle; and $Q(\lambda)$ is the ratio of upwelling irradiance to upwelling radiance, $Q(\lambda) = E_u(\lambda)/L_u(\lambda)$ [34].

By making approximations for these latter terms [35], $R_{rs}(\lambda)$ can be related to the subsurface remote sensing reflectance, $r_{rs}(\lambda)$, as follows:

$$R_{rs}(\lambda) = \frac{0.5r_{rs}(\lambda)}{1 - 1.5r_{rs}(\lambda)}. \quad (2)$$

In Case II Water, the total absorption $a(\lambda)$ includes the absorption of seawater a_w , phytoplankton $a_{ph}(\lambda)$, and colored dissolved and detrital organic matters $a_{cdm}(\lambda)$:

$$a(\lambda) = a_w(\lambda) + a_{ph}(\lambda) + a_{cdm}(\lambda). \quad (3)$$

The total backscattering coefficient $b_b(\lambda)$ is the scalar sum of the backscatter values by pure water $b_{bw}(\lambda)$ and particulates $b_{bp}(\lambda)$:

$$b_b(\lambda) = b_{bw}(\lambda) + b_{bp}(\lambda), \quad (4)$$

where $b_{bp}(\lambda)$ is defined as

$$b_{bp}(\lambda) = b_{bp}(\lambda_0) \left(\frac{\lambda_0}{\lambda} \right)^Y. \quad (5)$$

$b_{bp}(\lambda_0)$ is the particulate backscattering coefficient at the scaling wavelength λ_0 . Y is the spectral slope of particulate backscattering coefficient.

According to (1)–(5), several semiempirical and semi-analytical algorithms have been proposed for deriving the IOPs. The algorithms typically used include the Garver-Siegel-Maritorena (GSM) algorithm [36–38] and the quasi-analytical algorithm (QAA) [39–41]. Thus, the existing models often differ only in the assumptions employed to define the eigenvectors. To facilitate a controlled evaluation of these various approaches, the NASA Ocean Biology Processing Group (OBPG) recently developed the Generalized IOP (GIOP) model that allows users to choose different IOP models by selecting from a wide assortment of published eigenvectors for constituent absorption and scattering properties [42, 43].

3. Methods

3.1. Phytoplankton Cultures. *Aureococcus anophagefferens* (*A. anophagefferens*) is a 2–3 μm spherical, nonmotile pelagophyte that has caused harmful brown tide blooms for extended periods in estuaries in the northeast and mid-Atlantic US [44], and the species was also found in the coastal seas of China in recent years.

The cultures were supplied by the Marine Biology Group of the National Marine Environmental Monitoring Center and were grown in an f2-enriched medium that was sterilized and filtered using 0.45 μm filter membranes. The cultures were incubated under banks of cool white fluorescent bulbs at $23 \pm 1^\circ\text{C}$ under a 12:12 dark:light cycle. A Hydrolab water quality instrument was placed in the culturing vat to observe the phytoplankton growth status continuously, and a collection frequency of 1 h was adopted. These cultures were not axenic, and the exponential growth of the cells was maintained by diluting them as needed with fresh media.

3.2. Measurement of Inherent Optical Properties. Measurements of spectral backscattering were carried out at 140° and six wavelengths (420, 442, 488, 550, 620, and 700 nm) with the Hydrosat-6 instrument (HS-6, HOBI Labs, Inc.). The measurements were conducted in a $400 \times 400 \times 500 \text{ mm}^3$ (length, width, and height) Plexiglass box built to replicate the manufacturer's standard calibration chamber. The face of the HS-6 instrument was immersed approximately 1 cm below the air-water interface, which was 27 cm from the container bottom [45]. An ac-s (WET Labs, Inc.) was attached in line with the calibration chamber and the sample medium was circulated through the system with a small pump. The measurements were recorded when stable absorption and attenuation readings were obtained. During each experiment, the container was covered with an opaque black cloth and a piece of black glass was placed below the Plexiglass box in order to prevent extraneous light from entering the container.

Serial dilution tests with the culture were conducted to check for the linearity of response over the chlorophyll concentrations. At the beginning of the experiments, the container was filled with 50 L of $0.2 \mu\text{m}$ filtered seawater for marine alga. Firstly, a steady clean-water baseline for each instrument was established, which was expected to represent the possible effects of the container or filtered media. Next, 500 mL to 1000 mL of the culture was added to the container and the measurements were taken after the algal suspension was thoroughly mixed. Sequential additions of culture were conducted in this fashion until the entire volume had been added. Lastly, the bigger error data were excluded and seven samples at different chlorophyll concentrations were used to analyse the optical properties of *A. anophagefferens*.

3.3. Measurement of Apparent Optical Properties. After each measurement of inherent optical properties, the water samples were placed in a bucket. In order to simulate the optical environment of deep water and avoid incident light potentially reflected by the barrel wall entering the water, the internal wall was painted with a black lacquer. At the same time, we chose the open area as the measurement site and all of the measurements were taken between 9:00 and 14:00 h local time.

The remote sensing reflectance (R_{rs}) spectra were derived from upwelling radiance and downwelling irradiance acquired by an ASD FieldSec spectral radiometer. With a field view of 25° , this instrument has a sensitivity range of 380–1050 nm. The resolution was transformed into 1 nm by the accompanying software. The measurement followed the Ocean Optical Protocols (Revision 3) by NASA (2002). Downwelling solar irradiance $E_s(0^+)$ measurements were performed using a Spectralon standard plate and the above-water upwelling radiance $L_{sfc}(0^+)$ was observed with an azimuth viewing direction of 135° from the sun and a nadir angle of 45° . The same parameters were used to measure the sky diffuse radiance $L_{sky}(0^+)$, including the same azimuth angle (135°), but with a zenith angle of 45° . For each radiometric measurement, at least seven continuous values were

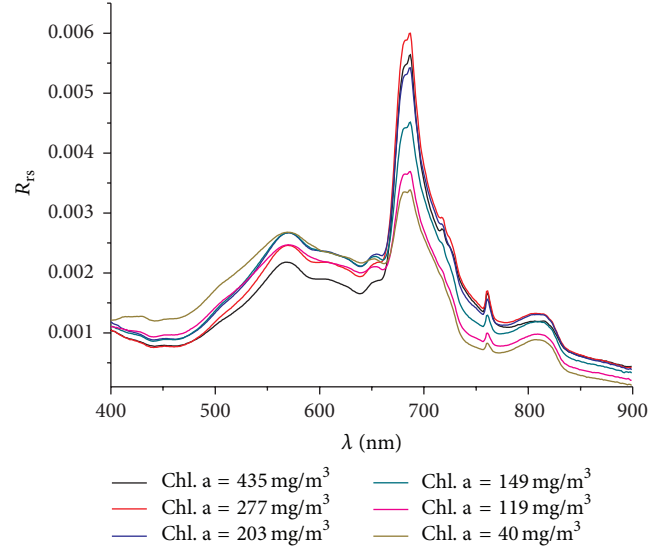


FIGURE 1: The remote sensing reflectance spectrum of *Aureococcus anophagefferens*.

recorded to produce an average value. R_{rs} was calculated according to Mueller and Fargion [46] by

$$R_{rs} = \frac{L_w(0^+)}{E_s(0^+)} = \frac{L_{sfc}(0^+) - \rho L_{sky}(0^+)}{E_s(0^+)}, \quad (6)$$

where $L_w(0^+)$ is the water-leaving radiance and ρ represents the reflectance of the skylight at the air-water interface. This value depends on the solar azimuth angle, wind speed, and cloud coverage. Under cloud-free and low wind speed (less than 10 m s^{-1}) conditions, ρ may be treated as independent of wavelength. When wind speeds are less than 5 m s^{-1} , the ρ value was chosen to be 0.028 [47].

The R_{rs} spectra of *A. anophagefferens* recorded at different chlorophyll concentrations are shown in Figure 1. A reflection peak appeared near 550 nm and a chlorophyll fluorescence peak emerged at 700 nm. As the chlorophyll concentration increased, the peaks became more and more obvious.

The field ASD $R_{rs}(\lambda)$ was used to derive the equivalent R_{rs} of MODIS bands via the MODIS spectral response function. The specific formula is as follows:

$$\langle R_{rs}(\lambda_i) \rangle = \frac{\int_{380 \text{ nm}}^{1050 \text{ nm}} R_{rs}(\lambda) F_s(\lambda) S_i(\lambda) d\lambda}{\int_{380 \text{ nm}}^{1050 \text{ nm}} F_s(\lambda) S_i(\lambda) d\lambda}, \quad (7)$$

where $\langle R_{rs}(\lambda_i) \rangle$ is the equivalent R_{rs} at a central wavelength λ_i , $F_s(\lambda)$ is the mean solar radiative flux at the top of the atmosphere, and $S_i(\lambda)$ is the spectral response function at the wavelength λ_i (http://oceancolor.gsfc.nasa.gov/DOCS/RSR_tables.html).

3.4. Ancillary Measurements. Chlorophyll a concentration was determined by a high-performance liquid chromatography (HPLC) analysis following the procedure described by Van Heukelem and Thomas [48]. Culture samples were

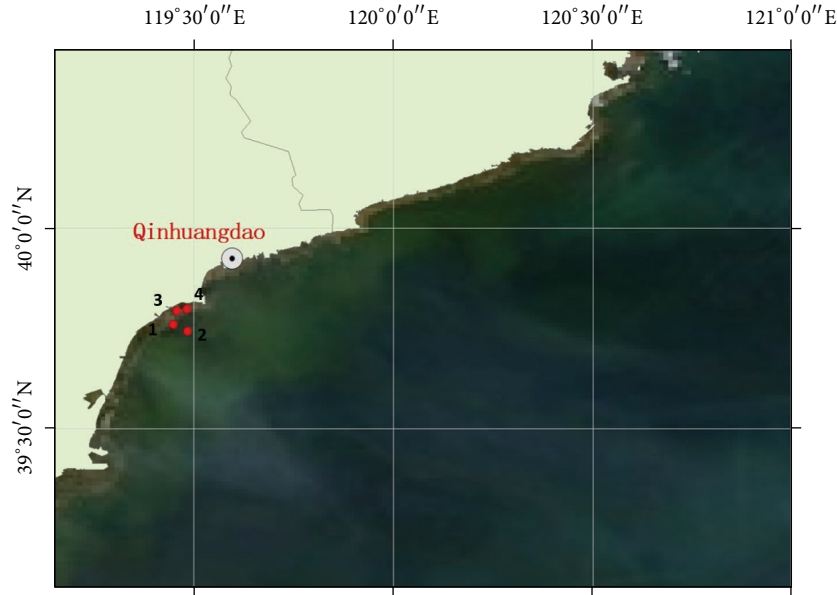


FIGURE 2: The MODIS data of study region and the stations (solid circles) in the Bohai Sea around Qinhuangdao of China.

TABLE 1: Summary of *A. anophagefferens* backscattering characteristics.

Bands	Backscattering coefficients		$b_{bp}^* \times 10^3 \text{ m}^2$ (mgchla) $^{-1}$
	$b_{bp}(\lambda) \text{ (m}^{-1}\text{)}$	Amplitude of variation	
420	0.0044–0.1639	36.25	0.570
442	0.0042–0.1432	33.09	0.527
488	0.0041–0.1616	38.41	0.538
550	0.0029–0.0920	30.72	0.341
620	0.0030–0.0934	30.13	0.353
700	0.0029–0.0818	27.21	0.324

filtered with GF/F filters prior to the optical measurements and frozen in cryotubes in liquid nitrogen until the analysis time. Cell counts of *A. anophagefferens* were performed using a high-power fluorescent microscope.

3.5. Satellite Data. Sampling was conducted in Bohai and adjacent coastal waters around Qinhuangdao city on June 6, 2012. Sampling stations are shown in Figure 2. The software SEADAS6.2 MODIS was used to process the L1B–L2 data with the atmosphere correction. We also chose the 2-band model option and an iterative NIR correction for the Aerosol mode with the other options on their default settings. Only cloud-free images were used for the cell density assessment.

4. Results and Discussion

4.1. Spectral Particulate Backscattering Coefficients. This is the first report of particulate backscattering coefficients at different chlorophyll concentrations, $b_{bp}(\lambda)$, for the red tide algae *A. anophagefferens* (Table 1, Figure 3). The backscattering coefficient value at each band increased with an increase

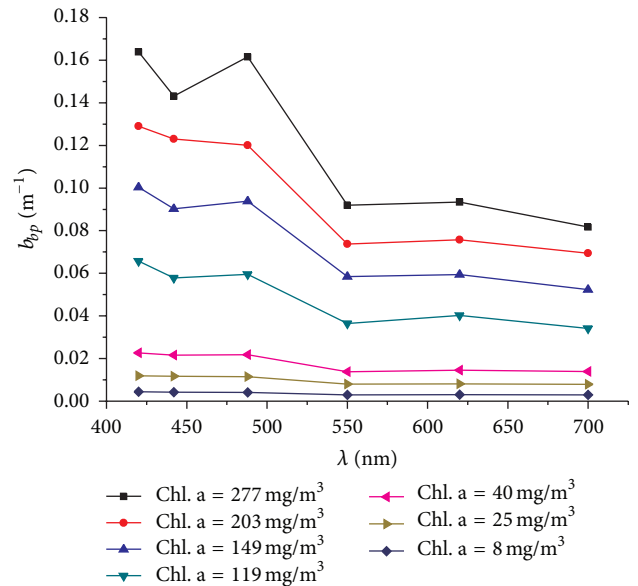


FIGURE 3: Spectral values of backscattering coefficients of *A. anophagefferens*. (Solid points are averaged data.)

in chlorophyll concentration and the amplitude of variation was larger than that of the nanophytoplankton [49–51]. The shape of the particulate backscattering coefficient spectra changed with increases in the chlorophyll concentrations in the visible range; although the maximum b_{bp} value was observed at 420 nm, the minimum value occurred at 550 nm for any chlorophyll concentration. An obvious depression at 442 nm appeared at high chlorophyll concentrations because of pigment absorption, consistent with the results of Stramski et al. [52]. Other research has shown that measurements of backscattering at 676 nm can be artificially elevated by

TABLE 2: Simulated results of double-band model.

Bands	Independent variable		
	$R_{rs}(443)/R_{rs}(488)$	$R_{rs}(488)/R_{rs}(678)$	$R_{rs}(551)/R_{rs}(678)$
420 nm	$Y = 15.13 - 21.06x$ $R^2 = 0.42$	$Y = -1.11 + 5.20x$ $R^2 = 0.36$	$Y = -1.55 + 3.55x$ $R^2 = 0.52$
443 nm	$Y = -4.69 + 6.23x$ $R^2 = -0.2$	$Y = -0.72 + 1.74x$ $R^2 = -0.18$	$Y = -0.80 + 1.05x$ $R^2 = -0.18$
551 nm	$Y = -7.93 + 17.37x$ $R^2 = 0.27$	$Y = 5.58 - 4.75x$ $R^2 = 0.35$	$Y = 6.02 - 3.32x$ $R^2 = 0.55$
620 nm	$Y = -8.10 + 14.37x$ $R^2 = 0.27$	$Y = 3.27 - 4.70x$ $R^2 = 0.65$	$Y = 3.60 - 3.06x$ $R^2 = 0.77$

Y is the spectral slope of particulate backscattering coefficient; x is reflectance ratio.

the fluorescent emission to detect backscattering at this wavelength [53–55]. However, the data we obtained at 620 nm were only a little higher than values at 700 nm and so we conclude there was no contamination of the signal by chlorophyll fluorescence.

In order to compare our results with others, we calculated the chlorophyll-specific backscattering coefficient, b^*_{bp} , with the units $m^2 \text{ mg chl } a^{-1}$ (Table 1). This represents the backscattering coefficient of the suspended cells at a concentration of 1 mg m^{-3} chlorophyll *a*. $b^*_{bp}(442)$ and $b^*_{bp}(620)$ were 0.000527 and 0.000353, respectively. This is lower than the backscattering coefficient of microbial cultures reported by Whitmire et al. [55] and Vaillancourt et al. [45] that were measured by HS-6 due to their relatively small particles. The spectral characteristics of *A. anophagefferens* are unique compared to measurements obtained by other researchers for phytoplankton [45, 49–52, 55, 56]. Our results are a good theoretical basis for future studies on picoplankton identification.

4.2. Backscattering Coefficient and Cell Density. Mie theory indicates that the backscattering coefficient is closely related to the cell size, density, composition, and refractive index [57]. Thus, particle density was one of the main factors that influenced the backscattering coefficient measurements. As particle density was a primary indicator of algal bloom, establishing the relationship between particle density and the backscattering coefficient could improve the accuracy of identifying red tide algae by remote sensing measurements of water color.

We found that there was a strong relationship between cell density and the backscattering coefficient that satisfies the following equation:

$$\lg N = ab_b(\lambda_0)^c, \quad (8)$$

where N is cell density recorded as cells/mL; a and c are the regression model parameters; and $b_b(\lambda_0)$ is the backscattering coefficient at each band. The regression coefficients were large at each band, with a minimum value of 0.97 at 488 nm and a maximum value of 0.98 at other bands (Figure 4).

4.3. Modeled Relationship between $R_{rs}(\lambda)$ and $b_b(\lambda)$. The bands 488 nm and 551 nm were selected as the representative

MODIS central bands, on the basis of the way the relation model was constructed by using the measured data and the biooptical theoretical analysis model (see Figure 5). We found a linear relationship between the backscattering coefficient and the remote sensing reflectance, with a regression coefficient of 0.89 at 488 nm and 0.57 at 551 nm. For this reason, 488 nm was chosen as the reference band to build the cell density inversion model.

For a comparison and a potentially more accurate model, a two-band ratio algorithm was also used and the MODIS bands b9 (443 nm), b10 (488 nm), b12 (551 nm), and b14 (678 nm) were selected to establish the relationship between the spectral slope of the particulate backscattering coefficient and reflectance:

$$Y \propto \frac{R_{rs}(\lambda_1)}{R_{rs}(\lambda_2)}. \quad (9)$$

In this study, $R_{rs}(443)/R_{rs}(488)$, $R_{rs}(488)/R_{rs}(678)$, and $R_{rs}(551)/R_{rs}(678)$ were chosen to be studied and the simulated results were as in Table 2.

Our results demonstrate no significant correlation between each band ratio and backscattering spectra at 443 nm. The strongest correlation appeared between the ratio $R_{rs}(551)/R_{rs}(678)$ and the backscattering spectra with a maximum regression coefficient of 0.77 at 620 nm. Therefore, we combined the simulated results of cell density and backscattering coefficients and the cell density inversion model was as follows:

$$b_{bp}(\lambda) = b_b(\lambda_0) \left(\frac{\lambda_0}{\lambda} \right)^Y,$$

$$b_b(\lambda_0) = 0.75 - 568.55R_{rs}(\lambda_0),$$

$$Y = 3.60 - 3.06 \frac{R_{rs}(551)}{R_{rs}(678)},$$

$$\lg N = 10.299 \cdot b_{bp}(\lambda)^{0.055}, \quad (10)$$

where λ_0 is at 488 nm and λ is at 620 nm.

4.4. Application of the Forward Model. By utilizing the cell density parameterizations of the IOPs, the model described

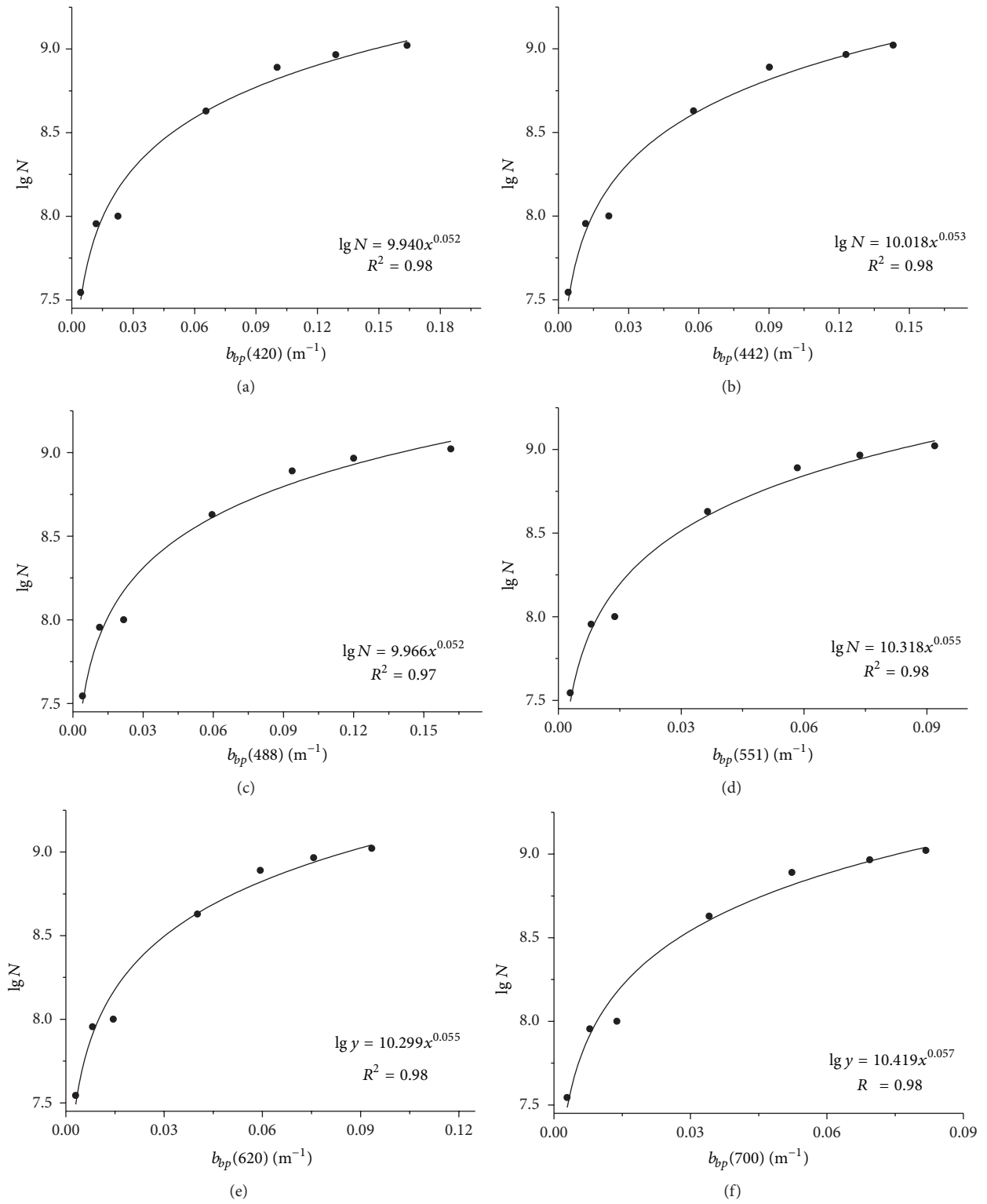


FIGURE 4: Particle backscattering coefficients versus cell density at six other wavelengths for *Aureococcus anophagefferens*. (a) 420 nm. (b) 442 nm. (c) 488 nm. (d) 550 nm. (e) 620 nm. (f) 700 nm.

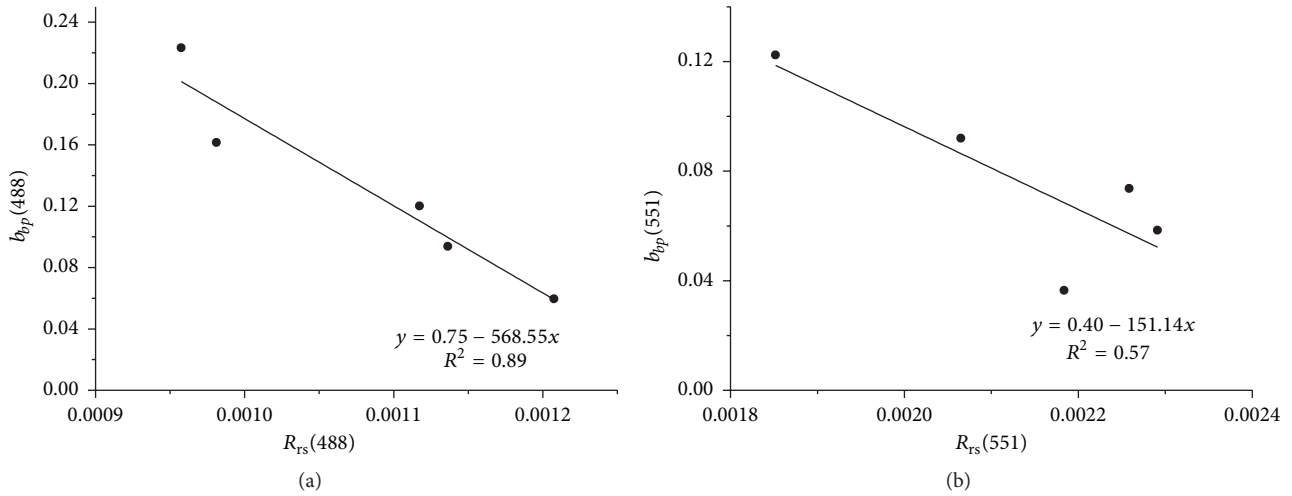


FIGURE 5: The backscattering coefficient versus remote sensing reflectance. (a) At 488 nm. (b) At 551 nm.

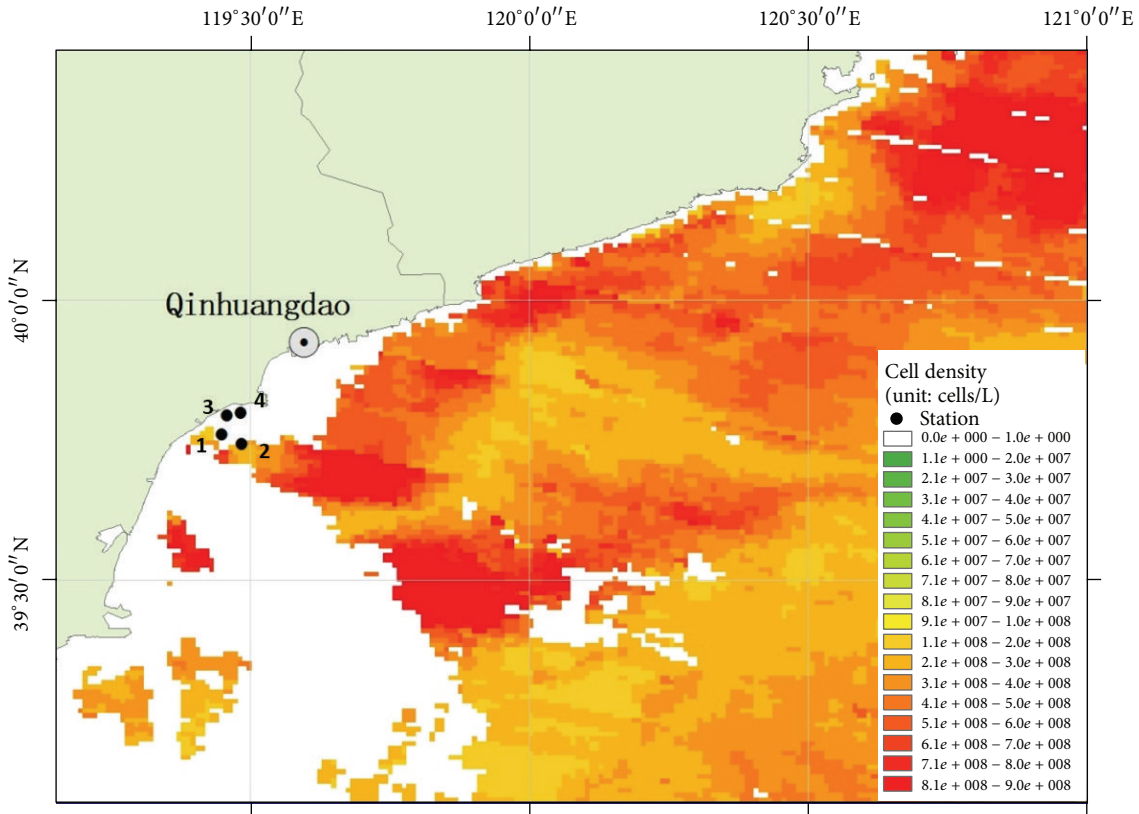


FIGURE 6: Cell density distribution of using multiband inversion model.

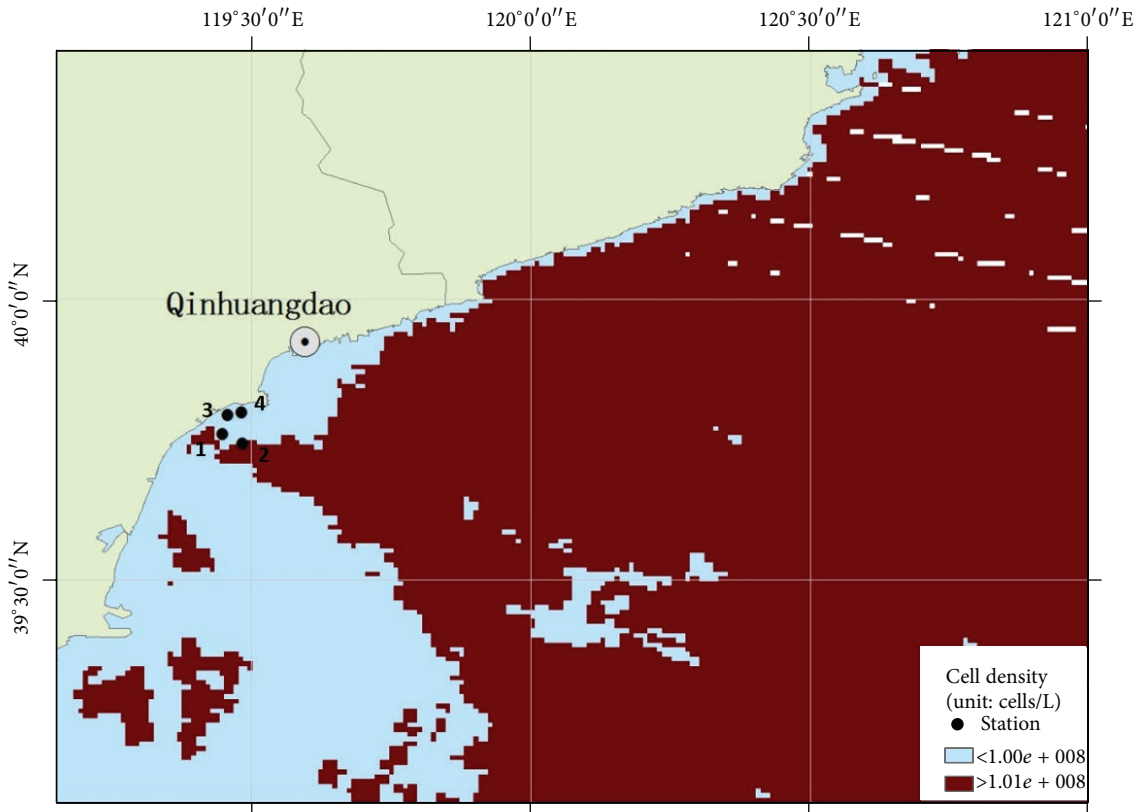
in (10) can be used to compute the $R_{rs}(\lambda)$ spectra for various cell density values. However, we found that the forecasted $b_b(\lambda_0)$ overestimated the true value because of a steeper slope between $b_b(\lambda_0)$ and $R_{rs}(\lambda_0)$ in (10). Therefore, three semianalytical algorithms (GSM, QAA, and GIOP) were trialed to calculate a corrected $b_b(\lambda_0)$. These results indicated that $b_b(\lambda_0)$ calculated by GSM and QAA was too high, but the value calculated by the GIOP method was similar to

the measured result. On this basis, the GIOP semianalytical model was chosen to predict $b_b(\lambda_0)$ by $R_{rs}(\lambda_0)$ and the cell density distribution was obtained for a given sea area (Figure 6).

The inversion values of cell density were similar to the field measurements at stations 1 and 2 (Table 3), the average relative error was only 8.9%, and there were no results at stations 3 and 4 because of cloud cover, while in offshore

TABLE 3: Comparison of monitoring result and inversion result (cells/L).

Stations	Longitude and latitude	Cell density by measurement	Cell density calculated by the multiband inversion model	Cell density calculated by the single-band inversion model
1	119°26.989'E 39°45.488'N	2.65×10^8	2.60×10^8	1.47×10^8
2	119°26.111'E 39°44.488'N	2.53×10^8	2.78×10^8	1.307×10^8
3	119°29.000'E 39°47.833'N	3.62×10^8	No result	No result
4	119°27.491'E 39°47.524'N	5.12×10^8	No result	No result

FIGURE 7: The distribution area of the *Aureococcus anophagefferens* red tide (multiband inversion).

waters the value was higher so that the red tide range was larger than the actual scope (Figure 7). In view of this, the single-band cell density remote sensing inversion model was established (Figures 8 and 9), in which 488 nm was the reference band λ_0 , the relationship model between $b_b(\lambda_0)$ and $R_{rs}(\lambda_0)$ was also determined by GIOP semianalytical model, and the formula $\lg N = 9.966 \cdot b_{bp}(\lambda_0)^{0.052}$ forms the simultaneous equations. By comparing the two methods, we found that the red tide distribution range for the whole sea area was more consistently computed by the single-band inversion model, but for the calculated values of the coastal waters, the average relative error was higher than that computed by the multiband inversion model. The main reason was that the multiband inversion model is more precise only in dense chlorophyll waters and it is difficult to

discern the red tide accurately from mixed pixels; however, the single-band inversion model just could eliminate the impact of the suspended sediments and make more accurate estimates of the red tide area.

5. Conclusions

Improvements in technological instrumentation, combined with the growing availability of large biooptical data sets, are resulting in the increasing use of remote sensing data to monitor red tides. This is carried out by algorithms to describe empirical relationships between oceanic reflectance and phytoplankton pigment concentrations. In fact, cell density plays an important role in recognizing red tides in the field and cell density has a large effect on the backscattering

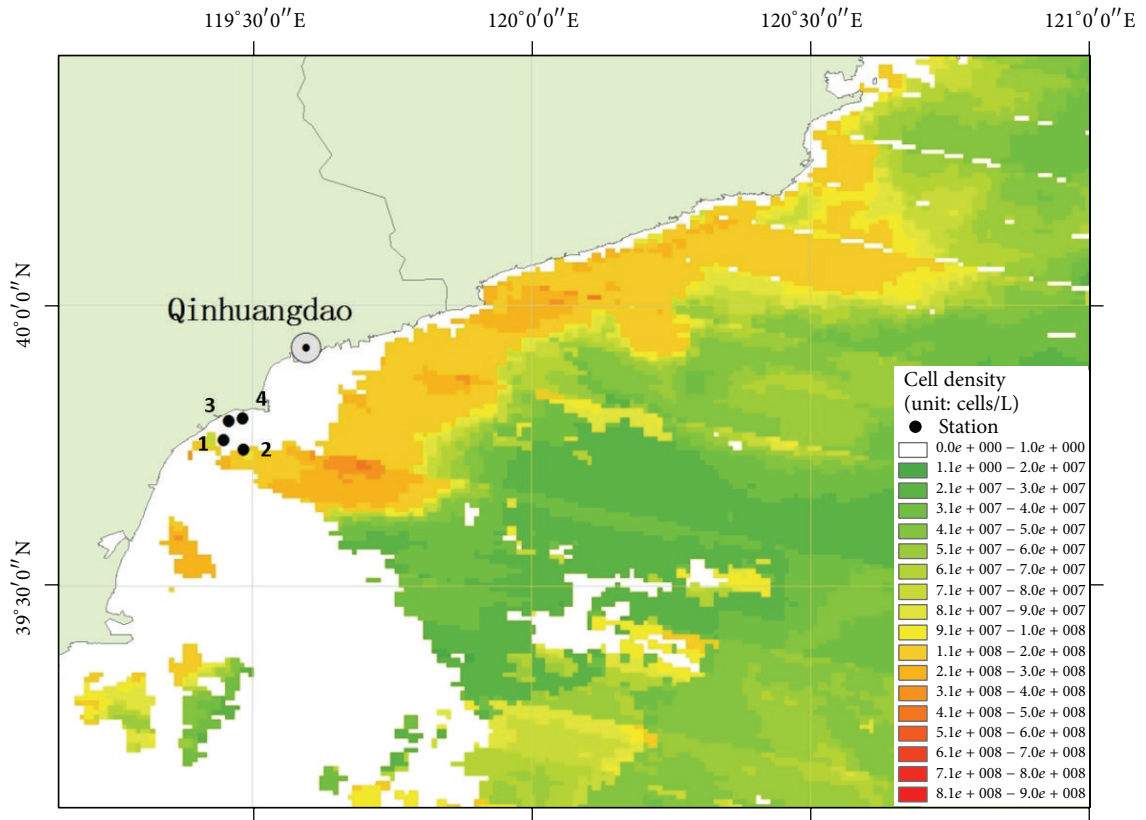


FIGURE 8: Cell density distribution of using single-band inversion model.

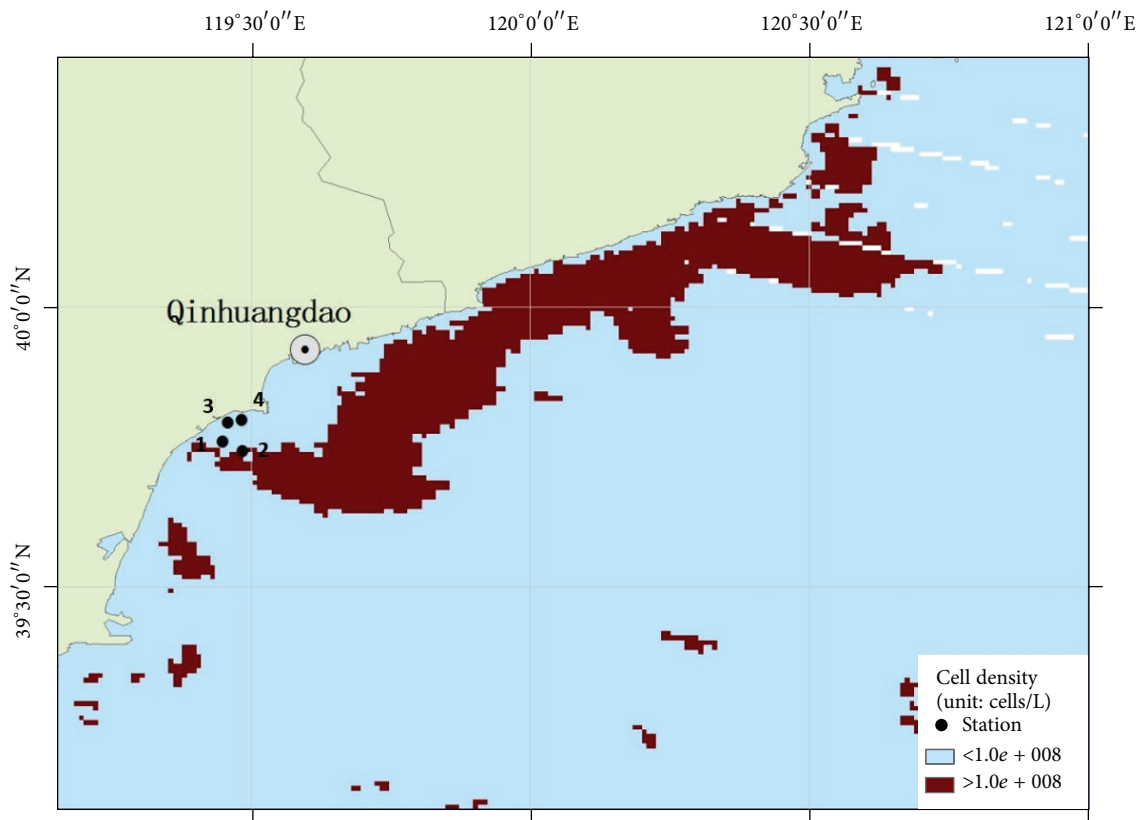


FIGURE 9: The distribution area of the *Aureococcus anophagefferens* red tide (single-band inversion).

properties of algae. Moreover, only a few models used to monitor red tides are based on the relationship between oceanic reflectance and cell density. In the present study, the backscattering properties of *A. anophagefferens* were examined and an empirical relationship between cell density and backscattering coefficients was found, in which the minimum regression coefficient was 0.97 at 488 nm. Additionally, the reflectance spectra were obtained, and with these values, single-band and multiband cell density inversion semianalytical models were employed, according to the MODIS central bands.

We used *in situ* measurement data to examine the accuracy and precision of models to predict red tides and found differences between the qualities of the models. Our results demonstrate that the cell densities calculated by the single-band inversion model are lower than those measured on site, but this bias is caused by suspended sediments. Although the value computed by the multiband inversion model was closer to the field-measured data, it could not accurately discern the red tide area in mixed pixels. In conclusion, cell density remote sensing inversion models have the potential to play a larger role in monitoring red tides in the future if they could distinguish inorganic particulate matter and phytoplankton from waters.

Conflict of Interests

The authors declare that there is no conflict of interests regarding the publication of this paper.

Acknowledgments

The authors thank the Marine Biology Group of the National Marine Environmental Monitoring Center for providing and cultivating the algal species and also the members of their team for helping them take the measurements. This work was supported by the National Marine Public Welfare Research Project of China under Grant no. 201305003, the National Natural Science Foundation of China under Grant no. 41276105, and the Fundamental Research Funds for the Central University under Grant no. 3132015081.

References

- [1] D. M. Anderson, P. M. Glibert, and J. M. Burkholder, "Harmful algal blooms and eutrophication: nutrient sources, composition, and consequences," *Estuaries*, vol. 25, no. 4, pp. 704–726, 2002.
- [2] D. M. Anderson, "Approaches to monitoring, control and management of harmful algal blooms (HABs)," *Ocean and Coastal Management*, vol. 52, no. 7, pp. 342–347, 2009.
- [3] K. D. Haddad, *Hydrographic factors associated with west Florida toxic red tide blooms: an assessment for satellite prediction and monitoring [M.S. thesis]*, University of South Florida, St. Petersburg, Fla, USA, 1982.
- [4] J. J. Cullen, Á. M. Ciotti, R. F. Davis, and M. R. Lewis, "Optical detection and assessment of algal blooms," *Limnology and Oceanography*, vol. 42, no. 5, pp. 1223–1239, 1998.
- [5] P. A. Tester and R. P. Stumpf, "Phytoplankton blooms and remote sensing: what is the potential for early warning," *Journal of Shellfish Research*, vol. 17, no. 5, pp. 1469–1471, 1998.
- [6] O. Schofield, J. Grzymiski, W. P. Bissett et al., "Optical monitoring and forecasting systems for harmful algal blooms: possibility or pipe dream?" *Journal of Phycology*, vol. 35, no. 6, pp. 1477–1496, 1999.
- [7] D. L. Pan, T. M. Mao, S. J. Li, and H. Huang, "Study on detection of coastal water environment of China by ocean color remote sensing," *Acta Oceanologica Sinica*, vol. 20, no. 1, pp. 51–63, 2001.
- [8] X. H. Xu, D. L. Pan, Z. H. Mao, and B. Y. Tao, "A new algorithm based on the background field for red tide monitoring in the East China Sea," *Acta Oceanologica Sinica*, vol. 33, no. 5, pp. 62–71, 2014.
- [9] R. P. Stumpf, M. E. Culver, P. A. Tester et al., "Monitoring *Karenia brevis* blooms in the Gulf of Mexico using satellite ocean color imagery and other data," *Harmful Algae*, vol. 2, no. 2, pp. 147–160, 2003.
- [10] M. C. Tomlinson, R. P. Stumpf, V. Ransibrahmanakul et al., "Evaluation of the use of SeaWiFS imagery for detecting *Karenia brevis* harmful algal blooms in the eastern Gulf of Mexico," *Remote Sensing of Environment*, vol. 91, no. 3-4, pp. 293–303, 2004.
- [11] M. C. Tomlinson, T. T. Wynne, and R. P. Stumpf, "An evaluation of remote sensing techniques for enhanced detection of the toxic dinoflagellate, *Karenia brevis*," *Remote Sensing of Environment*, vol. 113, no. 3, pp. 598–609, 2009.
- [12] C. Hu, F. E. Muller-Karger, C. Taylor et al., "Red tide detection and tracing using MODIS fluorescence data: a regional example in SW Florida coastal waters," *Remote Sensing of Environment*, vol. 97, no. 3, pp. 311–321, 2005.
- [13] Y.-H. Ahn and P. Shanmugam, "Detecting the red tide algal blooms from satellite ocean color observations in optically complex Northeast-Asia Coastal waters," *Remote Sensing of Environment*, vol. 103, no. 4, pp. 419–437, 2006.
- [14] J. Ishizaka, Y. Kitaura, Y. Touke et al., "Satellite detection of red tide in Ariake Sound, 1998–2001," *Journal of Oceanography*, vol. 62, no. 1, pp. 37–45, 2006.
- [15] R. P. Stumpf, "Applications of satellite ocean color sensors for monitoring and predicting harmful algal blooms," *Human and Ecological Risk Assessment*, vol. 7, no. 5, pp. 1363–1368, 2001.
- [16] F. H. Chang, M. Uddstrom, and M. Pinkerton, "Studies of the winter 2000 *Gymnodinium catenatum* outbreaks in New Zealand using remotely sensed sea surface temperature and chlorophyll a data from satellites," in *Proceedings of the Marine Biotoxin Science Workshop*, vol. 15, pp. 165–173, May 2001.
- [17] A. A. Gitelson, J. F. Schalles, and C. M. Hladik, "Remote chlorophyll-a retrieval in turbid, productive estuaries: Chesapeake Bay case study," *Remote Sensing of Environment*, vol. 109, no. 4, pp. 464–472, 2007.
- [18] J. E. O'Reilly, S. Maritorena, D. A. Siegel et al., "Ocean color chlorophyll a algorithms for SeaWiFS, OC2 and OC4: version 4," in *SeaWiFS Postlaunch Calibration and Validation Analysis*, S. B. Hooker and E. R. Firestone, Eds., Part 3, pp. 9–27, NASA Goddard Space Flight Center, Greenbelt, Md, USA, 2000.
- [19] K. L. Carder, F. R. Chen, Z. P. Lee, S. K. Hawes, and D. Kamykowski, "Semianalytic Moderate-Resolution Imaging Spectrometer algorithms for chlorophyll α and absorption with bio-optical domains based on nitrate-depletion temperatures," *Journal of Geophysical Research: Oceans*, vol. 104, no. 3, Article ID 1998JC900082, pp. 5403–5421, 1999.

- [20] S. Sathyendranath, G. Cota, V. Stuart, H. Maass, and T. Platt, "Remote sensing of phytoplankton pigments: a comparison of empirical and theoretical approaches," *International Journal of Remote Sensing*, vol. 22, no. 2-3, pp. 249–273, 2001.
- [21] D. A. Siegel, S. Maritorena, N. B. Nelson, and M. J. Behrenfeld, "Independence and interdependencies among global ocean color properties: reassessing the bio-optical assumption," *Journal of Geophysical Research C: Oceans*, vol. 110, no. 7, pp. 1–14, 2005.
- [22] Y. B. Son, J. Ishizaka, J.-C. Jeong, H.-C. Kim, and T. Lee, "Cochlodinium polykrikoides red tide detection in the South Sea of Korea using spectral classification of MODIS data," *Ocean Science Journal*, vol. 46, no. 4, pp. 239–263, 2011.
- [23] D. Z. Zhao, F. S. Zhang, L. Zhao, and P. F. Cong, "Detect of chlorophyll a and red tide in coastal water using band ration of AVHRR," *Marine Environmental Science*, vol. 22, no. 4, pp. 9–12, 2003.
- [24] C. Hu, F. E. Muller-Karger, D. C. Biggs et al., "Comparison of ship and satellite bio-optical measurements on the continental margin of the NE Gulf of Mexico," *International Journal of Remote Sensing*, vol. 24, no. 13, pp. 2597–2612, 2003.
- [25] R. M. Letelier and M. R. Abbott, "An analysis of chlorophyll fluorescence algorithms for the moderate resolution imaging spectrometer (MODIS)," *Remote Sensing of Environment*, vol. 58, no. 2, pp. 215–223, 1996.
- [26] W. E. Esaias, M. R. Abbott, I. Barton et al., "An overview of MODIS capabilities for ocean science observations," *IEEE Transactions on Geoscience and Remote Sensing*, vol. 36, no. 4, pp. 1250–1265, 1998.
- [27] M. Babin, A. Morel, and B. Gentili, "Remote sensing of sea surface sun-induced chlorophyll fluorescence: consequences of natural variations in the optical characteristics of phytoplankton and the quantum yield of chlorophyll a fluorescence," *International Journal of Remote Sensing*, vol. 17, no. 12, pp. 2417–2448, 1996.
- [28] D. Z. Zhao, F. S. Zhang, F. Du, H. Guo, and L. Zhao, "Fluorescence peak near 700 nm on the reflectance spectrum of algae in water: the relationship of fluorescence line height with chlorophyll a concentration," *High Technology Letters*, vol. 14, no. 5, pp. 68–72, 2004.
- [29] H. M. Dierssen, R. M. Kudela, J. P. Ryan, and R. C. Zimmerman, "Red and black tides: quantitative analysis of water-leaving radiance and perceived color for phytoplankton, colored dissolved organic matter, and suspended sediments," *Limnology and Oceanography*, vol. 51, no. 6, pp. 2646–2659, 2006.
- [30] J. P. Cannizzaro, K. L. Carder, F. R. Chen, C. A. Heil, and G. A. Vargo, "A novel technique for detection of the toxic dinoflagellate, *Karenia brevis*, in the Gulf of Mexico from remotely sensed ocean color data," *Continental Shelf Research*, vol. 28, no. 1, pp. 137–158, 2008.
- [31] H. Sasaki, A. Tanaka, M. Iwataki et al., "Optical properties of the red tide in Isahaya Bay, southwestern Japan: influence of chlorophyll a concentration," *Journal of Oceanography*, vol. 64, no. 4, pp. 511–523, 2008.
- [32] H. R. Gordon, O. B. Brown, R. H. Evans et al., "A semi-analytic model of ocean color," *Journal of Geophysical Research*, vol. 93, pp. 10909–10924, 1988.
- [33] K. L. Carder, S. K. Hawes, R. G. Steward, T. G. Peacock, and C. O. Davis, "Model for the interpretation of hyperspectral remote-sensing reflectance," *Applied Optics*, vol. 33, no. 24, pp. 5721–5732, 1994.
- [34] R. W. Austin, "The remote sensing of spectral radiance from below the ocean surface," in *Optical Aspects of Oceanography*, N. G. Jerlov and Steemann-Nielsen, Eds., pp. 317–344, Academic Press, London, UK, 1974.
- [35] Z. Lee, K. L. Carder, C. D. Mobley, R. G. Steward, and J. S. Patch, "Hyperspectral remote sensing for shallow waters. I. A semianalytical model," *Applied Optics*, vol. 37, no. 27, pp. 6329–6338, 1998.
- [36] S. A. Garver and D. A. Siegel, "Inherent optical property inversion of ocean color spectra and its biogeochemical interpretation I. Time series from the Sargasso Sea," *Journal of Geophysical Research*, vol. 102, no. 8, pp. 18607–18625, 1997.
- [37] S. Maritorena, D. A. Siegel, and A. R. Peterson, "Optimization of a semianalytical ocean color model for global-scale applications," *Applied Optics*, vol. 41, no. 15, pp. 2705–2714, 2002.
- [38] S. Maritorena and D. A. Siegel, "Consistent merging of satellite ocean color data sets using a bio-optical model," *Remote Sensing of Environment*, vol. 94, no. 4, pp. 429–440, 2005.
- [39] Z. P. Lee and K. L. Carder, "Effect of spectral band numbers on the retrieval of water column and bottom properties from ocean color data," *Applied Optics*, vol. 41, no. 12, pp. 2191–2201, 2002.
- [40] Z. Lee, K. L. Carder, and K. Du, "Effects of molecular and particle scatterings on the model parameter for remote-sensing reflectance," *Applied Optics*, vol. 43, no. 25, pp. 4957–4964, 2004.
- [41] Z. Lee, R. Arnone, C. Hu, P. J. Werdell, and B. Lubac, "Uncertainties of optical parameters and their propagations in an analytical ocean color inversion algorithm," *Applied Optics*, vol. 49, no. 3, pp. 369–381, 2010.
- [42] P. J. Werdell and C. S. Roesler, "Remote assessment of benthic substrate composition in shallow waters using multispectral reflectance," *Limnology and Oceanography*, vol. 48, no. 1, pp. 557–567, 2003.
- [43] B. A. Franz and P. J. Werdell, "A generalized framework for modeling of inherent optical properties in remote sensing applications," in *Proceedings of the Ocean Optics*, Anchorage, Alaska, USA, September–October 2010.
- [44] C. J. Gobler, D. L. Berry, S. T. Dyhrman et al., "Niche of harmful alga *Aureococcus anophagefferens* revealed through ecogenomics," *Proceedings of the National Academy of Sciences of the United States of America*, vol. 108, no. 11, pp. 4352–4357, 2011.
- [45] R. D. Vaillancourt, C. W. Brown, R. R. L. Guillard, and W. M. Balch, "Light backscattering properties of marine phytoplankton: relationships to cell size, chemical composition and taxonomy," *Journal of Plankton Research*, vol. 26, no. 2, pp. 191–212, 2004.
- [46] J. L. Mueller and G. S. Fargion, *Ocean Optics Protocols for Satellite Ocean Color Validation*, NASA Goddard Space Flight Center, Greenbelt, Md, USA, 2002.
- [47] C. D. Mobley, "Estimation of the remote-sensing reflectance from above-surface measurements," *Applied Optics*, vol. 38, no. 36, pp. 7442–7455, 1999.
- [48] L. Van Heukelem and C. S. Thomas, "Computer-assisted high-performance liquid chromatography method development with applications to the isolation and analysis of phytoplankton pigments," *Journal of Chromatography A*, vol. 910, no. 1, pp. 31–49, 2001.
- [49] L.-L. Jiang, L. Wang, D.-Z. Zhao, and X. Wang, "Backscattering characteristics of *Amphidinium carerae* Hulbert," *Spectroscopy and Spectral Analysis*, vol. 33, no. 7, pp. 1892–1896, 2013.
- [50] L. L. Jiang, L. Wang, D. Z. Zhao, X. Wang, and X. X. Wang, "Spectral variability of particulate backscattering of nanoplankton and microplankton—focusing on *skeletonema costatum*

- and proroentrum micans,” *Marine Environmental Science*, vol. 32, no. 6, pp. 884–888, 2013.
- [51] L. L. Jiang, D. Z. Zhao, and L. Wang, “Backscattering properties of marine phytoplankton *Prorocentrum micans*,” *International Journal of Remote Sensing*, vol. 35, no. 11-12, pp. 4275–4286, 2014.
- [52] D. Stramski, A. Bricaud, and A. Morel, “Modeling the inherent optical properties of the ocean based on the detailed composition of the planktonic community,” *Applied Optics*, vol. 40, no. 18, pp. 2929–2945, 2001.
- [53] Y.-H. Ahn, A. Bricaud, and A. Morel, “Light backscattering efficiency and related properties of some phytoplankters,” *Deep Sea Research Part A, Oceanographic Research Papers*, vol. 39, no. 11-12, pp. 1835–1855, 1992.
- [54] G. Dall’Omo, T. K. Westberry, M. J. Behrenfeld, E. Boss, and W. H. Slade, “Significant contribution of large particles to optical backscattering in the open ocean,” *Biogeosciences*, vol. 6, no. 6, pp. 947–967, 2009.
- [55] A. L. Whitmire, W. Scott Pegau, L. Karp-Boss, E. Boss, and T. J. Cowles, “Spectral backscattering properties of marine phytoplankton cultures,” *Optics Express*, vol. 18, no. 14, pp. 15073–15093, 2010.
- [56] W. Zhou, G. F. Wang, Z. H. Sun et al., “Variations in the optical scattering properties of phytoplankton cultures,” *Optics Express*, vol. 20, no. 10, pp. 11189–11206, 2012.
- [57] A. Morel and Y. H. Ahn, “Optics of heterotrophic nanoflagellates and ciliates: a tentative assessment of their scattering role in oceanic waters compared to those of bacterial and algal cells,” *Journal of Marine Research*, vol. 49, no. 1, pp. 177–202, 1991.